2015

Modelling of inverter interfaced renewable energy resources to investigate grid interactions

Brian K. Perera
University of Wollongong, bkp389@uowmail.edu.au

School of Electrical, Computer and Telecommunications Engineering

Modelling of Inverter Interfaced Renewable Energy Resources to Investigate Grid Interactions

Brian Perera, BSc (Eng)

Supervisors

Dr Philip Ciufo and Professor Sarath Perera

This thesis is presented as part of the requirements for the

Award of the Degree of

Doctor of Philosophy

of the

University of Wollongong

March 2015

Dedicated to my parents and my family...

Acknowledgements

I wish to express my sincere appreciation to all the people who helped me in many ways throughout my PhD candidature at the University of Wollongong.

I would like to pay my greatest gratitude and appreciation to my principal supervisor, Dr Phil Ciufo and my co-supervisor, Professor Sarath Perera of the University of Wollongong (UOW), for providing me the opportunity to pursue postgraduate studies at UOW. My supervisors' dedication, patience, knowledge and experience could not have been surpassed. I admire their guidance towards growing me up academically and personally over last few years.

My PhD research project was funded by the Australian Research Council (ARC) and Essential Energy through the Linkage Grant LP100100618. Without the financial support received from these organisations, my dream to complete a PhD degree may not have been realised. The guidance of Chief Investigators of this research project, Associate Professor Kashem Muttaqi, Professor Danny Sutanto and my supervisors and the Partner Investigator, Leith Elder, Senior Engineer, Essential Energy to reach the goals of the project is also highly appreciated.

The personal and administrative support provided by Sasha Nikolic, Roslyn Causer-Temby, Raina Lewis, Megan Crowl and Esperanza Gonzalez at various stages of my PhD degree are acknowledged with gratitude. Special thanks go to Dr Vic Smith, Dr Sridhar Pulikanti, Sean Elphick, Hamid Ghasemabadi and Dr Douglas Carter for their generous technical support provided while establishing the laboratory experimental setup of my research project. Timely technical assistances received from Carlo Giusti, Frank Mikk, Steve Petrou and Neil Wood were key factors of being able to commission the experimental setup of my research project within a short period of time. I am very much thankful to them.

I would like to thank Dr Nishad Mendis and Dr Upuli Jayatunga for the support given during my candidature. Thanks also go to my fellow graduate students Devinda Perera, Amila Wickramasinghe, Dothinka Ranamuka and Athmi

Jayawardena for their valuable input to my research work.

Last but not least, I would like to thank my parents, Damian Perera and Marie Fernando, my wife, Aishanee Weerasundara and the rest of my family for their unconditional love and continuous support. I would not have been able to complete this Thesis without them.

Certification

I, Brian Perera, declare that this thesis, submitted in fulfilment of the requirements for the award of Doctor of Philosophy, in the School of Electrical, Computer and Telecommunications Engineering, University of Wollongong, is entirely my own work unless otherwise referenced or acknowledged. This manuscript has not been submitted for qualifications at any other academic institute.

Brian Perera

Abstract

The public low voltage (LV) electricity networks are being increasingly impacted by the connection of many small-capacity solar photovoltaic (PV) systems. These PV systems offer financial benefits to owners while bringing environmental benefits by reducing the electricity generation using fossil fuels. However, there are technical challenges that should be addressed in order to enable the smooth integration of PV systems to public LV electricity networks.

A detailed simulation model of a PV system is a useful tool for analysing the system-level impact of integrating multiple PV systems to public LV electricity networks. Therefore, such a simulation model of a grid-connected single-phase two-stage PV system with associated controllers is developed in this Thesis. The accuracy of the developed simulation model is validated by comparing simulation results with experimental results obtained from a comparable experimental PV system established in the laboratory. The developed simulation model of a PV system forms the basis for the rest of the work presented in this Thesis.

The introduction of multiple PV systems may result in public LV electricity networks becoming more susceptible to voltage variations and fluctuations caused by the injected active power variations from the PV systems. Furthermore, if the power generation by PV systems exceeds that of the local load demand, there is a possibility of power flowing into the grid for which the traditional LV systems are not designed. As a result, there can be over voltages in the LV network leading to tripping of PV systems. The voltage rise in public LV electricity networks integrated with multiple PV systems is a critical technical problem that should be addressed. Traditional voltage control techniques are not adequate under such situations. As a consequence, there is a demand for fast acting dynamic voltage regulating devices which can respond within a short period of time to the variations and restore the system to its normal operation.

An opportunity exists to regulate the respective point of common coupling (PCC) voltages by dynamically controlling both active and reactive power injec-

tion by PV systems that are integrated to an public LV electricity network via voltage source converters. In this Thesis, two closed-loop controllers that are able to regulate the PCC voltage by dynamically controlling the active and reactive power of a PV system are developed. The dynamic behaviour of each controller is analysed in detail. By combining the dynamic active and reactive power controllers, two novel operating strategies for PV systems; fixed minimum power factor operation and fixed maximum apparent power operation, are proposed. The simulation results are validated using experimental work confirming the accuracy of the derived plant models, the robustness of the designed controllers and the feasibility of implementing the proposed novel operating strategies in PV systems.

In a public LV electricity network, to which multiple PV systems are integrated, the grid voltage can be controlled if each PV system regulates their respective PCC voltage. In such an application of PV systems, the possibility of control interactions between PV systems exists since PV systems operate electrically close to each other. In this Thesis, possible control interactions between multiple PV systems are investigated and results of simulation studies are presented. The small-signal model of an LV radial power distribution feeder with multiple PV systems developed in this Thesis is used to perform modal analysis to verify identified control interactions. The experimental results presented confirm that there are control interactions between multiple PV systems when these systems control the grid voltage dynamically by absorbing reactive power from the grid. The control techniques that can be applied to minimise the effects of control interaction between PV systems are discussed and validated experimentally.

According to applicable standards for grid-integrated PV systems, a PV system must be disconnected from the grid when the terminal voltage of the PV system exceeds a defined maximum voltage. With this directive, in certain situations, PV systems connected at nodes at which the voltage sensitivity is high, may get disconnected from the grid while PV systems connected at less sensitive

nodes continue to operate. In such a situation, owners whose PV systems are connected at nodes at which the voltage sensitivity is high, may lose their revenue. In order to minimise the impact of such a disadvantage, a power sharing methodology that can be implemented in PV systems connected to a radial distribution feeder is developed in this Thesis. In the developed method, power sharing is achieved by operating PV systems within an allocated voltage bandwidth that is applicable to the PCC voltage of a PV system. The developed power sharing methodology provides a pathway to share power injection by PV systems instead of leading to the disconnection of some PV systems and not others, which leads to an inequitable operating environment.

The analytical tools and experimentally validated simulation models that are developed in this Thesis will be beneficial for electricity distribution utilities who at present, have to deal with uncertainties related to the impact of high penetration levels of PV systems in their LV electricity networks. Further, advanced control and coordination techniques and methodologies developed in this Thesis will also enable the development of proper coordination and control strategies which should be adopted for voltage control and reactive power compensation while improving system stability and efficiency.

List of principal symbols and abbreviations

A/D	analog to digital
AC	alternating current
BW_x	bandwidth
C_{b}	base capacitance
C_{dc}	DC-link capacitor of a VSC
C_{f}	capacitor of an LCL filter
C_{pv}	filtering capacitor at the output of a PV array
CSC	current source converter
D	duty ratio
D/A	digital to analog
DC	direct current
δ	power angle
ΔI_x	small change in current
ΔV_{dc}	magnitude of the DC-link voltage ripple
ΔV_x	small change in voltage
DSP	digital signal processor
DSTATCOM	distribution static synchronous compensator
En_{p}	PCC V_P controller enable signal
En_{q}	PCC V_Q controller enable signal
f_{dc}	switching frequency of a DC-DC boost converter in Hz
f_{res}	resonant frequency in Hz
f_{sw}	switching frequency of a VSC in Hz
FACTS	flexible AC transmission system
H_{bp}	gain of a band-pass filter
HC	harmonic compensator
i	output current of a VSC
I_{dc}	current flow through the DC-link
I_{dpv}	current conducted by the diode of a PV cell model
i_{g}	current injected to the grid by a VSC
I_{g}	rms value of i_{g}
I_{gp}	active current component of I_{g}
I_{gmp}	peak value of I_{gp}

I_{gq}	reactive current component of I_{g}
I_{gmq}	peak value of I_{gq}
I_{gmq0}	initial value of I_{gmq}
I_{gpmref}	current reference of I_{gpm}
i_{gref}	current reference of i_{g}
I_{pv}	current output of a PV array or PV cell
I_{pvref}	current reference of I_{pv}
I_{gqmref}	current reference of I_{gqm}
I_{scpv}	saturation current of the diode of a PV cell model
IGBT	insulated gate bi-polar transistor
InC	incremental conductance
k	Boltzmann's constant (1.38×10^{-23} J/K)
$k_{\mathrm{i}x}$	integral gain
$k_{\mathrm{p}x}$	proportional gain
L	live conductor
L_{dc}	inductor of a DC-DC boost converter
L_{fc}	inductance of the converter-side inductor of an LCL filter
L_{fg}	inductance of the grid-side inductor of an LCL filter
L_{g}	inductance of X_{g}
LMS	least-mean-square
LV	low voltage
m	modulation signal
MOSFET	metaloxidesemiconductor field-effect transistor
MPP	maximum power point
MPPT	maximum power point tracking
N	neutral conductor
n_d	diode quality factor (1¡n¡2)
N_x	electrical node
nh	harmonic number
ω	fundamental frequency in rad/s
ω_{e}	estimated frequency of v_{g} in rad/s
ω_{bp}	centre frequency of a band-pass filter in rad/s
ω_c	cut-off frequency in rad/s
P	active power

P & O	perturb and observe
P_{c}	active power output of a VSC
P_{dc}	power flow through the DC-link
P_{g}	active power injected to the grid by a PV system
P_{mpp}	power available at MPP
P_{n}	nominal active power
P_{pv}	power output of a PV array
P_{ref}	active power reference of P_{g}
PCC	point of common coupling
PI	proportional-integral
PLL	phase-locked-loop
PR	proportional-resonant
PSS	power system stabiliser
PV	solar photovoltaic
q	electron charge (1.602×10^{-19} As)
Q	reactive power
Q_{bp}	quality factor of a band-pass filter
Q_{c}	reactive power output of a VSC
Q_{g}	reactive power injected to the grid by a PV system
Q_{ref}	reactive power reference of Q_{g}
R/X	resistance to reactance
R_{d}	damping resistor in series with C_{f}
R_{fc}	resistance of the converter-side inductor of an LCL filter
R_{fg}	resistance of the grid-side inductor of an LCL filter
R_{g}	resistive component of grid impedance
R_{shpv}	shunt resistance of a PV cell
R_{srpv}	series resistance of a PV cell
rms	root-mean-square
S_{b}	base power
S_{r}	kVA rating of a VSC
s-PLL	synchronous reference frame PLL
SPWM	sinusoidal pulse-width modulation
τ_{d}	time constant of a first-order lag element
THD	total harmonic distortion

ϑ	estimated phase angle of v_{g}
$U_{\max}$	253 V
v	output voltage of a VSC
V_{α}	α-axis voltage
V_{β}	β-axis voltage
v_0	fundamental voltage component of v
V_{b}	base voltage
v_{c}	voltage across C_{f} and R_{d}
V_{dc}	DC-link voltage of a VSC
V_{dcavg}	average DC-link voltage
V_{dcref}	DC-link voltage reference
V_{dpv}	voltage across the diode of a PV cell model
v_{g}	voltage at the PCC of a VSC
V_{g}	rms value of v_{g}
V_{gm}	peak value of v_{g}
V_{gm0}	initial value of V_{gm}
V_{gmref}	voltage reference of V_{gm}
V_{mpp}	voltage at MPP
V_{mpp0}	initial V_{mpp}
V_{ocpv}	open circuit voltage of a PV array
V_{pv}	voltage output of a PV array or a PV cell
V_{pvref}	voltage reference of V_{pv}
v_{s}	voltage of the equivalent Thévenin voltage source
V_{s}	rms value of v_{s}
V_d	d-axis voltage
V_{gx}	rms voltage at node x
V_q	q-axis voltage
VCO	voltage-controlled-oscillator
VSC	voltage source converter
X_{g}	reactive component of grid impedance
$x_{\mathrm{q}x}$	state variable
Y_{ij}	admittance between node i and j
Z_{b}	base impedance

Publications Arising from the Thesis

1. Brian Perera, Phil Ciufo and Sarath Perera. Simulation Model of a Grid-Connected Single-Phase Photovoltaic System in PSCAD/EMTDC. In *Proc. IEEE International Conference on Power System Technology (POWERCON)*, Auckland, New Zealand, October 2012.

2. Brian Perera, Phil Ciufo and Sarath Perera. Power Sharing among Multiple Solar Photovoltaic (PV) Systems in a Radial Distribution Feeder. In *Proc. Australasian Universities Power Engineering Conference (AUPEC 2013)*, Vienna, Austria, October 2013.

3. Brian Perera, Phil Ciufo and Sarath Perera. Point of Common Coupling (PCC) Voltage Control of a Grid-Connected Solar Photovoltaic (PV) System. In *Proc. 39th Annual Conference of the IEEE Industrial Electronics Society (IECON'13)*, Vienna, Austria, November 2013.

4. Brian Perera, Phil Ciufo and Sarath Perera. Advanced Point of Common Coupling Voltage Controllers for Grid-Connected Solar Photovoltaic (PV) Systems. Accepted for publication in *Elsevier - Renewable Energy Journal*.

Table of Contents

List of Figures

List of Tables

Chapter 1

Introduction

1.1 Statement of the Problem

The overwhelming political drive towards promoting, developing and introducing sustainable energy technologies is a hallmark of the beginning of the twenty first century. The main aim of such a political drive is to minimise the dependency on and also the usage of rapidly depleting fossil fuel resources such as coal, petroleum and natural gas. There is also a strong desire to reduce the associated pollution of fossil fuel based electricity generation and to reduce global warming. As a result of these factors, many developed countries around the world are seen to be taking initiatives to promote, develop and introduce sustainable energy technologies in order to minimise the percentage use of fossil fuels to meet their energy demand.

Electricity is one of the main forms of energy on which people largely depend and is conventionally generated by large scale centralised power generating plants. Fossil fuels are the main source of energy in most of these power generating plants. With the efforts to promote sustainable energy technologies in order to minimise the dependency on fossil fuels, renewable energy resources such as solar, wind, hydro, tides, waves and geothermal heat have been identified as viable sources of energy to generate electrical power. Among the identified renewable energy sources, solar and wind have been further identified as the most promising sources of renewable energy to generate electrical power. Solar and wind are well known

to be dispersed energy sources with low energy concentration. As a result, a large number of medium to small scale distributed solar photovoltaic (PV) systems and wind-power systems are being integrated to the electrical power grid.

Governments and electricity utilities around the world are making significant changes to their traditional policies in order to allow external parties to integrate their own renewable power generating systems to the electrical power grid with efforts to promote sustainable energy technologies. Further, commercially attractive rebates, grants and credit schemes are being introduced to increase the participation of external parties in renewable power generation. These actions have resulted and will continue to make significant changes to the traditional electrical power grid. One such significant change is the integration of a large number of small scale PV systems (up to 10 kW) to low voltage (LV) public electricity networks, leaving power distribution utilities with many technical challenges to deal with.

Electrical power generated from a PV system solely depends on factors such as solar irradiance and ambient temperature. These factors are subjected to sudden or slow variations, resulting in changes in the output power. As PV systems are interfaced to LV power grids through power electronic converters (inverters) and as no mechanical inertia is involved, changes in power flow can take place in relatively short periods . Such changes can cause rapid voltage fluctuations at the point of common coupling (PCC)[1] of a PV system and can lead to over-voltage, under-voltage and/or flicker problems. Further, switching frequency and low-order harmonic levels may increase with the addition of PV systems to LV power grids, possibly deteriorating the quality of power supply.

Simulation studies can be performed in order to investigate the terminal characteristics of a PV system under different operating conditions and to analyse how LV power grids will behave when multiple PV units are integrated. In order to

[1]In most of the analysis presented in this Thesis, the impedance of the service wire of a PV system is neglected. Therefore, the point of connection (POC) of a PV system is referred to as the point of common coupling (PCC) in this Thesis.

perform such simulation studies, the development of accurate simulation models of PV systems is necessary. A detailed simulation model of a PV system that represents the dynamic behaviour of all the physical components of a grid-connected PV system and also the associated control loops is essential to investigate the dynamic behaviour of a single or multiple grid-connected PV systems under different operating conditions.

If a detailed simulation model of a PV system is used to represent PV systems in a multiple PV installation, the actual time required to simulate a case may be quite prohibitive in a conventional and commonly available simulation platform. Therefore, in certain simulation studies, a simplified simulation model that optimally represents the dynamic characteristics of a grid-connected PV system is also required.

The steady-state voltage of an LV power grid may rise above the limits specified in the applicable standards as a consequence of integrating multiple PV systems. Such operating conditions in an LV power grid may occur especially in situations when the power generation from PV systems is greater than loads at a peak and the load on the LV power grid is at a minimum. The over-voltage operating conditions in an LV power grid may result in the disconnection of PV systems and also in certain situations the loads designed to operate within standard voltage limits in an LV power grid may get exposed to excessive voltage levels as well. The voltage variation in an LV power grid with high penetration of PV systems is highly dynamic because of the frequent variation of solar irradiance and ambient temperature. As a result, conventional static voltage regulation techniques such as fixed tap settings at the distribution transformers, step voltage regulators and fixed capacitors are not adequate to regulate the voltage of an LV power grid that is highly penetrated with PV systems. Therefore, the deployment of fast acting dynamic voltage regulating devices in LV power grids are required or PV systems may have to be built with such voltage regulating capabilities.

The speed of response of a PV system is very fast. Further, the PCC voltage

of a PV system is sensitive to the power flow of the PV system which can be dynamically controlled. Therefore, PV systems that are integrated to an LV power grid via appropriately designed power electronic converter systems and controls can be deployed to regulate the grid voltage dynamically by regulating the PCC voltage of each PV system. Furthermore, dedicated dynamic voltage control devices such as distribution-static synchronous compensators (DSTATCOMs) can also be integrated to regulate the voltage of an LV power grid dynamically. In order to utilise PV systems and DSTATCOMs to dynamically regulate the voltage of an LV power grid effectively and efficiently, the development and integration of additional control loops, control strategies and algorithms are necessary.

In the future, with a high penetration of PV systems, DSTATCOMs and PV systems may be deployed to regulate the voltage dynamically. In such an LV power grid, since PV systems and DSTATCOMs operate very close to each other, there can be operational and control interactions between these devices. The control action of a PV system or a DSTATCOM may significantly affect the operation and control of another PV system or a DSTATCOM and may lead to unstable operating conditions in the LV power grid. Therefore, the identification of any control and operational interactions when multiple PV systems and DSTATCOMs dynamically regulate the grid voltage and the development of techniques to mitigate any negative impact of interaction among PV systems and DSTATCOMs on the operation and control of an LV power grid is essential.

The negative impact of a limited number of PV systems is tolerable in the operation and control of existing LV power grids. Therefore, the operation of PV systems connected to LV power grids is not monitored to the same extent as conventional, large generators. However, once PV systems are highly penetrated, their collective impact on the operation and control of LV power grids will be significant. Therefore these PV systems need to be incorporated with proper coordination and control schemes for smooth operation of LV power grids. However, it is unclear whether or not all PV systems should provide voltage support,

or should there be a staged introduction of this support. For staged introduction of voltage support, development of mechanisms for conveying the appropriate changes to control parameters in a coordinated and timely manner is necessary. While coordinated control schemes can be implemented with the aid of a common communication media, the first stage is seen to be one that does not depend on such a media.

1.2 Research Objectives and Methodologies

The research studies presented in this Thesis focus on high density, grid-connected PV installations where multiple numbers of small scale PV systems operate physically very close to each other. The main objective of the work presented in this Thesis is to facilitate the power distribution utilities with new and improved methodologies and tools to perform advanced system level studies in LV power grids to which multiple PV systems are integrated and to identify and implement the possibilities of utilising PV systems to improve the operation and control aspects of LV power grids. These objectives are achieved through:

- The development of detailed and optimised simulation models of a grid-connected PV system, in order to perform system level simulation studies to identify adverse effects on the performance of LV power grids as a consequence of integrating multiple PV systems.

- The development of advanced PCC voltage controllers and control strategies for grid-connected PV systems and DSTATCOMs for the purpose of regulating grid voltage dynamically.

- The identification and quantification of interaction among multiple PV systems and DSTATCOMs if these systems regulate the voltage of an LV power grid dynamically.

- The establishment of novel control and coordination strategies that do not

rely on a communication media for smooth and efficient operation of LV power grids with highly penetrated PV systems.

A simulation model of a PV system should be able to represent the dynamic behaviour of an actual PV system connected to an LV power grid. Therefore, the dynamic behaviour of all the physical components and all control loops that a PV system contains should be accurately modelled. In order to develop such a detailed model, the design details of commercially available PV systems should be available. Since such design details were not readily available due to the commercial aspects of these systems, an alternative approach was undertaken. The detailed simulation model was developed after an extensive review of the recently published technical literature on the power electronic design and the control of grid-connected PV systems. The completed design was modelled in both PSCAD/EMTDC and MATLAB/Simulink. These simulation platforms have been identified as the most appropriate simulation programs to model and investigate power systems in general. The model developed in PSCAD/EMTDC was initially used to examine the performance of a grid-connected PV system under varying operating conditions in an LV power grid and subsequently this study was extended to a multiple PV installation.

The simulation models of a grid-connected PV system should be verified against an actual PV system for the accuracy of the representation of critical dynamics. Therefore, a laboratory scale experimental platform that consists of two, grid-connected PV systems was implemented. The design of each experimental PV system was similar to that of the simulation model developed. In the experimental platform, PV arrays were established through sophisticated PV array emulators, and commercially available power electronic systems were used to implement the converters in experimental PV systems. The control systems of PV systems were implemented using dSPACE rapid control prototyping systems and the detailed simulation model developed in MATLAB/Simulink was utilised to implement the digital control systems in dSPACE control systems. In

the experimental platform, the power distribution grid was established through a programmable voltage source and a passive impedance network. The experimental platform provided great flexibility to perform experimental studies under variable grid conditions and solar irradiance levels and, more importantly, enabled the implementation and testing of novel control systems and coordination strategies developed. The experimental platform was initially utilised to verify the accuracy of the simulation models and later it was utilised for system level studies, testing of novel control systems and coordination strategies, and to identify dynamic interaction between multiple PV systems. The results of both simulation and experimental studies were used to derive a simplified model to optimally represent the dynamic characteristics of a grid-connected PV system.

The advanced control loops should be built into a PV system to dynamically regulate the PCC voltage of the PV system. Firstly, for a given LV power grid, the sensitivity of the PCC voltage to injected active and reactive power from a PV system was evaluated. Then, closed-loop controllers that are able to regulate the PCC voltage by dynamically controlling the active and reactive power response of the PV system were proposed. The plant model of each controller has been theoretically derived. Further, different types of compensators were evaluated to identify a suitable compensator for the closed-loop PCC voltage controllers to regulate the PCC voltage at a given reference voltage. By combining the dynamic active and reactive power controllers proposed, novel operating strategies have been introduced for effective utilisation of PV systems to control the grid voltage dynamically. The simulation and experimental results have been used to validate and confirm the accuracy of the derived plant models, the robustness of the designed controllers, and the feasibility of implementing the proposed novel operating strategies in PV systems.

A key research objective was to identify possible interactions when multiple PV systems and DSTATCOMs actively control the PCC voltage of each individual system in order to regulate the grid voltage dynamically. Simulation studies

were carried out to identify interactions in a multiple PV installation where the voltage at each PCC is actively regulated, starting with two PV systems connected to an LV power grid. Further, a small signal model of a grid-connected PV system was derived to mathematically quantify the level of interaction between multiple PV systems when dynamic voltage regulation is enabled. The experimental platform that was established by integrating two PV systems was effectively used to validate the simulation results obtained to identify dynamic interaction between multiple PV systems and also to validate the accuracy of the small signal model derived. Finally, DSTATCOMs that were supplied by the industry partner of this research project were integrated to the implemented experimental platform to perform rigorous experimental tests to identify dynamic interaction between DSTATCOMs as well as between DSTATCOMs and PV systems when they operated close to each other.

The establishment of novel control and coordination strategies for an LV power grid with high level of penetration of PV systems was carried out considering the availability of communication systems. Considering that there exists no communication media, a power sharing methodology was proposed for PV systems that are connected to a radial distribution feeder by allocating a grid voltage bandwidth for each PV system to operate. The closed-loop PCC voltage controllers were utilised to implement the proposed power sharing methodology. The effectiveness of the proposed power sharing methodology was evaluated through simulation and experimental studies following integration of the control algorithms to both the simulation models and the experimental setup.

1.3 Outline of the Thesis

A brief description on the contents of the remaining chapters is given here.

Chapter 2 is a literature review providing an overview on the design, operation and control of a grid-connected PV system. Further, the power electronic converter topologies and overall control and modelling philosophies of grid-connected

PV systems are reviewed. The technical challenges that the power distribution utilities may face with integration of multiple PV systems to LV power grids are discussed in this chapter. This chapter also describes the importance and the necessity for development of advanced PCC voltage controllers for PV systems, identifying dynamic interaction among multiple grid-connected PV systems and establishing novel control and coordination strategies for multiple grid-connected PV systems. Chapter 2 also provides the background knowledge for the work presented in Chapters $5 - 7$.

In Chapter 3, a generalised model of a grid-connected PV system that is capable of injecting both active and reactive power to the grid is developed. The selection criteria of the critical components in the PV system are described and design details and selection of control parameters of the control system of the PV system are elaborated. Finally, the dynamic performance of the developed simulation model is presented under rapid variation of solar irradiance and grid voltage. In the last section of this chapter, the dynamic characteristics of the simulation model are verified against the dynamic performance of implemented experimental PV systems. The simulation model developed in this chapter and the established experimental platform forms the basis for most of the work presented in this Thesis.

Chapter 4 focuses on the design and development of dynamic PCC voltage controllers for grid-connected PV systems. Firstly, the plant models of the PCC voltage controllers that regulate the PCC voltage of a PV system dynamically which control the active and reactive power response of a PV system are derived theoretically. With regard to this, three different types of compensators are evaluated to identify a suitable compensator for the closed-loop PCC voltage controllers and the sensitivity of the controller gains and the grid impedance on the response time of the closed-loop PCC voltage controllers are discussed. Secondly, two advanced PCC voltage control strategies developed based on the closed-loop PCC voltage controllers are presented.

The important findings of the extensive studies performed with the developed simulation models and the experiments carried out with the implemented experimental platform and DSTATCOMs provided by the industry partner of this research project, in order to identify any dynamic interaction among multiple PV systems and DSTATCOMs, are illustrated in Chapter 5. Methodologies are discussed to mitigate the identified dynamic interactions. In the final part of this chapter, a small signal model of a grid-connected PV system is derived, taking into consideration the critical dynamics represented at the terminals of a grid-connected PV system that regulates the PCC voltage dynamically with PCC voltage controllers derived in Chapter 4. In Chapter 6, a simplified model of a grid-connected PV system that optimally represents the terminal characteristic of a grid-connected PV system that dynamically regulates the PCC voltage is derived analysing simulation and experimental results presented in Chapters 3, 4 and 5.

Chapter 7 establishes novel control and coordination strategies for a power distribution grid with high penetration of PV systems. In this chapter, a power sharing methodology that utilises the closed-loop PCC voltage controllers presented in Chapter 4 is established. The developed power sharing methodology is applicable for PV systems integrated to a radial power distribution feeder and that is based on allocating a voltage bandwidth for each PV system to operate. The methodology to determine the voltage bandwidth of each PV system is elaborated. The experimental and simulation results obtained to verify the robustness of the proposed power sharing methodology are presented in a latter part of this chapter followed by a discussion on identified limitations in effectively implementing the proposed power sharing methodology in actual PV systems.

Finally, in Chapter 8, the major outcomes of the work presented in this Thesis are summarised, and recommendations and suggestions are made for future work.

Chapter 2

Literature Review

2.1 Introduction

This chapter provides an overview of the operation and control of grid-connected PV systems, covering associated challenges when these PV systems are operated in a multiple PV installation. Section 2.2 gives a brief introduction to PV energy conversion and modelling aspects of a PV array. Sections 2.3–2.5 cover widely used power electronic converter topologies for integrating PV systems to the grid, giving significant attention to the operation and control of a PV system integrated to a grid via a current-controlled voltage source converter (VSC); the focus of this Thesis. The impact of integrating multiple PV systems to a public LV electricity network is discussed in Section 2.6. The application of PV systems in the voltage control in LV power grids is discussed in Sections 2.7 and 2.8 and provides the basis for Chapter 4 of this Thesis. Two key sections of this chapter, Sections 2.9 and 2.10, discuss the dynamic interaction between multiple converter systems and coordination strategies that are applicable to the operation of multiple converters integrated to a grid respectively. These two sections form the background for Chapters 5, 6 and 7. Finally, this chapter is summarised in Section 2.11.

2.2 Solar photovoltaic energy

The solar photovoltaic energy is the energy converted from sunlight to electricity. This energy conversion is achieved by using solar panels. PV cells are the main building blocks of a solar panel. A conventional PV cell is made of semiconductor materials such as silicon that exhibit the photovoltaic effect.

2.2.1 Equivalent circuit of a PV cell

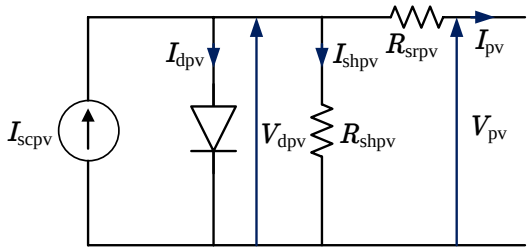

Figure 2.1: Equivalent circuit of a PV cell

The equivalent circuit of a PV cell is shown in Fig. 2.1. The DC current that is generated when a PV cell is exposed to sunlight is I_{scpv} and varies linearly with solar irradiance. The output current of the model of a PV cell, I_{pv} shown in Fig. 2.1 can be determined according to (2.1) [1]-[2].

$$I_{\text{pv}} = I_{\text{scpv}} - I_{\text{dpv}} - \left(\frac{V_{\text{pv}} + I_{\text{pv}} R_{\text{srpv}}}{R_{\text{shpv}}}\right) \tag{2.1}$$

In (2.1),

$I_{\text{dpv}} = \; I_{\text{scpv}} \left[e^{q(V_{\text{pv}}+I_{\text{pv}}R_{\text{srpv}})/n_d kT_{\text{pv}}} - 1\right]$

I_{dpv} current conducted by the diode

I_{scpv} saturation current of the diode

V_{pv} output voltage of the PV cell

R_{shpv} shunt resistance

R_{srpv} series resistance

I_{pv} output current of the PV cell

q electron charge (1.602×10^{-19} As)

n_d diode quality factor ($1 < \mathrm{n} < 2$)

k Boltzmann′s constant (1.38×10^{-23} J/K)

T_{pv} absolute temperature (in K)

2.2.2 Terminal characteristics of a PV cell

Approximate terminal characteristics of a PV cell, derived using (2.1), are shown in Fig. 2.2. According to (2.1) the terminal characteristics of a PV cell are dependent on the irradiance and temperature at the solar cell.

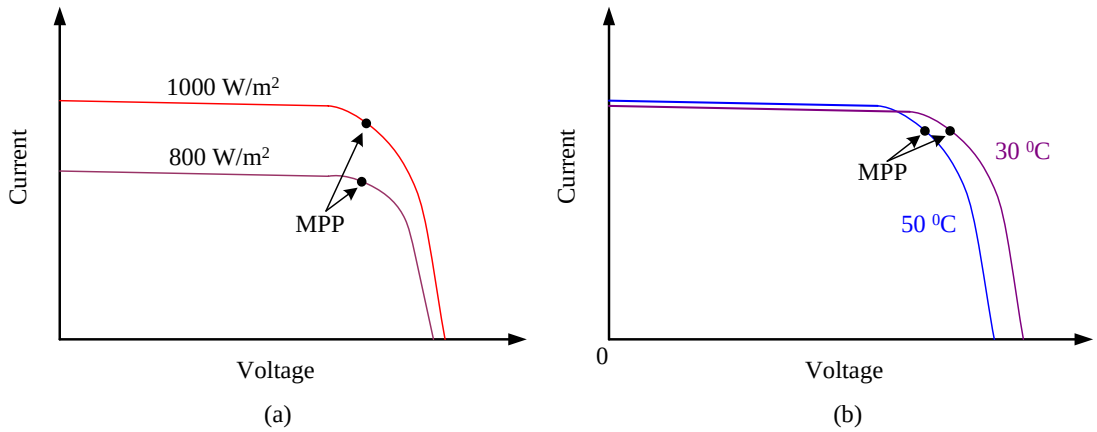

Figure 2.2: Terminal characteristics of a PV cell

Fig. 2.2(a) shows the characteristics of a PV cell when irradiance is varied. According to Fig. 2.2(a), the short-circuit current of a PV cell is proportional to irradiance and open-circuit voltage increases slightly as irradiance increases. Fig. 2.2(b) shows the characteristics curves of a PV cell when the temperature at the PV cell is varied. According to Fig. 2.2(b), the open-circuit voltage of a solar cell decreases as the temperature increases.

The terminal characteristics of a PV cell are non-linear as shown in Fig. 2.2. The non-linear behaviour is mainly due to the non-linear characteristics of the diode current, I_{dpv} shown in Fig. 2.1. As a result, the maximum power that can be extracted from a PV cell occurs when the PV cell is operated at the voltage of the maximum power point (MPP). As the terminal characteristics of a solar cell

are dependent on the irradiance and temperature the MPP of a PV cell moves as illustrated in Fig. 2.2.

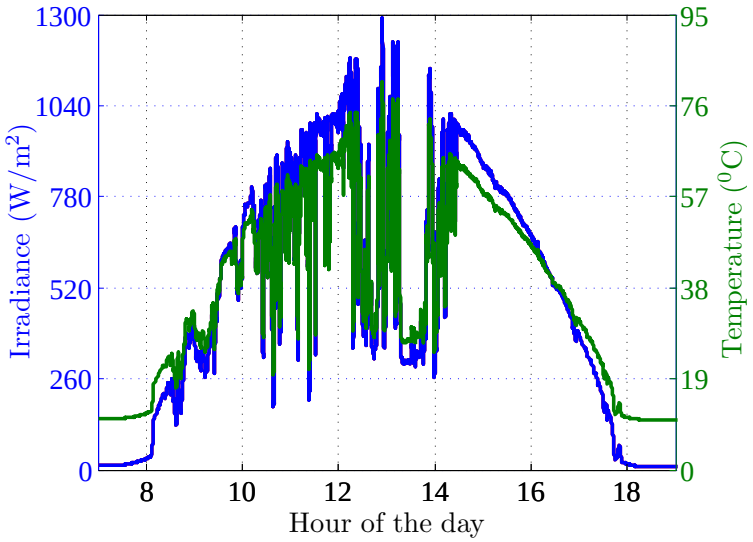

Figure 2.3: Variation of solar irradiance and temperature

The irradiance level and temperature at a solar cell undergo rapid changes as a result of changing environmental conditions. Such possible variations of solar irradiance during a day is shown in Fig. 2.3. Since a solar cell can experience significant changes in irradiance and temperature, the terminal characteristics of a solar cell continuously vary.

2.2.3 Maximum power point tracking (MPPT)

Additional control methodologies are required to ensure the operation of a PV cell at MPP which varies with the level of solar irradiance and the ambient temperature, in order extract maximum power from a PV array. Therefore a maximum power point tracking (MPPT) algorithm that is capable of identifying a change in the available maximum power of a PV array and moving the operating point to the MPP is integrated to the control system of grid-connected PV systems.

There are different MPPT algorithms that have been developed for PV systems. The perturb and observe (P & O) method has been identified as a simple MPPT algorithm because of the simplicity in the algorithm. The P & O method

needs only one sensor. The P & O method has been identified as a slow tracking algorithm compared to other available MPPT algorithms discussed in the literature. Sometimes, the P & O method fails in the presence of rapid variations of the environmental conditions [3]. The continuous oscillations around the MPP is a major drawback of the P & O method.

The next advanced MPPT algorithm is the incremental conductance (InC) method. The InC method tracks the MPP quickly and accurately compared to the P & O method [4]. In the InC method, once an MPP is found, theoretically there are no oscillations around that point, as in the P & O method, until the MPP changes due to variations in available solar irradiance and atmospheric temperature. The InC method requires output current and voltage feedback of the PV array. Hence a current sensor and a voltage sensor are needed to implement the InC method. It is one sensor more than that is needed to implement the P & O method. The InC method is a reasonably accurate, less complex and easily implementable MPPT algorithm compared to quite sophisticated MPPT algorithms that are discussed in recently published literature.

2.3 Power converters for integrating PV systems to the grid

PV arrays are inherently DC power sources. Therefore, to integrate such systems to an AC power distribution system, DC power from a PV array should be converted to AC power. In order to perform the DC to AC power conversion, power electronic converter systems are required. These utility interconnected power electronic converter systems that convert DC power to AC power are categorised based on the application, operation and control.

The authors of [5] categorise converters that interface PV systems to the grid according to different power electronic circuit configurations presented in Fig. 2.4 as a summary. The PV array configuration[1] and the nominal voltage

[1]Mainly the open circuit voltage of the PV array.

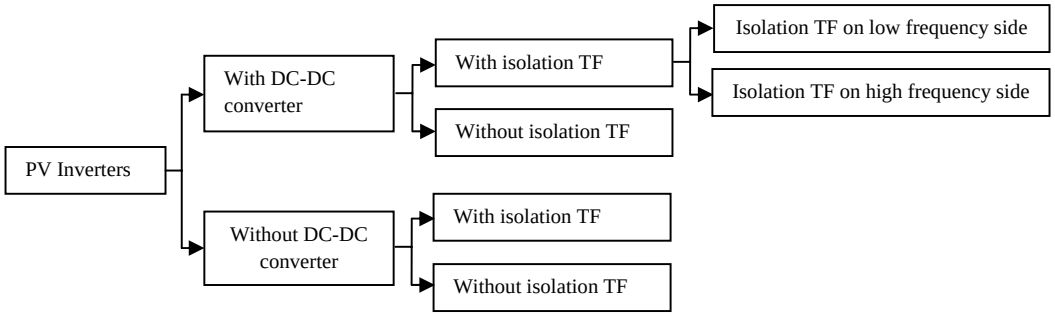

Figure 2.4: Different configurations of power electronic converters that interface PV systems to the grid

of the AC grid to which the PV system is connected, determines the necessity of having a DC-DC power conversion stage to provide a suitable DC voltage for the inverter stage[2]. The DC-DC power conversion stages can be eliminated with careful selection of the PV array to closely match with the required DC voltage required for the inverter ultimately leading to higher efficiency [5]. This may not be always possible with small capacity PV installations which may need to boost the output voltage of the PV array in order to achieve the required DC side voltage of a PV system. In such situations a DC-DC boost converter can be used to boost the output voltage of the PV array as suitable for integrating to the grid.

Generally, galvanic isolation of inverters is considered to be a safety requirement. However, standards for grid connected energy systems via inverters permit the elimination of such isolation, provided the inverters are carefully designed to mitigate the problems with DC current injection, islanding, flicker and harmonics [6], [7], [8], [9] and [10]. Since an isolation transformer introduces increased losses and also adds to the cost of a PV system [11], [12], converters (inverters) without galvanic isolation are usually preferred for relatively small domestic rooftop PV installations.

Categories of converters can be grouped according to the commutation process used in the design; as either line commutated converters or force commutated converters. The latter is applicable in utility interactive systems such as grid-

[2]This refers to DC to AC power conversion.

connected PV systems where limitations on the harmonic current injection are required [9].

DC-AC converters can be further categorised based on voltage and current waveforms at their DC-links as either; voltage source converters or current source converters (CSC). In a VSC, DC-link terminals are connected in parallel with a relatively large capacitor and hence simulates characteristics of a voltage source. The DC-link voltage of a VSC retains the same polarity and the direction of the converter average power flow as determined by the polarity of the DC-link current. In a CSC, the DC-link is connected in series with a relatively large reactor and hence simulates the characteristics of a current source. The DC-link current retains the same polarity and the direction of the average power flow is determined by the DC-link voltage. In order to be able to fully control the power flow through a CSC, it should be made from fully controllable bipolar power electronic switches. Currently, such switches are commercially available only for very high power converter markets. Unlike in a CSC, power flow of a VSC can be fully controlled if the converter is made of reverse conducting power electronic switches. Such power electronic switches are commercially available as IGBT or MOSFET and those are suitable for low power converter applications [13]. Therefore, VSCs have become the most suitable type of power electronic converters to interface low power PV systems to the grid.

2.4 Operation and control of a VSC

2.4.1 Basic operation of a VSC

The basic structure of a single-phase VSC that interfaces a DC power source to the grid is shown in Fig. 2.5. The single-phase VSC is made of an H-bridge[3]. In Fig. 2.5, C_{dc} is the DC-link capacitor and V_{dc} is the DC-link voltage.

The control of power flow across a VSC is similar to the control of power flow

[3]This is also referred to as a full-bridge.

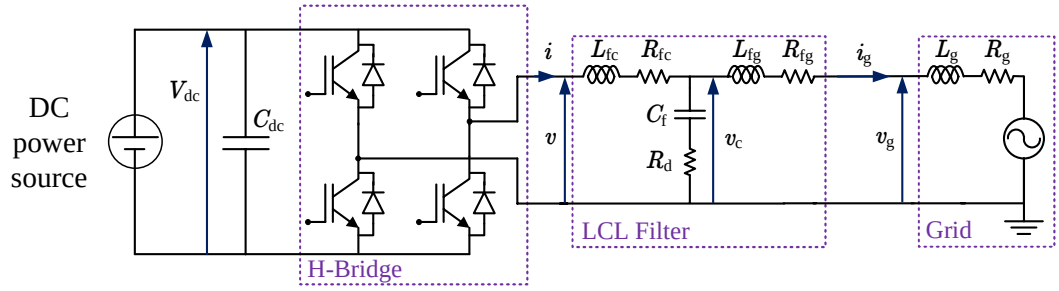

Figure 2.5: Basic structure of a single-phase VSC

of a synchronous machine. The magnitude and the phase angle of the output voltage of a synchronous machine determine the amount of power flow. Similarly, in the single-phase VSC shown in Fig. 2.5, the amount of power injected or absorbed by a VSC is adjusted by controlling the magnitude and the angle of the terminal voltage at the output of the H-bridge, v, of the VSC with reference to the grid side voltage, v_g. In a VSC there is a complex control system to control the power flow across the VSC that ultimately determines the magnitude and the phase angle of v.

Sinusoidal pulse-width modulation (SPWM) techniques are used to generate a desired voltage at the output of the H-bridge. There are two SPWM techniques commonly used in VSCs; bipolar-SPWM and unipolar SPWM. In both of these PWM techniques, a sinusoidal reference signal known as the modulation signal (m) is compared against a high frequency triangular signal as shown in Fig. 2.6(a). The magnitude of m is proportional and the phase angle and frequency of m is similar to the magnitude, phase angle and frequency of voltage that should be generated at the output of the H-bridge. The output of the comparison of m and the high frequency triangular signal is a pulse-width modulated switch-ON and switch-OFF pattern similar to the pattern shown in Fig. 2.6(b). The switching pattern is then applied to the power electronic switches of the H-bridge.

Fig. 2.7 and Fig. 2.8 illustrate the output voltage of the H-bridge of Fig. 2.5, v, when bipolar-SPWM and unipolar-SPWM techniques are used respectively. As shown in Fig. 2.7 and Fig. 2.8, the output voltage of the H-bridge is a pulse-width modulated switching voltage waveform of which the fundamental voltage is equal

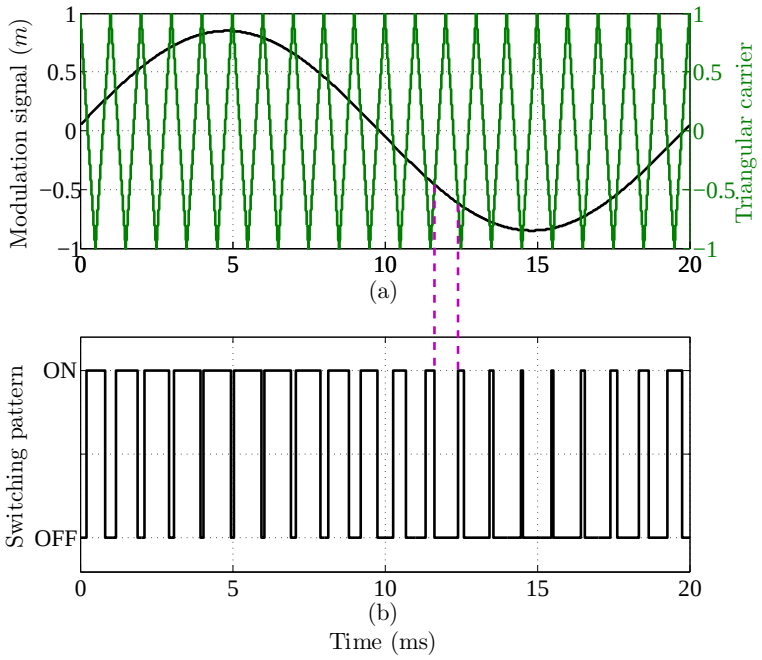

Figure 2.6: Generation of PWM switching pulses

to the desired voltage at the output of the H-bridge. Since the output voltage of the H-bridge, v, is a switching voltage waveform, the resulting current can be highly distorted. In order to minimise the distortion in the current injected by the VSC to the grid, a filtering mechanism is needed.

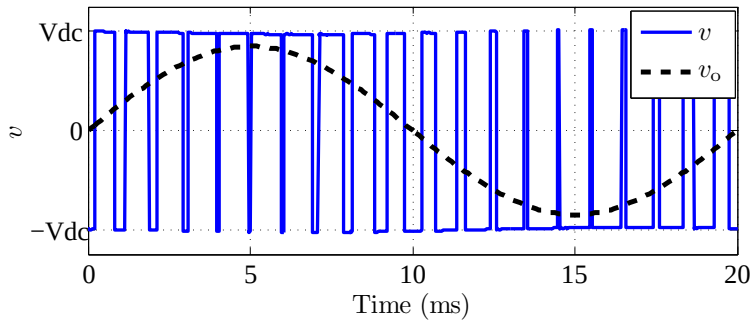

Figure 2.7: Output voltage of a H-Bridge of a VSC that uses bipolar-SPWM technique

A VSC is integrated to the grid via a coupling inductor[4]. The coupling inductor reduces the ripple in the output current of a VSC and minimises the effect of the PWM switching voltage developed at the output of a VSC. However, a coupling inductor has limited capability of attenuating the switching current rip-

[4]Also referred to as a smoothing reactor.

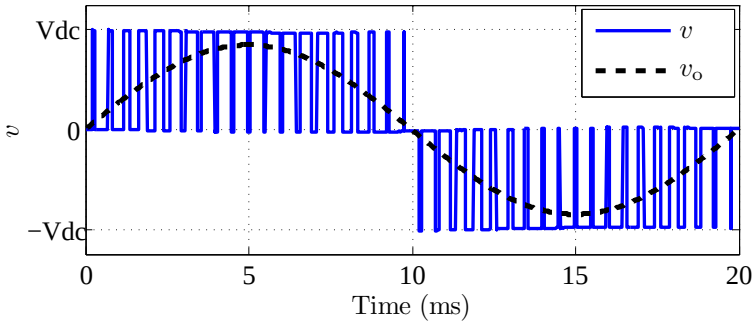

Figure 2.8: Output voltage of a H-Bridge of a VSC that uses unipolar-SPWM technique

ple of a VSC. In order to obtain improved filtering than that is achievable using only a coupling inductor, LCL filters are often used in grid-connected VSCs. The structure of an LCL filter is shown in Fig. 2.5. The switching ripple current attenuation provided by a coupling inductor and a comparable LCL filter is shown in Fig. 2.9. According to Fig. 2.9, an LCL filter attenuates high frequency switching ripple current of a VSC better than a coupling inductor. An LCL filter should be carefully designed in order to obtain desired results. Further, the dynamic performance of the control system of a grid-connected VSC is affected by the design of the LCL filter. Therefore, the design procedure of an LCL filter of a grid-connected VSC is further explored and presented in Appendix A of this Thesis.

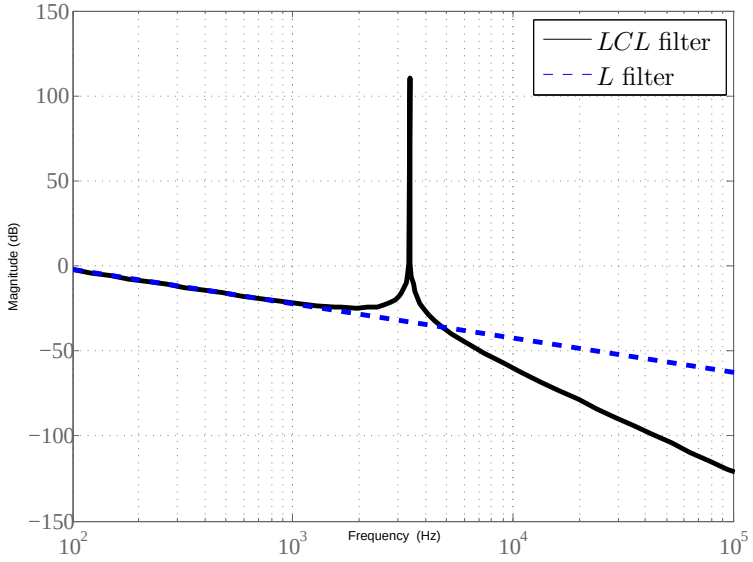

Figure 2.9: Frequency response of a coupling inductor and an LCL filter

2.4.2 Four-quadrant operation of a VSC

A VSC can be controlled to inject or absorb real and reactive power to the grid. The real and reactive power exchange between a VSC and an AC system can be controlled independently. Therefore, any combination of real power injection or absorption along with reactive power injection or absorption is achievable [14]. Such an operational capability of a VSC is referred to as four-quadrant operation and that can be represented in four quadrants of a Cartesian coordinate system as shown in Fig. 2.10. The sample operating scenarios of a VSC indicated in Fig. 2.10 are as follows.

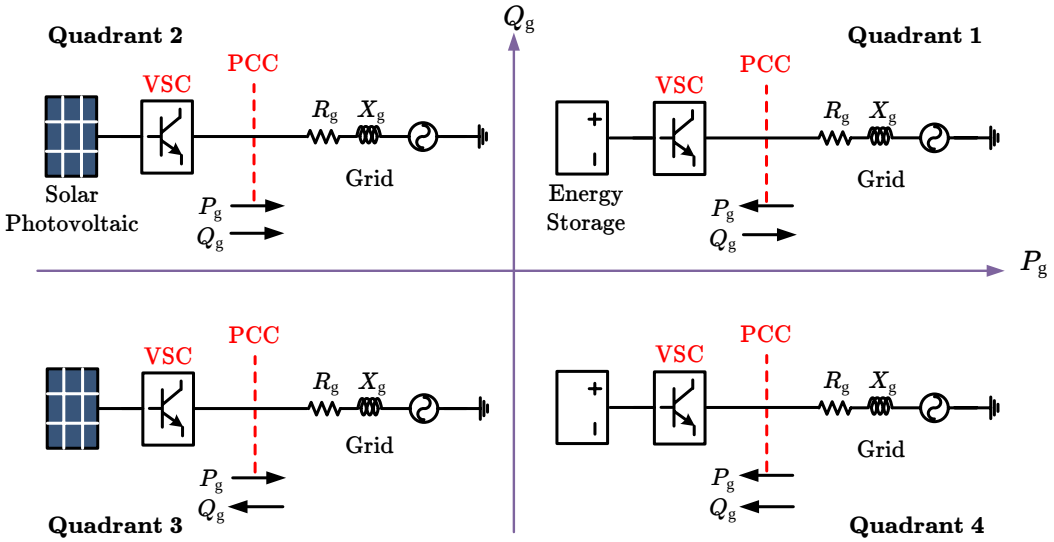

Figure 2.10: Four-quadrant operation of a VSC

- Quadrant 1 - Charging a battery bank while operating at a leading power factor.
- Quadrant 2 - A PV system operating at a leading power factor.
- Quadrant 3 - A PV system operating at a lagging power factor.
- Quadrant 4 - Charging a battery bank while operating at a lagging power factor.

Fig. 2.10 introduces counting directions used in this Thesis for active and reactive power flow outputs of a grid-connected VSC. In this Thesis, active power

injected and reactive power absorbed (inductive operation) by a VSC are counted negative and active power absorbed and reactive power injected (capacitive operation) by a VSC are counted positive.

The real and reactive power injection or absorption by a VSC is limited only by the converter current carrying capacity. The operating limits of an ideal VSC are illustrated in Fig. 2.11. In Fig. 2.11, the kVA rating of the converter is represented by a vector of magnitude S_{r}. As per Fig. 2.11, when a VSC is injecting active power P_{g} to the grid, the VSC is able to either absorb Q_{g} amount of reactive power from the grid or inject Q_{g} amount of reactive power to the grid. This means that a VSC is capable of absorbing or injecting the same magnitude of reactive power for a given P_{g}. It is evident from Fig. 2.11 that when active power is zero, the converter is capable of operating at its maximum reactive power limit that is equal to the rated kVA capacity of the VSC.

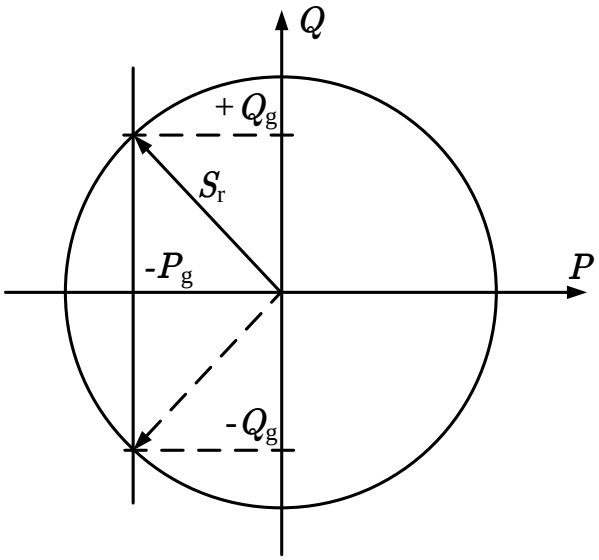

Figure 2.11: Operating limits of an ideal VSC

2.4.3 Control systems in a VSC

A VSC can be categorised based on the control philosophy as either voltage-controlled or current-controlled. In a voltage-controlled VSC, the real and reactive power output are controlled by adjusting the phase angle and the magnitude

of the output voltage of the VSC relative to the PCC voltage. There are fewer control loops in this type of a VSC and there is no closed-loop to control its output current. Hence the VSC is not protected by the control system against over current.

In a current-controlled VSC, the output current of the VSC is controlled by a closed-loop current controller. Hence, such a VSC is inherently protected against over current. In a current-controlled VSC, the control of the active and reactive power outputs is achieved by controlling the output current by adjusting the magnitude and phase angle of the output voltage of the VSC with respect to the grid voltage. Since a current-controlled VSC provides better protection against over current, avoiding disconnection in such situations, these are increasingly being used to integrate PV systems to the grid. In a current controlled VSC, the closed-loop current controller and grid synchronisation mechanism are the two main control systems.

Current controller of a VSC

In three-phase VSCs, synchronous reference frame[5] current controllers are widely used. Such a current controller provides flexibility by independently controlling the injected or absorbed active and reactive power. The synchronous reference frame current controller requires the transformation of measured AC signals, output current and voltage of a VSC, into DC signals using the Park Transformation. The measured output current and voltage of a VSC that is transformed to DC signals are the inputs to a synchronous reference frame current controller. These DC signals are passed through a proportional and integral (PI) regulator[6] in the synchronous reference frame current controllers and generate control inputs to the PWM generator of the VSC in synchronous reference frame.

The application of a synchronous reference frame current controller to a single-

[5]Also known as rotating frame or dq frame.

[6]A PI regulator is used to achieve zero steady-state error since such a regulator provides an infinite gain for DC signals.

phase VSC is not straightforward in the absence of two independent phases. The Park Transformation is a key component in synchronous reference frame current controller and requires at least two independent orthogonal phases. Therefore, applying this transformation to a single-phase VSC is difficult. However, in recently published literature, alternative methods have been proposed to minimise such difficulties. In a single-phase VSC, in order to realise an independent orthogonal second phase, an imaginary phase can be created by phase shifting the available phase by $\pi/2$ rad. According to the published literature, this orthogonal imaginary phase can be created in two ways; time delaying original signal by $T/4$ where T is the period of original signal [15] or by differentiating original signal [16]. The time delay method requires storing sampled data of the original waveform for a period of $T/4$. This can be realised with available low cost DSPs in the market today [16], [17] and [18]. However, the time delay method has a major drawback. If the time delay method is used to generate an imaginary orthogonal signal, there is always a delay of $T/4$ for changes to appear from the original signal in the created imaginary orthogonal system. This may lead to instabilities in the current controller. Further, the use of such techniques to generate an imaginary orthogonal signal may cause difficulties in tuning the regulator of the current controller [19]. The technique of generating an imaginary orthogonal signal developed in [16] requires differentiating the measured current or voltage of a single-phase VSC. Generally, the output voltage and current of a VSC are distorted in the presence of switching harmonics and low order harmonics. The differentiation of such signals may create highly distorted signals.

In a single-phase VSC, transformation of measured output voltage or current signals using Park Transformation is not required if there is a regulator which is capable of tracking a sinusoidal reference with zero steady-state error. If such a regulator is available in the current controller of a VSC, the measured AC signals can be directly processed by such a regulator to gain zero steady-state error. A PI regulator has poor tracking capability of sinusoidal reference signals. Therefore,

in order to track sinusoidal signals with zero steady-state error, a stationary frame regulator named proportional resonant (PR) controller has been proposed in [20]. This regulator is readily applicable for both three phase and single phase VSCs. A PR regulator achieves zero steady-state error for signals at the designed frequency. Hence, signal transformation from AC to DC and back to AC, as is required for a synchronous reference frame current controller, is not necessary. Furthermore, the formation of an imaginary orthogonal signal is not necessary in stationary frame current controllers. Hence, the dynamic performance of a stationary frame current controller in a single-phase VSC is superior compared to the synchronous frame current controller of a single-phase VSC.

Grid synchronisation of a VSC

In a VSC, a grid synchronisation mechanism is used for synchronising the VSC to the grid. Further, in a current-controlled VSC, the grid synchronisation mechanism is also used for generating an accurate current reference signal in order to inject the desired amount of active and reactive power to the grid. There are different grid synchronisation mechanisms that are used to synchronise a VSC to the grid according to recently published literature. Depending on the application and type of current controller used in the VSC, a suitable grid synchronisation method should be chosen.

One of the simplest grid synchronisation methods is the voltage zero crossing detection. Since voltage zero crossings occur every half a cycle, the dynamic performance of the voltage zero crossing detection method is quite low [21]. However, the voltage zero crossing detection method for synchronising a VSC to the grid can fail in the presence of harmonics in the grid because of multiple zero crossings [22].

Other grid synchronisation methods are mostly based on a phase-locked-loop (PLL). Among different PLL methods, synchronous reference frame based PLL (s-PLL) has been identified as suitable for a single-phase VSC [21], [23]. In the

s-PLL, the peak value of the measured grid voltage can be obtained easily.

2.5 Grid-connected PV system

LV power grids in Australia are undergoing significant changes with the connection of a large number of small capacity PV systems. Small scale PV systems ($0 - 10$ kW) are the type of renewable energy units that are mostly connected to these networks. Commercially attractive rebates and concession schemes that were introduced by the Australian government for installing small scale PV systems along with price reductions in PV panels and power electronic converter systems, are the main reasons for the increased number of grid-connected small scale PV systems in LV power grids. The majority of small scale PV systems are domestic roof-top type installations and are generally single-phase systems [24].

The basic structure of a grid-connected single-phase PV system is shown in Fig. 2.12. This is a generic representation of a domestic roof-top PV system. The PV system consists of a DC-DC converter, a VSC and an LCL filter. The PCC is where the PV system is connected to the grid.

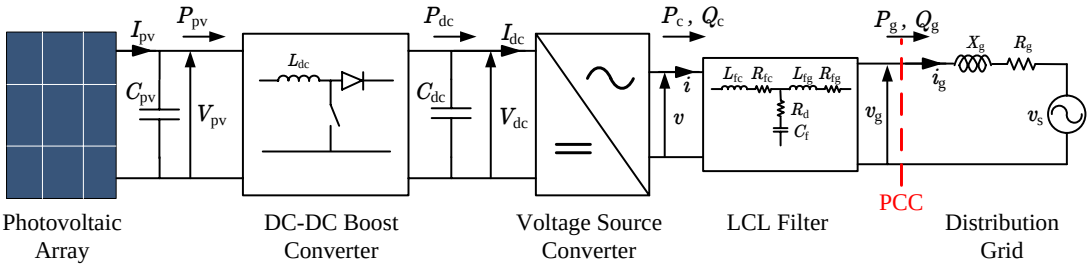

Figure 2.12: Basic structure of a grid-connected PV system

In the grid-connected PV system shown in Fig. 2.12, the DC-DC converter steps up or steps down the output voltage of the PV array to a suitable level at the output of the DC-DC converter. An MPPT algorithm determines the MPP of the PV array at a given time and the DC-DC converter is controlled in such a way that the PV array is operated at the MPP. The output of the MPPT algorithm is an input to the controller of the DC-DC converter.

The PV system shown in Fig. 2.12 is integrated to the grid via a VSC. A VSC with an ability to control output voltage magnitude and phase angle with reference to the voltage at the PCC and is able to operate in all four quadrants, provides a significant flexibility in controlling the active and reactive power injected or absorbed by or from the grid. Therefore, VSCs are becoming more attractive in PV grid integration especially with the additional capability of providing reactive power support, voltage regulation [25] and managing battery storage.

The output power from a PV array is a function of solar irradiance and ambient temperature. Since solar irradiance and ambient temperature vary, the power output of a PV array is not constant. If the grid-connected PV system shown in Fig. 2.12 is controlled to inject a constant amount of power to the grid at times when power level varies at the PV array, the DC-link capacitor, C_{dc} may be charged or discharged affecting the DC-link voltage, V_{dc}. However, maintaining a constant DC-link voltage is necessary in order to minimise the appearance of low-order harmonics at the output of the VSC as a result of PWM switching of the power electronic switches of the VSC. Therefore, in a grid-connected PV system a controller is used to control the DC-link voltage at a suitable level by controlling the active power flow of the PV system.

2.6 Impact of the integration of multiple PV systems on an LV power grid

Operational or power quality problems may occur in LV power grids as a result of integration of a large number of small scale multiple PV systems. The integration of small scale multiple PV systems means that LV power grids may have an increased susceptibility to voltage fluctuations due to injected active power variations from the PV systems, depending on conditions such as the time of day and weather. Such variations in output power can cause voltage fluctuations (either slow or fast) in LV power grids where concentrated PV installations exist

[26]. Since PV systems are interfaced to LV power grids through power electronic converters, which is equivalent to a condition where there is no mechanical inertia, the speed of response of PV systems in relation to reduction or increase in available power can be very fast indeed [27]. Therefore, in a power distribution feeder to which multiple PV systems are integrated there is a possibility that feeder voltage can vary significantly as a result of variable power injections from PV systems.

There may be operational and control interactions between PV systems or with the grid if multiple PV systems are integrated into the LV power grid [25], [28], [22] and [29]. These interactions may cause unintentional tripping of PV systems, possibly making the grid unstable or a system may fail to disconnect when it is necessary to do so, creating a hazardous situation. Therefore, possible mechanisms and causes for operational and control interactions should be identified first, to propose any mitigation techniques to avoid undesirable interactions between multiple PV systems for a stable operation of LV power grids. Furthermore, there can be potential instabilities within a grid-connected PV system if the operating point of the PV array is moved towards the constant current region of the characteristic curve of a PV array [30]. The prior identification of the possibility of occurring such problems in an LV power grid containing multiple PV systems is critical for both power utilities and PV system designers.

In order to investigate possible rapid and slow voltage fluctuations at the grid interface, operational and control interactions in the presence of multiple grid-connected PV systems and also to evaluate potential instabilities, a detailed model of a grid-connected single-phase PV system is necessary. The knowledge on component level modelling of a grid-connected PV system is available with recently published literature for both 3-phase and single-phase systems [31],[32]. However, a complete model of a grid-connected single-phase PV system with associated control design methodologies is not readily available. Therefore, the development of a detailed model of a grid-connected single-phase two-stage PV

system with component level models and associated control design procedures is necessary. In order to confidently use the simulation models in system level studies, evaluation and validation of such simulation models are necessary. This can be achieved by establishing a comparable experimental setup of which the practical results can be compared with the results obtained from the simulation model.

2.6.1 Steady-state voltage rise with connection of PV systems to a power distribution feeder

The steady-state voltage rise when grid-connected PV systems inject active power to the grid can be explained by using a model of a PV system connected to a power distribution feeder as shown in Fig. 2.13. In Fig. 2.13, a part of the grid is modelled with an equivalent Thévenin voltage source of which the rms voltage is V_s. The grid impedance seen at the PCC by the PV system is $R_g + jX_g$. The rms voltage at the PCC of the PV system is V_g. The PV system injects active and reactive power, P_g and Q_g respectively, to the grid resulting in an rms current of I_g.

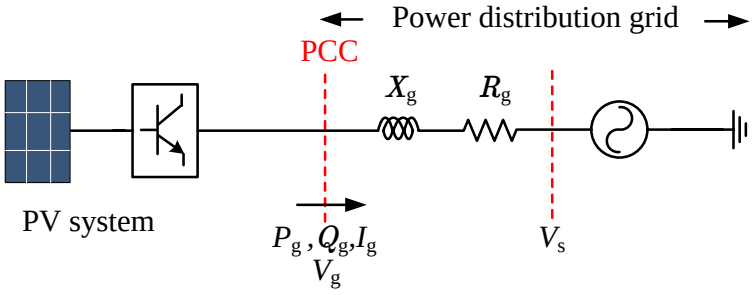

Figure 2.13: Simplified model of a power distribution feeder

If the PV system in Fig. 2.13 is injecting only active power to the grid at a given time, a phasor diagram can be drawn as shown in Fig. 2.14(a). In Fig. 2.14(a), I_{gp} is the rms value of the active current injected to the grid. If the active power injected by the PV system is increased, the phasor diagram should be updated as shown in Fig. 2.14(b) where $I_{gp1} > I_{gp}$, $\delta_1 > \delta$ and $V_{g1} > V_g$.

As shown in Fig. 2.14(b) when the active power injected by the PV system is increased, the PCC voltage of the PV system also increases as a result of the additional power flow.

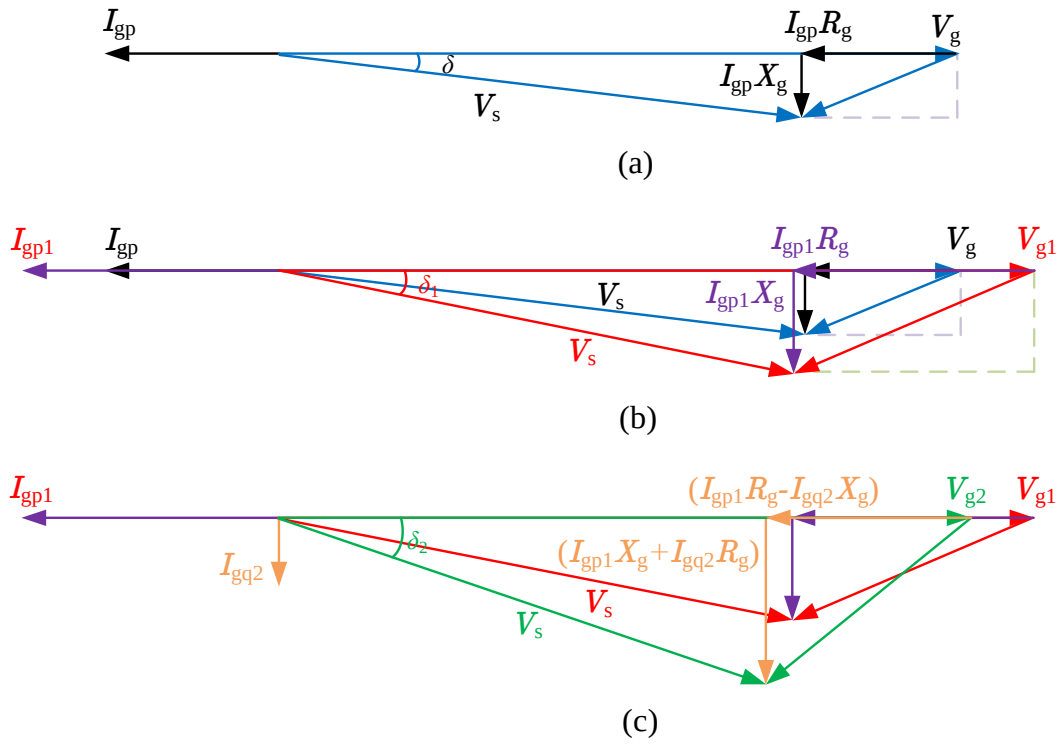

Figure 2.14: Phasor diagram of a grid-connected PV system

The PCC voltage can be reduced if reactive power is absorbed by the converter that integrates the PV system to the grid. The phasor diagram shown in Fig. 2.14(c) illustrates this scenario. In Fig. 2.14(c) I_{gq2} is the rms value of the reactive current that is absorbed by the converter. As Fig. 2.14(c) illustrates that the PCC voltage can be reduced by absorbing reactive power ($V_{g2} < V_{g1}$).

The sensitivity of the PCC voltage of a PV system for either active power or reactive power can be derived theoretically. The complex power at the PCC of the PV system shown in Fig. 2.13 is given by (2.2)

$$\vec{V}_g \vec{I}_g^* = -P_g + jQ_g. \tag{2.2}$$

Further,

$$\vec{V}_{\mathrm{g}} - \vec{V}_{\mathrm{s}} = \vec{I}_{\mathrm{g}}(R_{\mathrm{g}} + jX_{\mathrm{g}}). \tag{2.3}$$

From (2.2) and (2.3),

$$\vec{V}_{\mathrm{g}} - \vec{V}_{\mathrm{s}} = \left(\frac{-P_{\mathrm{g}} + jQ_{\mathrm{g}}}{\vec{V}_{\mathrm{g}}}\right)^{*} (R_{\mathrm{g}} + jX_{\mathrm{g}}),$$

$$\vec{V}_{\mathrm{g}} - \vec{V}_{\mathrm{s}} = \frac{(-P_{\mathrm{g}} - jQ_{\mathrm{g}})(R_{\mathrm{g}} + jX_{\mathrm{g}})}{\vec{V}_{\mathrm{g}}^{*}}. \tag{2.4}$$

If the phase angle deviation of $\vec{V}_{\mathrm{s}}$ with reference to $\vec{V}_{\mathrm{g}}$ is assumed negligible and considering $\vec{V}_{\mathrm{g}}$ to be the reference phasor, (2.4) can be simplified as,

$$V_{\mathrm{g}} - V_{\mathrm{s}} = \frac{-P_{\mathrm{g}}R_{\mathrm{g}} + Q_{\mathrm{g}}X_{\mathrm{g}}}{V_{\mathrm{g}}},$$

$$\Delta V_{\mathrm{g}} = \frac{-P_{\mathrm{g}}R_{\mathrm{g}} + Q_{\mathrm{g}}X_{\mathrm{g}}}{V_{\mathrm{g}}}, \tag{2.5}$$

where $\Delta V_{\mathrm{g}} = V_{\mathrm{g}} - V_{\mathrm{s}}$ which is the steady-state voltage rise. As per the simplified expression (2.5) the steady-state voltage rise, ΔV_{g} increases as active power injected to the grid, P_{g}[7] increases and ΔV_{g} can be decreased by absorbing reactive power from the grid. If active power injected by a PV system can be controlled, ΔV_{g} can also be controlled by controlling both active power, P_{g} and reactive power, Q_{g} injected by the PV system.

2.6.2 Voltage level variations in an LV power grid integrated with multiple PV systems

The integration of multiple PV systems to an LV power grid is now known to cause grid voltage rise problem [33], [34] and [35]. The grid voltage may exceed the specified highest voltages in the applicable standards such as Australian Standard

[7]Note that active power injection to the grid is counted negative.

AS4777.2 [7] and IEEE Standard 929-2000 [9], especially in situations when the power generation from PV systems is at a peak and the load on the grid is at a minimum. According to Australian Standard AS4777.2 [7] the maximum grid voltage up to which a PV system can remain connected is 230 V + 10%. The disconnection of PV systems from the grid leads to loss of energy yield from the installed PV systems and income for the resource owner. If the voltage regulation at the PCC of the PV system is possible by any means, increased and continuous active power injection can be achieved from the connected PV systems.

In a power distribution feeder where multiple PV systems are integrated, there is a possibility for reverse power flow in the feeder. This scenario depends on the load demand and available power from PV systems. Conventional distribution voltage regulation devices such as fixed capacitors, tap changers at distribution transformers and step voltage regulators are not capable of regulating the feeder voltage in such a situation [9]. However, if dynamic voltage regulators are added to the system, conventional devices can be properly coordinated to operate the grid within safe limits [36].

Impact on the voltage levels of an LV power grid integrated with a large number of PV systems can be quite significant. High penetration of PV systems may cause over-voltages or severe voltage fluctuations in the grid. Therefore, in order to operate a grid within safe margins while harnessing the maximum active power from PV, fast and dynamic voltage regulating systems must be installed and operated in the grid.

2.7 Voltage control in an LV power grid integrated with multiple PV systems

The PCC voltage of a PV system is sensitive to both active and reactive power injected by a PV system and the grid impedance according to (2.5). PV systems are integrated to the grid via power electronic converters and, more specifically,

often via VSCs [5], [37]. A VSC is capable of operating in all four quadrants when designed appropriately and such systems have been shown to be a fast, efficient and cost effective means of regulating voltage and power factor for nearby loads [38], [39], [40] and [41]. Further, the active and reactive power outputs of a PV system that is integrated to the grid via a VSC can be controlled independently. Therefore, fast voltage control in an LV power grid can be achieved by PV systems integrated to the grid via VSCs. Therefore, it is beneficial for both utilities and consumers to utilise the added value capabilities of modern PV systems to improve power quality in the grid.

The Australian and IEEE standards applicable for grid-integrated PV systems, Australian Standard AS4777.1 [7] and IEEE Standard 1547-2003 [10] respectively, permit the use of PV systems for the purpose of voltage support but do not permit active voltage regulation at the PCC of a PV system. However, in Australian Standard AS4777.1 [7] there is a provision given for active voltage regulation by grid-integrated PV system. According to that particular standard, the utility who owns the LV power grid to which a PV system is integrated has the authority to permit active voltage regulation by the PV system.

The static voltage support methodologies provided by PV systems, such as constant and variable power factor, have been identified as inefficient as these methods may cause additional reactive power flow in the grid even when the grid voltage is well within the limits and may lead to overloading of the distribution transformer [33]. A droop based reactive power control method (referred to as $Q(U)$ method) has been proposed in [42] which aims to minimise the drawbacks of the static reactive power control methodologies. In order to implement the $Q(U)$ reactive power control method effectively, grid specific studies or additional decision making control algorithms such as the fuzzy logic based adaptive controller presented in [43] are necessary. Further, $Q(U)$ reactive power control method is not able to maintain the PCC voltage of a PV system below the maximum allowable voltage all the time.

The PCC voltage of a PV system can be regulated by a closed-loop controller that dynamically controls the reactive power response of the PV system. Such a controller has been identified as an efficient way of regulating PCC voltage with reactive power [33]. The ability to regulate the PCC voltage with a closed-loop controller that dynamically controls the reactive power injected to the grid by the PV system is limited. This limitation is mainly due to the limited rating of the VSC that interfaces the PV system to the grid. When the PV system is injecting a certain amount of active power to the grid, only the excess capacity of the VSC, if any, can be used to inject/absorb reactive power. The available limited reactive power capacity of the PV system at a given time may not be adequate to regulate the PCC voltage at 230 V + 10% or at any other specified voltage reference depending on the voltage sensitivity of the PCC. In such a situation active power curtailing is an option to control the PCC voltage in the absence of energy storage systems [35], [44] and [45]. Similar to closed-loop reactive power control of a PV system, closed-loop active power control can be proposed as an effective way of regulating PCC voltage of a PV system.

In the published literature, little attention has been given to adequate technical details and guidelines for practically implementing closed-loop controllers that control the active and reactive power response of a PV system in order to regulate the PCC voltage of the PV system. Therefore, detailed design procedures of closed-loop active and reactive power controllers that are capable of dynamically regulating the PCC voltage of a grid-connected PV system need to be developed. The sensitivity of active and reactive power controllers to the gains of the controllers and the grid impedance should be evaluated. Once closed-loop active and reactive power controllers are developed, by combining the operation of closed-loop active and reactive power controllers, novel operating strategies can be proposed for grid-connected PV systems. The robustness of the designed closed-loop active and reactive power controllers and the feasibility of implementing novel operating strategies for grid-connected PV systems should be validated

experimentally.

2.8 Application of distribution static synchronous compensator (DSTATCOM)

A DSTATCOM is a VSC which is primarily used to exchange reactive power with the AC system. In power distribution systems, DSTATCOMs are mainly used for voltage regulation [13], [14]. A DSTATCOM is usually operated as a shunt connected static var compensator of which capacitive and inductive output current can be controlled independent of the AC system voltage. Hence a DSTATCOM can be used to either provide voltage support or active voltage control in an LV power grid.

A PV system that is integrated to the grid via a VSC can be operated as a DSTATCOM. The active power injection by a PV system is possible only at times when there is adequate solar irradiance. When there is not enough solar irradiance[8] ideally the rated capacity of the VSC that interfaces PV system to the grid can be operated as a DSTATCOM. Therefore, PV systems that are interfaced to the grid via VSCs can be fully deployed to provide voltage support or active voltage control at times when there is not enough solar irradiance to generate electrical power, by operating those as DSTATCOMs.

The application of DSTATCOMs for distribution network voltage regulation has been examined [46], [47] and [48]. Although this is the case, suitability of using multiple DSTATCOMs for providing voltage support or grid voltage control in a grid to which multiple PV systems are integrated has not been evaluated. Therefore, identifying the suitability of using the DSTATCOM for providing voltage support or grid voltage control in a grid to which multiple PV systems are integrated is necessary. Further, the development of control coordination strategies for operation of multiple DSTATCOMs will also be beneficial.

[8]For an example, at night time.

2.9 Operational and control interactions between multiple PV systems

In the presence of multiple PV units that are connected to an LV power grid, there can be operational conflicts. These units may interfere or interact with each other's operation and control. Therefore, it is of utmost importance to identify the possible conflicts between different converter systems that would disturb their smooth operation. Mitigation techniques and necessary design modifications should be recognised. Algorithms must be developed to achieve ride-through capability of renewable resources and avoid unintentional shut down of PV systems to avoid abrupt changes in the grid.

In an LV power grid to which multiple PV systems are integrated, the grid voltage can be controlled by regulating the PCC voltage of each PV system [35], [49], [34], [33] and [42]. A PV system that is integrated with a closed-loop PCC voltage controller is able to regulate the PCC voltage of a PV system dynamically at a set reference voltage with zero steady-state error by absorbing reactive power from the grid. Such a controller has been identified as an efficient way of regulating the PCC voltage of a PV system [33]. Therefore, multiple PV systems that are connected to a grid and that are integrated with a closed-loop PCC voltage controller can be used to control the grid voltage dynamically. However, when multiple PV systems operate electrically close to each other while dynamically controlling the grid voltage, there may be control interactions between PV systems.

The control interactions between power system stabilisers (PSS) and flexible AC transmission system (FACTS) devices operating in high voltage transmission networks have been well investigated in the published literature [50], [51], [52], [53] and [54]. However, there is only a limited number of published articles available on the control interaction between dynamic voltage control devices that are connected to an LV power grid. This is an emerging topic of discussion amongst

researchers. The dynamic interaction between DSTATCOMs connected to a radial power distribution feeder is analysed in [55] and simulation results of control interaction between PV systems are presented in [56]. In [55], the research scope is limited to DSTATCOMs that are made of voltage controlled VSCs and the sensitivity of the gains of controllers to the stability of the individual DSTATCOM has been overlooked. The negative interaction between multiple PV systems identified in [56] of PV systems interfaced to the grid via current controlled VSCs does not appear if a dead-band is added to the PCC voltage controller of a PV system.

Control and operational interaction between multiple PV systems can be identified using accurate simulation models and validated mathematical models. However, since such simulation and mathematical models are not readily available those should be developed and validated. The development of such tools will be beneficial for power utilities who are, at present, quite uncertain about the impact, a high penetration of PV systems will have on the grid. Further, simulation and mathematical models that will enable the identification of operational and control interactions between PV systems will also enable the development of proper coordination and control strategies which could be adopted for voltage control and reactive power compensation by PV systems while improving system stability and efficiency. In order to develop such analytical tools, a thorough knowledge on the operation and control of grid-integrated PV systems and practical techniques used to establish control systems is necessary.

2.10 Control and coordination of the operation of multiple PV systems

The operation of small scale PV systems is not currently monitored like in the case of conventional large power generators, since the impact of such PV systems is tolerable in existing power systems. However once multiple PV systems are

present in the grid, their collective impact on the system operation and control will be significant. Therefore these units should be integrated with proper coordination and control practices for acceptable operation of the grid. Further, it is unclear whether or not all PV systems integrated to an LV power grid should provide voltage support, or should there be a staged introduction of this support. For staged introduction of voltage support, development of mechanisms for conveying the appropriate changes to control parameters in a coordinated and timely manner will be necessary. The majority of existing LV power grids does not have any established communication facilities with it. Therefore, initially, methodologies should be developed for proper coordination and control of multiple PV systems without the use of communication infrastructure and later these developed methodologies should be extended as suitable for LV power grids integrated with multiple PV systems in which communication infrastructure exists.

When a certain amount of active and reactive power is injected to the grid by a PV system, the PCC voltage of the PV system is a function of the voltage sensitivity at the PCC. Further, the voltage sensitivity at the PCC of a PV system is a function of the grid impedance seen by the PV system at the PCC. Therefore, in certain operating situations, the voltage at the PCC of a PV system where voltage sensitivity is high may reach unacceptable high voltage levels while the PCC voltages at locations of other PV systems connected to the grid are lower. In such a situation, the PV system that is connected to the grid at a node where voltage sensitivity is high may disconnect in order to comply with the requirements of the Australian Standard AS477.2 [7] while other PV systems will continue to operate. The discussed scenario highlights that in certain operating situations, owners of PV systems whose PV systems are integrated to the grid at nodes where voltage sensitivity is high are disadvantaged over the other PV system owners whose PV systems are connected to the grid at nodes where voltage sensitivity is less.

A droop based active power sharing methodology is proposed in [45] for PV

systems connected to a radial distribution feeder. Since the droop coefficients derived in [45] are based on the voltage sensitivity, the proposed method in [45] can be applied to minimise the disadvantages that PV system owners may experience as a result of their PV systems being connected to nodes where voltage sensitivity is high. However, droop based active power sharing methodology proposed in [45] can fail if conditions in the grid such as voltage at the power distribution transformer and irradiance level, are different to which was considered when deriving droop coefficients. Further, safe voltage limits may not be maintained in the grid by the power sharing methodology developed in [45], in the absence of closed loop PCC voltage controllers integrated to PV systems. Therefore active power sharing methodologies that are able to maintain the grid voltage within safe limits irrespective of operating conditions in the grid should be developed to apply in multiple PV installations.

2.11 Chapter summary

This chapter has provided general information in relation to the operation and control of a grid-connected PV system in a multiple PV environment.

Sections 2.6–2.8 emphasised the importance of integrating fast acting dynamic voltage controllers to grid-connected PV systems. In addition the performance of voltage support techniques currently used to enhance the integration of multiple PV system to a grid were discussed. Further, existing knowledge and theory presented in current literature in relation to the modelling aspects of system components and control approaches of a PV system were examined establishing the background for the proceeding chapters. Based on the literature review, it can be concluded that further research attention should be paid to improve existing control and coordination techniques used in grid-connected PV systems. Further, detailed component level modelling of PV systems, detailed investigation of system response of PV systems and investigation of dynamic interaction between PV systems have not received much research attention which forms the basis for

the work presented in this Thesis.

Chapter 3

Simulation model of a PV system

3.1 Introduction

The integration of multiple, small scale, PV systems into LV power grids bring many benefits, but it may also introduce many issues of concern. Among those issues of concern, grid voltage fluctuations, high voltage levels and operational and control interactions between PV systems have been identified as key issues as discussed in Chapter 2. In order to ensure an orderly transition from traditional LV power grids to those which are rich in distributed generation, such as solar PV, it is imperative that the operational and functional characteristics of these devices are well understood.

The identification of potential problems in LV power grids with multiple PV systems is critical for both power utilities and PV system designers. The possible mechanisms, causes and impact of issues arising as a result of integrating multiple PV systems to LV power grids should first be identified in order to propose mitigation techniques required to avoid any adverse impact. In order to investigate probable voltage fluctuations, high voltage levels, potential instabilities within a PV systems and potential control and operational interaction between PV systems a detailed simulation model of a PV system is necessary.

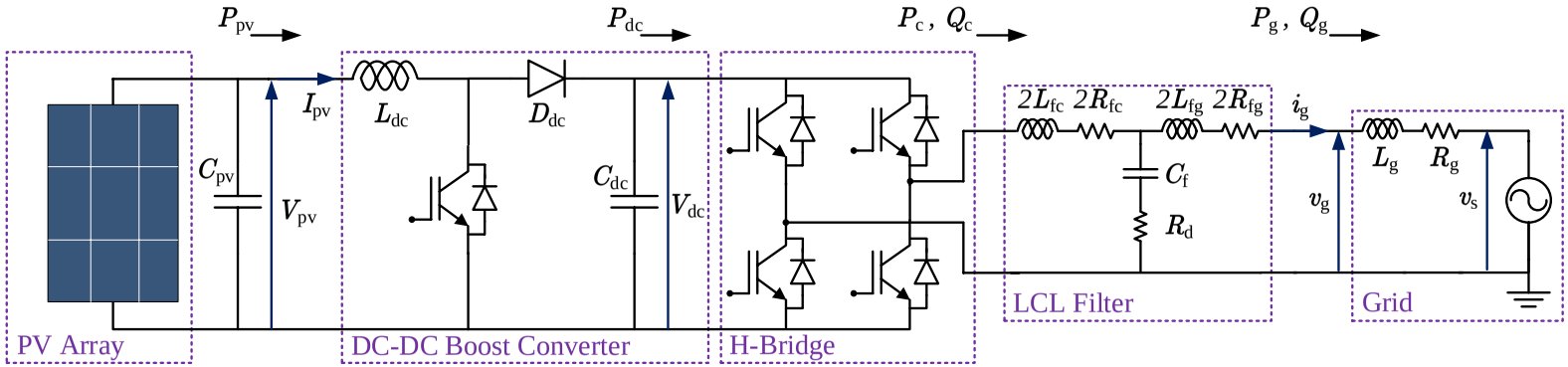

Figure 3.1: Grid-connected PV system with a two-stage converter

In Chapter 2, a grid-connected single-phase two-stage PV system in which the power electronic converter system is made of a DC-DC boost converter and a VSC has been identified as a generic representation of a PV system that is connected to an LV power grids. In this chapter, a detailed model of such a PV system with component level models and associated control systems, is developed using the PSCAD/EMTDC simulation program.

3.2 Modelling

An illustration of the PV system to be modelled is shown in Fig. 3.1. The model developed consists of component models of the PV array, DC-DC boost converter, VSC, LCL filter and the LV power grid. Models of the solar PV system components are described in this section including the MPPT algorithm utilised.

3.2.1 PV array

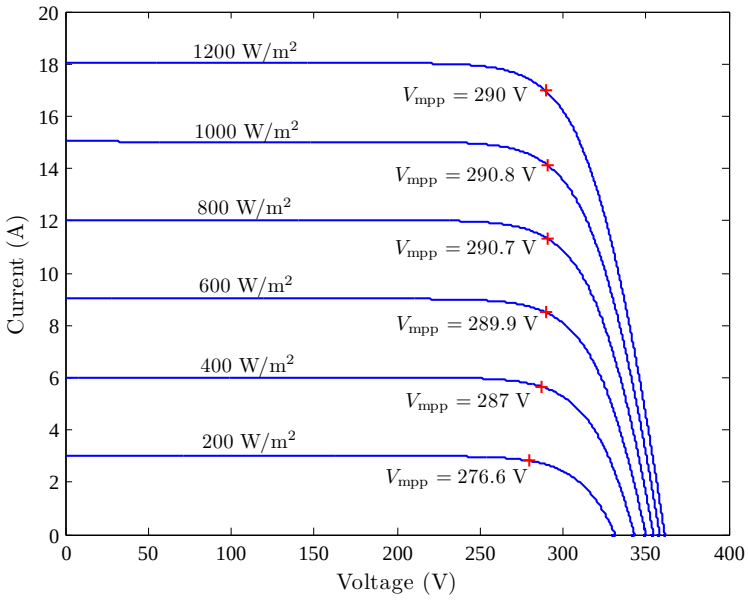

Figure 3.2: V–I characteristic curves of the PV array

The model of a PV array developed in [57] that is based on the single-diode PV cell model is adopted. The V–I and V–P characteristic curves of the adopted PV array model are shown in Fig. 3.2 and Fig. 3.3 respectively, for different solar

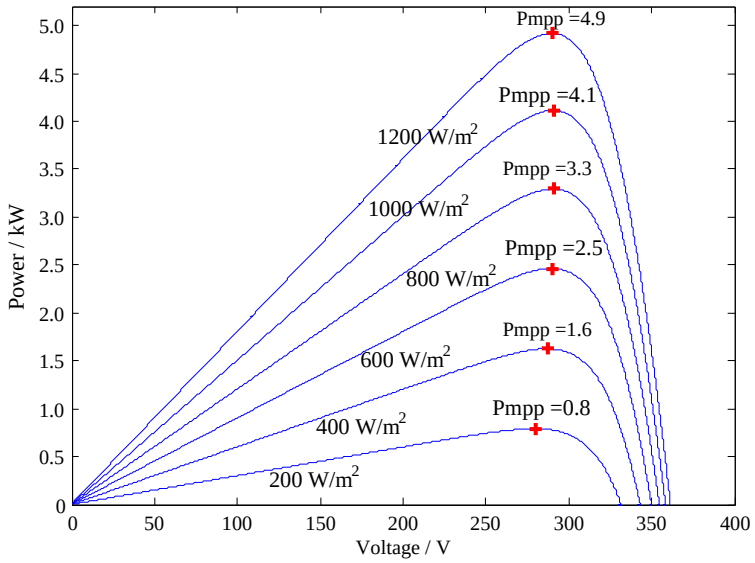

Figure 3.3: V-P characteristic curves of the PV array

irradiance levels while the ambient temperature is maintained at 30 °C. The voltage and power levels at the MPP, V_{mpp} and P_{mpp}, at each irradiance level are indicated in Fig. 3.2 and Fig. 3.3 respectively.

3.2.2 MPPT algorithm

The maximum power that can be extracted from a PV array at any given time is a function of the solar irradiance and the ambient temperature. Since the solar irradiance and the ambient temperature are changing continuously, an MPPT algorithm is necessary to track the MPP. In Chapter 2, InC method was identified as an MPPT algorithm with adequate performance to use in the simulation model of the PV system. Hence, the InC algorithm is implemented in the developed simulation model of the PV system.

In the flowchart of Fig. 3.4 that illustrates the InC algorithm, t and $(t-1)$ indicate the current sample time and the previous sample time, ΔV_{pv} and ΔI_{pv} represent the difference between two consecutive samples of the output voltage, V_{pv}, and current, I_{pv}, at the PV array output respectively. $V_{\text{pvref}}(t)$ is the voltage of the tentative MPP that is determined by the InC algorithm at the end of an iteration and δV_{pv} is the magnitude of voltage that is added/subtracted to/from

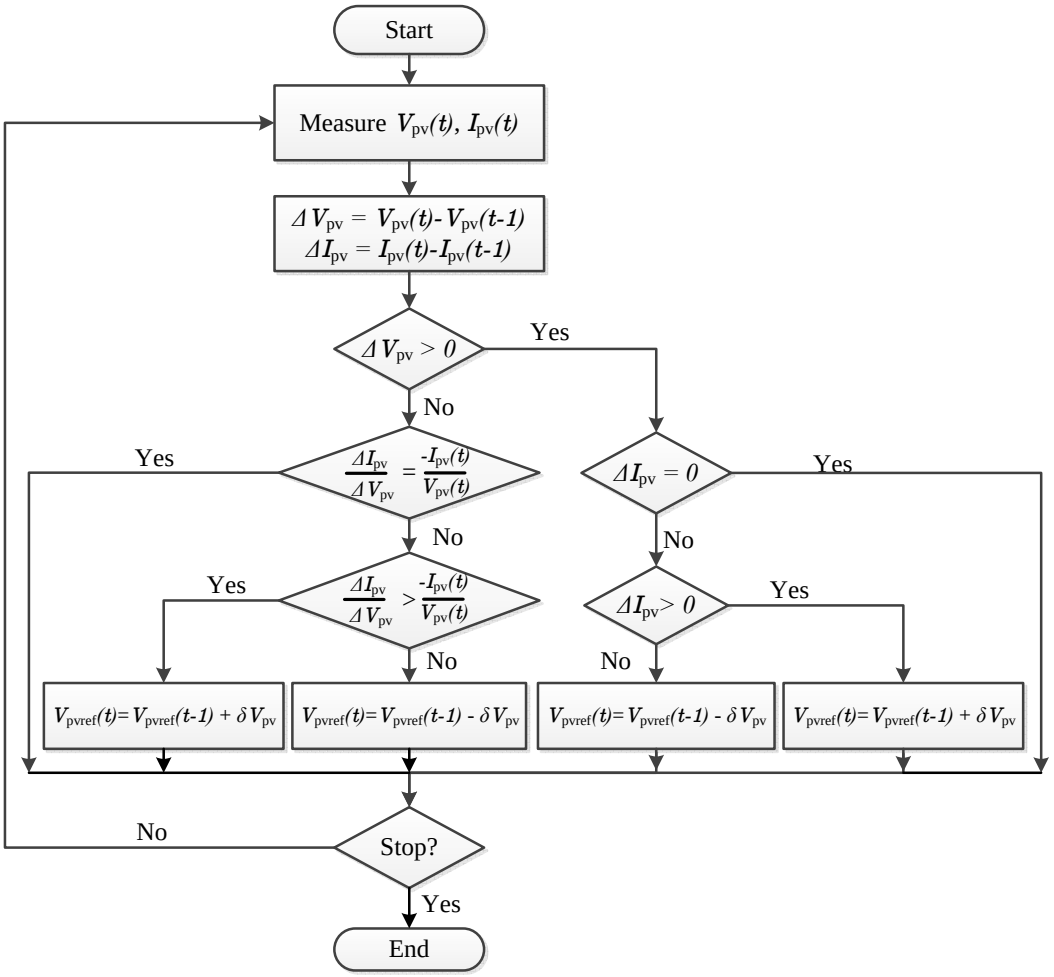

Figure 3.4: Flow chart of the InC algorithm [4]

$V_{\text{pvref}}(t-1)$ to determine $V_{\text{pvref}}(t)$ at the end of each iteration in the process of finding the true MPP.

The InC algorithm is capable of identifying the true MPP through the iterative process. Once the true MPP is found, the output of the InC algorithm, $V_{\text{pvref}}(t)$, does not change until there is a change in the true MPP of the PV array due to a change in the irradiance level or the temperature. If the true MPP of the PV array is changed when the PV array is operating at the true MPP at any given time, the InC algorithm is capable of identifying such a change and the iterative process is restarted to determine the new MPP of the PV array.

3.2.3 Voltage source converter

The VSC in Fig. 3.1 is a full-bridge converter that utilises insulated gate bi-polar transistor (IGBT) switches. The VSC is able to operate in all four quadrants provided that necessary control algorithms for such operation are implemented in the controller of the VSC. The kVA ratting of the VSC, S_{r}, is 5.4 kVA. The spare capacity of the VSC when injecting a certain amount of active power is used for injecting or absorbing reactive power. The switching frequency of the VSC, f_{sw}, is 25 kHz and a unipolar sinusoidal pulse width modulation technique is used [58].

3.2.4 LCL filter

The values of the inductors and the capacitor of the LCL filter of the PV system shown in Fig. 3.1 were determined as $L_{\mathrm{fc}} = 150\ \mu$H, $L_{\mathrm{fg}} = 75\ \mu$H and $C_{\mathrm{f}} = 2.2\ \mu$F, by following the design guidelines established in [59][1]. Resistances of inductances L_{fc} and L_{fg} are assumed as $R_{\mathrm{fc}} = R_{\mathrm{fg}} = 0.001\ \Omega$[2]. The total inductance of the designed LCL filter is less than 0.1 pu (using a base - $S_{\mathrm{b}} = 5.4$ kVA, $V_{\mathrm{b}} = 230$ V) and the resonant frequency, f_{res}, is 10.7 kHz; less than $0.5 f_{\mathrm{sw}}$. A damping resistor $R_{\mathrm{d}} = 2\ \Omega$, calculated as one third of the impedance of C_{f} at f_{res}, is added in series with C_{f} to improve the stability of the current controller[3] [60].

3.2.5 Selection of DC-link capacitor

In a single-phase, grid-connected VSC, the DC-link voltage, V_{dc}, consists of an average DC component, V_{dcavg}, as well as a 100 Hz voltage ripple. The existence of this 100 Hz voltage ripple in the DC-link voltage of a single-phase grid-connected

[1]The detailed design procedure of the LCL filter is described in Appendix A.

[2]The damping of the current controller of a PV system is increased if resistance of LCL filter inductors are high. However, since a higher resistance increases losses, LCL filter inductors are designed to have a low resistance.

[3]The dynamic performance of the current controller with and without the damping resistor, R_{d} is analysed in Appendix B.

VSC is explained in Appendix C. An expression for the peak-to-peak 100 Hz voltage ripple, ΔV_{dc}, of the DC-link voltage can be derived as (3.1). The detailed derivation of (3.1) is given in Appendix C.

In (3.1), P_{g} is the active power injected to the grid, C_{dc} is the DC-link capacitance and ω is the fundamental angular frequency of the grid voltage, v_{g}.

$$\Delta V_{\mathrm{dc}} = \frac{P_{\mathrm{g}}}{C_{\mathrm{dc}} V_{\mathrm{dcavg}}\ \omega} \tag{3.1}$$

In the modelled PV system, C_{dc} is calculated as 2200 μF to limit ΔV_{dc} to approximately 5% of V_{dcavg} when the VSC is injecting 5.4 kW of active power to the grid and V_{dcavg} is 400 V.

3.2.6 DC-DC boost converter

The rated capacity of the DC-DC boost converter shown in Fig. 3.1 is 5 kW and the switching frequency, f_{dc}, is 10 kHz. The current passing through the inductor L_{dc} of the DC-DC boost converter consists of a DC component and a switching ripple. The size of the inductor, L_{dc}, can be determined using (3.2) [58] in order to limit the switching frequency associated current ripple, ΔI_{dc}, of the current that is flowing through the inductor. In (3.2), V_{pv} is the voltage across the PV array.

$$L_{\mathrm{dc}} = \frac{V_{\mathrm{pv}}(V_{\mathrm{dcavg}} - V_{\mathrm{pv}})}{\Delta I_{\mathrm{dc}} f_{\mathrm{dc}} V_{\mathrm{dcavg}}} \tag{3.2}$$

If the PV array is operated close to the MPP, V_{pv} is close to 300 V as per Fig. 3.2 and Fig. 3.3. Hence, the inductor L_{dc} can be calculated as 9 mH to limit ΔI_{dc} to 5% of the DC current through the inductor L_{dc} when the DC-DC boost converter is operating at the rated capacity.

The DC-DC boost converter is able to decouple the PV array from AC-side dynamics [61]. In modelling the grid-connected PV system, the capacitor C_{pv} at the PV array output is chosen to be 2.5 times the DC-link capacitor, C_{dc}. With

the selected value for C_{pv}, the 100 Hz voltage ripple that appears across the PV array terminals is reduced to 10% of the 100 Hz voltage ripple of the DC-link when the VSC is operated at the rated capacity. The large time constant of C_{pv} effectively decouples the PV array from AC-side dynamics of the grid-connected PV system. The capacitor, C_{pv} also minimises the switching frequency ripple current that is drawn from the PV array.

3.2.7 LV power grid

The LV power grid is modelled with an equivalent Thèvenin voltage source, v_{s}, and a series impedance, $(R_{\text{g}} + j\omega L_{\text{g}})$, as shown in Fig. 3.1. The reference impedance for low voltage public supply systems that is given in [62] for electrical apparatus testing purposes is used to model the LV power grid. Hence, the grid impedance, $(R_{\text{g}} + j\omega L_{\text{g}})$ is $(0.4 + j0.25)\ \Omega$. This represents high impedance power distribution feeders in Australia. Since the impact of integrating multiple PV systems to high impedance feeders may be significant in terms of network voltage rise, the impedance, $(0.4 + j0.25)\ \Omega$ is used to model power distribution grids in this Thesis.

3.3 Control system design

The control system design for the PV system includes a grid synchronisation mechanism, a current controller, a DC-link voltage controller, a power factor controller and a DC-DC boost converter controller. The design procedures of these control systems are described in this section.

3.3.1 Grid synchronisation

The synchronous reference frame phase-locked-loop (s-PLL) is implemented in the developed simulation model of the PV system. The s-PLL is able to determine the phase angle, peak value and the frequency of the grid voltage, v_{g}, of the grid-connected PV system. The information obtained from the s-PLL is used

throughout the control system of the PV system and to synchronise the PV system to the grid.

The structure of the single-phase s-PLL is as depicted in Fig. 3.5. The s-PLL implemented in the single-phase PV system requires the generation of an imaginary orthogonal signal from the grid voltage, v_{g}. Such an imaginary orthogonal signal is obtained by passing v_{g} through a second order band-pass filter, $G_{\mathrm{bp}}(s)$ and an integrator that is scaled by the nominal grid frequency, $\omega = 100\pi$ rad/s. This structure creates an imaginary orthogonal signal without any time delay and also filters out the harmonics in the measured grid voltage, v_{g}. The transfer function of the standard second order band-pass filter is given in (3.3) [63]. In (3.3), ω_{bp} is the centre frequency (in rad/s) of the band-pass filter, Q_{bp} is the quality factor and H_{bp} is the desired DC gain for a signal of the frequency ω_{bp}. The bandwidth, BW_{bp}, of the second order band-pass filter is given in (3.4).

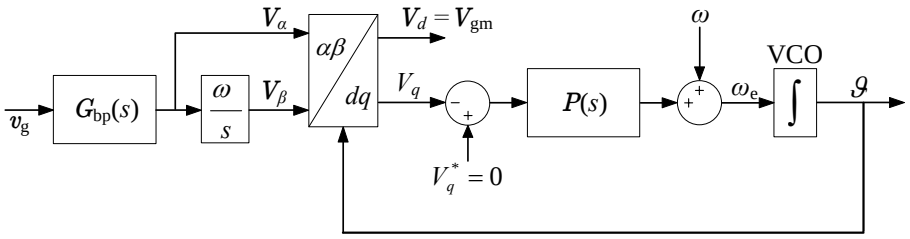

Figure 3.5: Structure of the single-phase s-PLL

$$G_{\mathrm{bp}}(s) = \frac{H_{\mathrm{bp}}(\omega_{\mathrm{bp}}/Q_{\mathrm{bp}})s}{s^2 + (\omega_{\mathrm{bp}}/Q_{\mathrm{bp}})s + \omega_{\mathrm{bp}}^2} \tag{3.3}$$

$$BW_{\mathrm{bp}} = \frac{\omega_{\mathrm{bp}}}{Q_{\mathrm{bp}}} \tag{3.4}$$

As indicated in Fig. 3.5, V_α and V_β are the filtered grid voltage signal and the imaginary orthogonal signal respectively. The Park transformation is applied to V_α and V_β to determine V_d and V_q. $P(s)$ is a compensator and, ω_{e} and ϑ are the estimated angular frequency and the phase angle of v_{g}. If ϑ is very close to the actual phase angle of v_{g}, $V_q \approx 0$ and $V_d \approx V_{\mathrm{gm}}$ where V_{gm} is the peak value of v_{g}.

The main function of the band-pass filter is to filter out the harmonics in v_{g}. Therefore, a narrow bandwidth is desired in the band-pass filter so that the low-order harmonics are well attenuated. Hence a higher Q_{bp} is desired according to (3.4). But a very low bandwidth slows down the dynamic response of the filter. Therefore a high value for Q_{bp} cannot be chosen. The chosen value of Q_{bp} is 1.25, so that the $BW_{\mathrm{bp}} = 40$ Hz for a signal of $\omega_{\mathrm{bp}} = 100\pi$ rad/s. Since neither attenuation nor gain is desired for the fundamental frequency grid voltage signal v_{g}, $H_{\mathrm{bp}} = 1$. The frequency response and the step response of the designed band-pass filter are shown in Fig. 3.6 and Fig. 3.7 respectively. As shown in Fig. 3.6, for a 50 Hz input signal, there is no gain or phase change in the output signal of the band-pass filter. Based on Fig. 3.7 settling time of the designed band-pass filter is 30 ms.

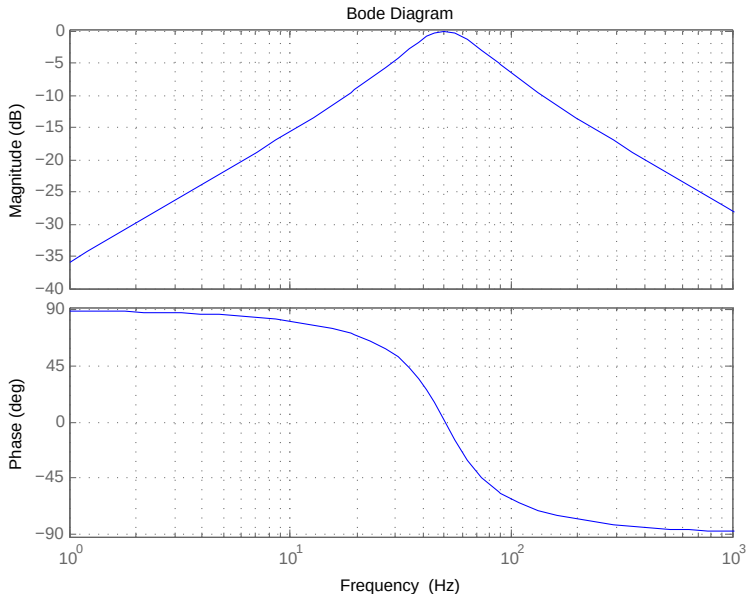

Figure 3.6: Frequency response of the band-pass filter

The control loop of the single-phase s-PLL consists only a pole at zero that is of the voltage-controlled-oscillator (VCO). A PI regulator is chosen as the compensator $P(s)$. The gains of the PI compensator are selected as $k_{\mathrm{ppll}} = 115$ and $k_{\mathrm{ipll}} = 6600$. The step response of the closed-loop system is shown in Fig. 3.8 demonstrating a settling time of approximately 70 ms.

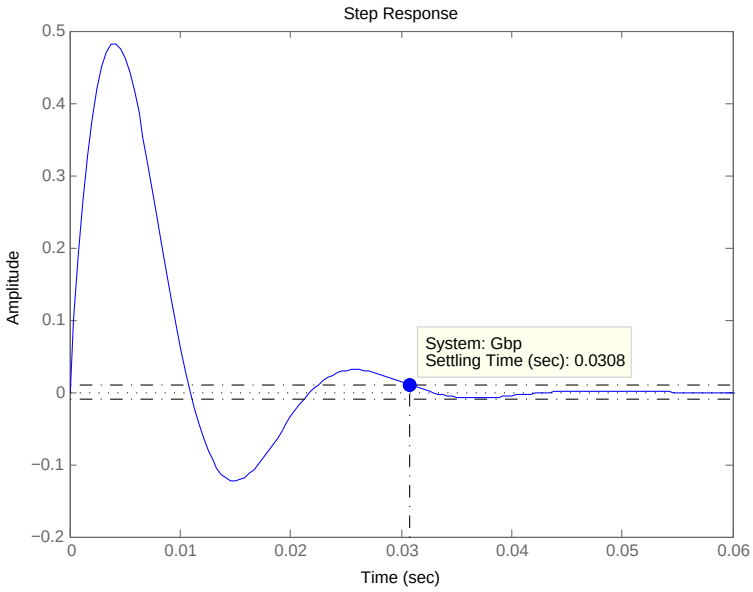

Figure 3.7: Step response of the band-pass filter of the s-PLL

3.3.2 Current controller

The current that is injected to the grid by the PV system is controlled by the current controller. The current controller is able to regulate the current injected by the PV system to follow a reference current signal that is generated by the rest of the control system of the PV system.

In the developed simulation model of the PV system, a stationary frame closed-loop current controller which is able to regulate the current injected to the grid by the PV system by following a sinusoidal current reference is used. The stationary frame closed-loop current controller is implemented using the PR regulator introduced in [20]. The transfer function of the non-ideal PR controller with fundamental frequency compensator and low-order odd harmonic compensators (HCs), is given in (3.5) [64]. The fundamental frequency compensator regulates the current injected to the grid with zero steady-state error while the low-order odd harmonic compensators minimise the low order harmonic currents injected to the grid by the PV system. In (3.5), k_{pc} is the proportional gain, k_{ich} is the integral gain and ω_c is the 3 dB cut-off frequency.

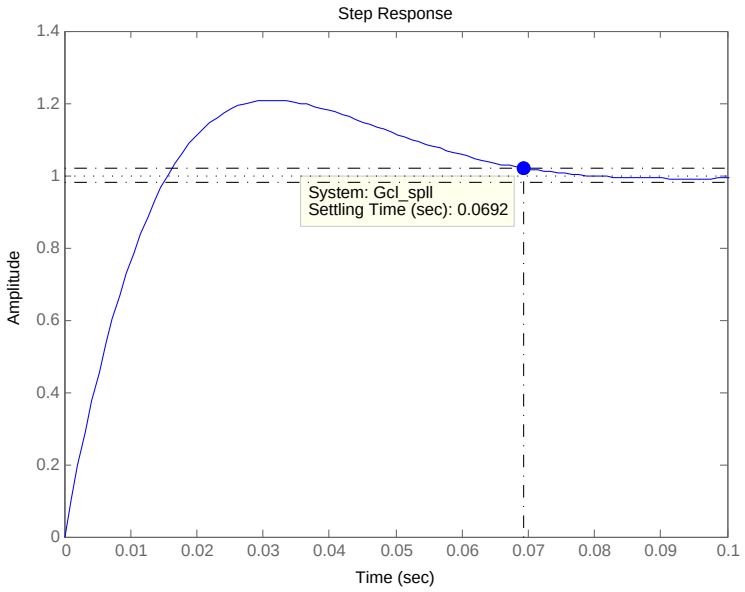

Figure 3.8: Step response of the s-PLL

$$C(s) = k_{\mathrm{pc}} + \sum_{h=1,3,5,7} \frac{2k_{\mathrm{ich}}\omega_c s}{s^2 + 2\omega_c s + (h\omega_o)^2} \tag{3.5}$$

The control plant model of the stationary frame current controller can be derived as (3.6) by simplifying the LCL filter to an L filter and neglecting the grid impedance[4]. In (3.6), $L_{\mathrm{T}} = 2(L_{\mathrm{fc}} + L_{\mathrm{fg}})$ and $R_{\mathrm{T}} = 2(R_{\mathrm{fc}} + R_{\mathrm{fg}})$.

$$C(s) = \frac{I_{\mathrm{g}}(s)}{V(s)} = \frac{1}{L_{\mathrm{T}}s + R_{\mathrm{T}}} \tag{3.6}$$

The closed-loop current controller is shown in Fig. 3.9 with a unity gain feedback loop. The current reference, i_{gref}, is calculated using (3.7), where V_{gm} and ϑ are obtained from the single-phase s-PLL and, P_{ref} and Q_{ref} are the active power reference from the output of the DC-link voltage controller and reactive power reference from the output of the power factor controller respectively. In Fig. 3.9, e_{c} is the difference between the current reference, i_{gref}, and the current injected to the grid, i_{g}, u_{c} is the output of the PR regulator $C(s)$, and m is the modulation index of the VSC.

[4]In Appendix B, the derivation of (3.6) is presented and the effect of the grid impedance on the performance of the current controller is discussed.

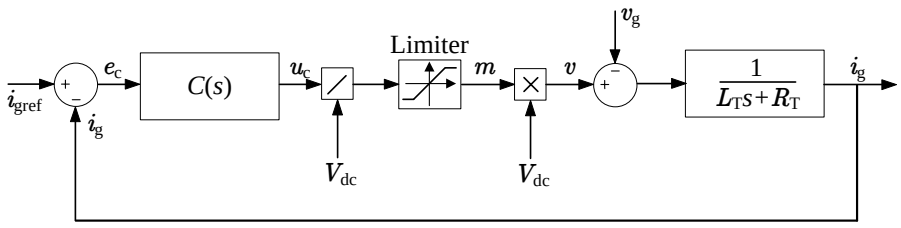

Figure 3.9: Closed-loop current controller of the single-phase VSC system

$$i_{\text{gref}} = \frac{2\sqrt{P_{\text{ref}}^2 + Q_{\text{ref}}^2}}{V_{\text{gm}}} \cos(\vartheta + \arctan(Q_{\text{ref}}/P_{\text{ref}})) \tag{3.7}$$

In the designed PR regulator, $k_{\text{pc}} = 4$ is calculated to obtain a 500 Hz bandwidth for the closed-loop current controller, $k_{\text{ic1}} = 100$ to have zero steady-state error and the integral gains of the HCs are $k_{\text{ich}} = 80$ ($h = 3, 5, 7$). The 3 dB cut-off frequency, ω_c, is selected to be 5 rad/s [64]. The frequency response of the designed closed-loop current controller is shown in Fig. 3.10. As illustrated by Fig 3.10, the designed closed-loop current controller has a unity gain and zero phase shift for fundamental and first three odd harmonic signals. Hence the designed current controller is able to regulate such signals with zero steady-state error.

3.3.3 DC-link voltage controller

The DC-link voltage controller regulates the DC-link voltage of the PV system at a set reference voltage level. In the developed model of the PV system, the DC-link voltage of the VSC is regulated at 400 V. The transfer function of the control plant model of the DC-link voltage can be derived as (3.8)[5] assuming that power balance exists on the AC and DC sides of the VSC.

$$G_{V_{\text{dc}}}(s) = \frac{V_{\text{dc}}^2(s)}{P_{\text{g}}(s)} = -\frac{2}{Cs} \tag{3.8}$$

The control block diagram of the DC-link voltage controller is given in Fig 3.11

[5]The detailed derivation of (3.8) is given in Appendix C.

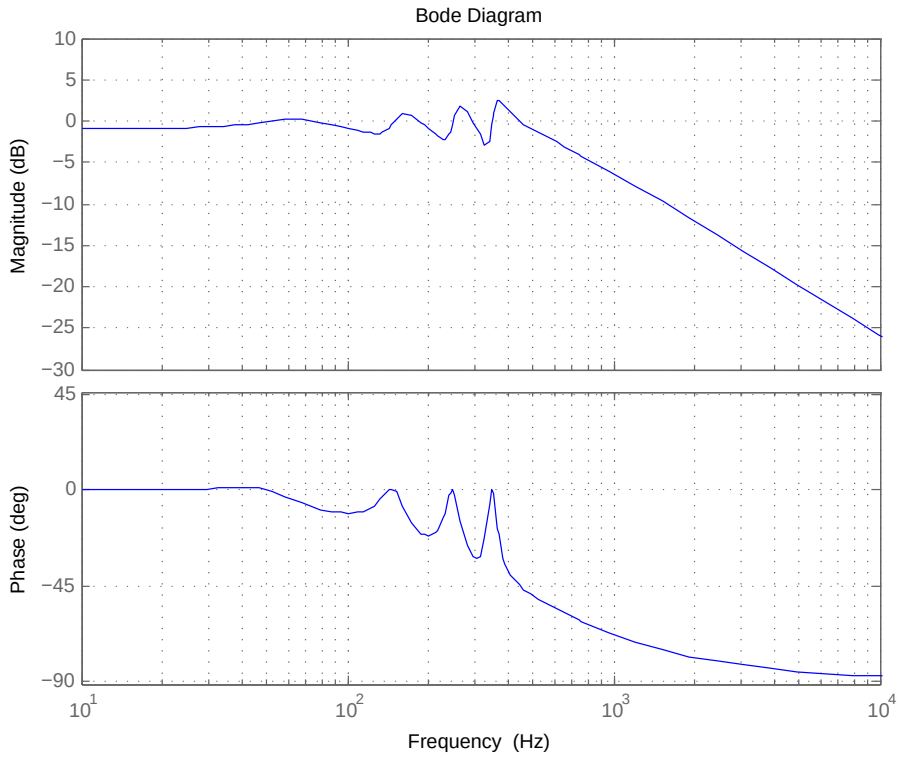

Figure 3.10: Frequency response of the closed-loop current controller

in which $D(s)$ is a compensator, e_{d} is the error between the squares of measured and reference DC-link voltages and u_{d} is the compensator output. In order to improve the dynamic response of the DC-link voltage controller in the presence of rapid changes of power at the PV array, the power feed-forward signal P_{pv} has been added to the controller [13]. P_{pv} is calculated from the measured voltage, V_{pv} and the current, I_{pv} that are shown in Fig 3.1. The compensator output u_{d} is the magnitude of power that is needed to compensate for the losses in the grid-connected PV system. In Fig 3.11, P_{ref} is the amount of active power that should be injected by the VSC to the LV power grid to control the average voltage of the DC-link at the set voltage reference, V_{dcref}. Hence P_{ref} is the active power reference of the current controller and the current control loop becomes an inner control loop of the DC-link voltage controller. Therefore, for proper tracking of V_{dcref}, the bandwidth of the DC-link voltage controller is chosen as one tenth of the bandwidth of the closed-loop current controller. Since the bandwidth of the DC-link voltage controller is much smaller than that of the current controller, the

dynamics of the current controller can be disregarded while designing the DC-link voltage controller.

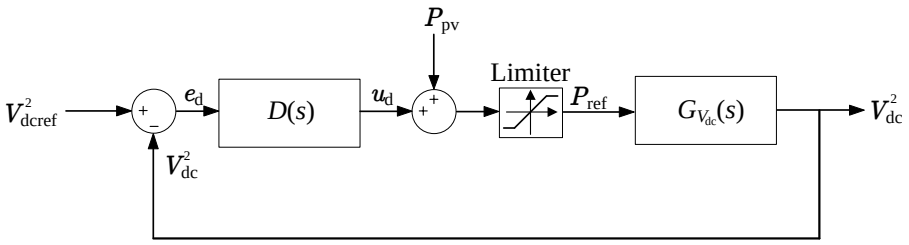

Figure 3.11: The DC-link voltage control diagram

In Fig 3.11, $D(s)$ represents a gain, k_{pd}. Assuming a unity gain feedback loop, the transfer function of the closed-loop DC-link voltage controller is given in (3.9). k_{pd} is calculated as -0.345 to obtain approximately a 50 Hz bandwidth, which is one tenth of the bandwidth of the current controller of the DC-link voltage controller. The frequency response of the closed-loop DC link voltage controller is shown in Fig. 3.12 from which it can be observed that the bandwidth of the designed closed-loop DC link voltage controller is approximately 50 Hz.

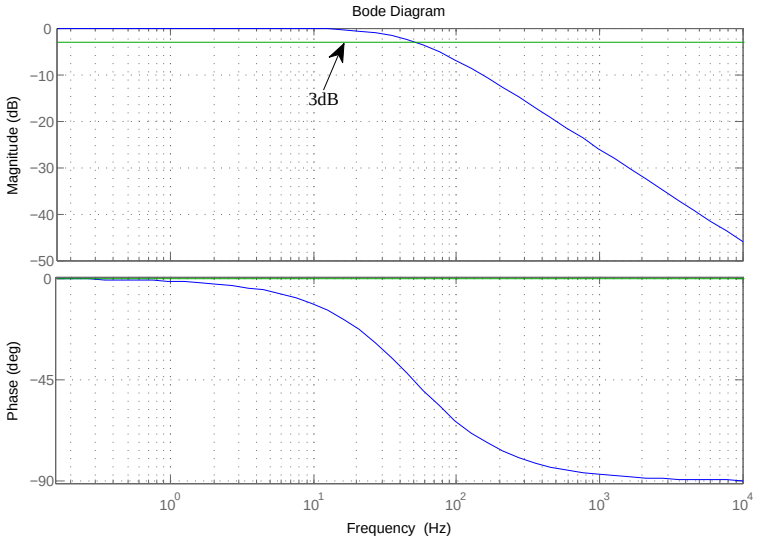

Figure 3.12: Frequency response of the closed-loop DC-link voltage controller

$$G_{\text{dc\_cl}}(s) = \frac{-2k_{\text{pd}}}{C_{\text{dc}}s - 2k_{\text{pd}}} \tag{3.9}$$

The DC-link voltage of the single-phase grid-connected PV system consists of

an average DC component as well as a 100 Hz voltage ripple which is about 5% of the average DC component[6]. The ripple is not desirable in the feedback signal of the DC-link voltage controller since such a component in the feedback signal may result in injecting increased amount of low order harmonic currents from the PV system to the grid. Therefore, the 100 Hz voltage ripple of the DC-link voltage feedback signal is filtered out by using a notch filter in the developed simulation model of the PV system. The notch filter is not shown in Fig. 3.11 to minimise the complexity of the diagram. The inclusion of the notch filter slightly changes the overall dynamic response of the DC-link voltage controller and such changes are discussed in Appendix C.

3.3.4 DC-DC boost converter controller

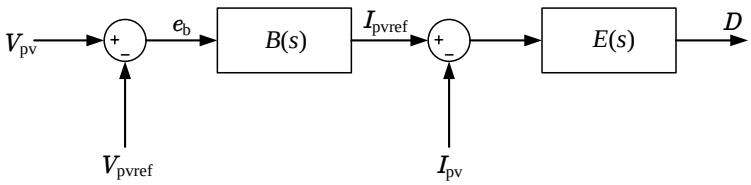

Figure 3.13: Controller of the DC-DC boost converter

The controller of the DC-DC boost converter is shown in Fig. 3.13. V_{pvref} is the voltage of the MPP calculated by the InC algorithm after each iteration and is used as the reference for the PV array side voltage of the DC-DC boost converter. V_{pvref} is compared with the voltage across the PV array, V_{pv}. The error signal, e_{b}, is processed by the compensator $B(s)$ to determine current reference, I_{pvref} for the output current of the PV array. The difference between the measured output current of the PV array, I_{pv} and I_{pvref} is passed through another compensator, $E(s)$. The output $E(s)$ is the duty cycle, D of the DC-DC boost converter. The PI regulators are chosen for compensators $B(s)$ and $E(s)$ and are tuned using a trial and error method. The controller of the DC-DC boost converter adjusts D in such a way that V_{pv} is regulated at V_{pvref}.

[6]This is explained in Appendix C.

3.3.5 Power factor controller

According to the Australian Std AS4777.2 [7], the VSC is allowed to operate in the range from 0.8 leading to 0.95 lagging power factor (considering the VSC as a load connected to the grid). Since the voltage rise at the PCC of a PV system when injects active power to the grid can be minimised by operating the VSC at a lagging power factor, the active and reactive power characteristic curve shown in Fig. 3.14 is implemented to operate the VSC at the maximum allowed lagging power factor. In Fig. 3.14, P_{g} is the active power injected to the grid, Q_{ref} is the reference of the reactive power injected to the grid, Q_{g}, $P_{\mathrm{o}} = 0.2S_{\mathrm{r}}$ kW (as per [7]), $-P_{\mathrm{max}} = -5$ kW and $-Q_{\mathrm{max}} = -1.65$ kVAr.

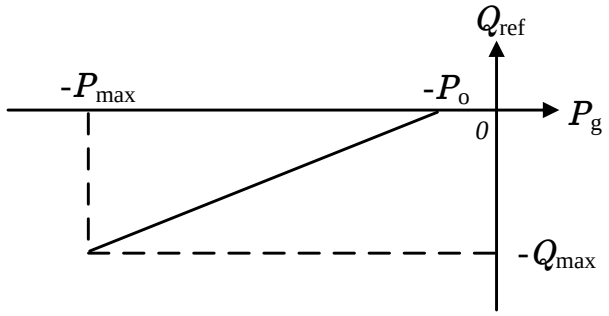

Figure 3.14: Active and reactive power characteristics of the VSC for power factor control

3.4 Simulation results

The simulation model of the grid-connected single-phase two-stage PV system was developed in the PSCAD/EMTDC simulation program. Simulation studies were performed to evaluate the effectiveness of models and controllers of the PV system. The surface temperature of the PV array was assumed to be constant at 30°C in all simulation scenarios.

The VSC was operated at the rated capacity with and without the low-order HCs. The total harmonic distortion (THD) of the simulated grid voltage was zero. The magnitudes of low-order current harmonics injected to the LV power grid as a percentage of the fundamental current is shown in Fig. 3.15. The calculated

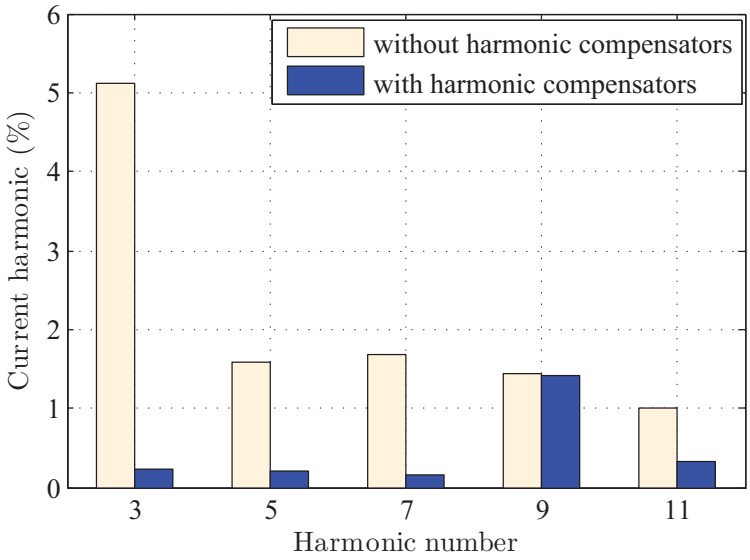

Figure 3.15: Harmonic spectrum of the measured grid current

current THD with and without HC was 5.9% and 1.5% respectively.

Fig. 3.16 illustrates the response of the closed-loop current controller and the DC-link voltage controller for step changes in solar irradiance (from 1200 to 800 W/m^2 at $t = 0.5$ s) and reactive power (from 0 to -1.5 kVAr at $t = 0.65$ s). In the designed PV system, a new current reference is generated upon an operating state change. As the closed-loop current controller closely tracks the generated current reference, the steady-state error is almost zero as shown in Fig. 3.16(a). Fig. 3.16(c) illustrates the capability of the designed current controller to independently control the injected active and reactive power.

The performance of the MPPT algorithm, controller of the DC-DC boost converter and the power factor controller of the VSC are shown in Fig. 3.17 with the variation of solar irradiance illustrated in Fig. 3.17(a). The controller of the DC-DC boost converter has closely regulated the PV array voltage, V_{pv} at V_{pvref} by adjusting the duty cycle of the DC-DC boost converter. The performance of the implemented power factor controller can be seen in Fig. 3.17(e).

Fig. 3.18 illustrates the MPP tracking path of the considered variations in the solar irradiance shown in Fig. 3.17(a). During the ramping time of the solar irradiance, the MPP has deviated away (B_1 and C_1) from the actual value (B_2

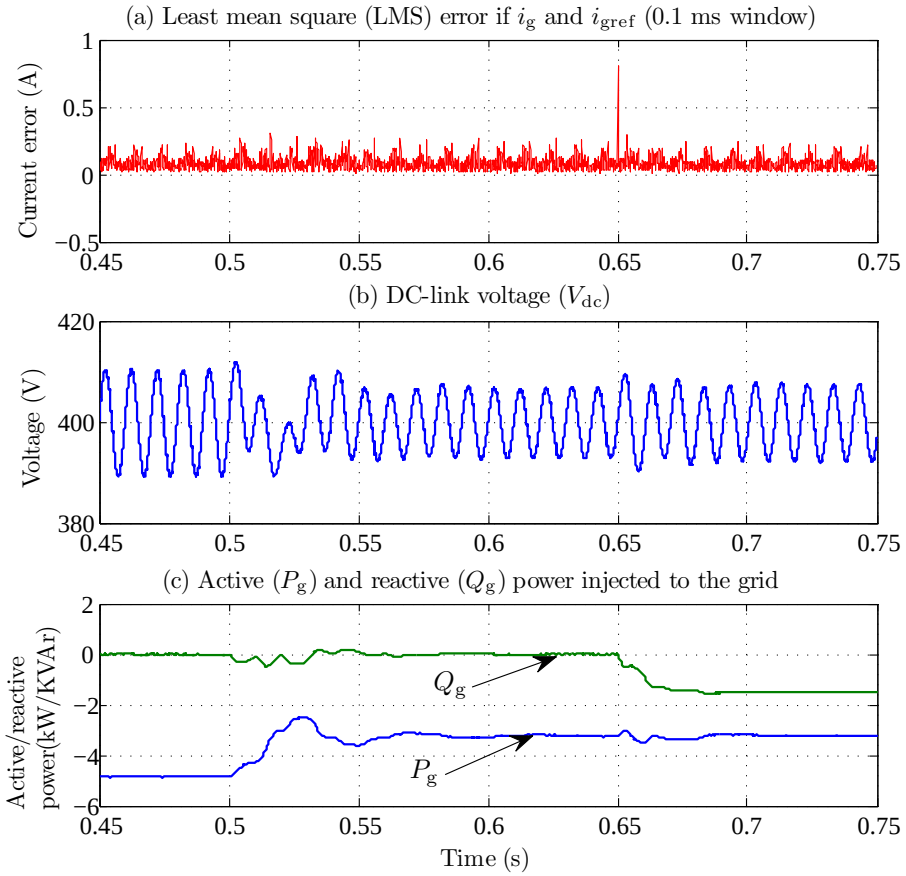

Figure 3.16: System response for step changes of solar irradiance and reactive power reference

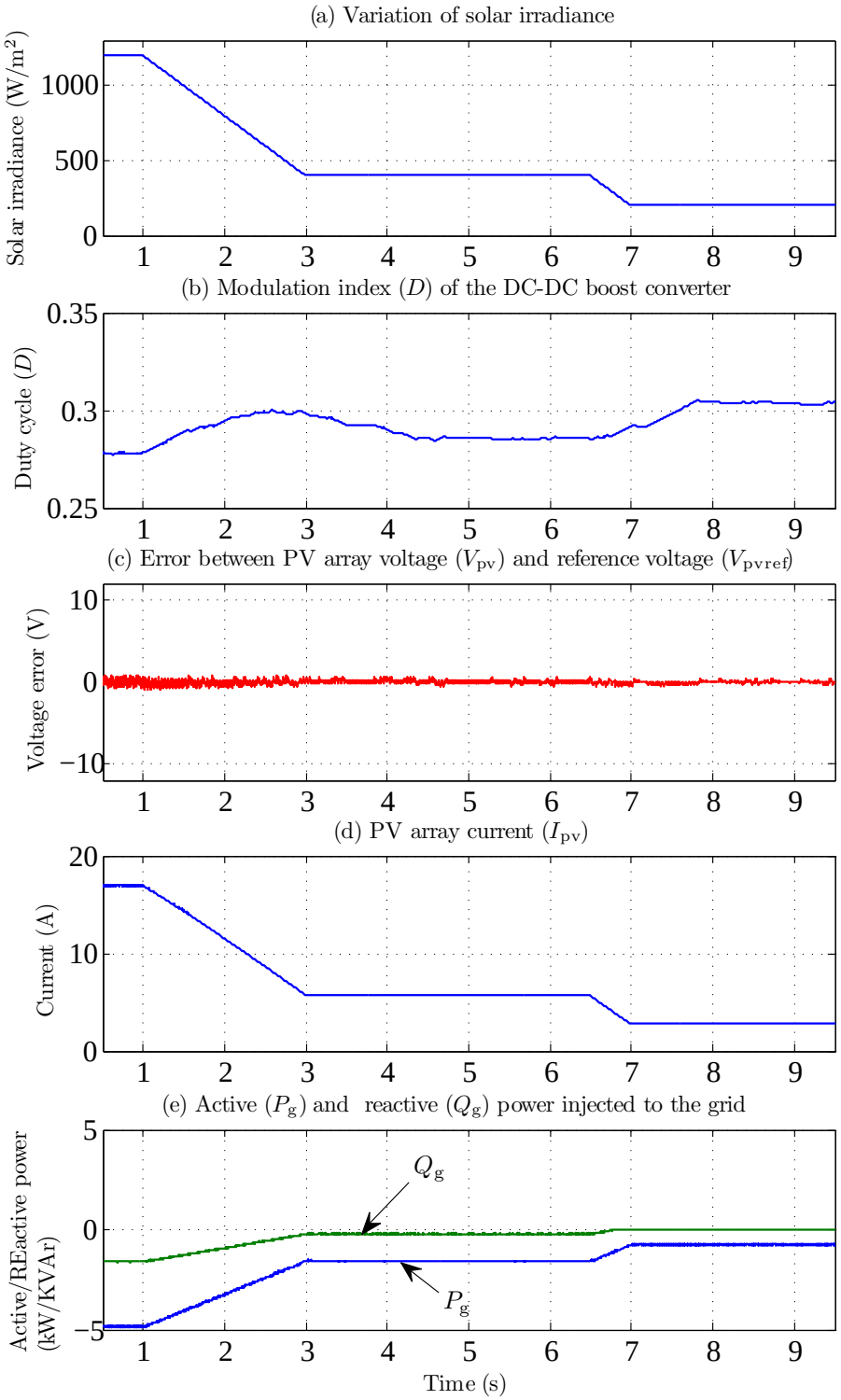

Figure 3.17: System response for a ramping solar irradiance variation

and C_2). However, once the solar irradiance is stabilised, the actual MPP has been found accurately by the MPPT algorithm.

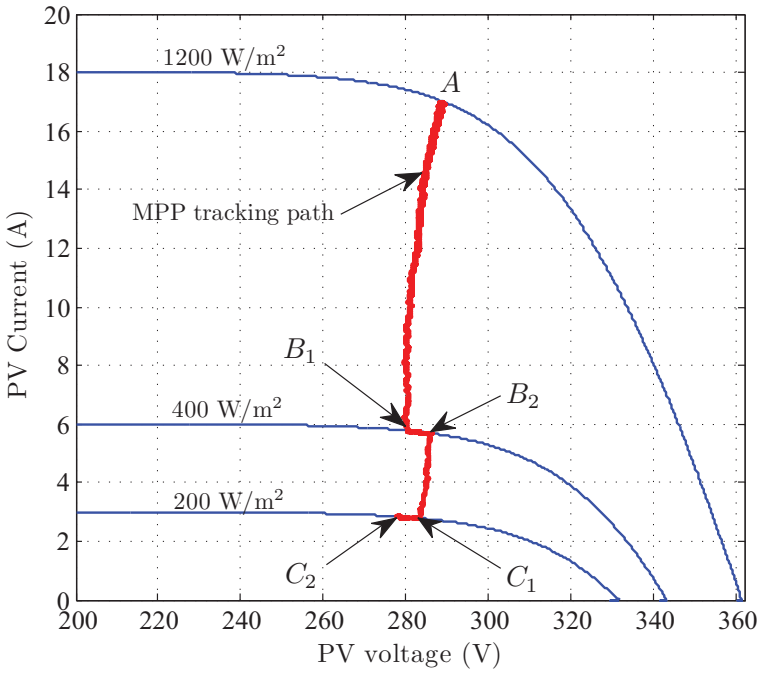

Figure 3.18: MPP tracking path

3.5 Experimental results

An experimental setup using a 5 kW grid-connected single-phase PV system was established in order to validate the simulation model of the PV system that is developed in PSCAD/EMTDC simulation program. The control algorithms that are developed in the simulation model were successfully implemented in the experimental setup of the PV system. Further details on the experimental setup including changes that were necessary in the control algorithms and hardware in the simulation model in order to eliminate practical difficulties when implementing the experimental setup of the PV system are described in Appendix D. The practical results obtained from the implemented experimental setup of the PV system are presented in this section. Further, practical results are compared with the simulation results of the developed simulation model of the PV system that were presented in Section 3.4 of this chapter, where applicable.

The steady-state performance of the s-PLL that is implemented in the experimental setup of the PV system is shown in Fig. 3.19. All signals shown in Fig. 3.19, except the measured grid voltage, v_g, were obtained through the controller of the implemented PV system and displayed on an oscilloscope via digital to analog (D/A) conversion channels. In the test performed, the rms value of voltage of v_g was 230 V. The band-pass filter of the s-PLL has been able to filter out the low-order harmonics in the measured grid voltage v_g since V_α, which is the output of the band-pass filter and that is shown in the Fig. 3.19, is nearly a pure sinusoid. The imaginary signal generated by the s-PLL, V_β lags V_α by approximately $\pi/2$ rad. The peak value of the grid voltage, V_{gm} as found by the s-PLL is close to 325 V.

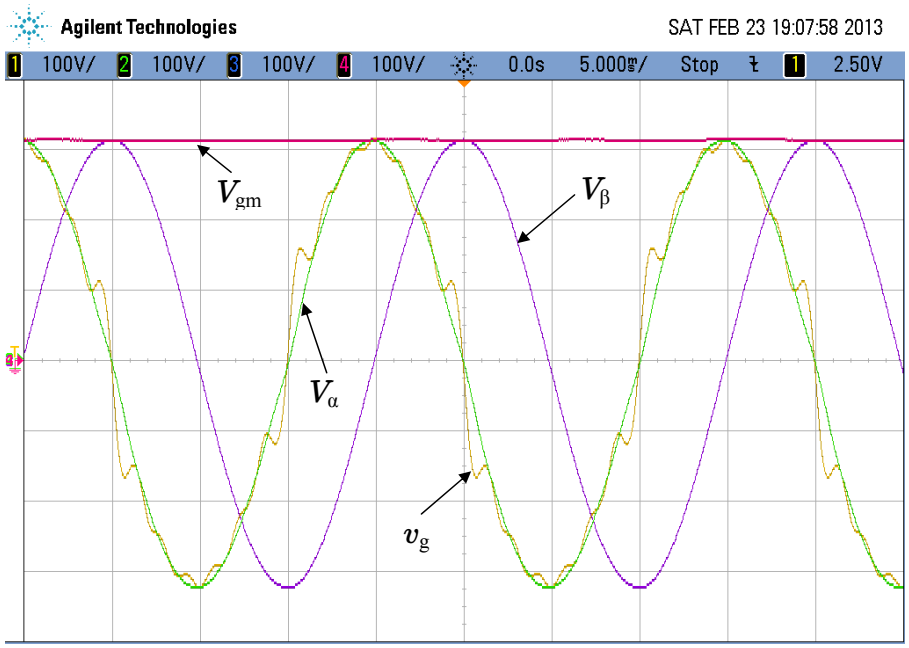

Figure 3.19: Steady-state performance of the s-PLL: Ch1: measured grid voltage (v_g) [100 V/div], Ch2: filtered grid voltage (V_α) [100 V/div], Ch3: imaginary orthogonal signal (V_β) [100 V/div], Ch4: peak value of the grid voltage (V_{gm}) [100 V/div], Time base [5 ms/div]

The dynamic response of the s-PLL is shown in Fig. 3.20 during a 10% step change in the magnitude of the grid voltage. The implemented s-PLL has been able to find the actual peak value of v_g within about 20 ms following the step change in the magnitude of the grid voltage. The tracking of the angle of the grid

voltage, ϑ is accurate and smooth even during the transient period as shown in Fig. 3.20.

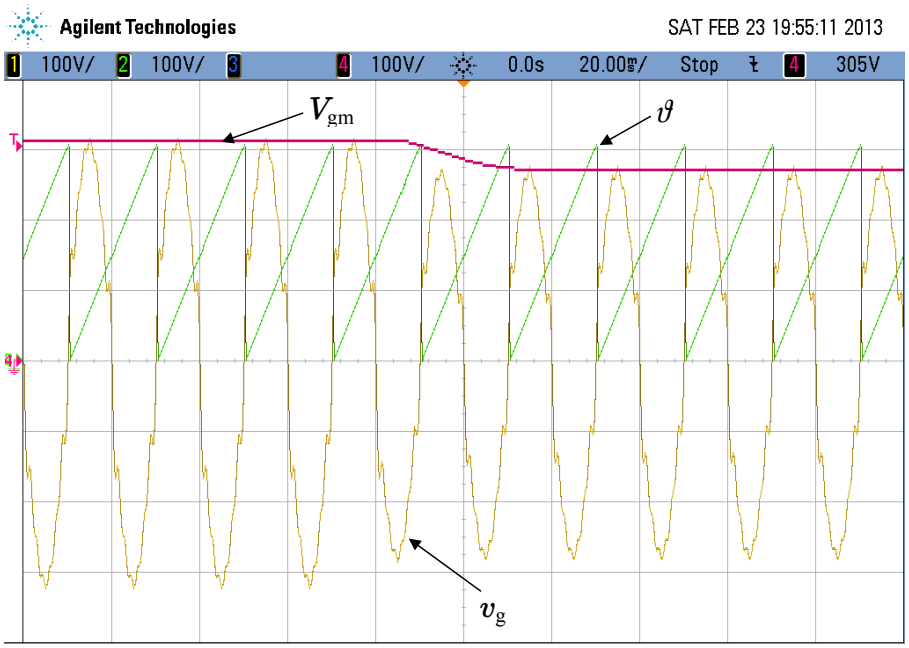

Figure 3.20: Dynamic performance of the s-PLL: Ch1: measured grid voltage (v_g) [100 V/div], Ch2: phase angle of the measured grid voltage, v_g (ϑ) [2 rad/div], Ch4: peak value of the grid voltage (V_{gm}) [100 V/div], Time base [20 ms/div]

The DC-link capacitor, C_{dc}, of the implemented PV system is 1100 μF and the expected peak-peak value of the 100 Hz DC-link voltage ripple is 34 V if the PV system is operated at the rated power[7]. The implemented experimental setup of the PV system could only be operated at a maximum of 2.7 kW due to operational limitations in the solar array simulator used. The 100 Hz DC-link voltage ripple when the PV system is injecting 2.7 kW to the grid is shown in Fig. 3.21 in which the peak-peak value of the DC-link voltage ripple is 20 V.

The dynamic response of the DC-link voltage controller of the implemented PV system is shown in Fig. 3.22 at the time of synchronising the PV system to the grid. The DC-link voltage, V_{dc}, of the PV system was increased when the PV system was connected to the grid since the DC-link capacitor of the PV system was charged by the active power absorbed from the grid soon after the PV

[7]Refer to Section D.2.7 of Appendix D.

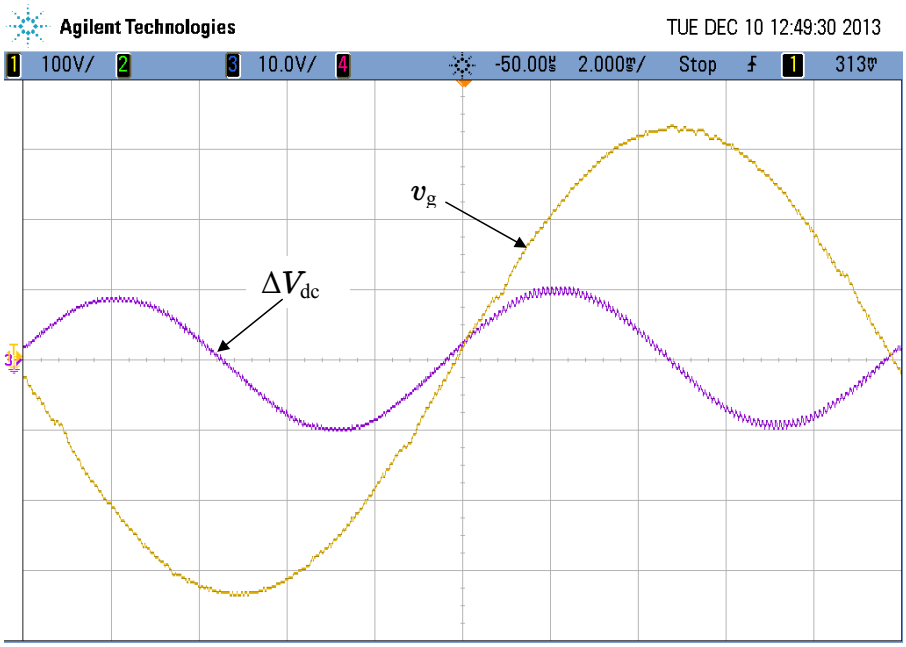

Figure 3.21: 100 Hz voltage ripple of the DC-link voltage: Ch1: measured grid voltage (v_g) [100 V/div], Ch3: Voltage ripple of the DC-link voltage (ΔV_{dc}) [10 V/div], Time base [2 ms/div]

system was connected to the grid. The DC-link voltage controller has been able to regulate the DC-link voltage at 420 V within a short period of time (about 20-30 ms) after the PV system was connected to the grid.

The DC-link voltage controller implemented in the PV system has dynamic characteristics typical of a second-order system as can be seen from the variation of V_{dc} in Fig. 3.22. This behaviour is mainly due to the notch filter that is used to eliminate the 100 Hz voltage ripple of the DC-link voltage feedback signal in the DC-link voltage controller as discussed in Section 3.3.3 of this chapter.

The waveforms of the current injected to the grid by the PV system, i_g, and the 100 Hz DC-link voltage ripple, ΔV_{dc}, of the PV system when the PV system was injecting about 2.3 kW of active power to the grid, is shown in Fig. 3.23. In this test, the reactive power reference of the PV system was zero. Fig. 3.23 illustrates the capability of the implemented current controller of the PV system to regulate i_g following the reference signal generated by the control system of the PV system since i_g was in phase with v_g as shown in Fig. 3.23 when the reactive power reference is zero.

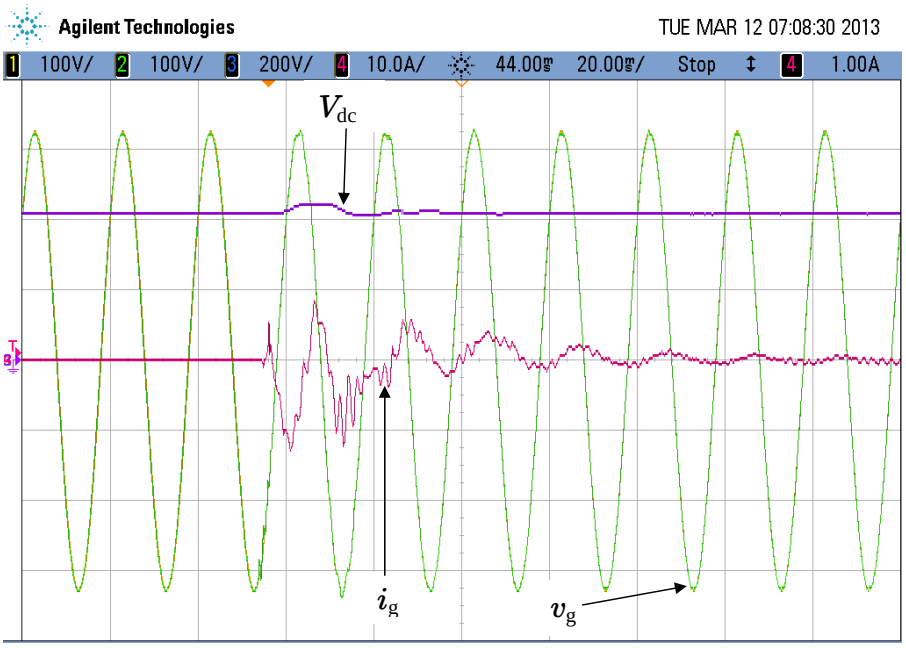

Figure 3.22: Dynamic response of the DC-link voltage controller: measured grid voltage (v_g) [100 V/div], Ch3: DC-link voltage (V_{dc}) [200 V/div], Ch4: current injected to the grid (i_g) [10 A/div], Time base [20 ms/div]

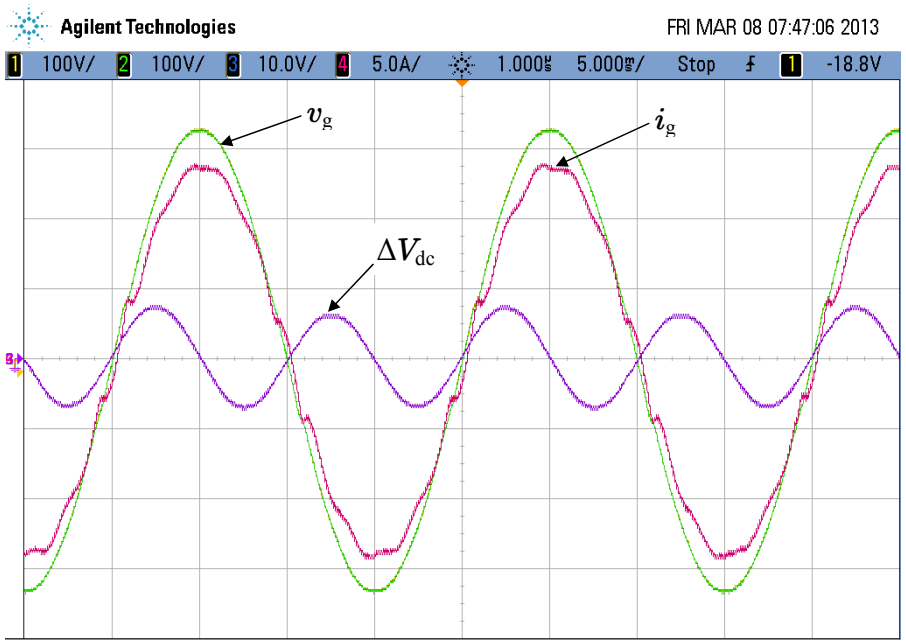

Figure 3.23: Active power injection from the PV system: Ch2: measured grid voltage (v_g) [100 V/div], Ch3: Voltage ripple of the DC-link voltage (ΔV_{dc}) [10 V/div], Ch4: current injected to the grid (i_g) [5 A/div], Time base [5 ms/div]

The output voltage of the PV array, V_{pv}, and the output current of the PV array, I_{pv}, during the test performed to obtain Fig. 3.23, is shown in Fig. 3.24. According to the figures, PV array was injecting about 2.5 kW of active power. The difference in active power injected to the grid as calculated from Fig. 3.23 and Fig. 3.24 is mainly due to losses in the converter system of the PV system.

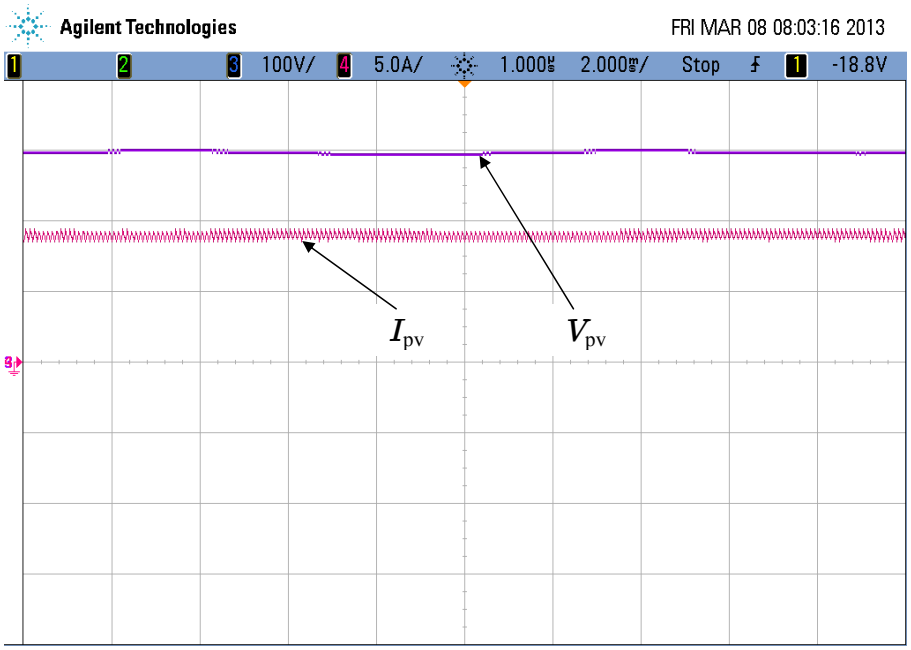

Figure 3.24: Outputs of the PV array: Ch3: output voltage of the PV array (V_{pv}) [100 V/div], Ch4: output current of the PV array (I_{pv}) [5 A/div], Time base [2 ms/div]

The 100 Hz voltage ripple on the DC-link of the PV system causes a 100 Hz ripple voltage and current in the output voltage and current of the PV array. Such voltage and current ripple at the output of the PV system can be minimised by appropriately tuning the PI regulators in the controller of the DC-DC boost converter of the PV system.

The voltage ripple, ΔV_{pv}, and the current ripple, ΔI_{pv}, at the output of the PV array during the test performed to obtain Fig. 3.23 and Fig. 3.24 is illustrated by Fig. 3.25. The high frequency component of ΔI_{pv} in Fig. 3.25 is the switching frequency current ripple of the output current of the PV array. According to Fig. 3.23 and Fig. 3.25, the controller of the DC-DC boost converter of the implemented PV system has been able to limit the peak-peak values of 100 Hz ripple

in ΔV_{pv} and ΔI_{pv} to about 5 V and 100 mA respectively when the peak-peak value of ΔV_{dc} was about 15 V.

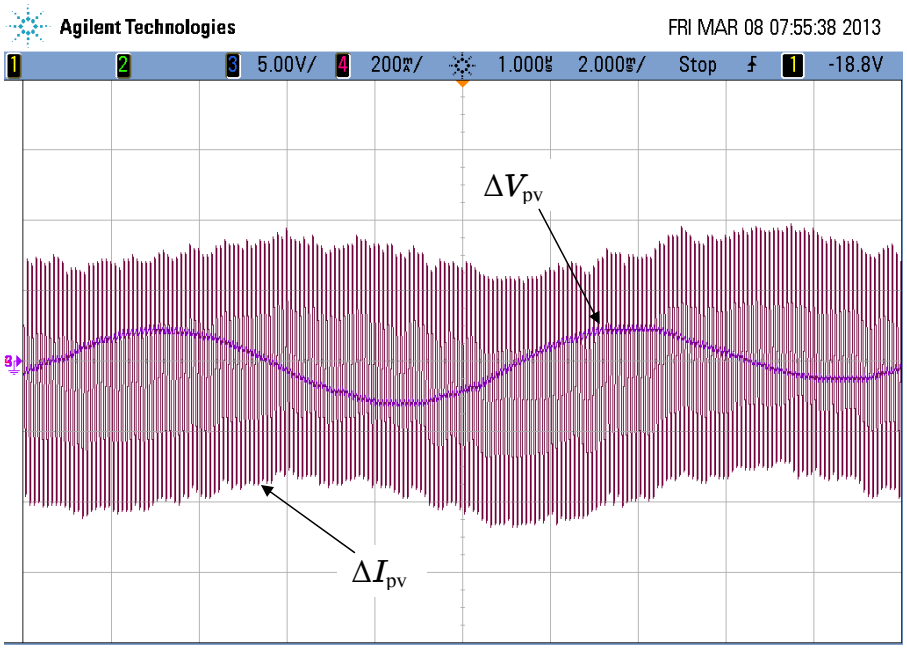

Figure 3.25: Voltage and current ripple at the output of the PV array: Ch3: voltage ripple (ΔV_{pv}) [5 V/div], Ch4: current ripple (ΔI_{pv}) [200 mA/div], Time base [2 ms/div]

In the current controller of the experimental setup of the PV system, 3^{rd}, 5^{th}, 7^{th} and 9^{th} HCs were implemented. The effectiveness of the implemented HCs were evaluated by performing three tests when the PV system was injecting 2.5 kW of active power to the grid. In the first test, HCs of the current controller were inactive and there was no harmonic distortion in the grid voltage, v_{g}. The HCs were active in the second test but there was zero harmonic distortion in the grid voltage. In the third test, HCs were active and v_{g} consisted of 3^{rd}, 5^{th}, 7^{th} and 9^{th} harmonics. The magnitude of each harmonic component in v_{g} was 5% of the fundamental voltage. The waveforms of the current injected to the grid, i_{g} captured from first, second and third tests are shown in Fig. 3.26, Fig. 3.27 and Fig. 3.28 respectively. The magnitudes of the low-order current harmonics injected to the grid as a percentage of the fundamental current are shown in Fig. 3.29. Similar to the performance of HCs in the simulation model of the PV system, HCs in the implemented PV system have been able to minimise the low-

order harmonic current injection to the grid as shown in Fig. 3.29. The calculated THD of i_g in the first test was 8.5%, in the second test was 4.8% and in the third test was 4.2%.

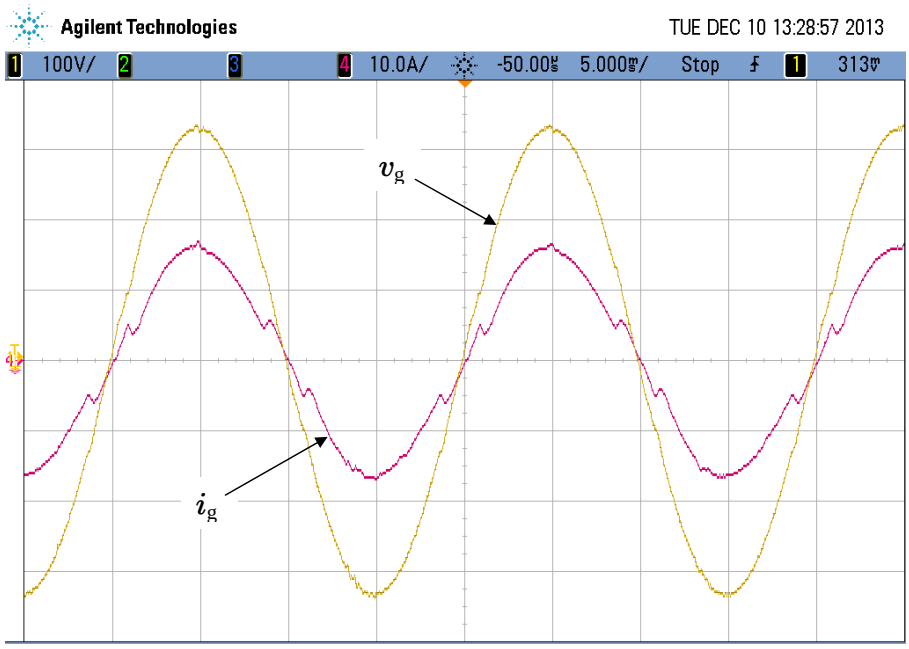

Figure 3.26: Current injected to the grid by the PV system, i_g when HCs were inactive and with zero harmonic distortion in the grid voltage, v_g - test 1: Ch1: measured grid voltage (v_g) [100 V/div], Ch4: current injected to the grid (i_g) [10 A/div], Time base [5 ms/div]

The dynamic behaviour of the DC-link voltage, V_{dc}, and the current injected to the grid by the PV system, i_g, once the reactive power reference of the PV system was instantaneously changed from 0 to 2 kVAr is shown in Fig. 3.30. In Fig. 3.30, i_g is in-phase with v_g at the beginning since the reactive power reference at the beginning of the performed test was zero. Once the reactive power reference was changed to 2 kVAr, i_g lags v_g since i_g was controlled by the current controller to allow both active and reactive power injection to the grid by the PV system. The transient in V_{dc} because of the step change in the reactive power reference has been stabilised within a short period of time.

The accuracy of operating the PV system at the MPP of the PV array can be obtained through the user interface of the PV array simulator that is used in the experimental setup. The variation of the accuracy of the MPP tracking

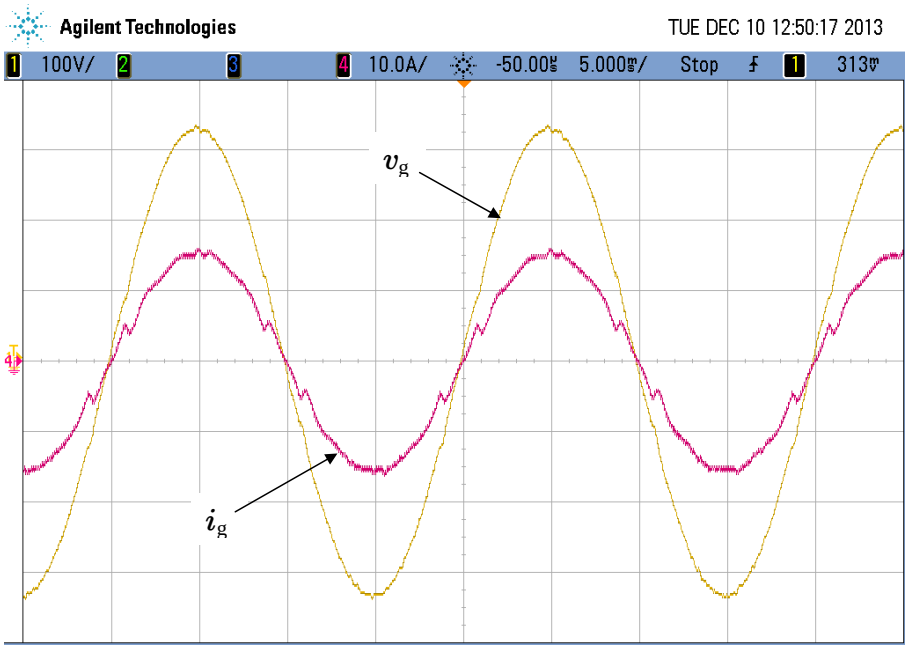

Figure 3.27: Current injected to the grid by the PV system, i_g when HCs were active and with zero harmonic distortion in the grid voltage, v_g - test 2: Ch1: measured grid voltage (v_g) [100 V/div], Ch4: current injected to the grid (i_g) [10 A/div], Time base [5 ms/div]

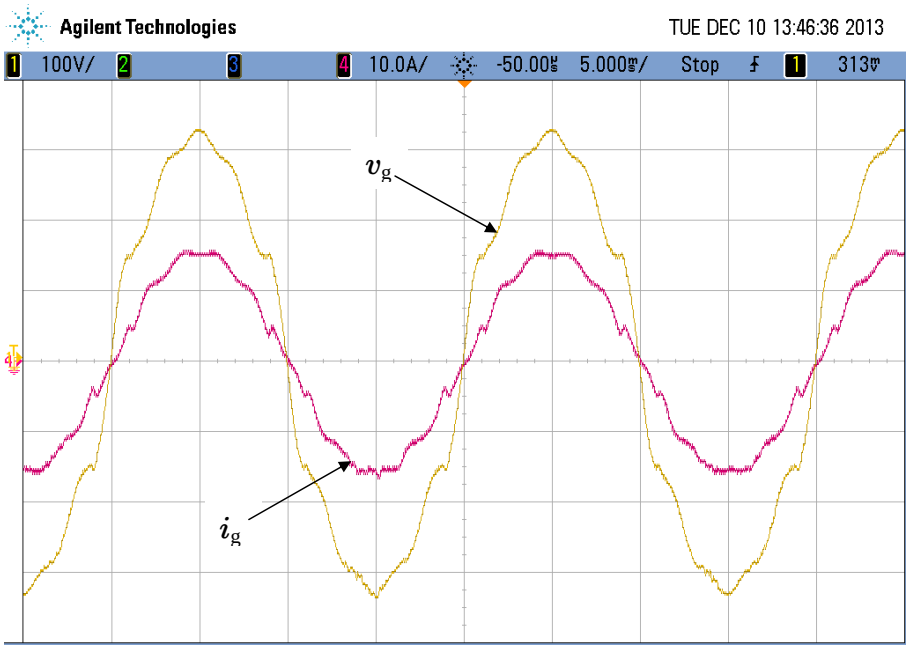

Figure 3.28: Current injected to the grid by the PV system, i_g when HCs were active and with harmonic distortions in the grid voltage, v_g - test 3: Ch1: measured grid voltage (v_g) [100 V/div], Ch4: current injected to the grid (i_g) [10 A/div], Time base [5 ms/div]

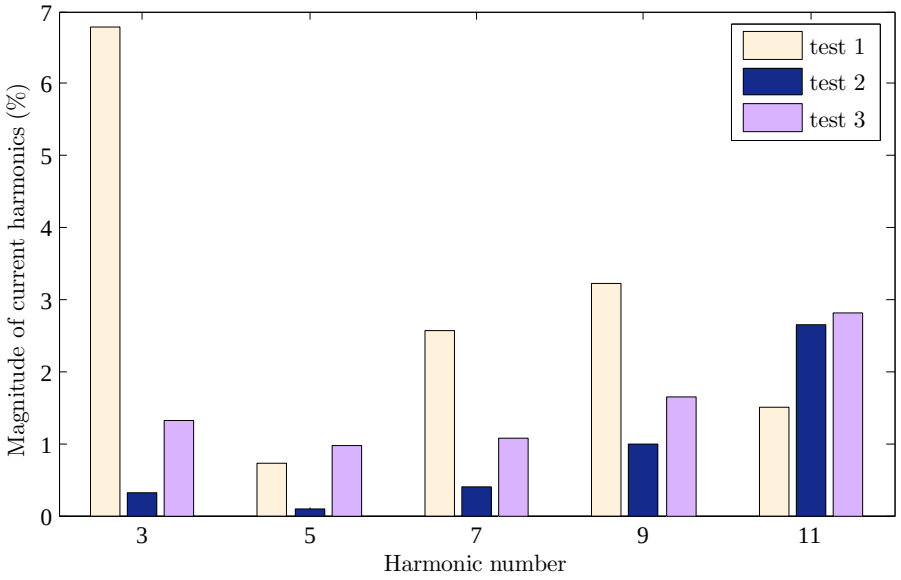

Figure 3.29: Magnitudes of low-order harmonic currents of i_g in three tests performed to evaluate the effectiveness of HCs

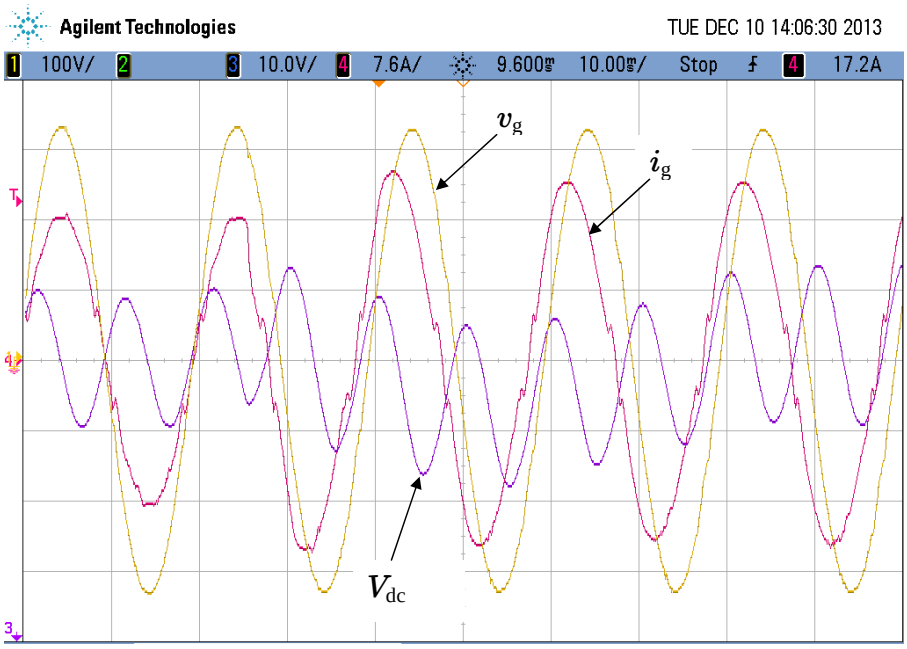

Figure 3.30: A step change in the reactive power reference of the PV system: Ch1: measured grid voltage (v_g) [100 V/div], Ch3: DC-link voltage (V_{dc}) [10 V/div], Ch4: current injected to the grid (i_g) [7.6 A/div], Time base [10 ms/div]

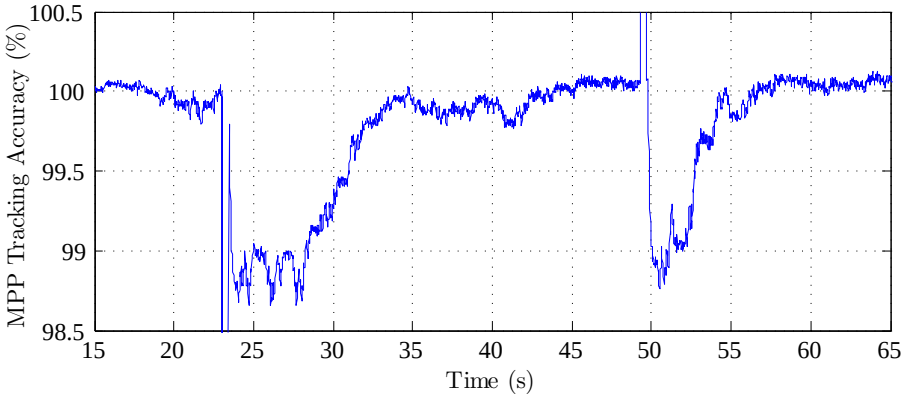

Figure 3.31: MPP tracking of the PV system

during two step changes of the solar irradiance level is shown in Fig. 3.31 which illustrates the effectiveness of the controller of the DC-DC boost converter to operate the PV system at the MPP and the accuracy of the MPPT algorithm in tracking the MPP. The accuracy of the MPP tracking has decreased slightly soon after each change in the solar irradiance level. However, since the controller of the DC-DC boost converter has been able to regulate the output voltage of the PV array accurately and the implemented MPPT algorithm has been able to track the MPP quickly, 100% MPP tracking accuracy has been established by the PV system within a short period of time after each change in the solar irradiance level.

3.6 Chapter summary

A detailed simulation model of a 5.4 kVA grid-connected single-phase two-stage PV system with associated control systems was developed in this chapter. The simulation model was developed using the PSCAD/EMTDC simulation program. This model of the PV system consists of component level models of a PV array, a DC-DC boost converter, a VSC and an LCL filter. Components of the LCL filter, the DC-link capacitor of the VSC and the inductor of the DC-DC boost converter were established theoretically and were used in modelling the PV system. The control architecture of the modelled PV system incorporates an s-PLL, a sta-

tionary frame current controller, a DC-link voltage controller, a DC-DC boost converter controller and a MPPT algorithm. The design methodologies that are followed to establish the control system of the PV system were described in detail.

The effectiveness of the developed model, with theoretically established component values and designed controllers was evaluated and verified using simulation studies. The robustness and the accuracy of the designed grid synchronisation mechanism, the stationary frame current controller and the DC-link voltage controller were verified by applying rapid changes in solar irradiance and reactive power reference.

An experimental setup of a PV system that is comparable with the developed simulation model of the grid-connected single-phase two-stage PV system, was established to verify the dynamic performance of the developed simulation model of the PV system. The control system of the PV system that was developed in the simulation model of the PV system was implemented in the controller of the experimental setup of the PV system. The experimental results that were obtained to verify the dynamic performance of the implemented PV system were presented and discussed. Based on the simulation results of the developed simulation model of the PV system and the experimental results obtained from the implemented PV system following conclusions can be made.

- The s-PLL implemented to synchronise the PV system to the grid was able to determine the phase angle and the peak value of the grid voltage accurately under steady-state and transient operating conditions of the PV system. Furthermore, since the s-PLL was implemented with appropriate low-pass filters, the overall steady-state and dynamic performance of the s-PLL was seen to be not affected when the grid voltage is distorted.

- The DC-link voltage controller determines the magnitude of the active power that should be injected/absorbed from/to the grid to regulate the DC-link voltage at a set reference. The DC-link voltage controller that was designed has been able to regulate the DC-link voltage at the set reference

within a short period of time after a transient condition and to maintain the DC-link voltage at the set reference during the steady-state operation.

- The current controller of the PV system was able to regulate the current injected to the grid by the PV system at a given sinusoidal current reference. The low-order harmonic current that was injected by the VSC of the PV system was minimised by the harmonic compensators that are implemented in the current controller.

- The active power injection to the grid was enhanced by adding a MPPT algorithm. The MPP tracking accuracy of the MPPT algorithm and the performance of the designed controller for the DC-DC boost converter have demonstrated under rapid variations of the solar irradiance. The simulation and experimental results verify that the implemented MPPT algorithm is able to determine the MPP accurately and quickly and the implemented controller of the DC-DC boost converter is able regulate the output voltage of the PV array at the reference voltage determined by the MPPT algorithm.

- The controller of the PV system was capable of independently controlling the active power and the reactive power injected to the grid. The reactive power injected by the PV system is controlled by operating the VSC at the maximum lagging power factor that is specified in the Australian Std. AS4777.2.

On the whole, the simulation results and experimental outcomes confirm that the modelling and control design approaches that were followed to develop the simulation model and the experimental setup of the PV system are robust and lead to a system with acceptable performance. The simulation model of the PV system developed is acceptable since the dynamic performance of the simulation model compared well against a comparable experimental setup of a PV system.

Chapter 4

PCC voltage control of a grid-connected PV system

4.1 Introduction

The integration of multiple PV systems to public LV electricity networks has led to a grid voltage rise problem as stated in Chapter 2. Since the PCC voltage of a PV system is sensitive to both active and reactive power injected to the grid by a PV system, an opportunity exists for PV systems to regulate the respective PCC voltages by dynamically controlling active and reactive power of the PV system and help maintaining network voltages within limits. The PCC voltage of a PV system can be regulated by a closed-loop controller that dynamically controls the reactive power response of the PV system. Furthermore, in situations where reactive power capability of a PV system is not adequate to regulate the PCC voltage, closed-loop active power control is an effective way of regulating PCC voltage of a PV system as proposed in Chapter 2.

As described in Chapter 2, in the published literature, only limited information is available on providing adequate technical details and guidelines for practically implementing closed-loop controllers that control the active and reactive power response of a PV system in order to regulate the PCC voltage of a PV system. Therefore, in this Chapter, a detailed design procedure of closed-loop

active and reactive power controllers that are capable of dynamically regulating the PCC voltage of a grid-connected PV system is provided. Plant models of closed-loop active and reactive power controllers are derived. Further, by combining the operation of closed-loop active and reactive power controllers, two novel operating strategies are proposed for grid-connected PV systems. Simulation results obtained following the integration of closed-loop active and reactive power controllers to the simulation model of the PV system that was developed in Chapter 3 are presented. Experimental results obtained after implementing novel control systems and operating strategies in the experimental setup of the PV system[1] are provided to demonstrate the robustness of the designed closed-loop active and reactive power controllers and the feasibility of implementing novel operating strategies for grid-connected PV systems proposed in this Chapter.

4.2 Simplified model of a distribution feeder

The dynamic active and reactive power controllers proposed in this Chapter are designed without considering the effects of the dynamic behaviour of loads and other inverter interfaced energy sources connected to the grid. Hence a simplified model of a power distribution feeder is considered in the design. The considered model of the power distribution feeder is shown in Fig. 4.1 where the grid is modelled with an equivalent Thévenin voltage source (of which the rms voltage at the terminal is V_{s}) that is connected in series with a resistor, R_{g}, and a reactance, X_{g}. The rms voltage at the PCC of the PV system is V_{g}. The term X_{f} represents the LCL filter of the PV system. At a given time, the PV system is considered to inject current I_{g} to the grid resulting in real power of P_{g} and reactive power of Q_{g}. I_{g} is the rms value of the current injected to the grid by the PV system.

The reference impedance for low voltage public supply systems given in [62] for electrical apparatus testing purposes is used as the impedance seen by the PV

[1]Refer to Appendix D for further details on the implemented experimental setup of the PV system.

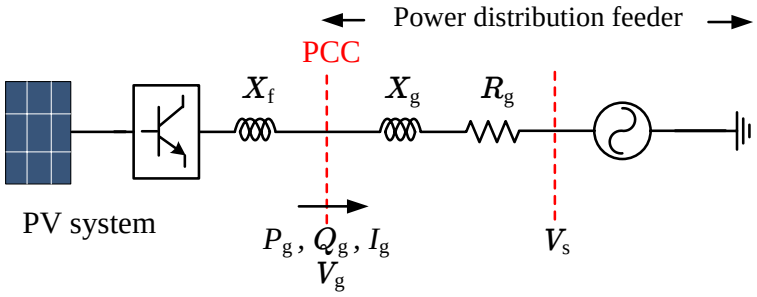

Figure 4.1: Simplified model of a power distribution feeder

system at the PCC when designing dynamic active and reactive power controllers. Hence the grid impedance of the simplified model of the power distribution feeder is $R_g + jX_g = (0.4 + j0.25)\ \Omega$. The R/X ratio of the considered grid is approximately 1.6. As will be shown in Section 4.3, with an R/X ratio greater than unity, an opportunity exists to regulate the PCC voltage by dynamically controlling the active and reactive power response of the PV system.

4.3 Decoupling of controllers

An expression for the PCC voltage rise, ΔV_g where $\Delta V_g = V_g - V_s$, when a PV system is injecting P_g and Q_g to the grid, can be derived as given by (4.1)[2] using Fig. 4.1.

$$\Delta V_g = \frac{-P_g R_g + Q_g X_g}{V_g} \tag{4.1}$$

The active power injected to the grid by a PV system is controlled by the DC-link voltage controller as described in Chapter 3. As proposed in this Chapter, PCC voltage controllers are designed to regulate the PCC voltage by controlling the active or reactive power injected to the grid by the PV system. According to (4.1), the PCC voltage, V_g is sensitive to both active and reactive power injected to the grid by the PV system. As a result, the DC-link voltage controller and PCC voltage controllers are dynamically coupled. Thus, there should be a decoupling mechanism for the DC-link voltage controller and PCC voltage controllers of the

[2]This is derived in 2.6.1

PV system to avoid any dynamic interactions between the controllers.

The DC-link voltage controller and PCC voltage controllers can be dynamically decoupled if the grid impedance is measured or estimated [65]. In order to decouple control systems in this manner, an algorithm to measure or estimate the grid impedance should be included in the controller design. An alternative way of decoupling the controllers is to make the response time of one controller relatively large compared to the response time of the second controller [13]. As a result of the difference in the response times of controllers, the dynamics are effectively decoupled. A first-order lag element can be utilised to change the response time of controllers [44]. Alternatively, if the controllers are closed-loop control systems, the desired response times can be obtained by tuning compensators. In this Thesis, the tuning of compensators to achieve desired response times is used in order to decouple controllers. This decoupling technique is commonly used in control systems of power electronic converters [13]. In order to decouple two dynamic systems, 2–10 times difference in the response times of the dynamic systems is adequate [13]. Therefore, in the grid-connected PV system shown in Fig. 4.1, PCC voltage controllers are made ten times slower than the DC-link voltage controller in order to decouple the dynamics of these control systems.

4.4 PCC voltage regulation with the dynamic reactive power controller - (PCC V_Q controller)

The design of the closed-loop PCC voltage controller that dynamically controls the reactive power response of the PV system (herein after referred to as the PCC V_Q controller) is described in detail in this Section.

4.4.1 Control plant model of the PCC V_Q controller

In grid-connected PV systems, a phase-locked-loop (PLL) is used to find the phase angle and the peak value of the PCC voltage. The response time of the PLL is

relatively short compared to that of the DC-link voltage controller. Since the PCC voltage controller is made even slower than the DC-link voltage controller, the dynamics of the PLL can be ignored in deriving the control plant model of the PCC V_Q controller. Therefore the angle deviations of the PCC voltage due to reactive power injection in order to regulate the PCC voltage can be disregarded while considering only the PCC voltage magnitude deviations caused by the reactive power injection to the grid by the PV system.

From Fig. 4.1, (4.2) can be derived. The peak value of the reactive current component of I_{g} is I_{gmq} and that of the active current component is I_{gmp}.

$$\vec{V_{\mathrm{g}}} - \vec{V_{\mathrm{s}}} = (R_{\mathrm{g}} + jX_{\mathrm{g}})\vec{I_{\mathrm{g}}} \tag{4.2}$$

A small change in the peak value of the reactive current injected to the grid by the PV system, ΔI_{gmq} is considered. The change in the peak value of the PCC voltage because of the voltage drop $jR_{\mathrm{g}}\Delta I_{\mathrm{gmq}}$, can be assumed to be negligible since $V_{\mathrm{gm}} >> |R_{\mathrm{g}}\Delta I_{\mathrm{gmq}}|$. Hence, the phase angle deviation between V_{g} and V_{s} because of the small change in the reactive current injected to the grid, can be disregarded. Therefore, for a small change in the reactive current injected to the grid by the PV system, (4.3) can be derived using (4.2). In (4.3), ΔV_{gm} is the change in the peak value of V_{g} because of ΔI_{gmq}.

$$\Delta V_{\mathrm{gm}} \approx -X_{\mathrm{g}}\Delta I_{\mathrm{gmq}} \tag{4.3}$$

The control plant model of the PCC V_Q controller can be obtained as given in (4.4) by applying the Laplace transformation to (4.3).

$$G_{V_{\mathrm{gQ}}}(s) = \frac{\Delta V_{\mathrm{gm}}(s)}{\Delta I_{\mathrm{gmq}}(s)} \approx -X_{\mathrm{g}} \tag{4.4}$$

4.4.2 PCC V_Q controller

The design of the PCC V_Q controller is described in this Section. Three different types of compensators are considered in the design of the controller. The control plant model of the PCC V_Q controller is used for designing and tuning compensators where applicable.

The proposed closed-loop PCC V_Q controller is shown in Fig. 4.2, where the error signal, e_{k}, is the difference between the peak value of the reference PCC voltage, V_{gmref}, and the peak value of the measured PCC voltage, V_{gm}, $G_{\mathrm{cc}}(s)$ is the closed-loop current controller of the PV system and finally $G_{V_{\mathrm{gQ}}}(s)$, is the control plant model of the PCC V_Q controller. Q_{ref}, I_{gmqref} and I_{gmq} are the reactive power reference, the peak value of the reactive current reference and the peak value of the reactive current injected to the grid by the PV system respectively.

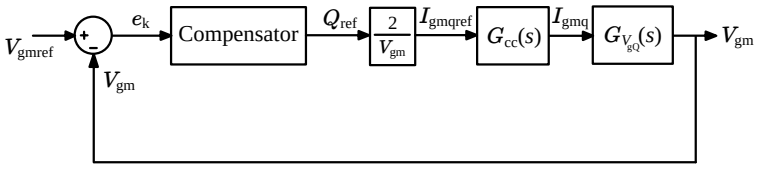

Figure 4.2: Control block diagram of the PCC V_Q controller

The response time for the DC-link voltage controller of the PV system is longer than that of the current controller. Further, the PCC V_Q controller should be made slower than the DC-link voltage controller to decouple the two controllers. Hence, the dynamics of the current controller can be disregarded assuming $G_{\mathrm{cc}}(s) = 1$ when designing the PCC V_Q controller. In Fig. 4.2, only the peak reactive current I_{gmq} is shown as the output of $G_{\mathrm{cc}}(s)$ since the PCC voltage is controlled by regulating I_{gmq} or the reactive power Q_{g} injected to the grid. However, in the implementation of the current controller that was developed using a stationary reference frame and a proportional resonant (PR) regulator as described in Chapter 3, both active and reactive current are regulated by a single controller.

4.4.3 PCC V_Q controller - with a proportional gain

A PCC V_Q controller with only a proportional gain as the compensator is first evaluated. The closed-loop transfer function of this controller is a gain since the plant model of the PCC V_Q controller that is given by (4.4) is also a gain. Therefore, the PCC voltage controller response cannot be made slower than the DC-link voltage controller of which the closed-loop transfer function is given by (4.5) as derived in Chapter 3, using only a proportional gain in the control loop.

$$G_{V_{\text{dc\_cl}}}(s) = \frac{1}{0.02s + 1} \tag{4.5}$$

Furthermore, as there is no integrator in the plant model of the PCC V_Q controller derived in (4.4), a zero steady-state error cannot be achieved with only a proportional gain. Therefore, the PCC V_Q controller with a proportional gain as the compensator, is not suitable for regulating the PCC voltage at a set reference voltage.

4.4.4 PCC V_Q controller - with a proportional gain and a first-order lag element

In this Section, the PCC V_Q controller is evaluated using a combination of a proportional gain, k_{pb}, and a first-order lag element, $G_{\text{d}}(s)$, as the compensator in the control loop of the PCC V_Q controller. $G_{\text{d}}(s)$ is given by (4.6) where τ_{d} is the time constant.

$$G_{\text{d}}(s) = \frac{1}{\tau_{\text{d}}s + 1} \tag{4.6}$$

The closed-loop transfer function of the PCC V_Q controller with k_{pb} and $G_{\text{d}}(s)$ in the control loop is given by (4.7).

$$G_{V_{\text{gQ\_clpd}}}(s) = \frac{2k_{\text{pb}}G_{\text{d}}(s)G_{V_{\text{gQ}}}(s)}{V_{\text{gm}} + 2k_{\text{pb}}G_{\text{d}}(s)G_{V_{\text{gQ}}}(s)} \tag{4.7}$$

Equation (4.7) can be simplified as,

$$G_{V_{\mathrm{gQ}}\_\mathrm{clpd}}(s) = \left(\frac{K_{\mathrm{pb}}}{K_{\mathrm{pb}}+1}\right)\frac{1}{\left(\frac{\tau_{\mathrm{d}}}{K_{\mathrm{pb}}+1}\right)s+1}, \tag{4.8}$$

where,

$$K_{\mathrm{pb}} = \frac{2k_{\mathrm{pb}}G_{V_{\mathrm{gQ}}}(s)}{V_{\mathrm{gm}}}.$$

The DC gain of (4.8) cannot be made equal to unity. Therefore, a steady-state error exists in the PCC V_Q controller with a proportional gain and a first-order lag element. If the steady-state error is designed to be 10%, then

$$\frac{K_{\mathrm{pb}}}{K_{\mathrm{pb}}+1} = 0.9,\ K_{\mathrm{pb}} = 9 \text{ and } k_{\mathrm{pb}} = -6235.$$

The desired response time of the PCC V_Q controller can be achieved by placing the pole of (4.8) appropriately. As per (4.5), the time constant of the DC-link voltage controller of the PV system, $G_{V_{\mathrm{dc}\_\mathrm{cl}}}(s)$ is 0.02 s. Therefore, in order to make the response time of the PCC V_Q controller ten times larger than that of the DC-link voltage controller,

$$\frac{\tau_{\mathrm{d}}}{K_{\mathrm{pb}}+1} = 0.2 \text{ and } \tau_{\mathrm{d}} = 2.$$

The step response of (4.8) for 10% steady-state error is shown in Fig. 4.3.

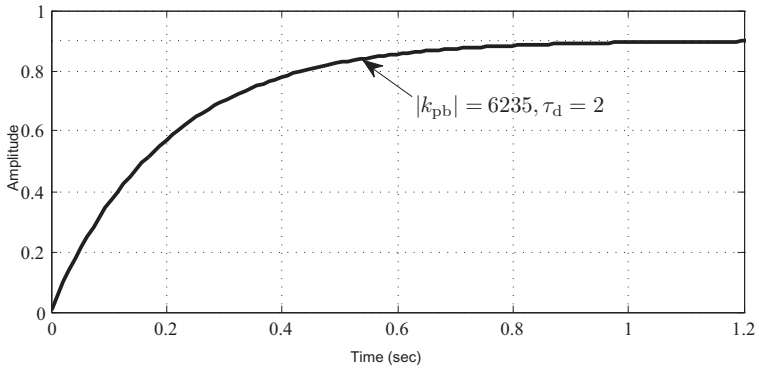

Figure 4.3: Step response of the closed-loop PCC V_Q controller with a proportional gain and a first-order lag element

The performance of the PCC V_Q controller, with a proportional gain and a first-order lag element was evaluated using the simulation model of the PV system designed in Chapter 3. The PCC voltage reference was set as $V_{\text{gmref}} = 245\sqrt{2}$ V in the controller. The calculated values for k_{pb} and τ_{d} were used in the simulation study and the results are shown in Fig. 4.4. In the simulation, the PCC voltage controller was not enabled initially and the rms value of the PCC voltage was set to approximately 248 V. At time $t = 0.5$ s, the PCC V_Q controller was enabled. As shown in Fig. 4.4, the designed controller has been able to regulate the PCC voltage approximately at 245.5 V.

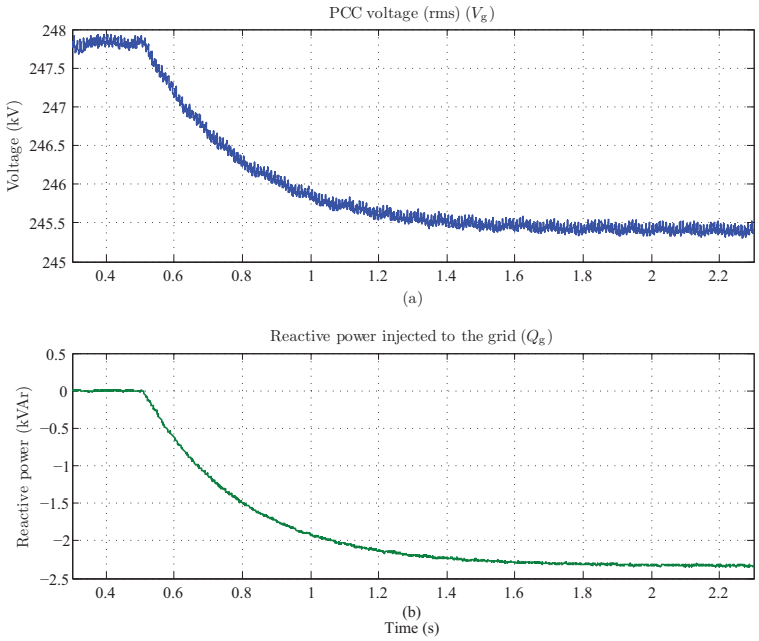

Figure 4.4: Dynamic performance of the PCC V_Q controller designed with a proportional gain and a first-order lag element

Fig. 4.4 illustrates that the steady-state value of the PCC voltage has been reached within approximately 1 s after the PCC V_Q controller was enabled. Since the time constant of (4.8) is 0.2 s, the steady-state PCC voltage has been reached within five time constants. This observation confirms the accuracy of the plant model of the PCC V_Q controller that is derived in this Chapter.

4.4.5 PCC V_Q controller - with a proportional gain and an integrator

A zero steady-state error can be achieved by the PCC V_Q controller only if the open-loop transfer function of the controller contains at least one pole that is closer to the origin. In order to place a pole that is closer to the origin in the open-loop transfer function of the PCC voltage controller, an integrator with a scalar can be used as the compensator shown in Fig. 4.2. The closed-loop transfer function of the PCC voltage controller with a scaled integrator as the compensator can be derived as,

$$G_{V_{\mathrm{gQ\_cli}}}(s) = \frac{2k_{\mathrm{pc}}G_{V_{\mathrm{gQ}}}(s)}{V_{\mathrm{gm}}s + 2k_{\mathrm{pc}}G_{V_{\mathrm{gQ}}}(s)}, \tag{4.9}$$

where k_{pc} is the scalar of the integrator. Equation (4.9) can be simplified as,

$$G_{V_{\mathrm{gQ\_cli}}}(s) = \frac{1}{K_{\mathrm{pc}}s + 1}, \tag{4.10}$$

where,

$$K_{\mathrm{pc}} = \frac{V_{\mathrm{gm}}}{2k_{\mathrm{pc}}G_{V_{\mathrm{gQ}}}(s)}.$$

The pole of $G_{V_{\mathrm{g\_cli}}}(s)$ is selected as one tenth of the pole of $G_{V_{\mathrm{dc\_cl}}}$ in (4.5). Therefore,

$$K_{\mathrm{pc}} = 0.2 \text{ and } k_{\mathrm{pc}} = -3465.$$

The pole-zero plot of (4.10) (the pole is labelled as $P_{V_{\mathrm{g\_cli}}}$) using the reference grid impedance and when $k_{\mathrm{pc}} = -3465$ is shown in Fig. 4.5. The location of the pole of the DC-link voltage controller (labelled as $P_{V_{\mathrm{dc\_cl}}}$) as given by (4.5) is also shown in Fig. 4.5.

The performance of the PCC V_Q controller was evaluated with the simulation model of the PV system developed in Chapter 3. The PCC voltage reference of the controller was set as $V_{\mathrm{gmref}} = 245\sqrt{2}$ V. Simulation results are shown in Fig. 4.6.

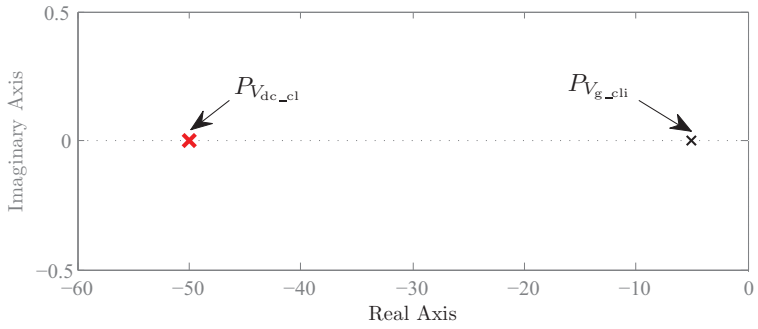

Figure 4.5: Pole-zero plot of the PCC V_Q controller with a scaled integrator and the DC-link voltage controller

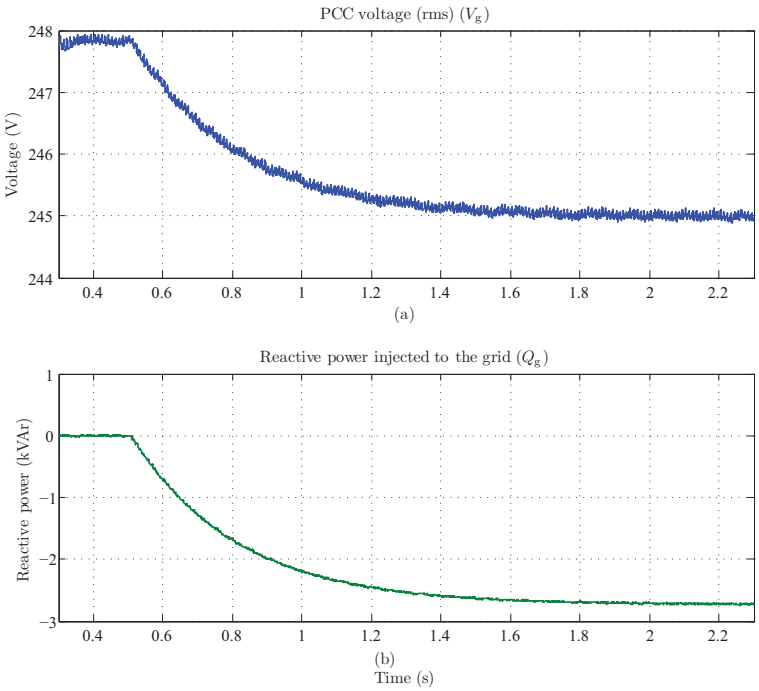

Figure 4.6: Dynamic performance of the PCC V_Q controller designed with a scaled integrator as the compensator

Initially, the PCC V_Q controller was not enabled but at $t = 0.5$ s it was enabled. As shown in Fig. 4.6(a), the controller is able to regulate the PCC voltage at the reference voltage level. The steady-state value has been reached within 1 s. Since the PCC V_Q controller with a scaled integrator is capable of driving the steady-state error to zero while effectively decoupling the PCC V_Q controller and the DC-link voltage controller, a scaled integrator is a suitable compensator for the PCC V_Q controller.

4.5 PCC voltage regulation with the dynamic active power controller - (PCC V_P controller)

The design of the closed-loop PCC voltage controller that dynamically controls the active power response of the PV system (herein after referred to as the PCC V_P controller) is described in this Section.

4.5.1 Control plant model of the PCC V_P controller

The control plant model of the PCC V_P controller is derived based on the simplified model of the power distribution feeder shown in Fig. 4.1. Further, since the PCC V_P controller is designed to have a long response time compared to that of the current controller of the PV system, steady-state operation of the network shown in Fig. 4.1 is considered while deriving the control plant model.

A small change in the peak value of the active current injected to the grid by the PV system, ΔI_{gmp}, is considered. The change in the peak value of the PCC voltage because of the voltage drop $jX_{\mathrm{g}}\Delta I_{\mathrm{gmp}}$, can be assumed to be negligible since $V_{\mathrm{gm}} >> |X_{\mathrm{g}}\Delta I_{\mathrm{gmp}}|$. Hence, the phase angle deviation between V_{g} and V_{s} that arises because of the small change in the active current injected to the grid can be disregarded. Therefore, for a small change in active current injected to the grid by the PV system, (4.11) can be derived from (4.2). In (4.11), ΔV_{gm} is the change in the peak value of V_{g} because of ΔI_{gmp}.

$$\Delta V_{\mathrm{gm}} \approx R_{\mathrm{g}}\Delta I_{\mathrm{gmp}} \tag{4.11}$$

The control plant model of the PCC V_P controller can be obtained as given by (4.12) by applying the Laplace transformation to (4.11).

$$G_{V_{\mathrm{gP}}}(s) = \frac{\Delta V_{\mathrm{gm}}(s)}{\Delta I_{\mathrm{gmp}}(s)} \approx R_{\mathrm{g}} \tag{4.12}$$

4.5.2 PCC V_P controller

The proposed closed-loop PCC V_P controller is shown in Fig. 4.7. This controller regulates the PCC voltage by controlling the active power injected by the PV system in situations where $V_{\text{gm}} > V_{\text{gmref}}$. In such a situation, the operating point of the PV system deviates from the MPP and the PV system is operated at a lower power level. Therefore, when the PCC V_P controller is enabled, MPP tracking is not needed. Hence the MPP tracking algorithm is configured to deactivate upon the activation of the controller. In order to prevent rapid turning-on and turning-off of MPP tracking during rapid voltage fluctuations in the grid, hysteresis has been built into the controller. However that hysteresis is not a part of controller shown in Fig. 4.7. In Fig. 4.7, V_{mpp0} is the voltage at the MPP where the PV array was operating before the PCC V_P controller commences regulating the PCC voltage. $G_{V_{\text{gP}}}(s)$ is the control plant model of PCC V_P controller.

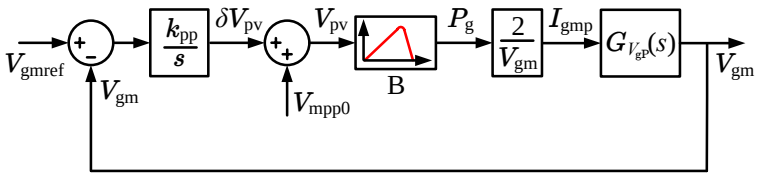

Figure 4.7: Control block diagram of the PCC V_P controller

Block B in Fig. 4.7 represents a mathematical relationship between the active power injected to the grid by the PV system, P_{g}, and the operating voltage of the PV array, V_{pv}. The mathematical relationship can be derived by considering the characteristic curves of the PV array. A typical terminal voltage and power characteristic curve of a PV array is shown in Fig. 4.8 when the solar irradiance level is 1200 W/m^2 and the ambient temperature is 30 °C. The voltage at the MPP, $V_{\text{mpp0}} = 290$ V and the power available at the MPP, P_{mpp}, is approximately 4.9 kW. The open circuit voltage of the PV array, V_{ocpv} is about 360 V. V_{pv} is an arbitrary voltage across the PV array at a given time and is controlled by the DC-DC boost converter controller. P_{g} is the amount of active power injected to the grid by the PV system if the voltage across the PV array is controlled at V_{pv},

assuming system losses are negligible. Such control action places the operating point of the PV array at A. In Fig. 4.7, I_{gmp} is the peak value of the active current injected to the grid. The closed-loop current controller of the PV system is not shown in Fig. 4.7 as it is considered to be a pure gain equal to unity.

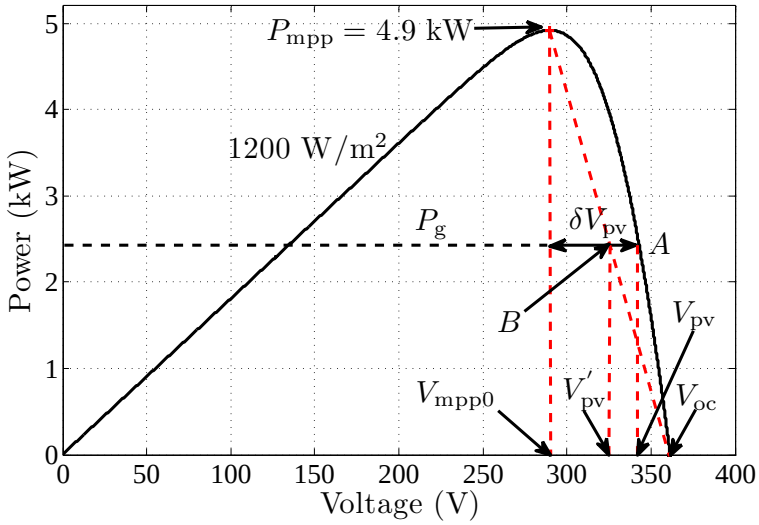

Figure 4.8: V–P characteristics of the PV array

The PCC V_P controller is designed in such a way that the operating point of the PV array is maintained at an operating point to the right-hand side of the vertical line P_{mpp}–V_{mpp0} in Fig. 4.8. In the PCC voltage controller shown in Fig. 4.7, δV_{pv} (> 0) is the voltage added to V_{mpp0} in order to curtail the active power injected by the PV system to control the PCC voltage by moving the operating point of the PV array to a lower power level, P_{g} ($< P_{\text{mpp}}$). The voltage peak value δV_{pv} that should be added to V_{mpp0} to control the PCC voltage is the output of the compensator. Since δV_{pv} is added to V_{mpp0} and also $\delta V_{\text{pv}} > 0$, when active power is curtailed, $V_{\text{pv}} > V_{\text{mpp0}}$. Thereby a stable operating point is always maintained in the PV array when the active power is dynamically controlled to regulate the PCC voltage.

In the characteristic curve of the PV array shown in Fig. 4.8, only the operating area bounded by V_{mpp0}–P_{mpp}–A–V_{oc} is of the interest since the PCC V_P controller ensures that the operating point of the PV array to be along the non-linear section defined by P_{mpp}–A–V_{oc}. In order to derive an approximated linear expres-

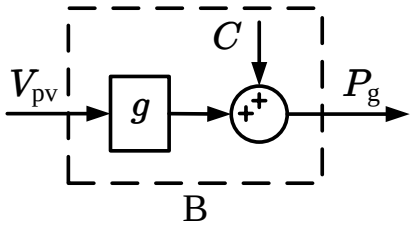

Figure 4.9: A detailed representation of Block B in Fig. 4.7

sion for Block B, the non-linear section P_{mpp}–A–V_{oc} of the characteristic curve of the PV array is approximated as the straight line P_{mpp}–V_{oc}. With the stated approximation, the operating point of the PV array becomes B when injecting an amount of active power equal to P_g to the grid, and the voltage of the PV array at B is $V_{pv}^{'}$. A linear expression for Block B can be derived using triangles V_{mpp0}–P_{mpp}–V_{oc} and $V_{pv}^{'}$–B–V_{oc} in Fig. 4.8, such that,

$$P_g = \underbrace{\frac{-P_{mpp}}{V_{oc} - V_{mpp0}}}_{g} V_{pv}^{'} + \underbrace{\frac{P_{mpp} V_{oc}}{V_{oc} - V_{mpp0}}}_{C}, \tag{4.13}$$

and

$$P_g = g V_{pv}^{'} + C. \tag{4.14}$$

The voltage and power at the MPP and the open circuit voltage of a PV panel at rated conditions is generally available in the data sheet of the PV panel. Hence, in general, the parameter g in Block B can be determined. For the given operating conditions of the PV array illustrated in Fig. 4.8, $g = -70$ W/V and $C = 25200$ W as given in (4.14). Block B in Fig. 4.7 can be represented as illustrated in Fig. 4.9 with the use of (4.14). The effect of the linear approximation that is made while deriving (4.14) is disregarded when representing Block B in detail in Fig. 4.9, so that $V_{pv}^{'}$ in (4.14) equals V_{pv}. When designing the PCC V_P controller, the loop gain, g of Block B, is only considered while disregarding C, considering that as a disturbance.

4.5.3 PCC V_P controller with a proportional gain and an integrator as the compensator

A suitable compensator for the PCC voltage controller should be chosen. The PCC V_P controller shown in Fig. 4.7 and the PCC V_Q controller shown in Fig. 4.2 demonstrate similar dynamic characteristics. The only difference between the two control loops is the static gains. Therefore, an integrator with a gain identified as a suitable compensator for the PCC V_Q controller can be applied in the PCC V_P controller as well.

The closed-loop transfer function of the PCC V_P controller with the chosen compensator can be derived as,

$$G_{V_{\mathrm{gPcli}}}(s) = \frac{\frac{2gk_{\mathrm{pp}}}{V_{\mathrm{gm}}s}G_{V_{\mathrm{gP}}}(s)}{1+\frac{2gk_{\mathrm{pp}}}{V_{\mathrm{gm}}s}G_{V_{\mathrm{gP}}}(s)}, \tag{4.15}$$

where k_{pp} is the gain of the integrator. Equation (4.15) can be simplified as,

$$G_{V_{\mathrm{gPcli}}}(s) = \frac{1}{\left(\frac{1}{K_{\mathrm{pp}}R_{\mathrm{g}}}\right)s+1}, \tag{4.16}$$

where

$$K_{\mathrm{pp}} = \frac{2gk_{\mathrm{pp}}}{V_{\mathrm{gm}}}.$$

According to (4.16), the dynamic performance that determines the time constant of the PCC V_P controller depends on the gain of the controller as well as the grid impedance that is seen by the PV system at the PCC. The time constant of $G_{V_{\mathrm{gPcli}}}(s)$ is set to 0.2 s when the grid impedance is $(0.4 + j0.25)\ \Omega$. The chosen time constant for the closed-loop PCC V_P controller is high enough to decouple this controller from the rest of the control system that is associated with the active power transfer of the PV system. With the chosen time constant for the PCC voltage controller,

$$\left(\frac{1}{K_{\mathrm{pp}}R_{\mathrm{g}}}\right) = 0.2,$$

and if the reference grid impedance is applied,

$$K_{\text{pp}} = 12.5.$$

For the given operating conditions of the PV array illustrated by Fig. 4.8, $g = -70$ W/V. Further $V_{\text{gm}} = 253\sqrt{2}$ V. Hence,

$$k_{\text{pp}} = 32.$$

The performance of the PCC V_P controller is evaluated by integrating that controller to the simulation model of the PV system developed in Chapter 3. At the beginning of the simulation study, the PCC V_Q controller of the PV system was disabled and the PCC voltage reference, V_{gmref}, was set to $253\sqrt{2}$. Simulation results of the PCC voltage controller are shown in Fig. 4.10. Initially, the PCC V_P controller was deactivated but at $t = 1$ s it was activated. As shown in Fig. 4.10(a), the controller was able to regulate the PCC voltage at the reference voltage. The steady-state has been reached within 1 s.

Since the time constant of the PCC voltage controller is chosen as 0.2 s, the steady-state should be attained within 1 s after a disturbance. The simulation results verify this performance criteria and hence the design criteria of the PCC V_P controller. Further, the dynamic response of the PCC V_P controller is slightly different to the dynamic response of a first order system. This deviation of the response is due to the linear approximation of the characteristic curve of the PV array that was made in deriving the expression for Block B in Fig. 4.7.

4.6 Advanced PCC voltage control strategies for PV systems

The PCC voltage of a grid-connected PV system can be regulated at a set reference voltage with the PCC V_Q controller and the PCC V_P controller discussed

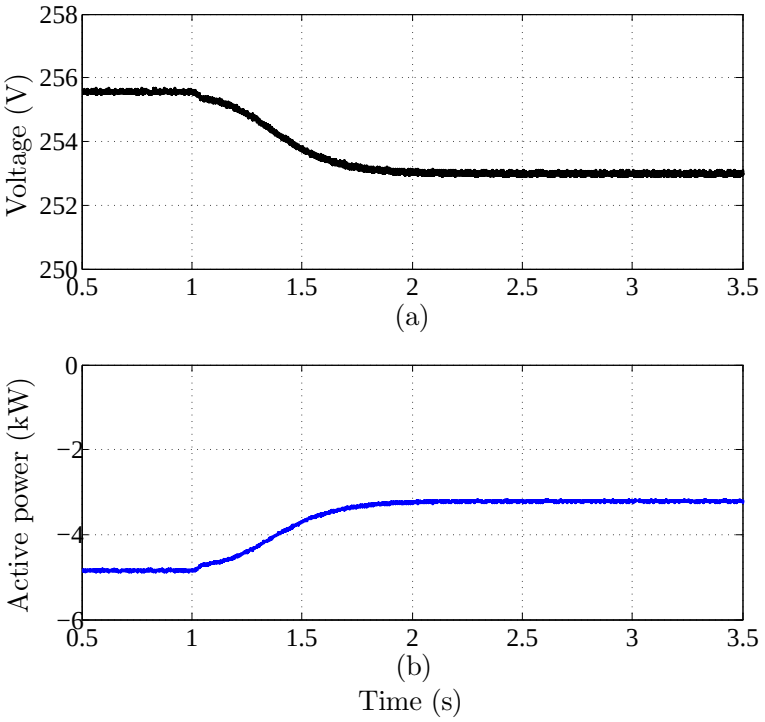

Figure 4.10: Dynamic performance of the PCC V_P controller; (a) rms voltage of the PCC (V_{g}) and (b) active power injected to the grid (P_{g}) by the PV system

in this Chapter. If power is curtailed in order to regulate the PCC voltage of the PV system as can be achieved using the PCC V_P controller, two different operating strategies that combine the operation of the PCC V_Q controller and the PCC V_P controller can be proposed.

4.6.1 Fixed minimum lagging power factor operation

The minimum lagging power factor at which a grid-connected energy system via an inverter should be operated is specified as 0.95 in the Australian standard AS4777.2 [7]. Even if the active power is curtailed to regulate the PCC voltage of the PV system, by adhering to this standard, the minimum lagging power factor of the PV system can be maintained at 0.95 and such an operation of the PV system is described in this Section.

In Fig. 4.11(a), the fixed minimum power factor operation of a PV system is illustrated using a $P-Q$ plane. Here, S_{r} is the rated apparent power capacity of the VSC that interfaces the PV system to the grid and the lagging power factor,

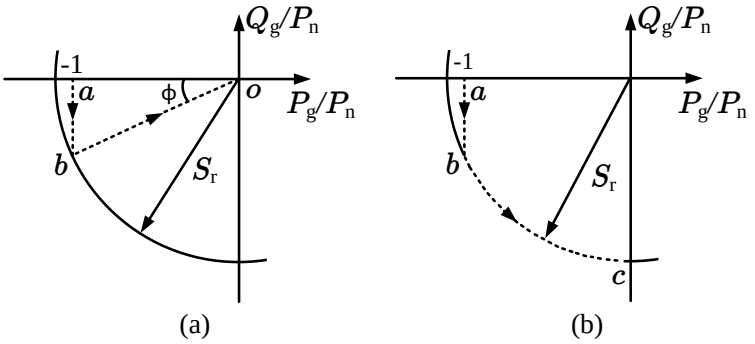

Figure 4.11: Advanced operating strategies for a PV system; (a) fixed minimum power factor operation and (b) fixed maximum apparent power operation

$\cos(\phi) = 0.95$. At a given time, the active power injected to the grid by the PV system is P_g. At the operating point a, the PV system is injecting the nominal active power, P_n, of the PV system to the grid and hence $P_g/P_n = -1$. The PCC V_Q controller is active from a to b, and the controller saturates at b as a result of the PV system reaching the minimum lagging power factor limit. After b, the MPPT of the PV system is disabled and the PCC V_P controller is activated. The operating point of the PV system moves towards o from b until the PCC voltage is regulated at the reference voltage. Although the PCC V_Q controller is active from b to o, it does not contribute to dynamic PCC voltage regulation actively since the controller is saturated.

The operation of the PV system at a minimum lagging power factor is ensured by the fixed minimum power factor operation of the PV system. In this operating mode, the full capacity of the PV system may not be utilised most of the time. Further, when the PCC V_P controller is enabled, in order to maintain the minimum lagging power factor, the reactive power absorbed from the grid is reduced in proportion to the amount of active power curtailed. The reduction in the amount of reactive power absorbed by the PV system causes further active power curtailment in order to regulate the PCC voltage at the reference level.

4.6.2 Fixed maximum apparent power operation

The purpose of defining a minimum power factor in the Australian standard AS4777.2 [7] is to minimise the reactive power flow in the grid in order to reduce the network losses and to avoid overloading the distribution transformer in a large installation of grid-connected energy systems via inverters. The weakest nodes in an LV grid are the most sensitive nodes to voltage variations and are the most effective nodes to regulate the voltage. If the reference voltages of dynamic active and reactive power controllers are properly selected, the PV systems at weak nodes may start regulating the respective PCC voltage before the other PV systems in the grid. If the PCC voltage regulation is enabled without limiting the reactive power absorption to a minimum lagging power factor operation but limiting to the available capacity of the VSC, the PV systems at the strong nodes of the grid may not need to contribute to the voltage regulation of the network. However, the PV systems at weak nodes may contribute to voltage regulation of the grid utilising their rated capacity. Hence reactive power flow in the network may be minimised.

The fixed maximum apparent power operation of a PV system is illustrated in Fig. 4.11(b). The operation of the PV system from a to b is the same as that was described in Section 4.6.1. At b, the PCC V_Q controller is saturated and the PCC V_P controller is activated. Unlike fixed minimum power factor operation, when power is curtailed to regulate the PCC voltage of the PV system, a proportional amount of reactive power is absorbed by the PV system. Hence, after b, active power curtailment as well as the additional reactive power absorbed by the PV system contribute to PCC voltage regulation. Although the PCC V_Q controller is enabled after b, it does not contribute to voltage regulation actively since the controller is saturated.

Since the rated capacity of the VSC that interfaces the PV system to the grid is used, the active power curtailment to regulate the PCC voltage in the fixed maximum apparent power operation is less compared to the fixed minimum power

factor operation of the PV system. In the fixed minimum power factor operation, the PV system may disconnect from the grid after curtailing active power up to a certain level. However, in fixed maximum apparent power operation the PV system stays connected to the grid even though injecting no active power while absorbing reactive power to regulate the PCC voltage.

4.7 Experimental results

The dynamic performance of the PCC V_Q controller and the PCC V_P controller, and the feasibility of implementing the novel operating strategies proposed for a PV system in this Chapter, were experimentally verified and the results are presented and discussed in this Section. The experimental setup of a single-phase, grid-connected, two-stage PV system established in the laboratory was used to obtain test results.

A California Instruments MX30 AC and DC power source in combination with an OMNI $3-75$ impedance bank was used to simulate the LV grid. The impedance of the simulated grid was $(0.25 + j0.25)$ Ω[3]. All experimental results presented in this Section consists of 4 waveforms; (1) the rms voltage at the PCC of the PV system, V_{g}, (2) reactive power injected to the grid, Q_{g}, (3) active power injected to the grid, P_{g}, and (4) the current injected to the grid by the PV system, i_{g}. The first three quantities, V_{g}, Q_{g} and P_{g}, were obtained through the controller and displayed on the oscilloscope via digital to analog (D/A) conversion channels. The ripple on the waveform of V_{g} is an artifact of the analog to digital (A/D) conversion of the measured PCC voltage.

In the controller of the experimental PV system, the voltage reference of the PCC V_Q controller and the PCC V_P controller was set as $253\sqrt{2}$ V. The practical results showing the dynamic performance of the PCC V_Q controller and PCC V_P controller and also the proposed novel operating strategies were obtained

[3]This impedance is different to that is used in simulation studies as specified in Section 4.2. This was because a matching impedance was not available at the time of testing.

by introducing a step voltage change in the grid that causes the peak value of the PCC voltage of the PV system to rise above $253\sqrt{2}$ V.

According to (4.4), the dynamic performance of the PCC V_Q controller depends on the reactance, X_g, but not on the resistance, R_g, of the grid impedance seen by the PV system at the PCC. The reactance values of the grid impedance as used in the simulation and experimental setup are similar. Hence, the gain of the integrator as used in the simulation work presented in Section 4.4.5 was used in the controller of the experimental PV system so that the steady-state of the PCC V_Q controller is reached within 1 s.

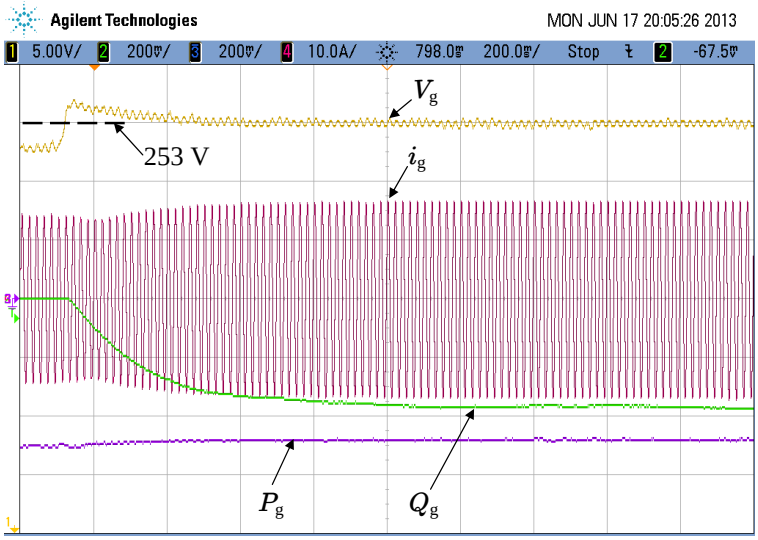

Figure 4.12: Performance of the PCC V_Q controller: Ch1: rms voltage of the PCC (V_g) [5 V/div] Ch2: reactive power injected to the grid (Q_g) [1 kVAr/div], Ch3: active power injected to the grid (P_g) [1 kW/div], Ch4: current injected to the grid (i_g) [10 A/div], Time base [200 ms/div]

The dynamic performance of the PCC V_Q controller is shown in Fig. 4.12. The controller was configured to activate once the peak value of V_g exceeds $253\sqrt{2}$ V. After the step voltage change in the grid, the PCC voltage is seen to be regulated at the reference level by absorbing approximately 1.75 kVAr of reactive power and the steady-state has been reached within approximately 1 s.

Unlike in the case of the PCC V_Q controller, the dynamic performance of the PCC V_P controller depends primarily on the resistance of the grid impedance, R_g, as per (4.12). The resistance of the grid impedance in the simulation work

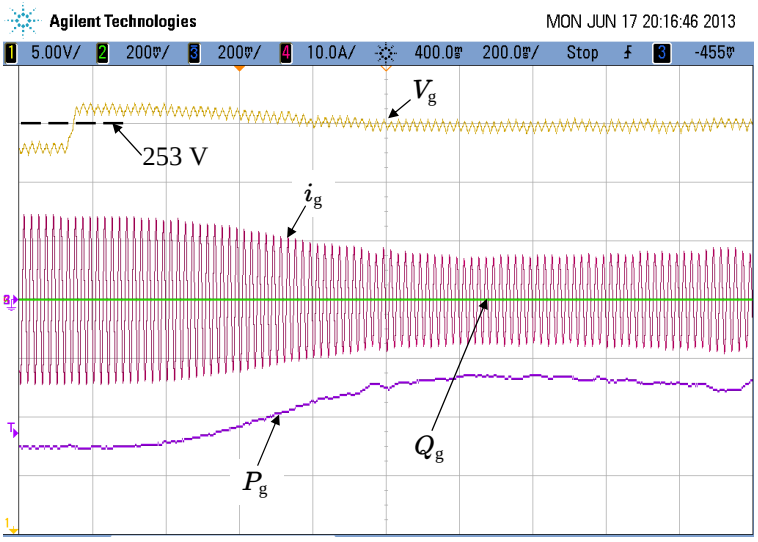

Figure 4.13: Performance of the PCC V_P controller: Ch1: rms voltage of the PCC (V_g) [5 V/div] Ch2: reactive power injected to the grid (Q_g) [1 kVAr/div], Ch3: active power injected to the grid (P_g) [1 kW/div], Ch4: current injected to the grid (i_g) [10 A/div], Time base [200 ms/div]

presented in Section 4.5.3 and the experimental PV system are different in magnitude. Therefore the gain of the integrator of the PCC V_P controller, k_{pp} is calculated as 51 to obtain the steady-state response of the PCC V_P controller of the experimental PV system within 1 s, assuming the characteristics of the PV array are as shown in Fig. 4.8.

Fig. 4.13 illustrates the dynamic performance of the PCC V_P controller. After the step change in voltage of the grid that causes the PCC voltage to rise above 253 V, the controller has been able to regulate the PCC voltage at 253 V by curtailing approximately 1 kW of active power. The steady-state has been reached within approximately 1 s. As shown, the smoothness of the P_g variation has been degraded when P_g is curtailed to regulate the PCC voltage. This behaviour is introduced by the PV emulator used in the experimental PV system since the PV emulator is unable to maintain a steady operating point at lower power levels. The variation of P_g as shown in Fig. 4.13 is comparable with that of Fig. 4.10(b).

The fixed minimum power factor operation and the fixed maximum apparent power operation of the experimental PV system are illustrated in Fig. 4.14 and Fig. 4.15 respectively. In the respective operating modes, the minimum power

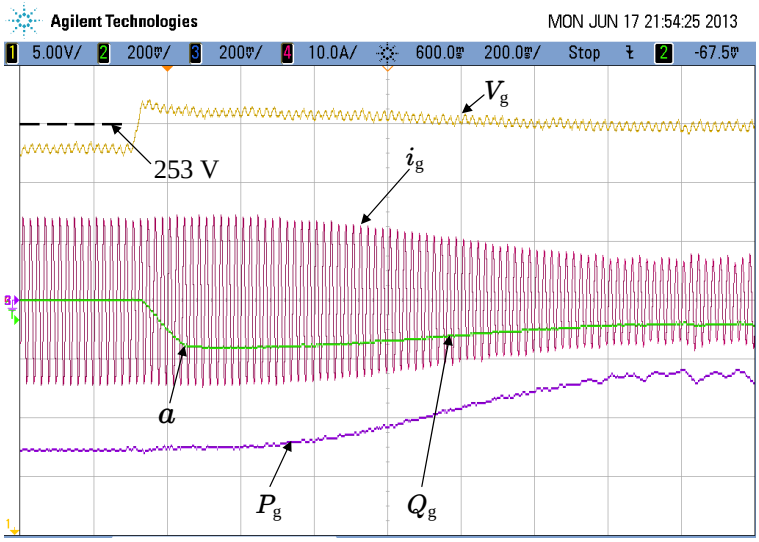

Figure 4.14: Fixed minimum lagging power factor operation of the PV system: Ch1: rms voltage of the PCC (V_g) [5 V/div] Ch2: reactive power injected to the grid (Q_g) [1 kVAr/div], Ch3: active power injected to the grid (P_g) [1 kW/div], Ch4: current injected to the grid (i_g) [10 A/div], Time base [200 ms/div]

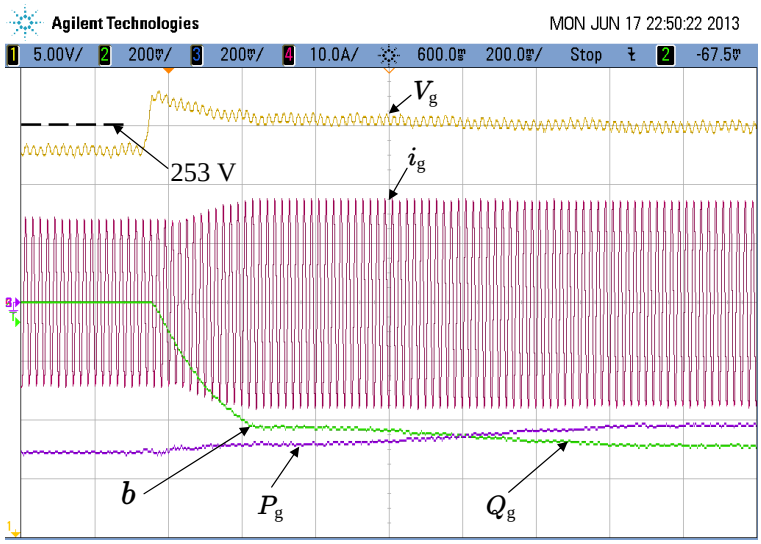

Figure 4.15: Fixed maximum apparent power operation of the PV system: Ch1: rms voltage of the PCC (V_g) [5 V/div] Ch2: reactive power injected to the grid (Q_g) [1 kVAr/div], Ch3: active power injected to the grid (P_g) [1 kW/div], Ch4: current injected to the grid (i_g) [10 A/div], Time base [200 ms/div]

factor was set as 0.95 lagging and the maximum apparent power of the VSC was limited to 3.2 kVA. In both operating modes, the PCC V_Q controller was triggered upon PCC voltage exceeding 253 V. This means that the corresponding controller saturates upon reaching the reactive power limit specified by the operating mode

at a and b in Fig. 4.14 and Fig. 4.15 respectively. In both operating modes, the PCC V_P controller has been triggered when the PCC V_Q controller saturates and power curtailment commenced in order to regulate the PCC voltage at 253 V. As illustrated in Fig. 4.15, in the fixed maximum apparent power operation of the PV system, the PCC voltage can be regulated by curtailing a smaller amount of active power and obviously absorbing a larger amount of reactive power from the grid, unlike in the fixed minimum power factor operation of the PV system as illustrated in Fig. 4.14.

4.8 Chapter summary

In this Chapter, two closed-loop PCC voltage controllers for grid-connected PV systems were proposed. The proposed PCC V_Q controller regulates the PCC voltage of a PV system dynamically by controlling the reactive power response of the PV system and PCC V_P controller regulates the PCC voltage of a PV system dynamically by controlling the active power response of the PV system. The plant models of the PCC V_Q controller and the PCC V_P controller were derived. Three different compensators were evaluated to identify suitable compensators for the proposed PCC voltage controllers. Two novel operating strategies, namely fixed minimum lagging power factor operation and fixed maximum apparent power operation were proposed. Based on the simulation and experimental results presented in this Chapter, following conclusions can be drawn.

- The PCC V_Q controller and the PCC V_P controller proposed in this Chapter are able to regulate the PCC voltage of a grid-connected PV system at a given reference voltage with zero steady-state error by controlling the active or reactive power response of the PV system.

- In order to accurately regulate the PCC voltage at a given reference level, a suitable compensator should be included in the proposed PCC voltage controllers. Between the three different compensators that were evaluated,

the scaled integrator has been found as the most suitable compensator for regulating the PCC voltage of the PV system at a given reference voltage leading to zero steady-state error.

- The derived plant models of The PCC V_Q controller and the PCC V_P controller are accurate since the dynamics of the designed PCC voltage controllers are predictable. Simulation results and experimental validations presented in this Chapter prove that the controller design procedures illustrated are accurate and robust.

- The fixed minimum power factor operation that was proposed by combining closed-loop PCC voltage controllers, minimises the reactive power consumption while staying connected to the grid until the power is curtailed to a specified level. Unlike in the fixed minimum power factor operation, the maximum apparent power operation proposed in the Chapter may utilise the full capacity of the VSC that interfaces the PV system to the grid. Therefore, with the maximum apparent power operation of a PV system, PCC voltage regulation may be achieved with minimum active power curtailment. Further, the maximum apparent power operation the PV system may provide voltage support with reactive power even without injecting any active power to the grid.

- Overall, the closed-loop PCC voltage controllers proposed in this Chapter will lead to effective and robust PCC voltage regulation of a PV system employing both active and reactive power. Further, the novel operation strategies proposed will enable effective utilisation of PV systems in order to contribute to grid voltage control.

PV systems integrated with dynamic PCC voltage controllers developed in this Chapter are used to identify interactions between PV systems. The identified interactions between PV systems are mainly discussed and illustrated in the next

chapter, Chapter 5. The key observations discussed in the current chapter form the basis for most of the analysis presented in Chapter 5.

Chapter 5

Dynamic interactions between multiple PV systems

5.1 Introduction

In a public LV electricity network to which multiple solar PV systems are integrated, the grid voltage can be controlled by regulating the PCC voltage of each PV system. A PV system that is integrated with a closed-loop PCC voltage controller, such as that covered in Chapter 4, is able to regulate the PCC voltage of the PV system dynamically at a set reference voltage level with zero steady-state error. Multiple PV systems that are connected to a grid and that are integrated with individual dynamic PCC voltage controllers, can be used to control the grid voltage dynamically. However, when such multiple PV systems operate electrically close to each other there is a possibility for control interactions to exist between different PV systems.

Only limited research studies exist related to control interactions between multiple PV systems which are equipped with individual dynamic reactive power controllers. Therefore, in this chapter, a detailed analysis is performed to identify such problems. In the current research, only PV systems that are interfaced to the grid via current-controlled VSC and those control the respective PCC voltage with PCC V_Q controllers developed in Chapter 4 are considered.

5.2 Dynamic performance of a PV system

The PCC voltage of a grid-connected PV system can be dynamically regulated by employing the PCC V_Q controller developed in Chapter 4. That controller controls the reactive power response of a PV system. The control system of a grid-connected PV system consists of a number of control loops that have different response times. In order to maintain the dynamic stability of the total control system and in certain situations to ensure decoupling between different control loops, the innermost control loops have shorter response times while the outer control loops have comparatively long response times. The overall dynamic performance of a PV system is dictated by the control loops that have longer response times as confirmed by the simulation and experimental results of a grid-connected PV system presented in Chapters 3 and 4. In a PV system that is able to dynamically regulate the PCC voltage, the most outer control loop is formed by the PCC V_Q controller. Since the PCC V_Q controller has the longest response time in the control system of the PV system as designed in Chapter 4, that controller determines the overall dynamic performance of the PV system. Therefore the dynamic performance of the PCC V_Q controller is of interest in this section to demonstrate the dynamic performance of a grid-connected PV system.

The dynamic behaviour of the closed-loop PCC V_Q controller of a PV system can be mathematically presented as given in (5.1) if a scaled integrator is used as the compensator. The derivation of (5.1) was given in Chapter 4. In (5.1), V_{gm} is the peak value of the PCC voltage of the PV system. The PCC V_Q controller is a first-order system according to (5.1). The response time of the controller is inversely proportional to the inductive part X_{g} of the grid impedance that is seen at the PCC of the PV system and the gain of the compensator, k_{pq}.

$$G_{V_{\mathrm{g}Q}}(s) = \frac{1}{\left(\frac{V_{\mathrm{gm}}}{2k_{\mathrm{pq}}X_{\mathrm{g}}}\right)s + 1} \tag{5.1}$$

The PSCAD/EMTDC simulation program was used to develop a simulation

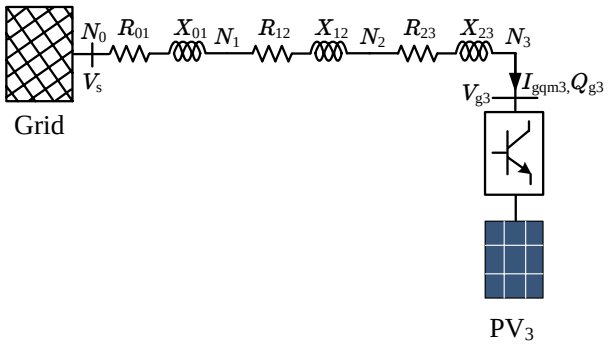

Figure 5.1: Network model of a grid-connected PV system

model of the network shown in Fig. 5.1. The simulation model of a PV system developed in Chapter 3 was integrated to the network as the PV system, PV_3. The PCC V_Q controller developed in Chapter 4 was integrated to PV_3 and a scaled integrator was used as the compensator. In Fig. 5.1, Q_{g3} is the reactive power absorbed by PV_3 and I_{gmq3} is the peak value of the resulting reactive current. V_{g3} is the rms voltage at the PCC of PV_3. The grid impedance at the PCC of PV_3 was $(0.28 + j0.27)$ Ω. With this impedance, the compensator gain of the PCC V_Q controller was set so that steady-state was obtained within 1 s. Further, the reference voltage of the PCC V_Q controller was $253\sqrt{2}$ V and the controller was configured to operate only if the peak value of the PCC voltage is greater than the reference voltage level.

Simulation results shown in Fig. 5.2 illustrates the dynamic performance of the PCC V_Q controller of PV_3 in the network model shown in Fig. 5.1 after a step change in the grid voltage, V_s at node N_0. As shown in Fig. 5.2, the PCC V_Q controller has been able to regulate the PCC voltage of PV_3 at the reference voltage level nearly within 1 s after the applied step change in the grid voltage. The dynamic variation shown in Fig. 5.2 is similar to that of the step response of a first-order system.

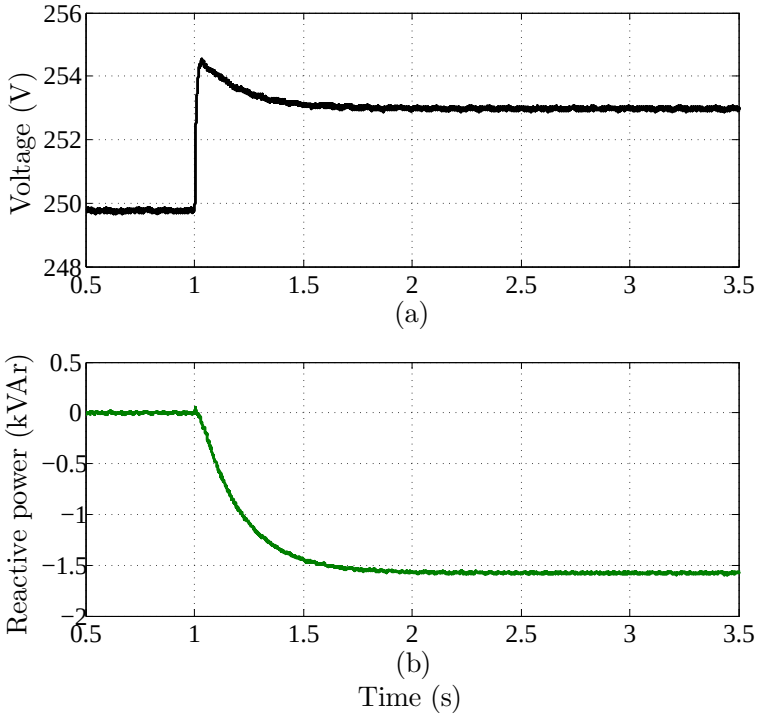

Figure 5.2: Single PV system operation - dynamic performance of the PCC V_Q controller following a disturbance; (a) rms voltage of the PCC and (b) reactive power absorbed from the grid (Q_g) by the PV system

5.3 Dynamic performance of a PV system in an installation of multiple PV systems

In a network with multiple PV systems that are operating electrically close to each other, the dynamic performance of an individual PV system may be different to that was described in Section 5.2 of this chapter as a result of control interaction between PV systems. In this section, results of simulation studies performed to identify possible control interactions between two PV systems that regulate the respective PCC voltage using PCC V_Q controllers are presented.

The dynamic responses of PCC V_Q controllers of two PV systems were obtained when these PV systems were connected at the same node. In the simulation study performed, PV_2 and PV_3 were connected to node N_3 of the network model shown in Fig. 5.3, at which the grid impedance was $(0.28 + j0.27)$ Ω. The PV systems were modelled using the detailed simulation model of the PV system developed in Chapter 3 and the control systems of PV systems, PV_2 and PV_3

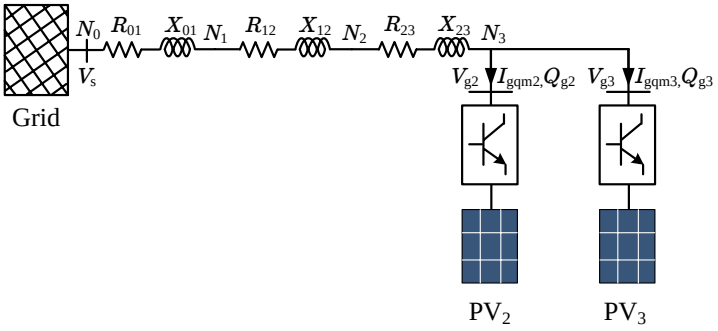

Figure 5.3: Network model of two PV systems connected at the same node

were identical. The PCC V_Q controller developed in Chapter 4 was integrated to both PV_2 and PV_3 and the gains of PCC V_Q controllers in both PV systems were set to the same value. The reference voltages of PCC V_Q controllers were set as $253\sqrt{2}$ V and the controllers were configured to operate only if the peak value of the PCC voltage is greater than the reference voltage.

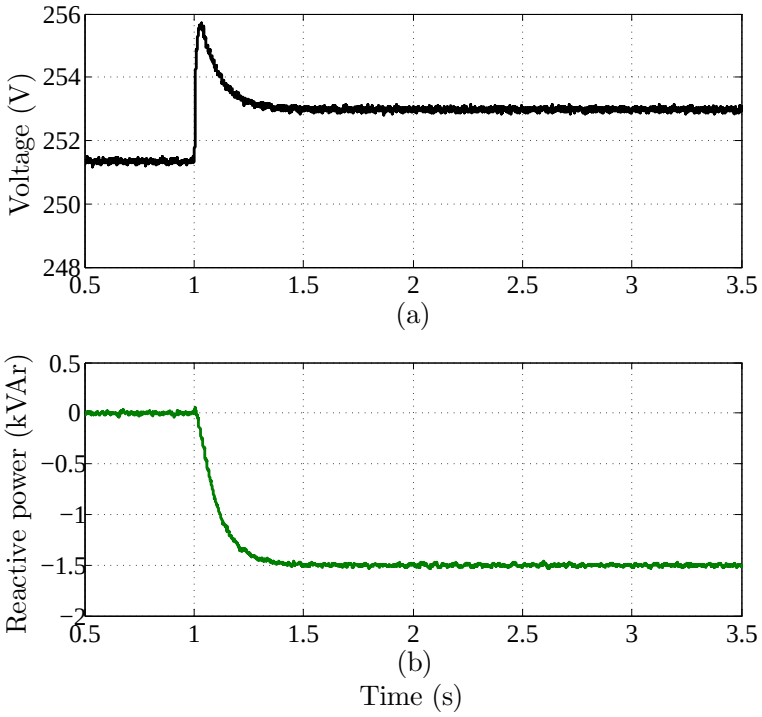

Figure 5.4: Operation two PV systems connected at the same node - dynamic performance of PCC V_Q controllers following a disturbance; (a) rms voltage of the PCC and (b) reactive power absorbed from the grid (Q_g) by the PV system

The simulation results shown in Fig. 5.4 demonstrate the dynamic behaviour of PCC V_Q controllers of PV_2 and PV_3 when both PV systems were connected at N_3 of the network shown in Fig. 5.3. In this simulation case, the gains of

PCC V_Q controllers were 3465. If PV_2 and PV_3 were operated individually when connected at node N_3 of the network shown in Fig. 5.3, the steady-state of PCC V_Q controllers should have been reached within 1 s. However, when PV_2 and PV_3 were operated simultaneously, the steady-state of PCC V_Q controllers have been reached within 0.5 s that is a half of the time to reach the steady-state if PV systems were operated individually when connected at node N_3 of the network shown in Fig. 5.3. Such a reduction in response time of PCC V_Q controllers of the two PV systems were because those controllers had similar dynamic characteristics and were controlling the voltage at the same node.

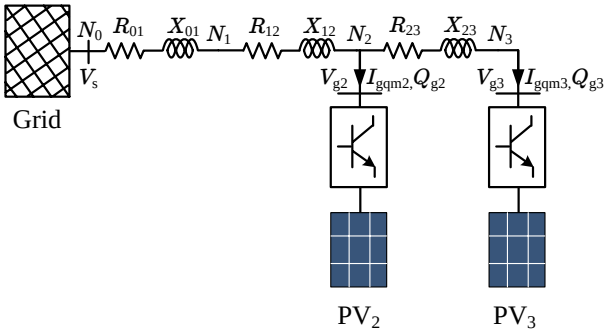

Figure 5.5: Network model of two grid-connected PV systems

The dynamic responses of PCC V_Q controllers of two PV systems were obtained when these systems were separated by a impedance as shown in Fig. 5.5. The network model shown in Fig. 5.5 was modelled in PSCAD/EMTDC simulation program. In the simulation model, the grid impedance at the PCC of PV_2 was $(0.25 + j0.25)\ \Omega$ and that at the PCC of PV_3 was $(0.28 + j0.27)\ \Omega$. If PV_2 and PV_3 were operated individually, the PCC V_Q controller in PV_2 would have reached the steady-state within 1.4 s and the PCC V_Q controller in PV_3 would have reached the steady-state within 1 s. The time difference in reaching the steady-state of PCC V_Q controllers in PV_2 and PV_3 when these PV systems are operated individually is due to the difference in grid impedance at the distinct PCCs of the two PV systems.

The dynamic behaviour of PCC V_Q controllers of PV_2 and PV_3 of Fig. 5.5 when these two PV systems were operated simultaneously during a grid voltage

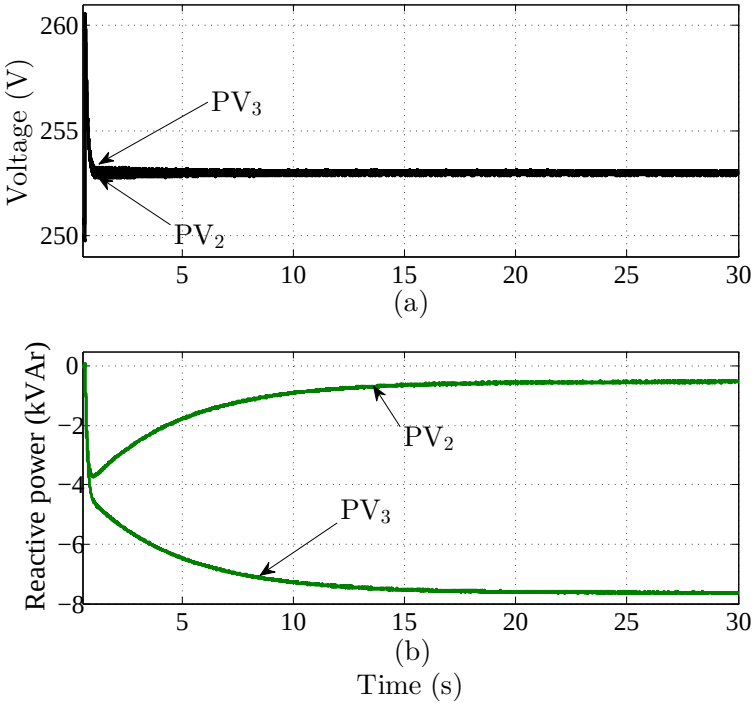

Figure 5.6: Operation of multiple PV systems - dynamic performance of PCC V_Q controllers following a disturbance; (a) rms voltage of the PCC and (b) reactive power absorbed from the grid (Q_g) by the PV system

disturbance is shown in Fig. 5.6. The figure illustrates that the steady-state of both controllers was reached within 25-30 s following the grid disturbance. The time taken by PCC V_Q controllers of the two PV systems to reach the steady-state when two PV systems were operated simultaneously was larger than was expected if these PV systems were operated individually. Fig. 5.2(b) and Fig. 5.6(b) clearly illustrates that when two PV systems are operated electrically close to each other, the dynamic behaviour of the PCC V_Q controller of one PV system is affected by the operation of the PCC V_Q controller of the other PV system because of dynamic interactions between PV systems. The dynamic response shown in Fig. 5.6(b) of the PV system is similar to the dynamic behaviour of a first-order system which has a considerably long response time.

Simulation studies were carried out further to identify the impact of set values of reference voltages of PCC V_Q controllers on the dynamic performance of PCC V_Q controllers of PV_2 and PV_3 in the network model shown in Fig. 5.5. The simulation results obtained after setting two different reference voltages have con-

firmed that the values of the reference voltages of PCC V_Q controllers have no impact on the overall dynamic behaviour of PCC V_Q controllers of PV_2 and PV_3.

The sensitivity of controller gains of PCC V_Q controllers on the dynamic performance of PV_2 and PV_3 were analysed by increasing the gains. When the gains of PCC V_Q controllers of PV_2 and PV_3 were increased, the steady-state of PCC V_Q controllers were reached within a shorter period of time than that is shown in Fig. 5.6. Simulation results of PV_3 obtained after increasing the gains of PCC V_Q controllers of PV_2 and PV_3 of the network model shown in Fig. 5.5 to 34650 from 3465 are shown in Fig. 5.7. According to Fig. 5.7, when gains were increased, the steady-state of PCC V_Q controller of PV_3 have been reached within a very short period of time. A similar difference was observed in the dynamic response of PV_2 as well.

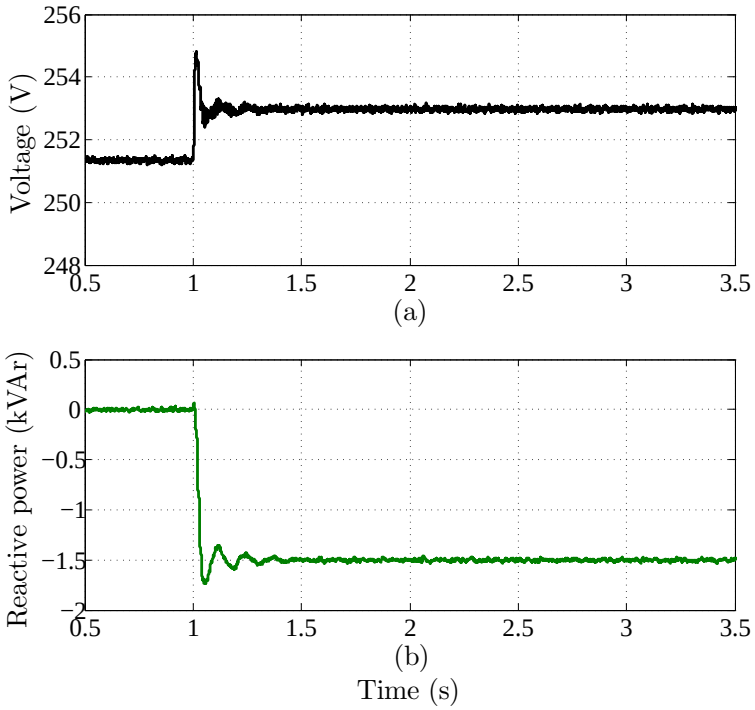

Figure 5.7: Operation of multiple PV systems with higher controller gains - dynamic performance of PCC V_Q controllers following a disturbance; (a) rms voltage of the PCC and (b) reactive power absorbed from the grid (Q_g) by the PV system

The dynamic response shown in Fig. 5.7 illustrates an oscillatory dynamic behaviour unlike the dynamic response shown in Fig. 5.6. This can be explained

as follows. The PCC V_Q controller is the most outer control layer of a PV system. Hence, the PCC V_Q controller is designed to have a longer response time in order to decouple the dynamics of that controller from the rest of the control system of the PV system. The required response time of the PCC V_Q controller is obtained by selecting a suitable gain for the compensator of the controller. When the gain of the PCC V_Q controller of a PV system is 3465 and the grid impedance at the PCC of the PV system is $(0.28 + j0.27)\ \Omega$, the steady-state of the PCC V_Q controller is reached within 1 s. The response time of 1 s in the PCC V_Q controller is adequate to decouple this controller from the rest of the control system of the PV system as shown in Chapter 4. When the gain of the PCC V_Q controller is increased from 3465 to 34650, the response time of the controller becomes very short. Further, dynamic decoupling between the PCC V_Q controller and the rest of the control system has been degraded resulting oscillatory dynamics as shown in Fig. 5.7. Therefore, though the dynamic interactions between PV systems demonstrated in Fig. 5.6 can be minimised by increasing gains of PCC V_Q controllers that is not the most suitable method to use.

Droop control is widely used in control systems for electrical machines and power electronic drives. Such a controller is able to extend the operating range of a power converter system that the controller is built into, improve the dynamic stability when multiple converter systems are operated electrically close to each other and to enforce automatic load sharing [14][66]. Therefore a droop controller was integrated to the PCC V_Q controller and control interactions between multiple PV systems were investigated.

The network model shown in Fig. 5.5 was used to investigate control interactions between PV systems when droop controllers are integrated to the PCC V_Q controllers of PV_2 and PV_3. The droop controller shown in Fig. 5.8 was integrated to the PCC V_Q controller of PV_2 and PV_3. In Fig. 5.8, Q_g is the reactive power injected by a PV system to the grid. The simulation results of PV_2 and PV_3 obtained during a grid voltage disturbance are shown in Fig. 5.9.

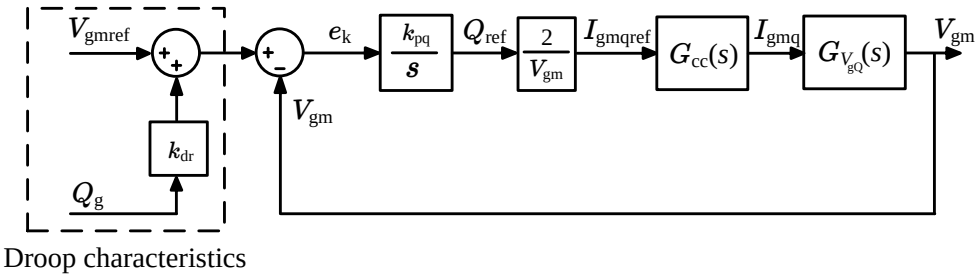

Figure 5.8: Control block diagram of the PCC V_Q controller integrated with a droop controller

According to Fig. 5.9, the PCC V_Q controllers of PV_2 and PV_3 have reached the steady-state within 1 s when droop controllers were integrated. When dynamic variations of Q_g in Fig. 5.6 and Fig. 5.9 are compared, the droop controller has been able to minimise the effect of control interactions between PV systems and improve the reactive power sharing between PV systems.

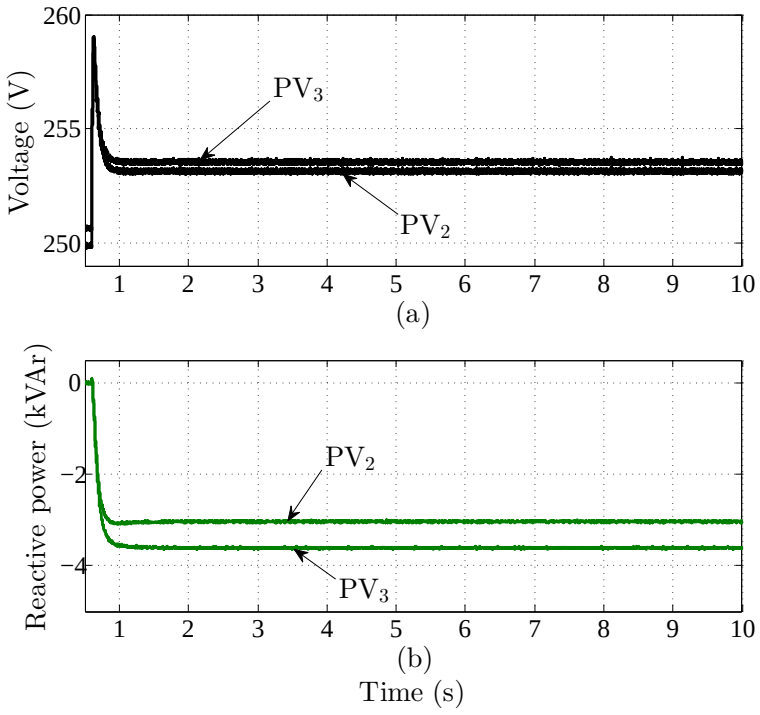

Figure 5.9: Operation of two PV systems integrated with droop control in PCC V_Q controllers - dynamic performance of PCC V_Q controllers following a disturbance; (a) rms voltage of the PCC and (b) reactive power absorbed from the grid (Q_g) by the PV system

The impact of the number of PV systems connected to a grid on the dynamic behaviour of PV systems were investigated by increasing the number of PV sys-

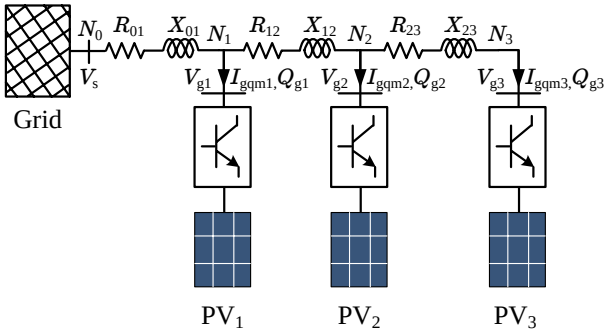

Figure 5.10: Network model of three grid-connected PV systems

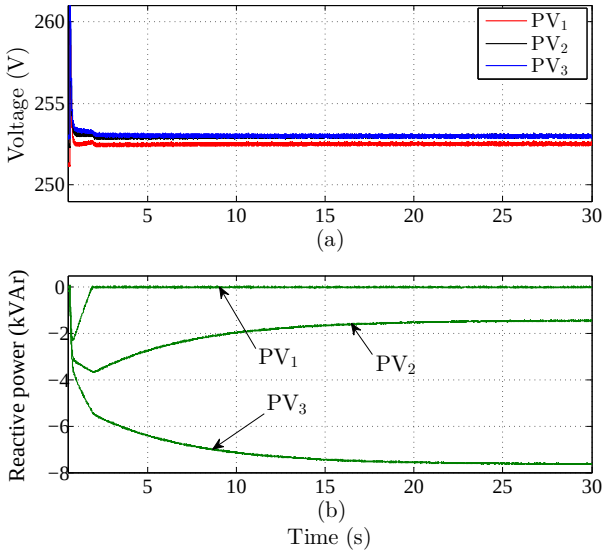

Figure 5.11: Operation of three PV systems - dynamic performance of PCC V_Q controllers following a disturbance; (a) rms voltage of the PCC and (b) reactive power absorbed from the grid (Q_g) by the PV system.

tems connected to the network model shown in Fig. 5.5. The network model shown in Fig. 5.10 was used to investigate the dynamic behaviour of PV systems when three PV systems are operated simultaneously. The dynamic behaviour of PCC V_Q controllers when all three PV systems, PV_1, PV_2 and PV_3, were operated simultaneously are shown in Fig. 5.11. According to the results shown, all three PV systems have attempted to regulate respective PCC voltage by absorbing reactive power from the grid followed by the disturbance. After about 2 s, PCC V_Q controller of PV_1 has saturated at zero since the controller had been configured only to absorb reactive power. As a result, after about 2 s of the simulation time only two PV systems were dynamically regulating the voltage. Hence,

the dynamic behaviour of PV systems illustrated after 2 s of the simulation is similar to that is shown in Fig. 5.6. These results will be further discussed in Section 5.5.

Simulation results presented in Fig. 5.6, Fig. 5.4, Fig. 5.7 and Fig. 5.11 confirm that the operation of the PCC V_Q controller of a PV system can affect the dynamic performance of the PCC V_Q controller of another PV system. Hence, there are control interactions between multiple PV systems. The ability of a droop controller to minimise the effects of identified control interactions between PV systems has been confirmed by the simulation results shown in Fig. 5.9. The existence of control interactions between multiple PV systems identified in this section and the ability of a droop controller to minimise the effects of control interactions between PV systems are mathematically and experimentally verified in following sections of this chapter.

5.4 Small-signal model of a multiple PV installation

The control interaction in a multi-machine power system can be analysed by developing a small-signal model and then performing modal analysis [67]. Similarly, control interaction between multiple PV systems can be analysed as identified in Chapter 2. Therefore, in this section, a small-signal model of a power distribution feeder to which multiple PV systems are integrated is developed. Further, modal analysis is performed by using the developed small-signal model to verify control interaction between PV systems identified in Section 5.3.

As stated in Section 5.2, the PCC V_Q controller is the outermost control loop of a PV system and is implemented to have a comparatively long response time relative to the response times of other control systems in the inner control loops system. As a result, the PCC V_Q controller is decoupled from the rest of the control system of the PV system and determines the overall dynamic performance of the PV system. Therefore, while developing the small-signal model of a PV system only the PCC V_Q controller is considered and the dynamic behaviour of

other controllers in the PV system are ignored.

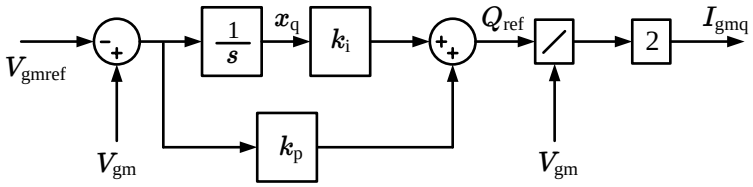

Figure 5.12: Forward path of the PCC V_Q controller

The forward path of the PCC V_Q controller of a PV system is shown in Fig. 5.12 where, V_{gmref} and V_{gm} are the reference voltage and the peak value of the measured voltage at the PCC of the PV system respectively. A PI regulator is used as the compensator where k_{p} and k_{i} are the proportional and integral gains of the PI regulator respectively. Q_{ref} is the reactive power reference determined by the PCC V_Q controller and I_{gmq} is the peak value of the reactive current absorbed by the PV system. In the actual control system of the PV system, Q_{ref} is an input to the current controller. Since the dynamics of the inner control loops are ignored while developing the small-signal model of the PV system, I_{gmq} can be considered to change instantaneously for a given change in Q_{ref}. In the actual PV system, the peak value of the PCC voltage, V_{gm}, and also the angle of the PCC voltage are obtained by a phase-locked-loop (PLL) as described in Chapter 3. Since the PLL also has a short response time compared to the PCC V_Q controller, any change in the PCC voltage is considered to appear in the PCC V_Q controller instantaneously. In Fig. 5.12, x_{q} is a state variable of the PCC V_Q controller that can be expressed as given in (5.2).

$$x_{\text{q}} = \frac{1}{s}(V_{\text{gm}} - V_{\text{gmref}}) \tag{5.2}$$

Equation (5.3) can be obtained by linearising (5.2).

$$\Delta \dot{x}_{\text{q}} = \Delta V_{\text{gm}} \tag{5.3}$$

Further,

$$Q_{\text{ref}} = k_{\text{p}}(V_{\text{gm}} - V_{\text{gmref}}) + k_{\text{i}}x_{\text{q}}, \tag{5.4}$$

and by linearising (5.4), (5.5) can be obtained.

$$\Delta Q_{\text{ref}} = k_{\text{p}}\Delta V_{\text{gm}} + k_{\text{i}}\Delta x_{\text{q}} \tag{5.5}$$

The output I_{gmq} of the PCC V_Q controller can be expressed as given in (5.6). When (5.6) is linearised, (5.7) can be obtained. In (5.7), V_{gm0} is the initial value of the peak value of the PCC voltage and I_{gmq0} is the initial value of the peak value of the reactive current absorbed by the PV system from the grid.

$$I_{\text{gmq}} = 2 \times Q_{\text{ref}} \times \frac{1}{V_{\text{gm}}} \tag{5.6}$$

$$\Delta I_{\text{gmq}} = \frac{2}{V_{\text{gm0}}}\Delta Q_{\text{ref}} - \frac{I_{\text{gmq0}}}{V_{\text{gm0}}}\Delta V_{\text{gm}} \tag{5.7}$$

From (5.5) and (5.7),

$$\Delta I_{\text{gmq}} = \frac{2}{V_{\text{gm0}}}(k_{\text{p}}\Delta V_{\text{gm}} + k_{\text{i}}\Delta x_{\text{q}}) - \frac{I_{\text{gmq0}}}{V_{\text{gm0}}}\Delta V_{\text{gm}},$$

$$\Delta I_{\text{gmq}} = \underbrace{\frac{2k_{\text{i}}}{V_{\text{gm0}}}}_{c}\Delta x_{\text{q}} + \underbrace{\left(\frac{2k_{\text{p}}}{V_{\text{gm0}}} - \frac{I_{\text{gmq0}}}{V_{\text{gm0}}}\right)}_{d}\Delta V_{\text{gm}}. \tag{5.8}$$

A model of a single-phase LV power distribution feeder to which n number of PV systems are integrated is shown in Fig. 5.13. In the figure, $Q_{\text{g}j}$ $(j = 1, 2, \ldots, n)$ indicates the reactive power absorbed by PV_j to regulate the voltage at the node N_j and $I_{\text{gmq}j}$ is the peak value of resulting reactive current. $V_{\text{g}j}$ is the PCC voltage and the peak value of $V_{\text{g}j}$ is $V_{\text{gm}j}$. The PCC V_Q controllers in all PV systems are expected to operate when the LV power distribution feeder is lightly loaded and in situations where the power generation from PV systems are high. Hence, the loads connected to the LV power distribution feeder are not considered and such loads are not shown in the figure. The LV power distribution feeder is considered

to be connected to a stiff voltage source V_s at the node N_0.

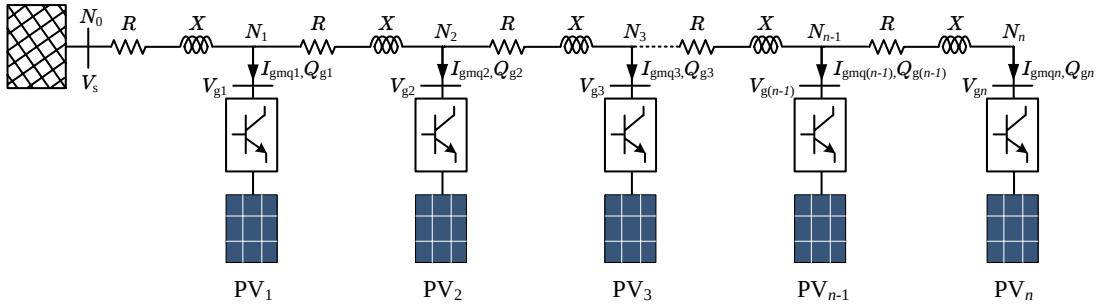

Figure 5.13: Network model of power distribution feeder with multiple PV systems

By applying nodal analysis on the network shown in Fig. 5.13, (5.9) can be derived. In (5.9), Y_{jj} and Y_{jk} $(j, k = 1, 2, \ldots, n)$ are the summation of all admittances connected to the node N_j, and the admittance between node N_j and N_k respectively. When reactive power is absorbed by a PV system to regulate the PCC voltage, the magnitude and the phase angle of the respective PCC voltage are affected. At the same time, the magnitude and the phase angle of voltages of other sensitive nodes are also affected. Since the dynamic response of the PLL that determines the phase angle of the PCC voltage of a PV system is considered to have a fast response while deriving the small-signal model of a PV system, only the sensitivity of the peak value of the PCC voltage, $V_{\mathrm{gm}k}$ of the PV system PV_k to the reactive current, $I_{\mathrm{gmq}j}$, that is absorbed by the PV system PV_j is represented in (5.9). In a grid-connected PV system, the change in the peak value of the PCC voltage as a result of absorbing reactive power is a function of the network impedance at the respective PCC. The network impedance is formed by both resistive and reactive components. The change in the peak value of PCC voltage when reactive power is absorbed by a PV system as a result of the resistance of the network impedance is insignificant compared to change in the peak value of voltage as a result of the reactance of the network impedance. Therefore, the

admittance matrix $[Y]$ can be considered to be formed by the reactances only.

$$\begin{bmatrix} I_{\text{gmq1}} \\ I_{\text{gmq2}} \\ \vdots \\ I_{\text{gmq}n} \end{bmatrix} = \underbrace{\begin{bmatrix} -Y_{11} & Y_{12} & \dots & Y_{1n} \\ Y_{21} & -Y_{22} & \dots & Y_{2n} \\ \vdots & \vdots & \vdots & \vdots \\ Y_{n1} & Y_{n2} & \dots & -Y_{nn} \end{bmatrix}}_{[Y]} \begin{bmatrix} V_{\text{gm1}} \\ V_{\text{gm2}} \\ \vdots \\ V_{\text{gm}n} \end{bmatrix} \tag{5.9}$$

When (5.9) is linearised, (5.10) can be obtained.

$$\begin{bmatrix} \Delta I_{\text{gmq1}} \\ \Delta I_{\text{gmq2}} \\ \vdots \\ \Delta I_{\text{gmq}n} \end{bmatrix} = \underbrace{\begin{bmatrix} -Y_{11} & Y_{12} & \dots & Y_{1n} \\ Y_{21} & -Y_{22} & \dots & Y_{2n} \\ \vdots & \vdots & \vdots & \vdots \\ Y_{n1} & Y_{n2} & \dots & -Y_{nn} \end{bmatrix}}_{[Y]} \begin{bmatrix} \Delta V_{\text{gm1}} \\ \Delta V_{\text{gm2}} \\ \vdots \\ \Delta V_{\text{gm}n} \end{bmatrix} \tag{5.10}$$

The dynamic behaviour of the PCC V_Q controller of the PV system PV_j ($j = 1, 2, \dots, n$) can be represented by (5.8). The dynamic behaviour of PCC V_Q controllers in all of the PV systems shown in Fig. 5.13 can be represented in a matrix form as given by (5.11).

$$\underbrace{\begin{bmatrix} \Delta I_{\text{gmq1}} \\ \Delta I_{\text{gmq2}} \\ \vdots \\ \Delta I_{\text{gmq}n} \end{bmatrix}}_{[\Delta I_{\text{Q}}]} = \underbrace{\begin{bmatrix} c_1 & 0 & \dots & 0 \\ 0 & c_1 & \dots & 0 \\ \vdots & \vdots & \vdots & \vdots \\ 0 & 0 & \dots & c_n \end{bmatrix}}_{[C]} \underbrace{\begin{bmatrix} \Delta x_{\text{q1}} \\ \Delta x_{\text{q2}} \\ \vdots \\ \Delta x_{\text{q}n} \end{bmatrix}}_{[\Delta X_{\text{Q}}]} + \underbrace{\begin{bmatrix} d_1 & 0 & \dots & 0 \\ 0 & d_1 & \dots & 0 \\ \vdots & \vdots & \vdots & \vdots \\ 0 & 0 & \dots & d_n \end{bmatrix}}_{[D]} \underbrace{\begin{bmatrix} \Delta V_{\text{gm1}} \\ \Delta V_{\text{gm2}} \\ \vdots \\ \Delta V_{\text{gm}n} \end{bmatrix}}_{[\Delta V_{\text{M}}]} \tag{5.11}$$

By substituting (5.10) in (5.11), (5.12) can be obtained.

$$[\Delta V_{\text{M}}] = [Y - D]^{-1}[C][\Delta X_{\text{Q}}] \tag{5.12}$$

Equation (5.12) can be further simplified by substituting (5.3) and leading to (5.13) where A is the system matrix and the eigenvalues of the system matrix corresponding to system modes. The dynamic stability of a system can be analysed by analysing system modes.

$$[\Delta \dot{X}_{\mathrm{Q}}] = \underbrace{[Y - D]^{-1}[C]}_{A}[\Delta X_{\mathrm{Q}}] \tag{5.13}$$

5.5 Modal analysis

The small-signal model of an LV power distribution feeder connected with PV systems, developed in Section 5.4 of this chapter is the subject of modal analysis in this section. The network model shown in Fig. 5.10 that is used to identify control interactions between two PV systems in Section 5.3 of this chapter is considered to perform the modal analysis. In the network shown in Fig. 5.5, three PV systems are connected to an LV power distribution feeder at the end of the feeder. The system parameters that are necessary to perform the modal analysis are given in Table 5.1. PCC V_Q controllers of all PV systems have identical gains. The initial conditions of all three PV systems are assumed to be similar.

The eigenvalues of the system matrix of the network model shown in Fig. 5.10 can be determined by using (5.13) and the parameters given in Table 5.1. Initially, simultaneous operation of only two PV systems were considered. Therefore,

Table 5.1: System parameters of the network model

Parameter	**Value**
$k_{\mathrm{p1}}, k_{\mathrm{p2}}, k_{\mathrm{p3}}$	0
$k_{\mathrm{i1}}, k_{\mathrm{i2}}, k_{\mathrm{i3}}$	3465
$V_{\mathrm{gm01}}, V_{\mathrm{gm02}}, V_{\mathrm{gm03}}$	$253\sqrt{2}$ V
$I_{\mathrm{q01}}, I_{\mathrm{q02}}, I_{\mathrm{q03}}$	0 A
X_{01}, X_{12}, X_{23}	0.23 Ω, 0.02 Ω, 0.02 Ω
R_{01}, R_{12}, R_{23}	0.22 Ω, 0.03 Ω, 0.03 Ω

modal analysis was performed considering that PV_1 of Fig. 5.10 was disconnected from the network. The corresponding eigenvalues obtained are given in (5.14). According to the eigenvalues obtained, there are no oscillatory modes in the system since all modes are critically damped. The critical mode is λ_{22} as that is closer to the origin in the complex plane than λ_{12}.

$$\begin{bmatrix} \lambda_{12} \\ \lambda_{22} \end{bmatrix} = \begin{bmatrix} -8.96 \\ -0.24 \end{bmatrix} \tag{5.14}$$

The time-domain response of the critical mode of (5.14) is shown in Fig. 5.14 for a step change in the system. The dynamic characteristics of the critical mode shown in Fig. 5.14 is similar to the slow dynamic variation that can be seen in Fig. 5.6(b). Hence, the presence of control interactions between PV systems that is identified in Section 5.3 is mathematically verified by the modal analysis.

The eigenvalues obtained considering all three PV systems were connected to the grid are given in (5.15). According to the results, the critical mode, that is λ_{33}, results PV systems to reach steady-state after about 60 s. However, such fact is not verifiable by results shown in Fig. 5.11(b) since the PCC V_Q controller of a PV system had been saturated at zero.

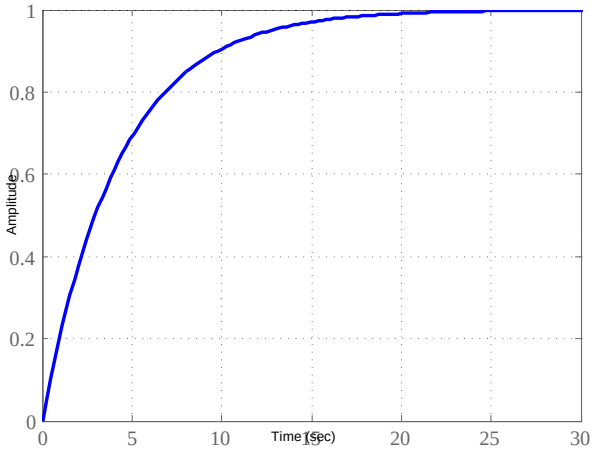

Figure 5.14: Time-domain response of the critical mode

$$\begin{bmatrix} \lambda_{13} \\ \lambda_{23} \\ \lambda_{33} \end{bmatrix} = \begin{bmatrix} -13.46 \\ -0.49 \\ -0.17 \end{bmatrix} \tag{5.15}$$

The behaviour of critical system modes with addition of more PV systems to the network shown in Fig. 5.10 can be analysed using the small-signal model developed in Section 5.4 of this chapter. Results obtained from such an analysis can be summarised as follows. If additional PV systems are connected beyond PV_3 of Fig. 5.10 after adding more line impedances beyond N_3, the critical mode of the system is critically damped and and will have a short response time than λ_{33}. If more PV systems are connected in between the grid and PV_1 in Fig. 5.10, the critical mode will continue to be critically damped but will have a long response time than λ_{33}. However, similar to simulation results presented in Fig. 5.11, these slow modes can disappear under actual unit operation as a result of saturated PCC V_Q controllers in PV systems.

5.6 Experimental results

The control interaction between PV systems that has been identified by simulation studies and analysis in this chapter was experimentally verified using an experimental setup of two, grid-connected PV systems. The experimental results are presented in this section.

The schematic diagram of the experimental setup is similar to that is shown in Fig. 5.5. A California Instruments MX30 AC/DC power source was used to emulate the grid and two AMETEK TerraSAS PV units were used to emulate PV arrays. In the experimental setup, network impedances are similar to that is given in Table 5.1 with reference to Fig. 5.5. The gains of PCC V_Q controllers of PV_2 and PV_3 were set to reach the steady-state within 1 s, if these PV systems were operated individually while connected to the network shown in Fig. 5.5. The values of the reference voltages of PCC V_Q controllers were $253\sqrt{2}$ V.

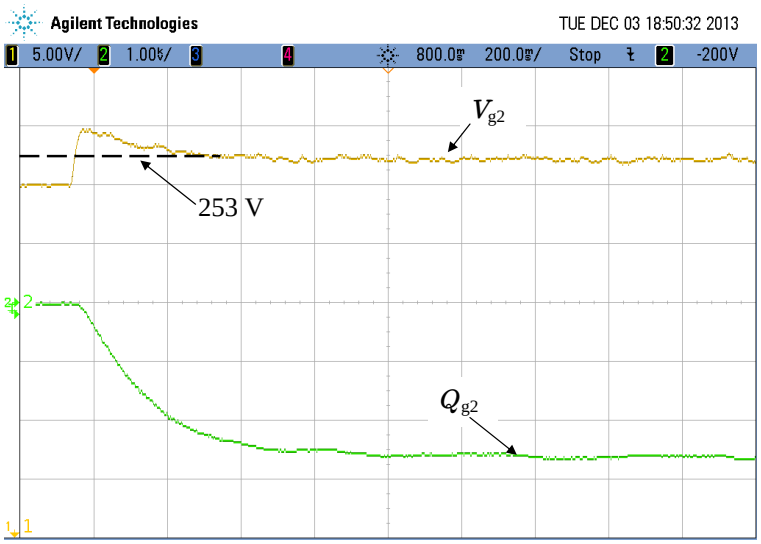

Figure 5.15: Single PV system operation - dynamic performance of the PCC V_Q controller in PV_2: Ch1: rms voltage of the PCC (V_g) [5 V/div], Ch2: reactive power injected to the grid (Q_g) [1 kVAr/div], Time base [200 ms/div]

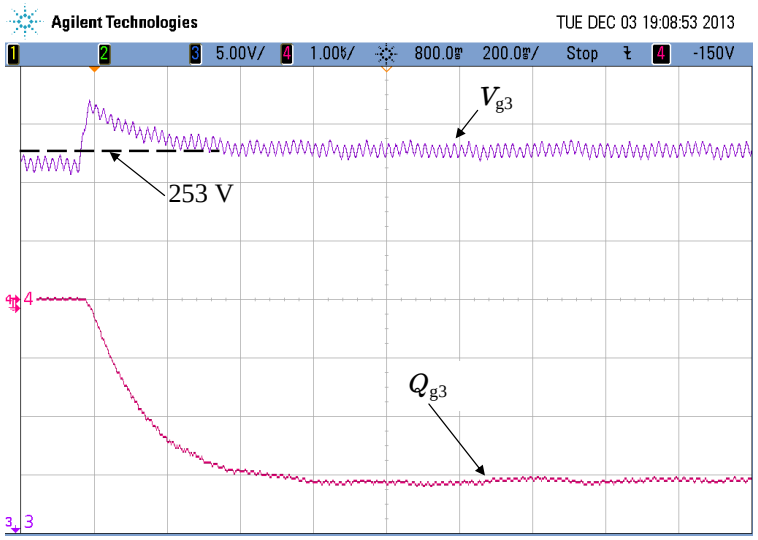

Figure 5.16: Single PV system operation - dynamic performance of the PCC V_Q controller in PV_3: Ch3: rms voltage of the PCC (V_g) [5 V/div], Ch4: reactive power injected to the grid (Q_g) [1 kVAr/div], Time base [200 ms/div]

The dynamic response of the PCC V_Q controller in PV_2 in the experimental setup when operated alone is shown in Fig. 5.15 during a disturbance in the grid. As per the experimental results shown in Fig. 5.15, the steady-state of the controller has been reached within about 1 s. Fig. 5.16 illustrates the dynamic behaviour of the PCC V_Q controller in PV_3 which is similar to the dynamic behaviour illustrated in Fig. 5.15 of PV_2. As shown in Fig. 5.15 and Fig. 5.16,

when PV_2 and PV_3 were operated individually the steady-states of PCC V_Q controllers in these PV systems have been reached within 1 s.

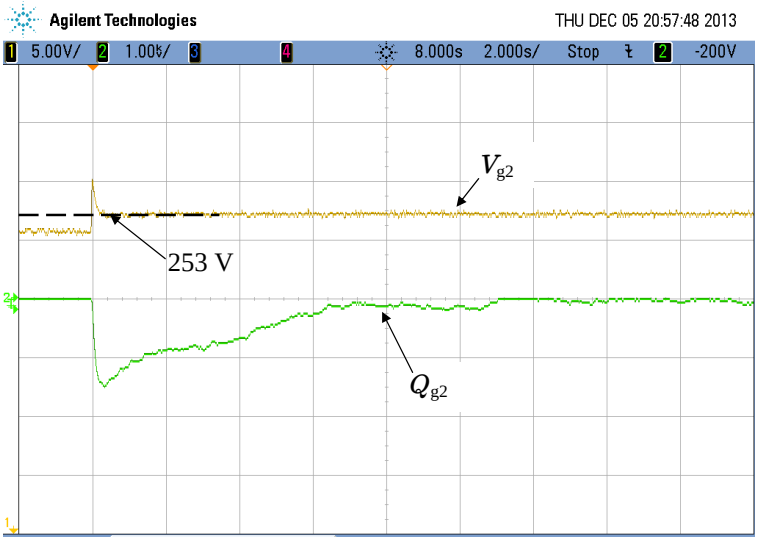

Figure 5.17: Operation of multiple PV systems - dynamic performance of the PCC V_Q controller in PV_2: Ch1: rms voltage of the PCC (V_g) [5 V/div], Ch2: reactive power injected to the grid (Q_g) [1 kVAr/div], Time base [2 s/div]

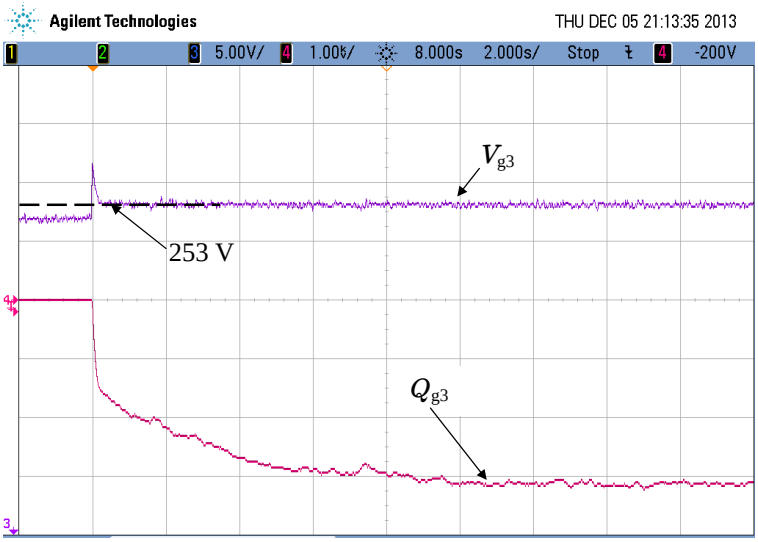

Figure 5.18: Operation of multiple PV systems - dynamic performance of the PCC V_Q controller in PV_3: Ch3: rms voltage of the PCC (V_g) [5 V/div], Ch4: reactive power injected to the grid (Q_g) [1 kVAr/div], Time base [2 s/div]

In Fig. 5.17 and Fig. 5.18, the dynamic behaviour of PCC V_Q controllers when PV_2 and PV_3 were operated simultaneously are shown. Similar to simulation results presented in Section 5.3, the PCC V_Q controllers in PV_2 and PV_3 have taken a longer time compared to the results in Fig. 5.15 and Fig. 5.16 to

reach the steady-state when these two PV systems were operated simultaneously. When PV_2 and PV_3 were operated simultaneously, the steady-states of PCC V_Q controllers in these PV systems have been reached within about 12 s. A close observation of experimental results reveals that the PCC V_Q controller of PV_2 has been saturated at zero after about 12 s. As a result, only PV_3 was actively regulating voltage after that time. The time difference of reaching the steady-state of PCC V_Q controllers in the simulation model of which results are presented in Fig. 5.6 of Section 5.3 and in the experimental setup is mainly due to saturation of PCC V_Q controller in a PV system of the experimental setup. Despite the fact that steady-state of PCC V_Q controllers have been reached within about 12 s because of the saturation of a controller, the experimental results verify the presence of control interaction between PV systems that was identified in Section 5.3. Due to limitations in kVA rating of PV systems used in the experimental setup, it was not possible to obtain experimental results that are comparable to simulation results presented in Fig. 5.6 of Section 5.3.

The dynamic behaviour of PV systems with double the gains in the PCC V_Q controllers of PV_2 and PV_3 and when the PV systems were operated simultaneously are shown in Fig. 5.19 and Fig. 5.20. With higher control gains, the steady-states of PCC V_Q controllers have been reached within about 4 s, which is shorter than time taken to reach the steady-state of PCC V_Q controllers with lower gains presented in Fig. 5.17 and Fig. 5.18. Therefore, these experimental results verify that the effect of control interaction between PV systems can be minimised by increasing the controller gains of PCC V_Q controllers in PV systems. However, the gain of the PCC V_Q controller in a PV system cannot be increased without bounds because the dynamic stability of the control system of the PV system can be affected. The dynamic behaviour of PV systems with five times larger gains in PCC V_Q controllers of PV_2 and PV_3 are shown in Fig. 5.21 and Fig. 5.22 when the PV systems were operated simultaneously. The oscillatory behaviour of PCC V_Q controllers when controller gains were further increased

can be clearly seen in Fig. 5.21 and Fig. 5.22.

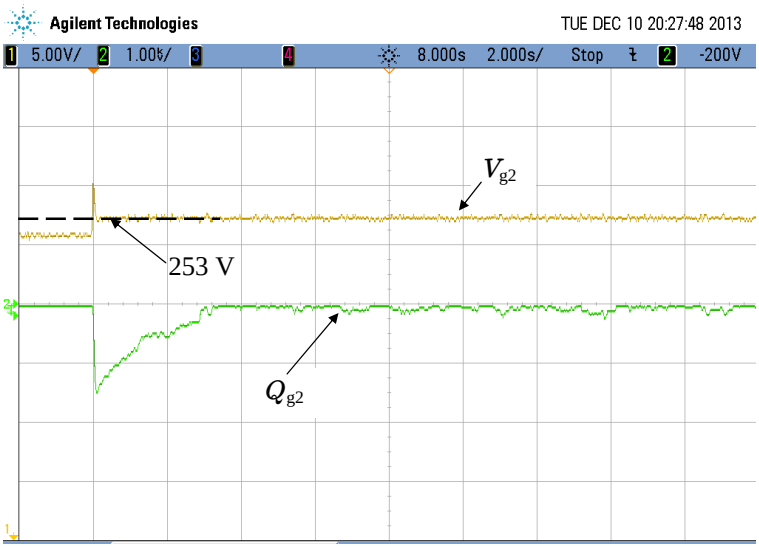

Figure 5.19: Operation of multiple PV systems with 2 times higher control gains - dynamic performance of the PCC V_Q controller in PV_2: Ch1: rms voltage of the PCC (V_g) [5 V/div], Ch2: reactive power injected to the grid (Q_g) [1 kVAr/div], Time base [2 s/div]

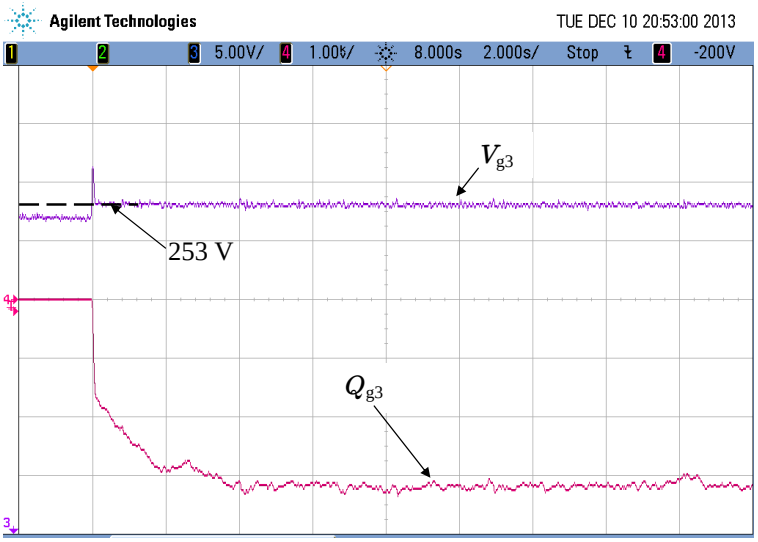

Figure 5.20: Operation of multiple PV systems with 2 times higher control gains - dynamic performance of the PCC V_Q controller in PV_3: Ch3: rms voltage of the PCC (V_g) [5 V/div], Ch4: reactive power injected to the grid (Q_g) [1 kVAr/div], Time base [2 s/div]

As stated in Section 5.3, droop control is widely used in control systems of electrical machines and power electronic drives to improve dynamic performances of such systems specially when multiple units are operated close to each other. The experimental results shown in Fig. 5.17 to Fig. 5.20 illustrates possible control

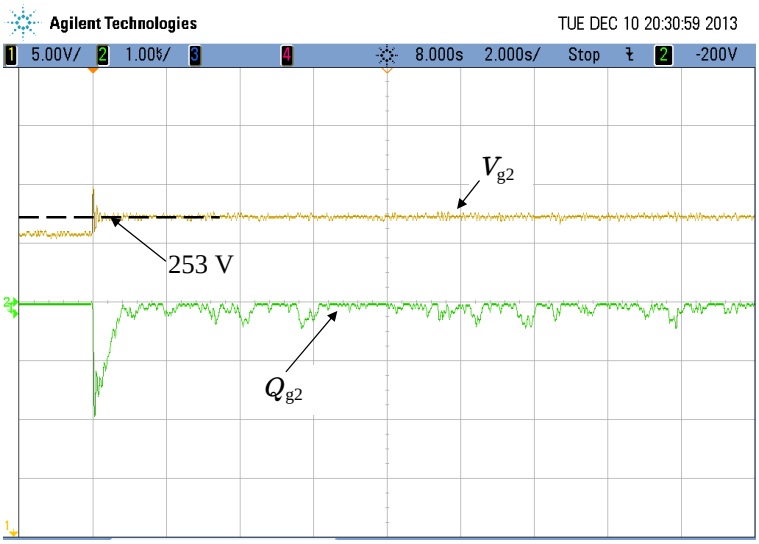

Figure 5.21: Operation of multiple PV systems with 5 times higher control gains - dynamic performance of the PCC V_Q controller in PV_2: Ch1: rms voltage of the PCC (V_g) [5 V/div], Ch2: reactive power injected to the grid (Q_g) [1 kVAr/div], Time base [2 s/div]

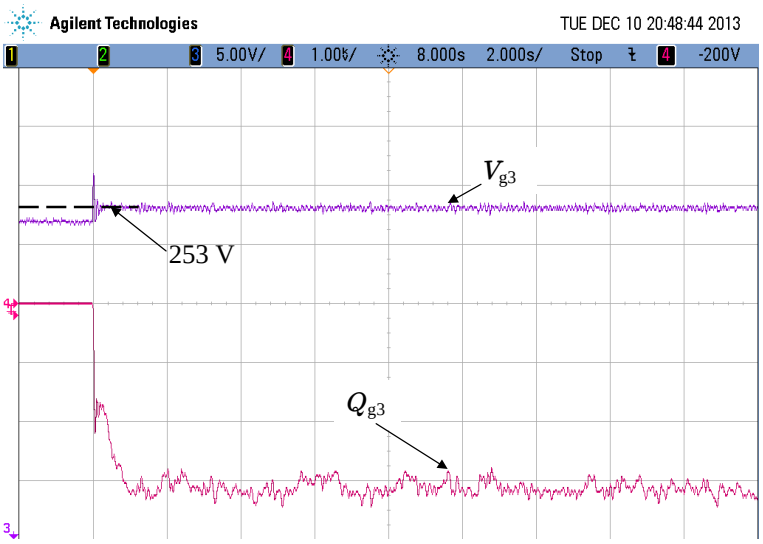

Figure 5.22: Operation of multiple PV systems with 5 times higher control gains - dynamic performance of the PCC V_Q controller in PV_3: Ch3: rms voltage of the PCC (V_g) [5 V/div], Ch4: reactive power injected to the grid (Q_g) [1 kVAr/div], Time base [2 s/div]

interactions as well as poor reactive power sharing between PV_2 and PV_3 in the experimental setup. The PV system at the node where the voltage sensitivity is high, that is PV_3, tends to control the grid voltage by absorbing reactive power while PV_2 hardly absorbs any reactive power in steady-state. Therefore, a droop controller is added to the PCC V_Q controller of each PV system in order to

improve the dynamic behaviour of the PV systems when operated simultaneously and the load sharing between PV systems.

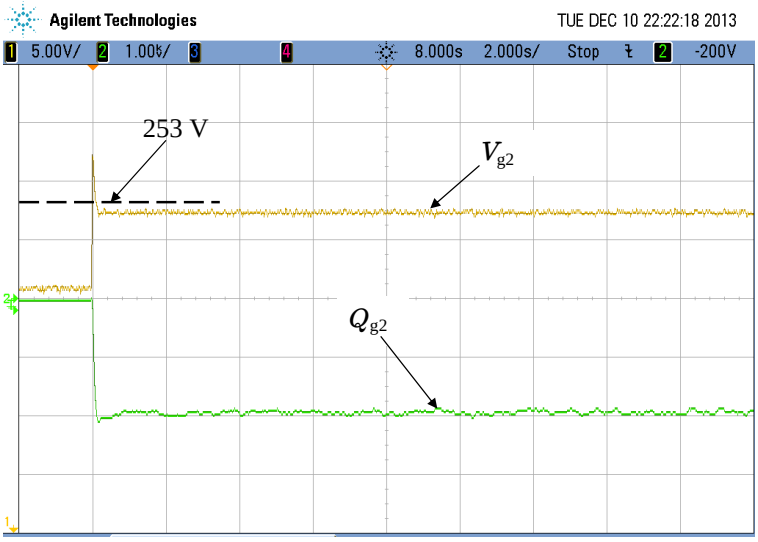

Figure 5.23: Operation of multiple PV systems with droop control - dynamic performance of the PCC V_Q controller in PV_2: Ch1: rms voltage of the PCC (V_g) [5 V/div], Ch2: reactive power injected to the grid (Q_g) [1 kVAr/div], Time base [2 s/div]

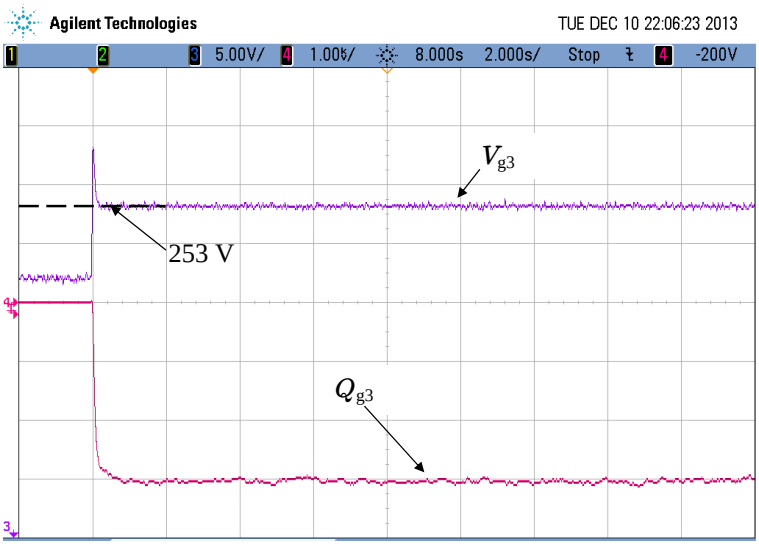

Figure 5.24: Operation of multiple PV systems with droop control - dynamic performance of the PCC V_Q controller in PV_3: Ch3: rms voltage of the PCC (V_g) [5 V/div], Ch4: reactive power injected to the grid (Q_g) [1 kVAr/div], Time base [2 s/div]

The results of an experiment performed with droop controllers built into PCC V_Q controllers of PV_2 and PV_3 and operating PV systems simultaneously are shown in Fig. 5.23 and Fig. 5.24. It can be observed that the reactive power

sharing between PV systems has been improved. Further, the steady-states of the PCC V_Q controllers have been reached within about 2 s. The experimental results confirm that a droop controller built into the PCC V_Q controller of a PV system is able to improve reactive power sharing between multiple PV systems and minimise the effect of control interactions.

Further experimental studies were carried out by considering different operating conditions of PV systems and also by integrating commercially available small-scale DSTATCOMs to the experimental setup. The results of such experimental studies are discussed in Appendix E of this Thesis. These experimental results do not indicate any dynamic interaction between converter systems that may impact the stable operation.

5.7 Chapter summary

In this chapter, the control interactions between multiple PV systems were identified by simulation studies performed. The PV systems considered in this research are interfaced to the grid via current-controlled voltage source converters. A small-signal model of a power distribution feeder to which multiple PV systems are integrated was developed while considering practical techniques used to establish the control system of a grid-connected PV system described in Chapter 3 and Chapter 4. Modal analysis was performed by using the developed small-signal model to verify the simulation results. The small-signal model developed in the current research was used to analyse the dynamic stability and system level behaviour of multiple PV systems that control the grid voltage dynamically. The accuracy of the small-signal model developed and simulation results presented in this chapter was verified using experimental results. Based on the simulation and experimental results presented and mathematical derivations in this chapter, the following conclusions can be drawn.

- The results of time-domain simulation studies of an LV power grid to which

multiple solar PV systems are integrated presented in this chapter, confirm that control interaction between multiple PV systems can exist when those systems regulate the respective PCC voltage dynamically by absorbing reactive power from the grid.

- The small-signal model of a multiple PV installation developed in this chapter is accurate and can be used to analyse the control interaction between multiple PV systems and to investigate the level of sensitivity of different parameters.

- The control interactions between multiple PV systems that is identified in this research does not cause any dynamic instability in the grid since all modes are critically damped, as demonstrated by the modal analysis performed.

- The effects of control interaction identified in the current research can be minimised by adding a droop controller to the dynamic PCC voltage controller of a PV system. Further, such a droop controller improves reactive power sharing between multiple PV systems.

The research outcomes presented in this chapter confirm that dynamic instability of the grid as result of control interaction between grid-connected multiple PV systems that control the PCC voltage with dynamic reactive power controllers is unlikely to occur. Therefore, multiple PV systems that dynamically control the PCC voltage can be deployed to control the voltage of a power distribution feeder without concerns.

Chapter 6

Simplified simulation model of a PV system

6.1 Introduction

In Chapter 3, a detailed simulation model of a grid-connected single-phase, two-stage PV system was developed. The simulation model consists of models of physical components and control systems of a comparable 5 kW PV system that may be installed in an LV electricity network. The accuracy of the developed simulation model has been verified with experimental results obtained from a laboratory setup of a PV system as described in Appendix D.

The detailed simulation model is a useful tool for analysing and understanding the dynamic performance of a single PV system or, for a few PV systems connected to an LV power grid. However, when analysing the dynamic performance of multiple PV systems connected to an LV power grid, extensive computational capacity is required. The actual time required to simulate a complex scenario with multiple instances of the detailed simulation model of a PV system is much larger. Hence there is a need for a simplified model of a PV system.

A simplified version of the simulation model developed in Chapter 3 is derived in this Chapter. In the process of deriving the simplified model, attention has been given so that the validity and accuracy of the dynamic performance aspects

are not compromised. The strategy that was adopted to simplify the detailed simulation model of the PV system is described and the dynamic performance of the detailed and simplified simulation models are compared.

6.2 Simplified model of a PV system

The PV system in the detailed simulation model developed in Chapter 3 was interfaced to the grid via a current-controlled VSC. Such a converter system can be modelled using a controlled current source. Therefore, in the simplified model, the PV system can be represented by a controlled current source.

There are several layers of control in a grid-connected PV system as described in Chapters 3 and 4. The control systems of the inner layers respond faster than the control systems of the outer layers to ensure the dynamic stability of the total control system and the overall dynamic performance of a PV system is determined by the dynamic performance of the outer control loops. Hence, if the characteristics of control systems in the outer layers are of primary interest with regard to the overall dynamic behaviour of the PV system, the inner control systems can be disregarded in the simplified model.

A simplified model of a PV system as suitable for analysing the dynamic performance of multiple PV systems connected to an LV power grid is developed. The intended use of this model is to identify possible dynamic interactions between multiple PV systems when each PV system is dynamically regulating its PCC voltage with the PCC voltage controllers developed in Chapter 4. As described in Chapter 4, the dynamic PCC voltage controllers, i.e. the PCC V_Q controller and PCC V_P controller, are at the most outer layers of the control for a PV system and determine the overall dynamic performance of the PV system. Hence, in the simplified model of a PV system, the dynamic behaviour of PCC voltage controllers are accurately presented while disregarding the dynamic behaviour of control systems in the inner layers such as the current controller, the DC-link voltage controller and the controller of the DC-DC boost converter.

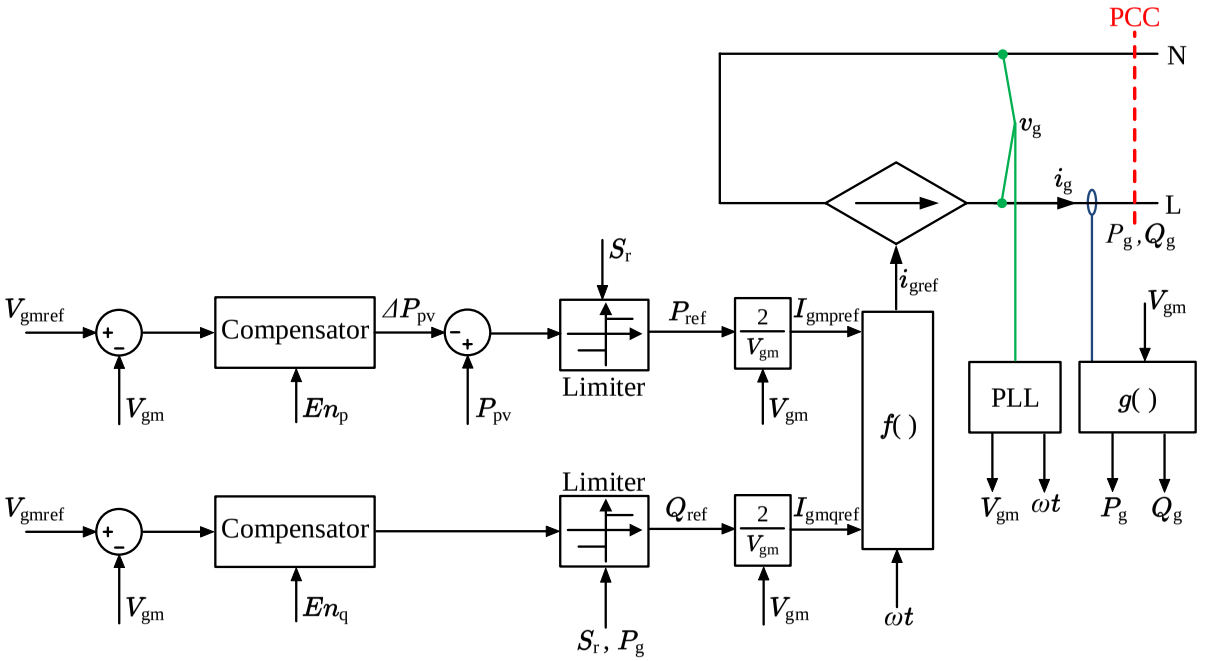

Figure 6.1: Schematic diagram of the simplified model of a PV system

An illustration of the simplified model of a PV system is shown in Fig. 6.1. The PLL structure used in the simplified model of the PV system is similar to that of the detailed model of a PV system developed in Chapter 3. The measured PCC voltage, v_{g}, is an input to the PLL. The peak value of v_{g}, V_{gm}, and the phase angle of v_{g}, ωt, are the outputs of the PLL. The rms value of v_{g} is V_{g}.

In order to calculate the active and reactive power injected to the grid, P_{g} and Q_{g} respectively, the current injected to the grid by the PV system, i_{g}, is measured. The signal processing block denoted by $g(\ )$ in Fig. 6.1 represents the mathematical calculations performed to determine P_{g} and Q_{g}. In the signal processing block $g(\ )$, the measured current i_{g} is passed through a band-pass filter, a scaled integrator and a Park transformation ($\alpha\beta$ to dq transformation) block similar to that which is done to the measured voltage at the PCC, v_{g}, in the PLL. The output of the Park transformation block in $g(\ )$ is the peak value of the active current component of i_{g}, I_{gmp}, and the peak value of the reactive current component of i_{g}, I_{gmq}. In $g(\ )$, P_{g} and Q_{g} are determined by using V_{gm}, I_{gmp} and I_{gmq} as given in (6.1) and (6.2) respectively.

$$P_{\mathrm{g}} = \frac{1}{2} V_{\mathrm{gm}} I_{\mathrm{gmp}} \tag{6.1}$$

$$Q_{\mathrm{g}} = -\frac{1}{2} V_{\mathrm{gm}} I_{\mathrm{gmq}} \tag{6.2}$$

In the simplified model of a PV system, other than the PLL, only dynamic PCC voltage controllers, i.e. the PCC V_Q controller and PCC V_P controller developed in Chapter 4, are implemented. In the PCC V_Q controller in Fig. 6.1, V_{gmref} is the reference voltage. The controller enable signal, En_{q}, represents conditions under which the dynamic voltage regulation is enabled, for an example, a defined PCC voltage above which the controller is responsive. The limiter is used to limit the reactive power injection to the available capacity of the VSC that interfaces the PV system to the grid or to limit the allowed maximum reactive power injection to the grid at a given time. S_{r} is the apparent power capacity of

the VSC.

The enable signal, En_{p}, represents conditions under which the PCC V_P controller is enabled. For an example, En_{p} can be a signal that indicates the saturation of the PCC V_Q controller. In the detailed simulation model of a PV system developed in Chapter 3, the level of solar irradiance primarily determines the active power injection unless power is required to be curtailed. However, in the simplified model, the available active power from the solar array, P_{pv}, should be provided to the model. ΔP_{pv} is the amount of active power curtailed to maintain the PCC voltage at the reference voltage, V_{gmref}. In situations in which the PCC V_P controller is inactive, ΔP_{pv} is zero. The limiter in the control loop limits the active power injection of the PV system to the rated apparent power capacity, S_{r}, of the VSC that interfaces the PV system to the grid.

In Fig. 6.1, P_{ref} and Q_{ref} are the active and reactive power references respectively. I_{gmpref} and I_{gmqref} are peak values of active and reactive current references respectively. The block $f(\ )$ represents an equation to calculate the grid current reference, i_{gref}, as given by (6.3). Since the dynamics of the current controller of a PV system are not included in the simplified model of a PV system, i_{gref} and the output of the controlled current source, i_{g} are similar.

$$i_{\mathrm{gref}} = \sqrt{I_{\mathrm{gmpref}}^2 + I_{\mathrm{gmqref}}^2}\cos(\omega t + \arctan(I_{\mathrm{gmqref}}/I_{\mathrm{gmpref}})) \tag{6.3}$$

6.3 Evaluation of the dynamic performance

The dynamic performance of the simplified model of a PV system developed in this chapter is evaluated and compared with results obtained from simulation studies using the detailed model. The simulation studies performed have confirmed that a simulation scenario that is modelled with the simplified model can be completed in only approximately 6% of the time[1] that is needed to simulate

[1]This is when simulations are performed utilising PSCAD X4, version 4.4.0.0 intalled on a PC with Microsoft Windows XP Professional, version 2002, service pack 3, Intel i7 CPU and 4GB RAM.

a comparable simulation scenario utlising the detailed model of a PV system. In this section, the dynamic performance of the detailed model of a PV system integrated with dynamic PCC voltage controllers developed in Chapter 4 and the dynamic performance of the simplified model of a PV system developed in this chapter are compared. In most of the graphs presented in this section, there are three traces: a variation of a measured parameter in the detailed model of a PV system during a simulation case, the variation of the same parameter in the simplified model of a PV system during a similar simulation case and the difference between the two variations.

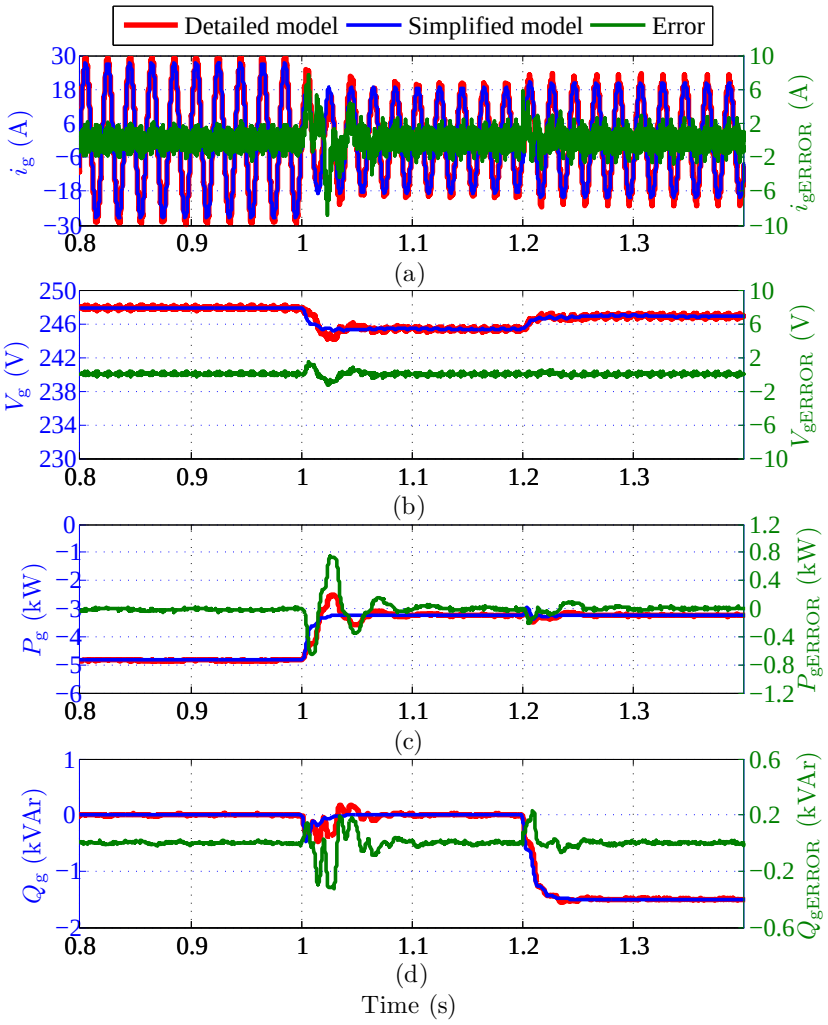

Figure 6.2: Dynamic response of the detailed and simplified model of a PV system during step changes in active power reference and reactive power reference

The dynamic behaviour of the detailed model of a PV system and the simplified model of a PV system during step changes of active and reactive power

reference are shown in Fig. 6.2. In these simulation cases, a single, grid-connected PV system was considered and the dynamic PCC voltage controllers were inactive in both PV system models. Fig. 6.2 illustrates that the steady-state operation of the detailed model and the simplified model of a PV system is almost identical. However, there are slight differences exhibited during transient conditions. The reason for these slight differences is as follows. In the simulation case developed by using the simplified model of a PV system, the dynamics of the PLL determines the dynamic behaviour of the system. In the detailed model of a PV system, the transient behaviour was determined by the DC-link voltage controller as well as the PLL in this simulation case. Therefore, the transient behaviour of the detailed model and the simplified model of a PV system was slightly different during step changes of the active and the reactive power references.

The response of detailed and simplified models of a PV system during a slow variation of solar irradiance level is shown in Fig. 6.3 when the dynamic PCC voltage controllers were inactive. In these simulation cases, both simulation models were configured to operate at 0.95 lagging power factor when active power injection is greater than 20% of the rated capacity of the PV system. The variation of the level of solar irradiance considered in this simulation case is proportional to active power variation illustrated in Fig. 6.3(c). Simulation results shown in Fig. 6.3 confirm that the dynamic behaviour of the detailed model of a PV system and the simplified model of a PV system are nearly identical during slow variations of solar irradiance levels since the differences in i_{g}, V_{g}, P_{g} and Q_{g} of the two models are nearly zero. The difference between i_{g} obtained using the two models is larger as seen in Fig. 6.3(a). This is because of the presence of switching ripple current in the detailed model of a PV system. In the simplified model of a PV system, the switching ripple current is not modelled.

The dynamic response of detailed and simplified models of a PV system were compared with simulation results obtained when dynamic PCC voltage controllers were active. In these simulation cases, a grid-connected PV system was consid-

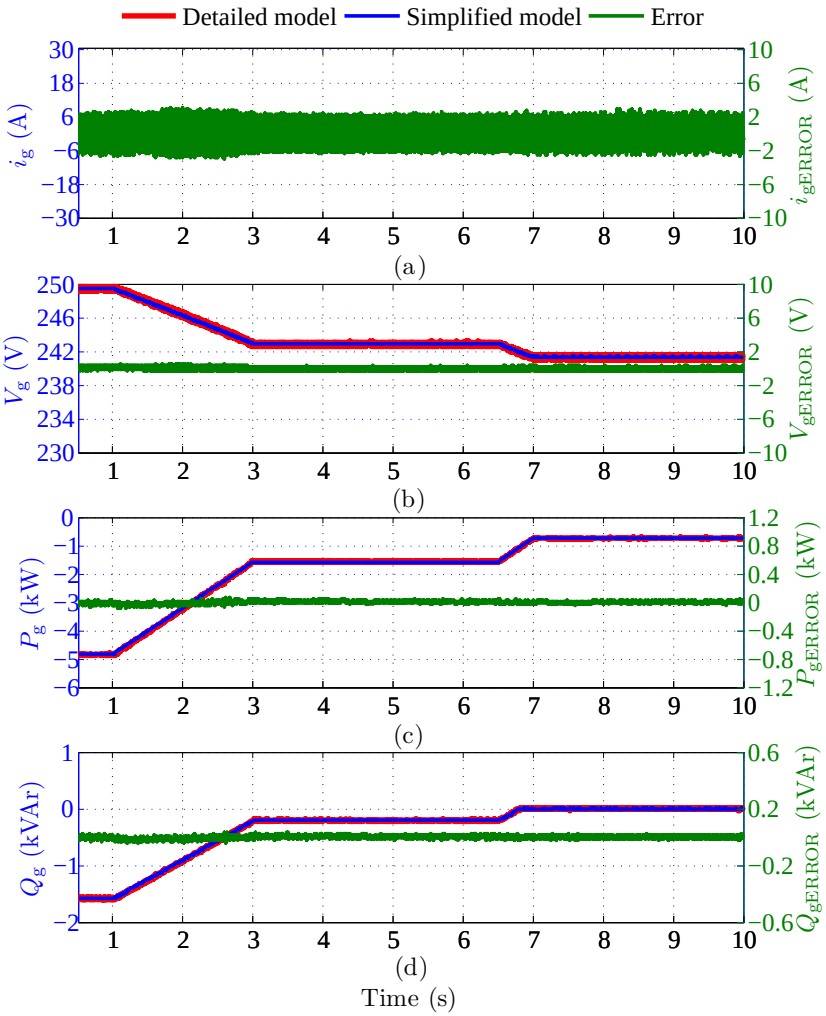

Figure 6.3: Dynamic response of the detailed and simplified model of a PV system during ramp variation in solar irradiance level

ered. The grid impedance at the PCC of the PV system was $(0.28 + j0.27)$ Ω. In the dynamic PCC voltage controllers of the detailed model of a PV system and the simplified model of a PV system, scaled integrators were used as compensators. The gain of each compensator was adjusted so that the steady-state is reached within 1 s.

The response of the PCC V_Q controller in both the detailed and simplified models of a PV system when the PCC V_P controllers were inactive is shown in Fig. 6.4. In the simulation studies, the PCC V_Q controllers of both simulation models were inactive at the beginning and were subsequently enabled at 1 s. The values of reference voltages of PCC V_Q controllers were $245\sqrt{2}$ V. As shown in Fig. 6.4, the steady-state of PCC V_Q controllers in both simulation models

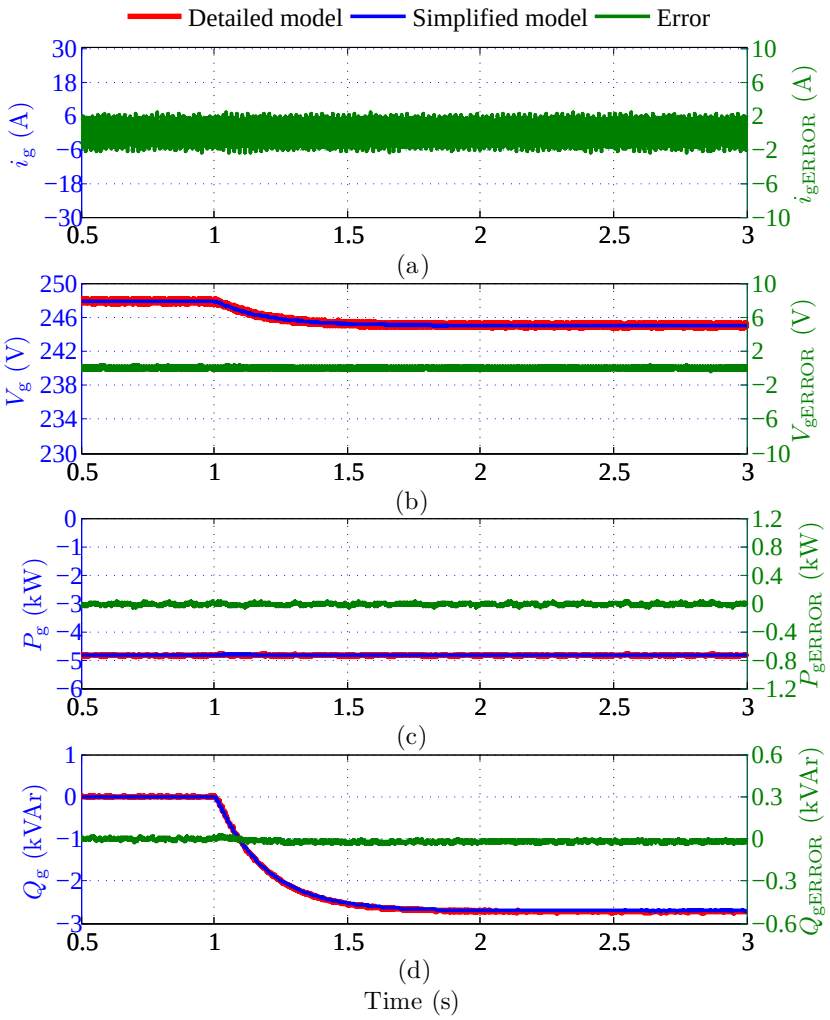

Figure 6.4: Dynamic performance of the PCC V_Q controller in the simplified model of a PV system and the detailed model of a PV system

has been reached within 1 s. Further, simulation results shown in Fig. 6.4 confirms that PCC V_Q controllers in both simulation models have similar dynamic behaviours.

The response of PCC V_P controllers of both the detailed and simplified models of a PV system when PCC V_Q controllers were inactive is shown in Fig. 6.5. Though the steady-state of PCC V_P controllers has been reached within 1 s, the transient behaviour of PCC V_P controllers in both models are slightly different as can be observed in Fig. 6.5.

The difference in the transient behaviour of PCC V_P controllers in detailed and simplified models of a PV system shown in Fig. 6.5 can be explained as follows. In the detailed model of a PV system, when active power is curtailed

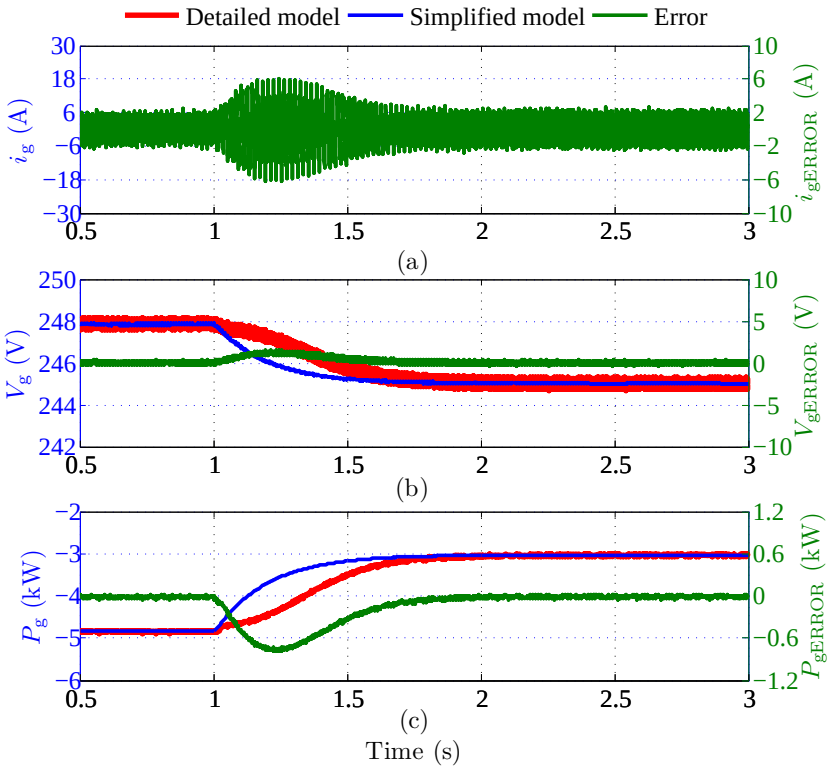

Figure 6.5: Dynamic response of the PCC V_P controller in the simplified model of a PV system and the detailed model of a PV system

to regulate the PCC voltage of the PV system by the PCC V_P controller, the reference voltage of the voltage across the PV array, V_{pvref} is changed. As designed in Chapter 3, the controller of the DC-DC boost converter regulates the output voltage of the PV array at V_{pvref}. In a PV array, $V - P$ characteristics at the knee-point (around the MPP) are non-linear. In the detailed model of a PV system, when the PV system is operating at the MPP and power curtailing is commenced as a result of the activation of the PCC V_P controller, the non-linearity of $V - P$ characteristics around the MPP of the PV array affects the dynamic characteristics of the PCC V_P controller as discussed in Section 4.5.3 of Chapter 4. In the simplified model of a PV system developed in this chapter, the power output of the PV array is modelled as a constant power source (refer to P_{pv} in Fig. 6.1) for a given operating condition and the non-linearity around the MPP of the PV array is not modelled. Therefore, the transient behaviour of the PCC V_P controller in the detailed model of a PV system and the simplified

model of a PV system is marginally different.

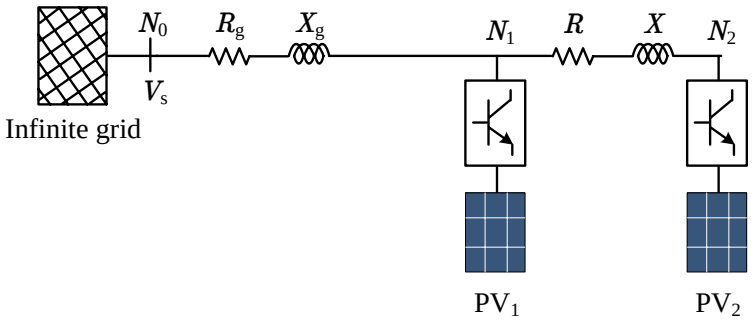

Figure 6.6: Two PV systems connected to an LV power grid

Simulation studies were performed using detailed and simplified models of a PV system to determine the suitability of using the simplified model of a PV system developed in this chapter to model an LV power grid integrated with multiple PV systems and for identifying dynamic interactions between PV systems. In these simulation studies, the network model shown in Fig. 6.6 was considered. In the network model shown in Fig. 6.6, $(R_g + jX_g)$ is $(0.25 + j0.25)$ Ω and $(R + jX)$ is $(0.03 + j0.02)$ Ω. The PCC V_Q controllers of two PV systems shown in Fig. 6.6 were active and PCC V_P controllers were inactive. The gains of PCC V_Q controllers of two PV systems were identical.

Results obtained from two simulation cases by modelling the network shown in Fig. 6.6 by using detailed and simplified models of a PV system are shown in Fig. 6.7 and Fig. 6.8. The PCC V_Q controllers of PV_1 and PV_2 were configured to reach the steady-state within 1 s if those PV systems were operated individually and when those were connected to the grid as shown in Fig. 6.6. As per the simulation results presented in Fig. 6.7 and Fig. 6.8, the dynamic behaviours of both detailed and simplified models of a PV system are identical in these simulation cases. The simulation results shown in Fig. 6.7 and Fig. 6.8 are of initial 10 s of the simulation study. At that time PCC V_Q controllers had not reached the steady-state. The steady-state of PCC V_Q controllers of PV_1 and PV_2 reached within about 30 s. The time taken to reach the steady-state of PCC V_Q controllers when these PV systems were operated simultaneously is longer than the time to

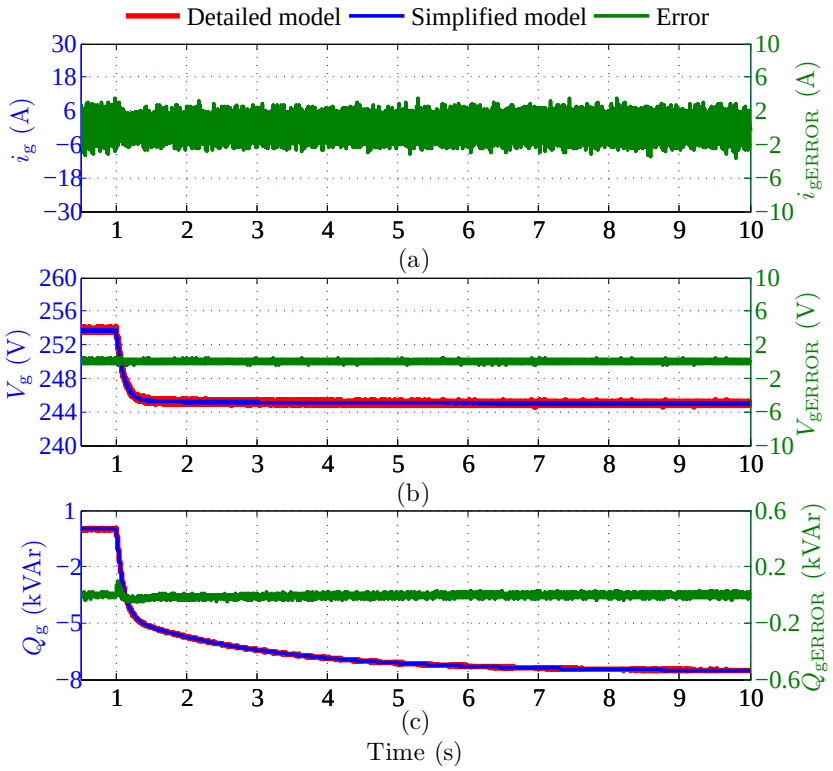

Figure 6.7: Dynamic behaviour of PV_2 in Fig. 6.6

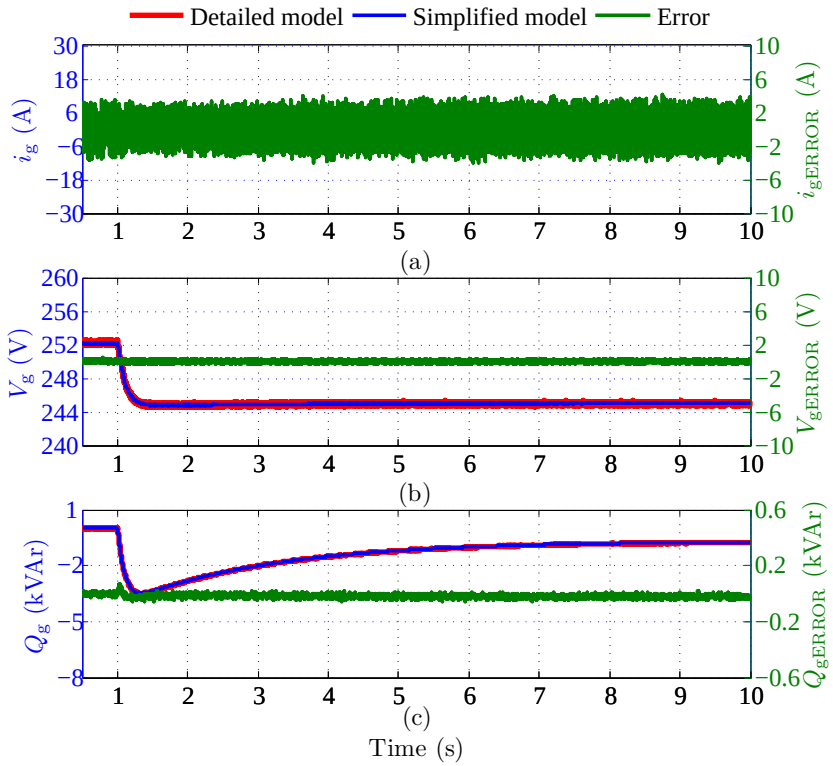

Figure 6.8: Dynamic behaviour of PV_1 in Fig. 6.6

reach the steady-state of PCC V_Q controllers if PV systems were operated individually. The time difference in reaching the steady-state of PCC V_Q controllers

when PV systems were operated individually and simultaneously arises because of dynamic interaction between PV systems that was identified in Chapter 5. The results obtained from simulation cases modelled with detailed and simplified models of a PV system are identical, as shown in Fig. 6.7 and Fig. 6.8, and the type of dynamic interaction identified in Chapter 5 is present in the network of Fig. 6.6 modelled with the simplified model of a PV system. Therefore, these simulation results confirm that the simplified model of a PV system developed in this chapter is accurate enough to model PV systems in a multiple PV installation to identify dynamic interaction between PV systems.

6.4 Chapter Summary

A simplified model of a PV system that controls the PCC voltage with dynamic PCC voltage controllers was developed in this chapter. The simplified model has been developed based on the terminal characteristics of a PV system obtained from the detailed model of a PV system developed in Chapter 3 and Chapter 4 and considered as suitable for analysing dynamic interactions taking place between multiple PV systems identified in Chapter 5. Since the dynamic PCC voltage controllers, namely the PCC V_Q controller and PCC V_P controller determine the dynamic behaviour of a PV system that controls the PCC voltage dynamically, the dynamic PCC voltage controllers are accurately modelled in the simplified model of a PV system.

The accuracy of the simplified model of a PV system developed in this chapter was evaluated by comparing simulation results obtained from comparable simulation cases modelled by using the simplified model of a PV system and the detailed model of a PV system developed in Chapter 3 and Chapter 4. According to the simulation results, the dynamic behaviour of the simplified model of a PV system is marginally inaccurate during step changes in the active and reactive power references of the PV system. However, the dynamic response of the simplified model of a PV system during slow variations of solar irradiance is close to that

predicted by the detailed model. Further, though the dynamic characteristics of the PCC V_Q controller has been modelled accurately in the simplified model of a PV system, the transient behaviour of the PCC V_P controller in the simplified model of a PV system is slightly different to that of the detailed model of a PV system. The inaccuracy in the transient characteristics of the PCC V_Q controller in the simplified model of a PV system arises because of the absence of non-linear characteristics of a PV array in that model.

The dynamic behaviour of inner control loops, the total control system of a PV system and MPPT algorithm are disregarded while developing the simplified model. Therefore, the simplified model of a PV system developed in this chapter may not be an accurate representation of an actual PV system for certain simulation studies. Hence the appropriateness of using the simplified model of a PV system in simulation studies should be evaluated before using this model.

The simulation results presented in this chapter confirm that the developed simplified model of a PV system is a sufficiently accurate model of a grid-connected PV system that controls the PCC voltage with dynamic PCC voltage controllers. Further, simulation studies have confirmed that a simulation case modelled with the simplified model of a PV system can be performed 15 times faster than a comparable simulation case that is modelled with the detailed model of a PV system. In this chapter, the operation of only one or two grid-connected PV systems were considered to demonstrate the accuracy of the developed simplified model of a PV system. The accuracy of the simplified model of a PV system to represent PV systems in an installation of more than two PV systems will be confirmed in Chapter 7 of this Thesis. Therefore, in order to model an LV power grid integrated with multiple PV systems to identify dynamic interaction between PV systems that control respective PCC voltage with dynamic PCC voltage controllers and to obtain simulation results within a short period of time, the simplified model of a PV system can be used.

Chapter 7

Power sharing between multiple solar PV systems in a radial distribution feeder

7.1 Introduction

In a grid to which multiple solar PV systems are integrated, network voltage rise has been identified in Chapter 2 as a critical technical matter that should be addressed. In such a grid, voltage may rise to considerably higher levels, especially during the day time when power generation from PV systems is at the highest level and load on the grid is at a minimum. The standards applicable to grid-integrated PV systems impose a maximum voltage level below which PV systems may stay connected to the grid. The Australian standard that is applicable to grid-integrated PV systems is AS4777.2 [7]. As per [7], the highest grid voltage that PV systems may stay connected is 230 V + 10% (herein after referred to as $U_{\max}$). If the PCC voltage of a PV system exceeds $U_{\max}$, after a defined time period the PV system should disconnect from the grid that leads to a loss of potential revenue to the owner of the PV system and loss of generation.

The voltage at the PCC of a PV system is a function of both the grid impedance and real and reactive power injected. Therefore, in certain operat-

ing situations, the voltage at the PCC of a PV system where voltage sensitivity is high may exceed $U_{\max}$ while the PCC voltages of other PV systems connected to the grid are below $U_{\max}$. In such a situation the PV system that is connected to the grid at a node where voltage sensitivity is high may disconnect in order to comply within the Australian standard AS477.2 [7] while other PV systems will continue to operate. This scenario highlights that in certain operating situations, owners of PV systems whose PV systems are integrated to the grid at nodes where voltage sensitivity is high are disadvantaged over the other PV system owners whose PV systems are connected to the grid at nodes where voltage sensitivity is less. Therefore, in this chapter a power sharing methodology is developed for PV systems that are integrated to a radial distribution feeder. The developed methodology will minimise the disadvantages associated with the voltage sensitivity at the PCC of a PV system that an owner of a grid-integrated PV system may experience.

In the power sharing method proposed in this chapter, a voltage bandwidth is determined for each PV system connected to a radial distribution feeder. Since the voltage bandwidth of a PV system is determined based on the voltage sensitivity at the PCC of the PV system, power sharing between PV systems connected to the radial distribution feeder is achieved. In the proposed method, closed-loop PCC voltage controllers developed in Chapter 4 are used to ensure that the PCC voltage of each PV system is maintained within the allocated bandwidth while sharing active power. Further, the use of closed-loop PCC voltage controllers in PV systems guarantee that the voltage of the radial distribution feeder at no location exceeds $U_{\max}$.

7.2 Model of a power distribution feeder

A single-phase power distribution feeder to which five PV systems are connected is considered in order to develop the power sharing methodology. The model of the distribution feeder is shown in Fig. 7.1. The power grid is modelled as

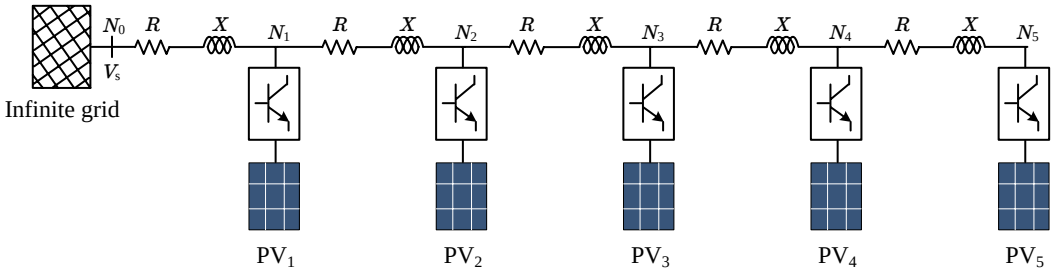

Figure 7.1: Model of a power distribution feeder

an equivalent Thévenin voltage source with an rms voltage $V_s = 240$ V. The impedances of high and medium voltage power lines and transformers are assumed to be negligible compared to that of the distribution feeder. Hence, the equivalent impedance of the grid is the impedance of the distribution transformer. The impedance of the the distribution transformer is 4%[1] and is incorporated with the feeder impedance.

The distribution feeder is modelled with five equally spaced line sections. Each line section has a resistance, R, and a reactance, X. The PV systems are assumed as directly connected to the distribution feeder without a service wire since the impedance of a service wire is generally small. The reference impedance for low voltage public supply systems that is given in [62] for electrical apparatus testing purposes is considered as the grid impedance seen by the PV system PV_5 located at the end of the distribution feeder. Hence the grid impedance seen by PV_5 is $(0.4 + j0.25)\ \Omega$.

The distribution feeder is connected with five PV systems that are equally spaced along the feeder. Since the PV systems are equally spaced and the impedance of the distribution transformer is considered equally distributed along the feeder, $R = 0.08\ \Omega$ and $X = j0.05\ \Omega$. PV systems $PV_1 - PV_5$ are connected at nodes $N_1 - N_5$ respectively. Nodes $N_1 - N_5$ are the points of common coupling (PCC) of the PV systems. The rated capacity of each PV array is 5 kW. The PV systems are integrated to the grid via VSCs. The rated capacity of each

[1]This is equivalent to the impedance of a typical 300 kVA low voltage power distribution transformer.

VSC is 5.4 kVA. Controllers that are able to regulate the PCC voltage of each PV system by dynamically controlling the active and reactive power response of the PV system developed in Chapter 4 are implemented in the control system of each PV system. All PV systems have similar operating and control capabilities. The power sharing methodology proposed in this chapter is enabled when power generation from PV systems is high and the local load on the distribution feeder is comparatively low. Therefore, a zero load condition is assumed in the grid while developing the power sharing methodology.

7.3 Steady-state voltage rise with PV

A PV system that is connected to the distribution feeder model in Fig. 7.1 is illustrated in Fig. 7.2. In the simplified model shown in Fig. 7.2, the grid impedance seen by the PV system at the PCC is Z_{T}, where $Z_{\mathrm{T}} = R_{\mathrm{T}} + jX_{\mathrm{T}}$. The values of active power and reactive power injected to the grid by the PV system are P_{g} and Q_{g} respectively and the resulting rms voltage and current at the PCC are V_{g} and I_{g} respectively.

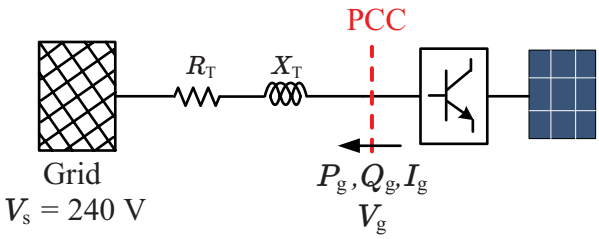

Figure 7.2: A simplified model of the network model with a single PV system

A simplified expression for the steady-state voltage rise at the PCC if the PV system is injecting P_{g} and Q_{g} to the grid respectively can be derived as given in (7.1).

$$V_{\mathrm{g}} - V_{\mathrm{s}} = \frac{P_{\mathrm{g}} R_{\mathrm{T}} + Q_{\mathrm{g}} X_{\mathrm{T}}}{V_{\mathrm{g}}} \tag{7.1}$$

In (7.1), $(V_{\mathrm{g}} - V_{\mathrm{s}})$ is the steady-state voltage rise. As per (7.1), the voltage at

the PCC is increased if active power is injected to the grid by the PV system and if reactive power is absorbed by the PV system, the PCC voltage can be reduced.

7.4 Determining a reference PCC voltage for each PV system to share active power

The reference PCC voltage of each PV system determines the setting above which the dynamic PCC voltage controllers are activated. The reference PCC voltage for each PV system is derived initially in such a way that if power curtailing is required to keep the network voltage within limits. Once power curtailing is done to bring the network voltage within limits, each PV system injects an equal amount of power to the grid irrespective of the point of connection of each PV system. In this section, the methodology that is used to determine the reference PCC voltage of each PV system is described in detail with reference to the model of a power distribution feeder shown in Fig. 7.1. In this section, PV systems are assumed to have no reactive power injection or absorption capabilities.

In the power distribution model shown in Fig. 7.1, the voltage rise at each node with respect to the immediately following node (towards the grid) can be found by using (7.1) at steady-state. Equation (7.1) is written as in (7.2) with different notations in order to mathematically represent the steady-state voltage rise in each node of the network model shown in Fig. 7.1. In (7.2), V_n is the voltage at the node N_n ($n = 1, 2, .., 5$) that is of interest to determine the steady-state voltage rise, V_{n-1} is the voltage at the node N_{n-1}, P_n and Q_n are the total active and reactive power that flows to the grid through the node N_n respectively, and R and X are the resistance and the reactance of the line section $N_n - N_{n-1}$.

$$V_n - V_{n-1} = \frac{P_n R + Q_n X}{V_n} \tag{7.2}$$

In order to find the steady-state voltage rise at node N_n ($n = 1, 2, .., 5$) with respect to node N_{n-1} by using (7.2) the voltage at node N_{n-1} and the power

that flows through node N_n should be known. Since the voltage at a node is a function of the active and reactive power injected by the PV system connected at that particular node as well as by other PV systems connected to the feeder, the voltage at each node can be found only by an iterative process. The iterative method that is used to determine the reference PCC voltage of each PV system is described here.

The active power injected by each PV system is assumed to be equal in each iteration. The network losses are disregarded. Since network losses are disregarded and a no-load condition is assumed, the active power that flows through a node is the summation of the active power injected by the PV system connected to the particular node and active power injected by all other PV systems that are connected to the distribution feeder downstream of the node of interest. If the active power injected by each PV system is P, then the active power flows to the grid at node N_n is $(6-n)P$ since the total number of PV systems in the network model in Fig. 7.1 is five.

The voltage at the node N_n when the active power flowing through the node to the grid is P and the reactive power flowing through the node is zero, can be found by solving (7.2) for V_n. The resulting equation is given in (7.3) that is used to iteratively determine the reference PCC voltage of each PV system to ensure equal share of active power.

$$V_n = \frac{V_{n-1} + \sqrt{V_{n-1}^2 + 4(6-n)PR}}{2} \qquad (n=1,2,..,5) \tag{7.3}$$

The active power injected by each PV system is set at the beginning of an iteration. Since the voltage at the node N_0 is 240 V, voltages at following nodes can be found by (7.3) when the power injected by each PV system is known. Since the voltage sensitivity of the node N_5 in the network model is higher than all other nodes, the voltage at N_5 reaches the maximum voltage limit, $U_{\max}$, first. Therefore, after finding voltages at all the nodes in an iteration, the voltage at node N_5, V_5, is compared with $U_{\max}$. If $V_5 \leq U_{\max}$ then node voltages calculated

in the current iteration are stored, the active power injected by each PV system that is set at the beginning of the current iteration is incremented and the next iteration is commenced. If $V_5 > U_{\max}$, the node voltages calculated at the previous iteration are considered as the reference PCC voltage of the respective PV system.

The reference PCC voltages that are calculated by the described iterative process for the network model shown in Fig. 7.1 are given in Table 7.1. According to the results obtained using the iterative method, each PV system should inject 2.69 kW of active power to the grid if the respective PCC voltage is regulated by curtailing active power at the reference PCC voltage given in Table 7.1.

Table 7.1: Reference PCC voltages for PV systems to share active power equally

PV system (PV_n)	**Reference PCC voltage (V)**
PV_1	244.4
PV_2	247.8
PV_3	250.4
PV_4	252.1
PV_5	253.0

7.5 Simulation results - Part A

The network model shown in Fig. 7.1 was simulated in the PSCAD/EMTDC simulation program. Each PV system was modelled by using the simulation model of a grid-connected PV system developed in Chapter 3. Furthermore, the dynamic PCC voltage controller that is able to regulate the PCC voltage of a PV system by controlling active power response of the PV system developed in Chapter 4 was integrated within the simulation models of PV systems. The reference voltage of the PCC voltage controller in each respective PV system was set using the voltages references given in Table 7.1. The solar irradiance level at each PV system was 1200 W/m^2 and the surface temperature of all the PV arrays were considered constant at 30 °C.

At the beginning of the simulation, all PV systems were operating at the

maximum power point and the PCC voltage controllers were inactive. At time $t = 1$ s, PCC voltage controllers were activated in all PV systems. The simulation was run for 20 s. The voltage variations at all five nodes that are connected with PV systems and the active power variation at each PV system are illustrated in Fig. 7.3. As shown in Fig. 7.3(a), once the controllers were activated, the PCC voltage at each PV system is regulated at the respective reference PCC voltage. The voltage profile of the network is shown in Fig. 7.4 before and after the PCC voltage controllers were activated.

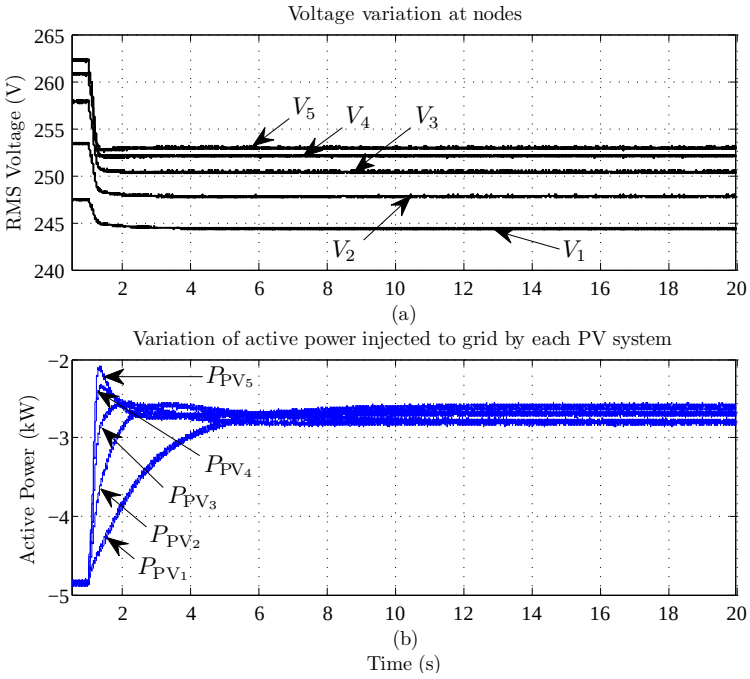

Figure 7.3: Simulation results - Part A - PCC voltage and active power variation of PV systems

The amount of active power injected by each PV system before controllers were activated and after power was curtailed to regulate the respective PCC voltage is shown in Fig. 7.5. Initially, each PV system was injecting about 4.85 kW of active power to the grid. Once active power was curtailed to regulate the PCC voltage and controllers reached steady-state, each of the PV systems was injecting about 2.69 kW of active power to the grid. This is the expected amount of active power injection by each PV system if the respective PCC voltage is regulated at the reference voltage given in Table 7.1. As per Fig. 7.5, there are slight

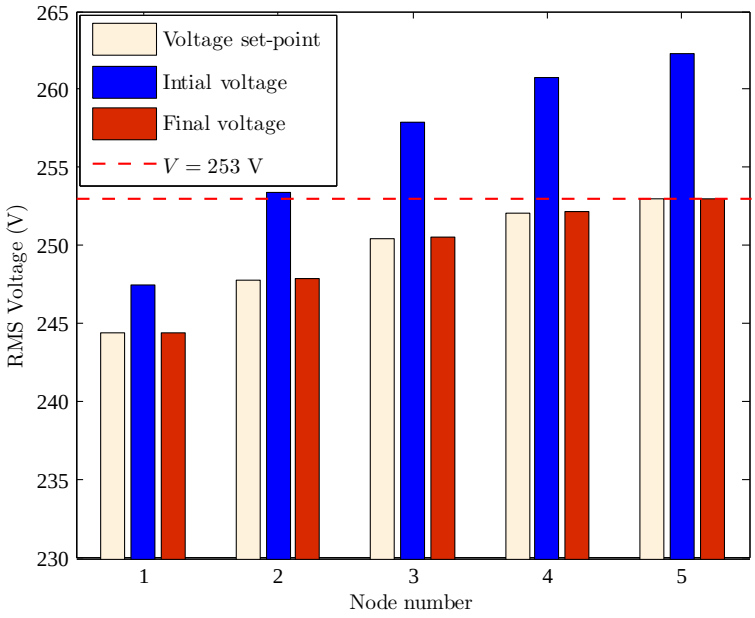

Figure 7.4: Simulation results - Part A - Voltage profile of the network

deviations in the amount of active power injected to the grid by each PV system from the value 2.69 kW after active power was curtailed. These deviations are due to the use of (7.2) that is a simplified equation, to find the reference PCC voltage of each PV system.

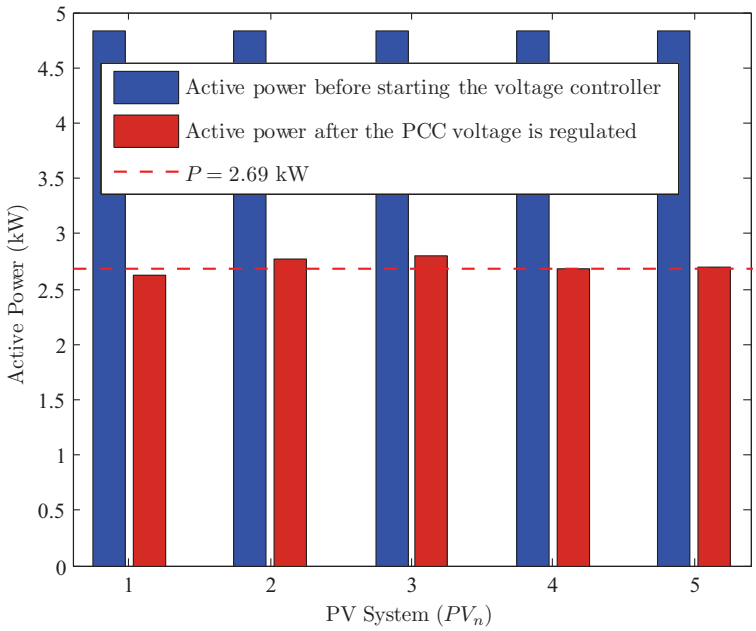

Figure 7.5: Simulation results - Part A - Active power injected by each PV system

7.6 Active power sharing between PV systems together with reactive power

PV systems can be built with reactive power capabilities as discussed in Chapter 2. In such a PV system, the PCC voltage can be dynamically regulated by controlling the reactive power response of the PV system and active power curtailment. The control system of a PV system can be configured to regulate the PCC voltage with reactive power initially if PCC voltage regulation is activated. Then, if the amount of reactive power absorbed by the PV system has reached a set limit[2], active power curtailment can be enabled.

$$V_n = \frac{V_{n-1} + \sqrt{V_{n-1}^2 + 4(6-n)(PR+QX)}}{2} (n=1,2,..,5) \tag{7.4}$$

The iterative method that was described in Section 7.4 can be modified to include the reactive power capabilities of PV systems to determine the reference PCC voltages for PV systems. The modified version of (7.3) in which reactive power capabilities of PV systems are incorporated is given in (7.4) where Q is the reactive power injected by each PV system. Since reactive power capabilities of all the PV systems shown in Fig. 7.1 are assumed to be similar, the reference PCC voltages calculated by using (7.4) are the same as those given in Table 7.1. If each PV system is limited to 0.9 lagging power factor operation and power curtailing is necessary to regulate the PCC voltage of each PV system at the respective reference voltage given in Table 7.1, the maximum active power injected by each PV system should be 3.86 kW and that is larger than what was obtained in Section 7.4 of this chapter.

[2]This limit can be derived either based on the rated capacity of the power electronic converter system that interface the PV system to the grid or based on the desired power factor.

7.7 Simulation results - Part B

The dynamic PCC voltage controller that regulate the PCC voltage by controlling the reactive power response of a PV system and developed in Chapter 4 is integrated with each PV system in the simulation model used in Section 7.5. The control system of each PV system is configured to utilise the reactive power capabilities of each PV system initially if PCC voltage regulation is necessary. The minimum lagging power factor of each PV system is set as 0.9. Once a PV system reaches the maximum reactive power limit, the respective controller is saturated and active power curtailing is enabled to regulate the PCC voltage. The minimum lagging power factor of a PV system is still maintained when power is curtailed to regulate the PCC voltage.

In order to demonstrate the robustness of the power sharing methodology presented in this chapter, a dynamically varying solar irradiance level was applied to the simulation model. The considered variation of solar irradiance at each PV system is illustrated in Fig. 7.6 and respective dynamic variations of PCC voltage, active and reactive power are shown in Fig. 7.7. The latter figure illustrates that PCC voltage regulation in each PV system is initially achieved by absorbing reactive power from the grid. Once the reactive power limit of each PV system is reached, active power has been curtailed to regulate the PCC voltage.

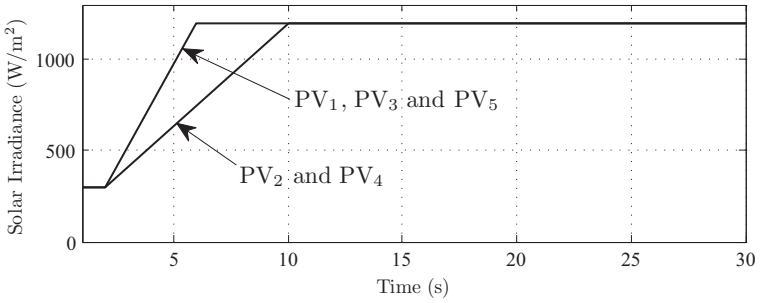

Figure 7.6: Variation of solar irradiance

The dynamic performance of the simplified model of a PV system developed in Chapter 6 of this Thesis was validated in Section 6.3 using simulation case studies that consisted of only one or two grid-connected PV systems. In order to

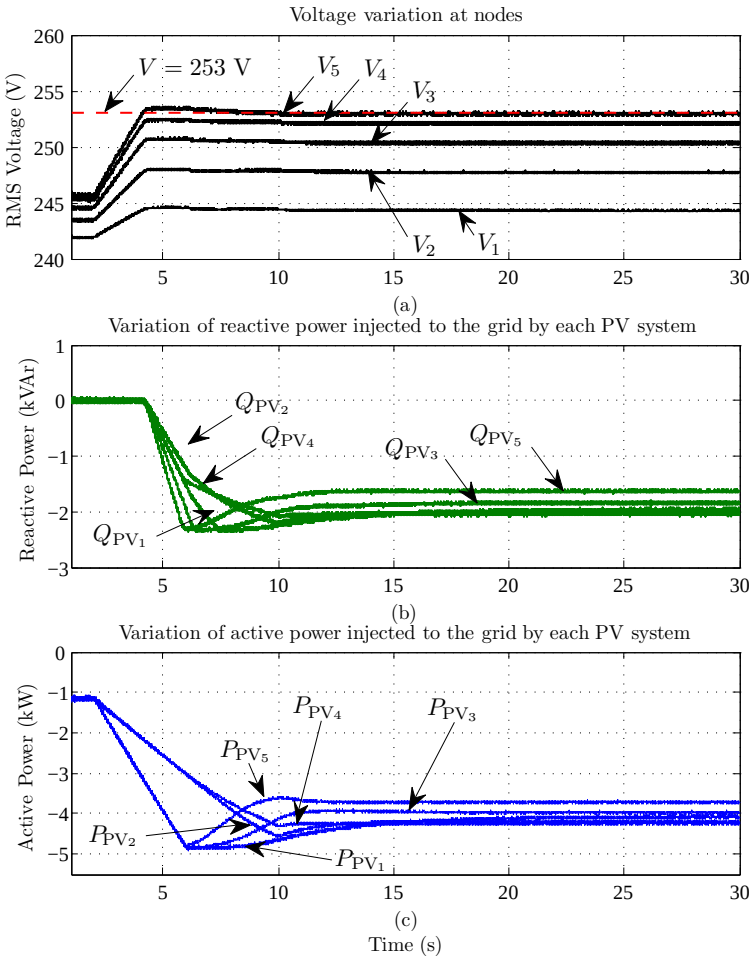

Figure 7.7: Simulation results - Part B - PCC voltage and active and reactive power variation of PV systems

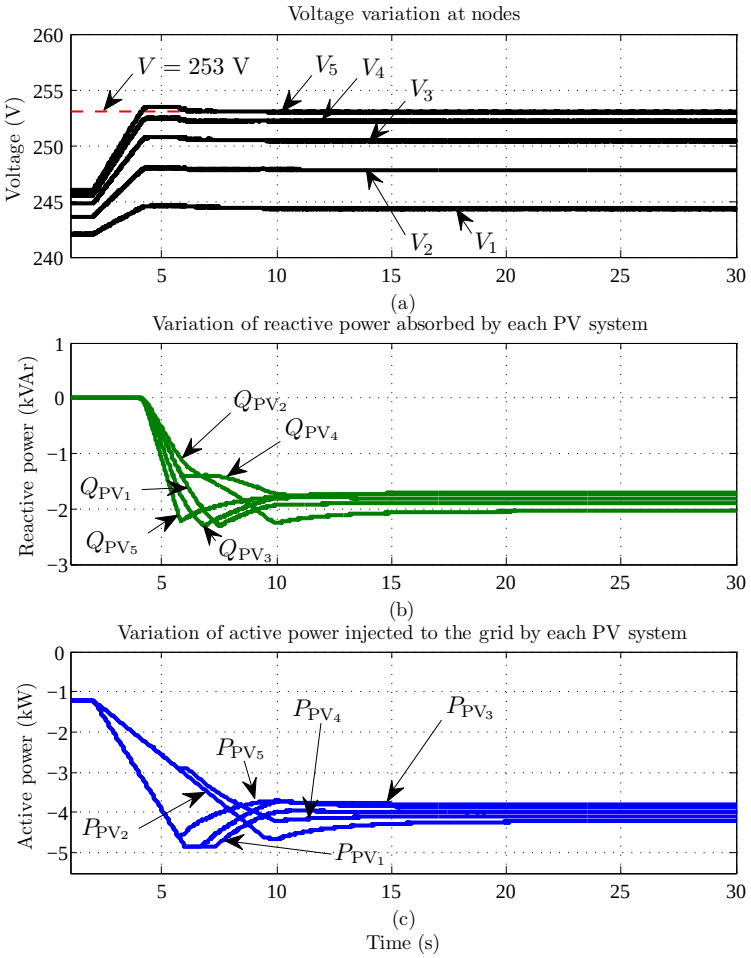

Figure 7.8: Simulation results - Part B - PCC voltage and active and reactive power variation of PV systems modelled by using the simplified model of a PV system

validate the dynamic performance of the simplified model of a PV system when used to model an LV feeder to which more than two PV systems are integrated, the simulation case study used to obtain results shown in Fig. 7.7 was redeveloped integrating simplified model of a PV system to represent PV systems in the case study. Simulation results obtained by applying the variation of solar irradiance shown in Fig. 7.6 to the redeveloped simulation case study are shown in Fig. 7.8. Simulation results shown in Fig. 7.7 and Fig. 7.8 match very closely. This comparison of results confirms further that simplified model of a PV system developed in Chapter 6 of this Thesis is accurate and that can be used to model PV systems in a multiple PV installation.

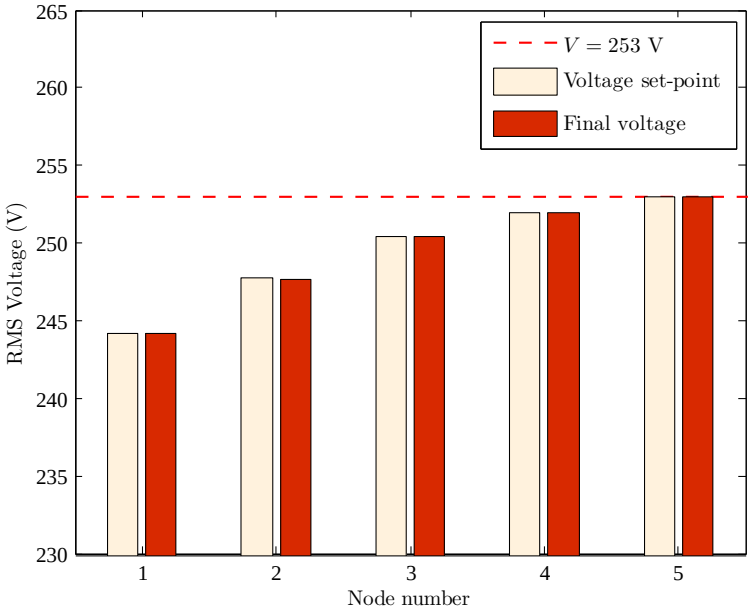

Figure 7.9: Simulation results - Part B - Voltage profile of the network

The following discussion applies to both case studies of which results are presented in Fig. 7.7 and Fig. 7.8. As per Fig. 7.9 that demonstrates the steady-state voltage profile of the network after solar irradiance has been stabilised, the respective PCC voltage has been regulated at the respective reference voltage. The steady-state active and reactive power injection by each PV system after solar irradiance was stabilised is illustrated in Fig. 7.10 and Fig. 7.11 respectively. As shown in Fig. 7.10, each PV system was injecting about 3.86 kW of active power to the grid after active power was curtailed. The reactive power absorbed

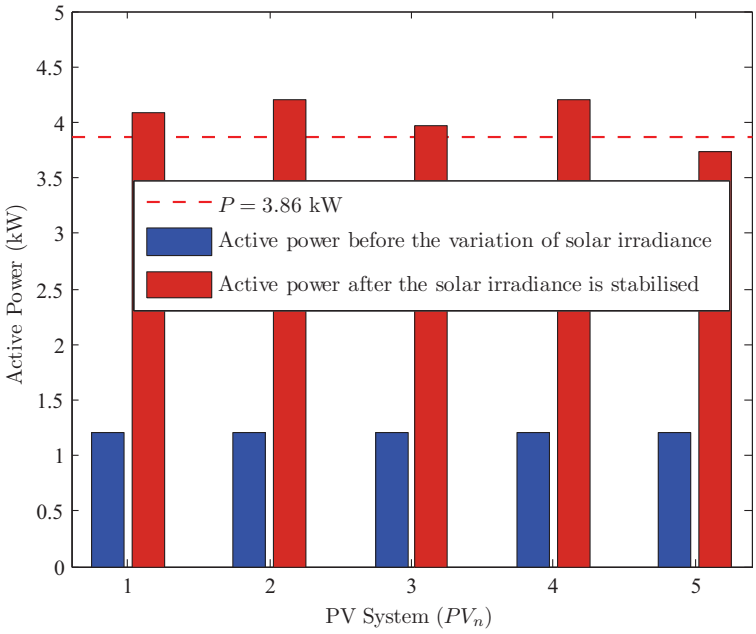

Figure 7.10: Simulation results - Part B - Active power injected by each PV system

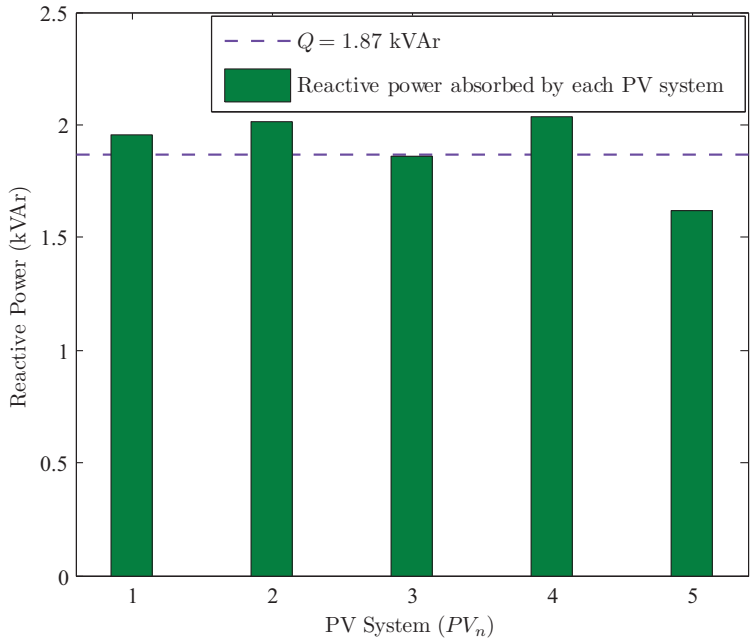

Figure 7.11: Simulation results - Part B - Reactive power absorbed by each PV system

by each PV system has been limited to 0.9 lagging power factor operation of the PV system as illustrated in Fig. 7.11. Simulation results presented in this section demonstrate that by operating each PV system of the network at the respective reference PCC voltage given in Table 7.1, active power sharing can be achieved in the network shown in Fig. 7.1.

7.8 Experimental results

The power sharing methodology proposed for PV systems connected to a radial power distribution feeder in this chapter was experimentally validated. The experimental setup that was used to obtain experimental results presented in Chapter 5 of this Thesis was used to validate the power sharing methodology developed in this chapter.

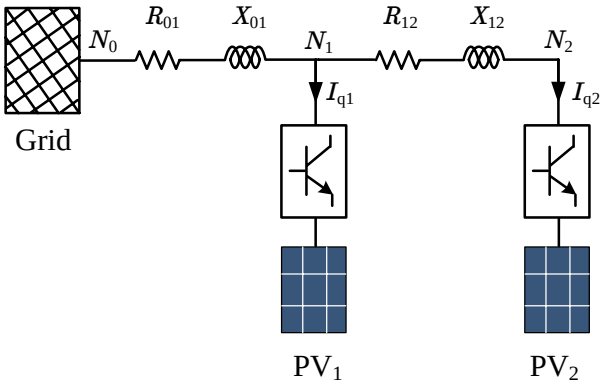

Figure 7.12: Schematic diagram of the experimental setup

A schematic diagram of the experimental setup used is shown in Fig. 7.12. In the experimental setup, $(R_{01} + jX_{01}) = (0.25 + j0.25)\ \Omega$ and $(R_{12} + jX_{12}) = (0.12 + j0.08)\ \Omega$ with reference to Fig. 7.12 and the grid voltage was set as 251 V. The reference voltages of PCC voltage controllers of PV_1 and PV_2 were set as $252.2\sqrt{2}$ V and $253\sqrt{2}$ V respectively and those values were determined by applying the iterative method described in Section 7.4 of this chapter to the network model of the experimental setup shown in Fig. 7.12. A Hioki 3196 power quality analyser was used to record active and reactive power injected by PV systems and PCC voltages of PV systems.

The experimental results obtained when PCC voltage control was done only by curtailing active power is shown in Fig. 7.13. In this experiment, reactive power controllers of PV systems were inactive. The step changes that can be seen in Fig. 7.13 are due to 400 W/m^2 to 1000 W/m^2 step changes of solar irradiance levels simulated in the experimental setup.

Fig. 7.13 illustrates that when solar irradiance level was 400 W/m^2 both PV

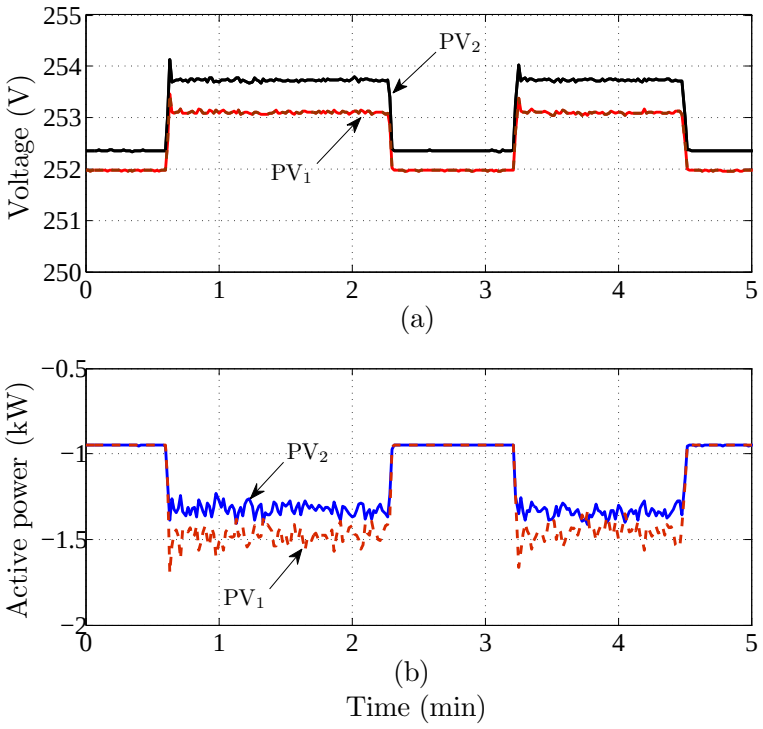

Figure 7.13: Power sharing when only reactive power controllers were active

systems were injecting nearly 1 kW of active power to the grid and PCC voltages of PV systems were below 253 V. When the solar irradiance level was increased to 1000 W/m^2 each PV system was supposed to inject approximately 2.7 kW of active power to the grid if PV systems were operated at the maximum power points (MPP). But when solar irradiance level was increased to 1000 W/m^2, PV$_1$ was injecting about 1.5 kW and PV$_2$ was injecting about 1.3 kW of active power to the grid. This is because of power curtailing applied to regulate the PCC voltage of each PV system at set reference voltages. According to the configuration of the control system of PV$_2$, the PCC voltage of that PV system should have been regulated at 253 V if power is curtailed to regulate the PCC voltage of PV$_2$. However, the PCC voltage of PV$_2$ has been regulated at 253.7 V as per the experimental results presented in Fig. 7.13 when the solar irradiance level was increased to 1000 W/m^2. This was found as a measurement error introduced by the Hioki 3196 power quality analyser that was used to record data. On the whole, there is a slight error in active power shared by PV systems when power was curtailed to regulate the PCC voltage of PV systems as shown in Fig. 7.13.

This error is mainly due to approximations applied to derive (7.3) which is used to determine reference PCC voltages and measurement errors of voltage sensors that provide PCC voltage feedback to control systems of PV systems.

The accuracy of the power sharing methodology developed in this chapter was validated when PCC voltage control of PV systems were carried out by controlling both active and reactive power. The control systems of both PV systems were configured to regulate the PCC voltage of PV systems with reactive power initially if the active power injected by a PV system is greater than 1.25 kW and PCC voltage of PV systems rises above the respective reference voltages. Then, when a PV system reaches a power factor of 0.95, active power curtailing is enabled to regulate the PCC voltage while maintaining a minimum power factor of 0.95.

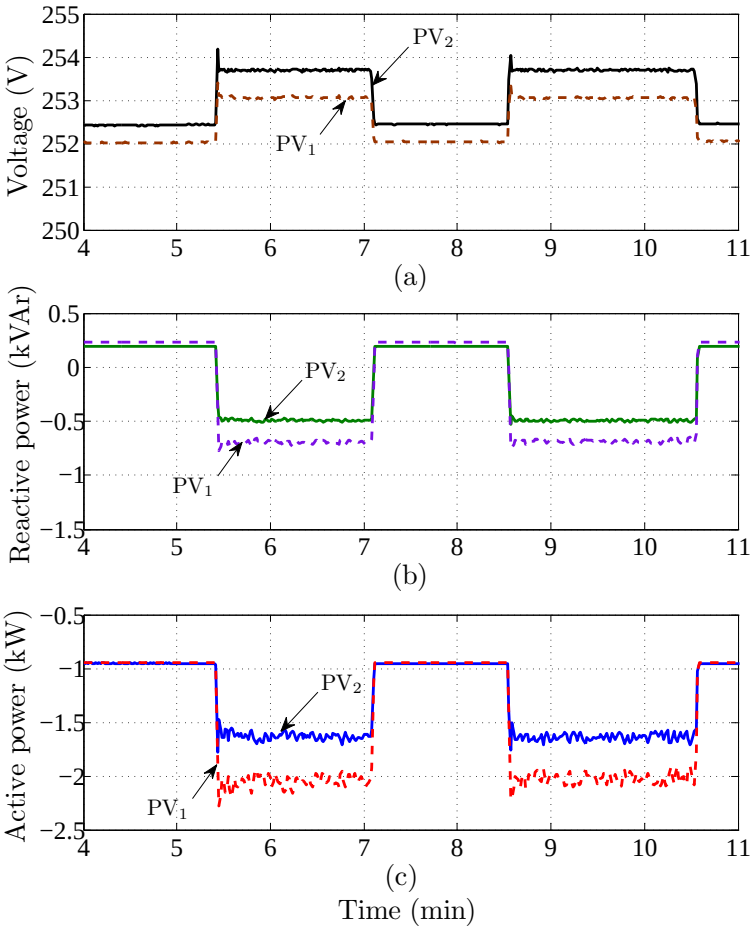

Figure 7.14: Power sharing when both active and reactive power controllers were active

The experimental results obtained when PCC voltages of PV systems were

regulated by controlling both active and reactive power are shown in Fig. 7.14. Similar to Fig. 7.13, the step changes that can be seen in Fig. 7.14 are due to 400 W/m^2 to 1000 W/m^2 step changes in solar irradiance levels simulated in the experimental setup.

Fig. 7.14 illustrates that when the solar irradiance level was 400 W/m^2 both PV systems were injecting about 1 kW of active power and no reactive power to the grid. When solar irradiance level was increased to 1000 W/m^2, PV_1 was injecting about 2 kW of active power while absorbing about 0.7 kVAr of reactive power from the grid and PV_2 was injecting about 1.6 kW of active power while absorbing about 0.5 kVAr of reactive power from the grid. The experimental results presented in Fig. 7.14 confirm that when solar irradiance level was increased to 1000 W/m^2, active power was curtailed by each PV system to regulate the PCC voltage since expected active power output of each PV system was about 2.7 kW. Further, PV systems have operated at 0.95 power factor when solar irradiance level was increased to 1000 W/m^2 and that confirms the regulation of PCC voltage of each PV system with reactive power before curtailing active power. As expected, active power injection by PV systems has increased in this experiment compared to the experimental results shown in Fig. 7.13. On the whole, the experimental results presented in Fig. 7.14 confirm that power sharing methodology developed for PV systems that control PCC voltages by controlling both active and reactive power, is acceptable and accurate enough despite the fact there were slight errors introduced by PCC voltage sensors of PV systems.

7.9 Discussion

The power sharing methodologies proposed in the current research have been successfully applied to the network shown in Fig. 7.1 in a simulation study. According to simulation results obtained, there are minor deviations in the amount of active power shared between PV systems from what is expected as shown in Fig. 7.5 and Fig. 7.10. These deviations are mainly due to the use of (7.3) or (7.4)

that are simplified expressions, based on assumptions to determine the reference PCC voltages for each PV system as given in Table 7.1. The stated deviations in active power shared by each PV system can be further minimised if reference PCC voltages are determined through a detailed load flow analysis of the network shown in Fig. 7.1.

In the network model shown in Fig. 7.1, upstream impedances are disregarded and the impedance of the distribution transformer is assumed as equally distributed along the distribution feeder. However, in a practical situation, there are upstream impedances and the impedance of the distribution transformer is a lumped impedance. Although the assumption is a significant deviation from a real situation, it does not introduce any inaccuracy to the developed power sharing methodology if it is implemented in an actual power system. This is because, in an actual power system, the upstream or downstream power flow through the distribution transformer causes the voltage to change in the whole distribution feeder equally.

The reference PCC voltages given in Table 7.1 are applicable only to the network shown in Fig. 7.1. If an additional PV system is integrated to the network, reference PCC voltages should be recalculated to suit the new network. If the developed power sharing methodology is practically implemented in a radial distribution feeder, since PV systems are being integrated to the grid continuously, there will be a need to change in the reference PCC voltage level of each PV system connected to the considered feeder when an additional PV system is integrated. Such a requirement can be minimised by zoning the feeder as shown in Fig. 7.15 and allocating a voltage reference for a particular zone. In this approach, all PV systems connected to a particular zone of a feeder will have the same PCC voltage reference.

The power sharing methodology developed in this chapter was applied to a power distribution feeder that was divided into three zones as shown in Fig. 7.15. In order to determine the reference PCC voltages of PV systems connected at

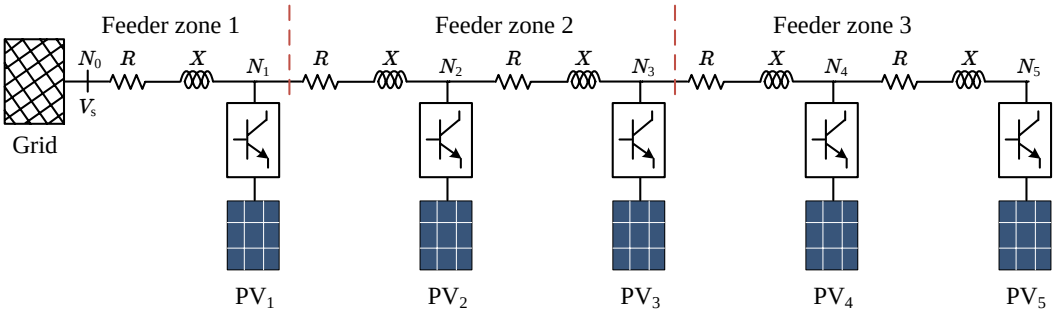

Figure 7.15: Model of a power distribution feeder divided into zones

each zone, (7.5) was used where n is the number of zones instead of number of PV systems as used in (7.4). In (7.5), R and X are the resistance and reactance of the power distribution feeder section in a particular zone and P and Q are the total active and reactive power flow through the feeder zone. The reference PCC voltages for each zone in power distribution feeder shown in Fig. 7.15 was calculated using (7.5) and the iterative process explained in Section 7.4 of this chapter assuming voltage at node N_0 was 240 V. The calculated reference PCC voltages are given in Table 7.2.

$$V_n = \frac{V_{n-1} + \sqrt{V_{n-1}^2 + 4(4-n)(PR+QX)}}{2} \qquad (n\text{=1,2 and 3}). \tag{7.5}$$

Table 7.2: Voltage set-points for PV systems in a particular feeder zone

Feeder segment	**Voltage (V)**
Feeder zone 1	246.5
Feeder zone 2	250.8
Feeder zone 3	253.0

The results obtained from a simulation model of the network model shown in Fig. 7.15 after applying reference PCC voltages in Table 7.2 to PCC voltage controllers of PV systems are shown in Fig. 7.16, Fig. 7.17, Fig. 7.18 and Fig. 7.19. The simulation results were obtained by simulating a variation of solar irradiance that is similar to the variation of solar irradiance shown in Fig. 7.6.

The simulation results shown in Fig. 7.16 and Fig. 7.17 demonstrate that even

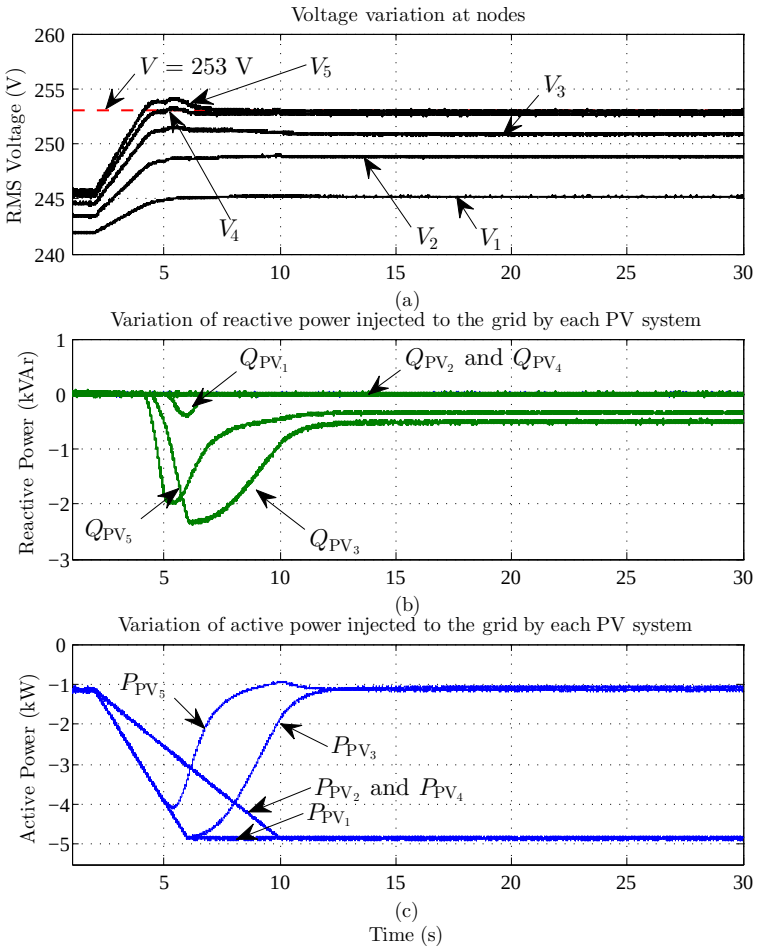

Figure 7.16: Simulation results - Feeder zones - PCC voltage and active and reactive power variation of PV systems

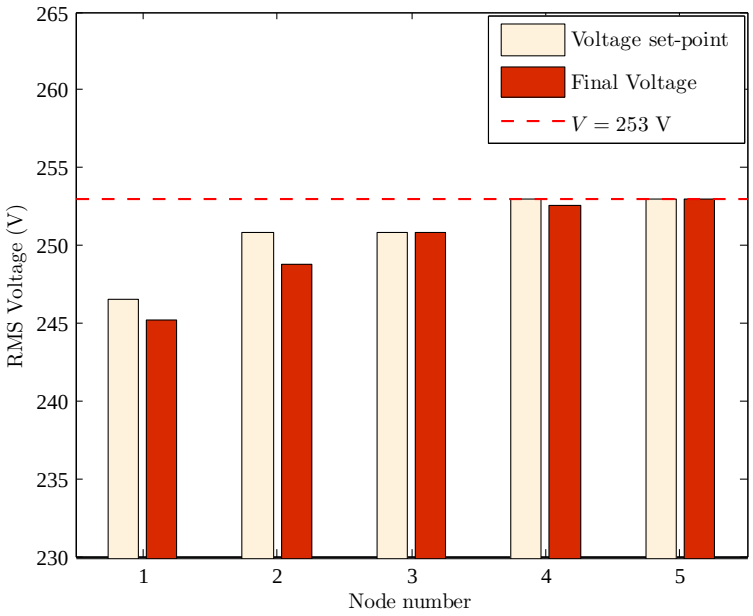

Figure 7.17: Simulation results - Feeder zones - Voltage profile of the network

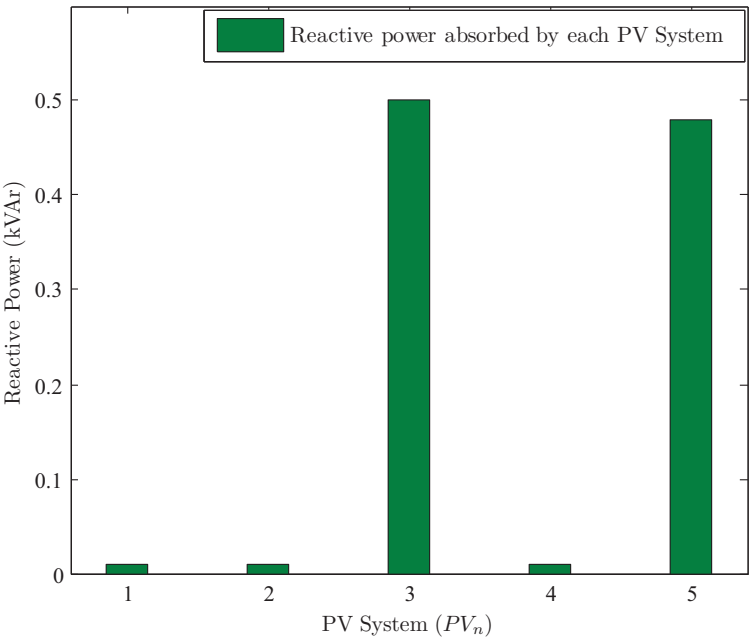

Figure 7.18: Simulation results - Feeder zones - Reactive power absorbed by each PV system

though the power distribution feeder was divided into zones, the voltage along the feeder has been maintained below 253 V at times when the voltage levels of the feeder was likely to exceed 253 V. Fig. 7.18 and Fig. 7.19 demonstrate that though the feeder voltage was maintained below 253 V, the accuracy of the power sharing methodology developed in this chapter has been compromised after

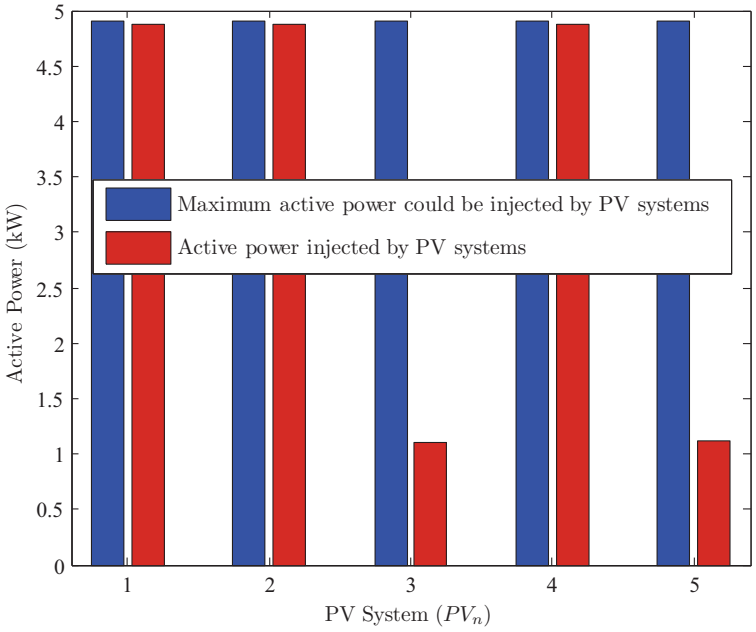

Figure 7.19: Simulation results - Feeder zones - Active power injected by each PV system

applying reference PCC voltages derived based on feeder zones shown in Fig. 7.15. On the whole, these simulation results confirm that zoning a power distribution feeder may minimise the need for frequent adjustment of control parameters of PV systems connected to a power distribution feeder to share active and reactive power but such an action may result in compromised performance in sharing power within a zone.

In developing the power sharing methodology using the network model shown in Fig. 7.1, the impedances of service wires are disregarded. In a practical application, where impedances of service wires should be accounted for, the developed power sharing methodology may not be accurate. Further, while obtaining experimental results presented in Section 7.8 of this chapter, slight adjustments had to be made to the calculated reference PCC voltages because of calibration errors in voltage sensors that measure PCC voltages of PV systems. In other words, the power sharing methodology developed in this chapter is sensitive to the accuracy of voltage sensors that measure PCC voltages of PV systems and the accuracy of the analog to digital conversion in control systems of PV systems. Such a problem exists in all PV systems that have voltage regulation capabilities. Therefore

in order to enhance the practical application and accuracy, the developed power sharing methodology should be further improved.

The practical application and the accuracy of the power sharing methodology developed in this chapter can be enhanced by using accurately calibrated voltage sensors to measure PCC voltages of PV systems. Further, if grid impedance measurement algorithms are integrated to PV systems, each PV system is able to determine the grid impedance seen at the PCC of the PV system. In such PV systems, reference PCC voltages can be made to be determined by the controller of the PV systems with reference to a preset maximum grid impedance. If there is an established communication medium in between PV systems in a power distribution feeder, that communication link can be used to identify the maximum grid impedance that a PV system sees. In such situations, the highest grid impedance measured by a PV system in a power distribution feeder can be utilised to determine reference PCC voltages and such technique will lead to accurate results in the developed power sharing methodology when practically implemented.

7.10 Chapter Summary

In this chapter, a power sharing methodology was proposed for PV systems that are integrated to a radial distribution feeder. In the power sharing method proposed in this chapter, a voltage bandwidth is determined for each PV system connected to a radial power distribution feeder. Since the voltage bandwidth is determined based on the voltage sensitivity, power sharing between PV systems connected to the radial distribution feeder is achieved. In the proposed method, closed-loop PCC voltage controllers are used to ensure that PCC voltage of each PV system is maintained within the allocated bandwidth while sharing active power. Further, the use of closed-loop PCC voltage controllers in PV systems guarantee that the voltage of the radial distribution feeder is maintained below 253 V that is the highest voltage that a PV system should remain connected to

the grid as per the Australian Standard AS4777.2. The proposed method enables equal power sharing between multiple PV systems in situations where disconnection of PV systems may be necessary due to the presence of high voltages in the grid in the absence of such a power sharing methodology.

Simulation and experimental results presented in this chapter verifies the validity and the robustness of the developed power sharing methodology. The voltage bandwidth that is determined for each PV system is derived based on a simplified equation. The power sharing methodology developed in this Chapter is sensitive to the voltage bandwidth. Hence there are inaccuracies in power sharing between PV systems that could be observed in both simulation and experimental results when the developed power sharing methodology was applied.

In the developed power sharing method, the allocated bandwidth for each PV system is a function of the number of PV systems integrated to the distribution feeder. Since PV systems are being continuously integrated, the allocated bandwidth for each PV system should be altered when an additional PV system is integrated to the feeder which is practically difficult in an actual power distribution feeder. Further, experimental results suggest that errors from voltage sensors in PV systems that measure the PCC voltage of PV systems may lead to inaccuracies in the developed method when practically implemented. In order to minimise such practical difficulties the work presented in the current research should be further improved.

Chapter 8

Conclusions and Recommendations for Future Work

8.1 Conclusions

A comprehensive literature review undertaken in this research revealed that most of the research and development activities on small scale grid-connected PV systems had been limited to improving the operation and control of individual PV systems. There was limited research attention on LV electricity networks integrated with multiple PV systems. Therefore, the research work presented in this Thesis was carried out in relation to the following aspects of the LV electricity networks integrated with multiple PV systems: (a) detailed modelling of PV systems, (b) development of advanced control techniques for controlling voltage in LV electricity networks integrated with multiple PV systems, (c) identifying and analysing dynamic interaction between multiple PV systems and (d) development of control and coordination methodologies. The main objective of the work presented in this Thesis was to enhance the integration of multiple PV systems to LV electricity networks while minimising the system level impact of operation and control of PV systems. The key conclusions and recommendations based on

the work undertaken are summarised as follows.

Development and validation of a detailed simulation model of a grid-connected PV system

A detailed simulation model of a PV system has been identified as a useful tool for identifying the dynamic behaviour of a PV system and for analysing system level impacts on LV electricity networks integrated with multiple PV systems. Since such detailed models are not completely presented in the published literature, in Chapter 3 of this Thesis, a detailed component level model of a grid-connected single-phase two-stage PV system with associated controllers was developed. In this research, a power electronic converter topology that consists of a current-controlled VSC and a DC-DC boost converter that form a two-stage converter was considered as suitable for integrating small scale PV systems to LV electricity networks. Current-controlled VSCs that provide great flexibility in controlling active and reactive power flow across the VSC are becoming increasingly popular for grid integration of small scale PV systems. A DC-DC boost converter is needed in a small scale PV system to boost the output voltage of the PV array to a suitable level as appropriate for integrating the PV system to the LV electricity network.

The effectiveness of the simulation model of the PV system developed in Chapter 3 of this Thesis with theoretically established component values and designed controllers, was evaluated with simulation studies. The robustness and the accuracy of the designed grid synchronisation mechanism, the stationary frame current controller and the DC-link voltage controller of the modelled PV system have been verified with time-domain simulation studies that are illustrated with rapid changes in solar irradiance and reactive power reference. The harmonic current that is injected by the VSC of the PV system was minimised by the harmonic compensators that are implemented in the current controller. In the simulation model, the controller of the PV system was capable of independently

controlling the active power and the reactive power injected to the grid. The active power injection to the grid was enhanced by adding an MPPT algorithm. The MPP tracking accuracy of the MPPT algorithm and the performance of the designed controller for the DC-DC boost converter have demonstrated under rapid variations of the solar irradiance. The reactive power injected by the VSC was controlled by operating the VSC at the maximum lagging power factor that is specified in the Australian Std. AS4777.2.

An experimental setup of two grid-connected PV systems was established in the laboratory. Each experimental PV system is comparable to the simulation model of a PV system developed in Chapter 3. The accuracy of the simulation model of a PV system developed in Chapter 3 has been evaluated with results obtained from an experimental PV system. An exact one-to-one comparison of the dynamic performance of the simulation model and that of the experimental PV system has not been carried out due to limited access to certain parameters in the experimental PV system. However, the experimental results presented at the end of Chapter 3 of this Thesis provided strong evidence to confirm that the dynamic characteristics of an actual PV system has been accurately modelled in the developed simulation model. Therefore, this simulation model can be confidently used to perform advanced simulation studies relevant to multiple PV systems integrated to LV electricity networks.

Advanced PCC voltage control techniques for grid-connected PV systems

In an LV electricity network to which multiple PV systems are integrated, maintaining the network voltage within allowable limits is a critical technical issue especially at times when power generation from PV systems exceeds the power demand by the loads connected to the local network. In such an LV electricity network, PV systems can be deployed to control the network voltage by regulating the active or reactive power response of each PV system. The technical

standards that are applicable for grid-connected PV systems allow PV systems to inject or absorb reactive power to provide voltage support. However, voltage support techniques have been identified as less efficient compared to dynamic voltage control with active and reactive power injection of PV systems. Hence, in the future, use of dynamic active and reactive power controllers in PV systems to control grid voltage is likely.

Dynamic voltage controllers have been identified as efficient ways to control grid voltage with multiple PV systems. However, the development of detailed design procedures and advanced analysis of dynamic performance of such controllers needed to be carried out due to the lack of relevant published research outcomes. Therefore, in this research, two closed-loop PCC voltage controllers were developed and that are presented in Chapter 4 of this Thesis. The developed closed-loop PCC voltage controllers were able to regulate the PCC voltage of a PV system at a reference level by dynamically controlling the active or reactive power response of the PV system. Simulation results and experimental validations presented in this Thesis demonstrate that the controller design procedures illustrated in Chapter 4 of this Thesis are accurate and the responses of the controllers are predictable. The closed-loop PCC voltage controllers developed in this Thesis lead to effective and robust PCC voltage regulation of a PV system with both active and reactive power.

Two advanced operating strategies that will lead to an optimised operation of a PV system in a multiple PV installation were proposed in Chapter 4 of this Thesis. These operating strategies have been developed by combining the operation of dynamic voltage controllers developed in this Thesis. The novel operating strategy, the fixed minimum power factor operation, minimises the reactive power consumption while staying connected to the grid until the active power of a PV system is curtailed to a specified level. Unlike fixed minimum power factor operation, using the second novel operating strategy, the maximum apparent power operation proposed in this Thesis may utilise the full capacity of the converter

that interfaces the PV system to the grid. Therefore, with the maximum apparent power operation of a PV system, PCC voltage regulation may be achieved with minimum active power curtailment. Further, the maximum apparent power operation of a PV system may dynamically control the network voltage with reactive power even without injecting any active power to the grid. The experimental results presented in Chapter 4 confirm the feasibility of implementing these novel operating strategies in a PV system without affecting the stability of the operation of a PV system.

Identification of dynamic interactions between multiple PV systems

In this research, possible dynamic interactions between multiple PV systems were identified by performing extensive simulation studies. The results of time-domain simulation studies of an LV electricity network to which multiple PV systems are integrated, presented in Chapter 5 of this Thesis, confirm that there is control interaction between multiple PV systems when those systems regulate the respective PCC voltage dynamically by absorbing reactive power from the grid. In a multiple PV installation, the dynamic voltage controller of a PV system takes a longer time to reach the steady-state because of interactions between other PV systems.

Small-signal studies have also been used in Chapter 5 of this Thesis to determine control interactions between multiple PV systems. The experimental results presented in Chapter 5 of this Thesis confirm that the small-signal model of a multiple PV installation developed is accurate and control interactions exist between multiple PV systems. The developed small-signal model can be used to analyse the control interaction between multiple PV systems and to investigate the level of sensitivity of different parameters.

The control interactions between multiple PV systems that are identified in this research and presented in Chapter 5 of this Thesis do not cause any dynamic instability in the grid since all modes are critically damped, as determined by the

modal analysis performed. However, the effects of control interaction identified in the current research can be minimised by adding a droop controller to the dynamic PCC voltage controller of a PV system. Further, such a droop controller improves reactive power sharing between multiple PV systems.

The detailed simulation model of a PV system developed in Chapter 3 of this Thesis is a useful tool in analysing and understanding dynamic performance of a PV system or few PV systems connected to an LV electricity network. But when analysing dynamic performance of multiple PV systems connected to an LV electricity network, the detailed simulation model of a PV system will demand a higher computational capacity. As a result, the actual time that is required to simulate a case study is significantly large. In such situations, a simplified and accurate model of a PV system may be useful to perform the simulation studies faster. Hence, in Chapter 6 of this Thesis, a simplified model of a PV system was developed by analysing the terminal characteristics of the detailed model of a PV system. Comparison of the simulation results obtained from the detailed simulation model and the simplified simulation model of a PV system confirm that the developed simplified simulation model of a PV system accurately represent the terminal characteristics of a PV system. A simulation study can be performed 15 times faster if the simplified model of a PV system is used. Therefore, the simplified model of a PV system can be used to perform system level simulation studies of LV electricity networks integrated with multiple PV systems providing reasonably accurate results within a short period of time.

Active and reactive power sharing methodology for multiple PV systems integrated to a radial distribution feeder

A power control and coordination methodology for PV systems that are integrated to a radial distribution feeder was proposed in this research. Such control and coordination methodologies are essential in future LV electricity networks in order to minimise any adverse impact with integration of multiple PV sys-

tems. The developed methodology determines a voltage bandwidth for each PV system to operate. The allocated voltage bandwidth of each PV system is proportional to the voltage sensitivity at the PCC of the PV system. The determined voltage bandwidth of each PV system ensures equal power sharing between PV systems if power curtailing is necessary to keep the operation of the PV system within the voltage bandwidth. Thereby, disadvantages associated with the voltage sensitivity at the point of connection of the PV system that an owner of a grid-integrated PV system may experience are minimised. In the developed power sharing method, the allocated bandwidth for each PV system is a function of the number of PV systems integrated to the distribution feeder. Since PV systems are being continuously integrated, the allocated bandwidth for each PV system should be altered when an additional PV system is integrated to the feeder. Further, experimental results have revealed that the developed power sharing methodology is sensitive to errors in voltage measurement systems in PV systems. Therefore, in order to minimise such practical difficulties the work presented in the current research should be further improved.

8.2 Recommendations for Future Work

The work presented in this Thesis can be extended by carrying out further research studies. The following is a description of further activities that can be undertaken in relation to LV electricity networks integrated with multiple PV systems;

- **Development of a detailed model of a PV system integrated to the grid via voltage-controlled VSC**

  The research work presented in this Thesis is based on PV systems that are interfaced to the grid via current-controlled VSCs. Such control methodologies are used in most of modern PV systems. The voltage-controlled VSCs that were used to integrate PV systems previously are an old tech-

nology and those converter control systems are no longer used in more modern systems. However, there can be substantial numbers of PV systems installed earlier that are integrated to the grid via voltage-controlled VSCs. Therefore, the development of a detailed model of a PV system integrated to the grid via a voltage-controlled VSC is beneficial in order to identify the terminal characteristics of such a PV system and to perform realistic system level simulation studies in LV electricity networks to which multiple PV systems are integrated via both voltage and current controlled VSCs.

- **System level studies on PV systems integrated to three-phase four wire power distribution systems**

  The bulk of the research work presented in this Thesis was focused on PV systems connected to single-phase power distribution feeders. However, the voltage control techniques and advanced operating and coordination strategies developed in this Thesis can be applied to PV systems integrated to three-phase, four-wire power distribution systems that are common in Australia. The robustness and the effectiveness of the voltage control techniques and advanced operating and coordination strategies developed in this Thesis can be evaluated by carrying out simulation studies on PV systems integrated to three-phase four wire systems.

- **Integration of battery storage systems to grid-connected PV systems**

  In the current research, advanced control systems were developed to dynamically regulate the PCC voltage of a PV system by curtailing active power of a grid-connected PV system at times that is needed. If a PV system is integrated with a battery storage system such power curtailing may not be necessary in certain situations. With the development of advanced, economical and safe battery technologies, PV systems are likely to

be integrated with a battery storage systems in the future. Therefore, the development of advanced control techniques to control PCC voltage of a PV system integrated with a battery storage is beneficial.

- **Further development of the control and coordination strategies**

  The power sharing methodology developed in this Thesis was able to enhance the integration of multiple PV systems to LV electricity networks. However, experimental results presented in this Thesis confirm that the developed power sharing methodology is sensitive to errors in the voltage measurement systems in a PV system. Therefore, further research work can be carried out to enhance the practical application and to improve the accuracy of the power sharing methodology developed in this Thesis by using accurately calibrated voltage sensors to measure PCC voltages of PV systems.

  A PV system is able to determine the grid impedance seen at the PCC of the PV system if grid impedance measurement algorithms are integrated to the PV system. In such PV systems, reference PCC voltages can be determined by the controller of the PV systems with reference to a preset maximum grid impedance. If a communication medium exists between PV systems in a power distribution feeder, that link can be used to help identify the maximum grid impedance that a PV system measured by the grid impedance measurement algorithm. In such situations, the highest grid impedance measured by a PV system in a power distribution feeder can be utilised to determine reference PCC voltages and such technique will lead to accurate results in the developed power sharing methodology when practically implemented. The above mentioned possibilities of improving the power sharing methodology proposed in this Thesis can be validated analytically and experimentally.

- **Field experiments to further validate the outcomes of this thesis**

  In this research, an extensive and rigorous experimental program has been carried out to validate the robustness of the developed advanced control and coordination methodologies and accuracy of the analytical tools developed. The experiments were carried out in a laboratory under controlled conditions. In an actual PV installation there may be operating conditions that are different to test conditions simulated at the laboratory. Therefore, by carrying out field experiments, the outcomes of this Thesis can be further validated.

References

[1] A. Labouret and M. Villoz. *Solar Photovoltaic Energy.* IET, 2010.

[2] H. Haberlin. *Photovoltaics: system design and practice.* Wiley, 2012.

[3] T. Esram and P.L. Chapman. Comparison of photovoltaic array maximum power point tracking techniques. *IEEE Trans. Energy Convers.*, 22(2):439–449, June 2007.

[4] K.H. Hussein, I. Muta, T. Hoshino, and M. Osakada. Maximum photovoltaic power tracking: an algorithm for rapidly changing atmospheric conditions. *Proc. IEE Generation, Transmission and Distribution*, 142(1):59–64, January 1995.

[5] S. B. Kjaer, J. K. Pedersen, and F. Blaabjerg. A review of single-phase grid-connected inverters for photovoltaic modules. *IEEE Trans. Ind. Appl.*, 41(5):1292–1306, September/October 2005.

[6] AS4777.1: Grid Connection of Energy Systems via Inverters - part 1: installation requirements. Technical report, Australian Standards, 2005.

[7] AS4777.2: Grid Connection of Energy Systems via Inverters - part 2: inverter requirements. Technical report, Australian Standards, 2005.

[8] AS4777.3: Grid Connection of Energy Systems via Inverters - part 3: grid protection requirements. Technical report, Australian Standards, 2005.

[9] IEEE STD 929-2000: IEEE Recommended Practice for Utility Interface of Photovoltaic (PV) Systems. Technical report, IEEE, 2000.

[10] IEEE STD 1547-2003: IEEE Standard for Interconnecting Distributed Resources with Electric Power Systems. Technical report, IEEE, 2003.

[11] T. Kerekes, R. Teodorescu, and U. Borup. Transformerless photovoltaic inverters connected to the grid. In *Proc. 22nd Annu. IEEE Applied Power Electronics Conf. (APEC)*, February 2007.

[12] H. Haeberlin. Evolution of inverters for grid connected pv-systems from 1989 to 2000. In *Proc. 17th European Photovoltaic Solar Energy Conf.*, October 2001.

[13] Amirnaser Yazdani and Reza Iravani. *Voltage-Sourced Converters in Power Systems*. Wiley/IEEE, 2010.

[14] N. G. Hingorani and L Gyugyi. *Understanding FACTS*. Wiley-IEEE Press, Piscataway, NJ, 2000.

[15] R. Zhang, M. Cardinal, P. Szczesny, and M. Dame. A grid simulator with control of single-phase power converters in D-Q rotating frame. In *Proc. 33rd Annu. IEEE Power Electronics Specialists Conf. PESC'02*, June 2002.

[16] A Roshan, R. Burgos, AC. Baisden, F. Wang, and D. Boroyevich. A D-Q frame controller for a full-bridge single phase inverter used in small distributed power generation systems. In *Proc. 22nd Annu. IEEE Applied Power Electronics Conf., APEC 2007*, February 2007.

[17] G. Franceschini, E. Lorenzani, C. Tassoni, and A Bellini. Synchronous reference frame grid current control for single-phase photovoltaic converters. In *Proc. IEEE Industry Applications Society Annu. Meeting, IAS'08*, October 2008.

[18] U. A Miranda, L. G B Rolim, and M. Aredes. A DQ synchronous reference frame current control for single-phase converters. In *Proc. 36th IEEE Power Electronics Specialists Conf., PESC'05*, June 2005.

[19] B. Crowhurst, E.F. El-Saadany, L. El Chaar, and L.A Lamont. Single-phase grid-tie inverter control using DQ transform for active and reactive load power compensation. In *Proc. IEEE Int. Conf. Power and Energy (PECon)*, November 2010.

[20] D.N. Zmood and D.G. Holmes. Stationary frame current regulation of PWM inverters with zero steady-state error. *IEEE Trans. Power Electron.*, 18(3):814–822, May 2003.

[21] D. Yazdani, M. Pahlevaninezhad, and A. Bakhshai. Single-phase grid-synchronization algorithms for converter interfaced distributed generation systems. In *Proc. Canadian Conf. on Electrical and Computer Engineering CCECE'09*, May 2009.

[22] J.H.R. Enslin and P.J.M. Heskes. Harmonic interaction between a large number of distributed power inverters and the distribution network. *IEEE Trans. Power Electron.*, 19(6):1586–1593, November 2004.

[23] S.A.O. da Silva, L.B.G. Campanhol, A. Goedtel, C.F. Nascimento, and D. Paiao. A comparative analysis of p-PLL algorithms for single-phase utility connected systems. In *Proc. 13th Europian Conf. on Power Electronics and Applications EPE'09*, September 2009.

[24] Australian Energy Market Operator (AEMO). Rooftop PV information paper. In *www.aemo.com.au*, June 2012.

[25] B. Kroposki et al. Benefits of power electronic interfaces for distributed energy systems. *IEEE Trans. Energy Convers.*, 25(3):901–908, September 2010.

[26] E. Caamaño et al. State-of-the-art on dispersed PV power generation: impact of PV distributed generation and electricity networks, July 2007.

[27] L. Freris and D. Infield. *Renewable Energy in Power Systems.* Wiley, 2008.

[28] E. Caamanõ-Martín et al. Interaction between photovoltaic distributed generation and electricity networks. *Progress in Photovoltaics: Research and Applications*, 16(7):629–643, August 2008.

[29] M. Liserre, R. Teodorescu, and F. Blaabjerg. Stability of photovoltaic and wind turbine grid-connected inverters for a large set of grid impedance values. *IEEE Trans. Power Electron.*, 21(1):263 –272, January 2006.

[30] J. Puukko, T. Messo, and T. Suntio. Effect of photovoltaic generator on a typical VSI-based three-phase grid-connected photovoltaic inverter dynamics. In *Proc. IET Conf. on Renewable Power Generation RPG'11*, September 2011.

[31] M.G. Molina and P.E. Mercado. Modeling and control of grid-connected photovoltaic energy conversion system used as a dispersed generator. In *Proc. IEEE/PES Transmission and Distribution Conf. and Exposition*, August 2008.

[32] M. Ciobotaru, T. Kerekes, R. Teodorescu, and A. Bouscayrol. PV inverter simulation using MATLAB/Simulink graphical environment and PLECS blockset. In *Proc. 32nd Annu. IEEE Conf. on Industrial Electronics, IECON'06*, November 2006.

[33] T. Stetz, W. Yan, and M. Braun. Voltage control in distribution systems with high level PV penetration - improving absorption capacity for PV systems by reactive power supply. In *Proc. 25th European Photovoltaic Solar Energy Conf. and Exhibition*, September 2010.

[34] E. Demirok et al. Local reactive power control methods for overvoltage prevention of distributed solar inverters in low-voltage grids. *IEEE Trans. Photovoltaics*, 1(2):174–182, October 2011.

[35] T. Stetz, F. Marten, and M. Braun. Improved low voltage grid-integration of photovoltaic systems in Germany. 4(2):534–542, April 2013.

[36] E Liu and J. Bebic. NREL/SR-581-42298: Distribution System Voltage Performance Analysis for High-Penetration Photovoltaics. Technical report, Ge Global Research,New York, February 2008.

[37] T. Kerekes, M. Liserre, R. Teodorescu, C. Klumpner, and M. Sumner. Evaluation of three-phase transformerless photovoltaic inverter topologies. *IEEE Trans. Power Electron.*, 24(9):2202–2211, September 2009.

[38] Y. Xu, D. T. Rizy, F. Li, and J. D. Kueck. Dynamic voltage regulation using distributed energy resources. In *Proc. CIRED 19th Int. Conf. on Electricity Distribution*, May 2007.

[39] H. Yu, J. Pan, and A. Xiang. A multi-function grid-connected PV system with reactive power compensation for the grid. In *Proc. Energy Conversion Congress and Exposition (ECCE'09)*, July 2005.

[40] H. Yu, J. Pan, and A. Xiang. A multi-function grid-connected PV system with reactive power compensation for the grid. *Proc. Solar Energy*, 79(1):101–106, July 2005.

[41] H. Seo et al. Harmonics and reactive power compensation method by grid-connected photovoltaic generation system. In *Proc. Int. Conf. on Electrical Machines and Systems (ICEMS 2009)*, November 2009.

[42] G. Kerber, R. Witzmann, and H. Sappl. Voltage limitation by autonomous reactive power control of grid connected photovoltaic inverters. In *Proc. Compatibility and Power Electronics (CPE '09)*, 2009.

[43] E. Demirok, D. Sera, P. Rodriguez, and R. Teodorescu. Enhanced local grid voltage support method for high penetration of distributed generators. In *Proc. 37th Annual Conf. of the IEEE Industrial Electronics Society (IECON'11)*, 2011.

[44] E. Demirok, D. Sera, R. Teodorescu, P. Rodriguez, and U. Borup. Evaluation of the voltage support strategies for the low voltage grid connected PV generators. In *Proc. IEEE Energy Conversion Congress and Exposition (ECCE)*, September 2010.

[45] R. Tonkoski, L. A. C. Lopes, and T. H. M. El-Fouly. Coordinated active power curtailment of grid connected PV inverters for overvoltage prevention. 2(2):139–147, April 2011.

[46] F. Magueed and H. Awad. Voltage compensation in weak grids using distributed generation with voltage source converter as a front end. In *Proc. Int. Conf. on Power Electronics and Drives Systems*, 2005.

[47] E. Twining and D. G. Holmes. Voltage compensation in weak distribution networks using multiple shunt connected voltage source inverters. In *Proc. IEEE Power Tech Conf.*, June 2003.

[48] B. Singh, P. Jayaprakash, and D.P. Kothari. Three single-phase voltage source converter based three-phase four wire DSTATCOM. In *Proc. Int. Conf. on Power Systems*, December 2009.

[49] R. K. Varma, E. M. Siavashi, B. Das, and V. Sharma. Novel application of a PV solar plant as STATCOM (PV-STATCOM) during night and day in a distribution utility network: Part 2. In *Proc. IEEE PES Transmission and Distribution Conf. and Exposition (T&D)*, May 2012.

[50] L. Cai and I. Erlich. Simultaneous coordinated tuning of PSS and FACTS damping controllers in large power systems. *IEEE Trans. Power Syst.*, 20(1):294–300, February 2005.

[51] H. J. Kim et al. Dynamic interactions among multiple FACTS controllers - a survey. In *Proc. IEEE Power and Energy Society General Meeting*, pages 1–8, July 2011.

[52] L. A. S. Pilotto et al. Analysis of control interactions on FACTS-assisted power systems, January 1998.

[53] S. Kincic, B. T. Ooi, D. Mcgillis, and A. Chandra. Voltage support of radial transmission lines by var compensation at distribution buses. *IEE Gener., Transm. and Distrib*, 153(1):51–58, January 2006.

[54] N. Mithulananthan, C.A. Canizares, and J. Reeve. Tuning, performance and interactions of PSS and FACTS controllers. In *Proc. IEEE Power Engineering Society Summer Meeting*, volume 2, pages 981–987, July 2002.

[55] L.B. Perera, G. Ledwich, and A. Ghosh. Multiple distribution static synchronous compensators for distribution feeder voltage support. *IET Gener., Transm. and Distrib*, 6(4):285–293, April 2012.

[56] A. Samadi, M. Ghandhari, and L. Soder. Reactive power dynamic assessment of a PV system in a distribution grid. *Energy Procedia*, 20:98–107, June 2012.

[57] A.D. Rajapakse and D. Muthumuni. Simulation tools for photovoltaic system grid integration studies. In *Proc. IEEE Electrical Power Energy Conf. EPEC'09*, October 2009.

[58] M. H. Rashid. *Power Electronics*. Prentice Hall, Upper Saddle River, NJ, third edition, 2004.

[59] M. Liserre, F. Blaabjerg, and S. Hansen. Design and control of an LCL-filter-based three-phase active rectifier. *IEEE Trans. Ind. Appl.*, 41(5):1281–1291, Sep.-Oct. 2005.

[60] M. Liserre, A. Dell'Aquila, and F. Blaabjerg. Stability improvements of an LCL-filter based three-phase active rectifier. In *Proc. 33rd Annu. IEEE Power Electronics Specialists Conf. PESC'02*, volume 3, 2002.

[61] F. Gao et al. Indirect DC-link voltage control of two-stage single-phase PV inverter. In *Proc. IEEE Energy Conversion Congress and Exposition ECCE'09*, September 2009.

[62] TR 60725: Electromagnetic Compatibility (EMC) - consideration of reference impedance and public supply network impedances for use in determining disturbances characteristics of electrical equipment having a rated current ≤ 75 A per phase. Technical report, IEC, June 2012.

[63] M. E. Van Valkenburg. *Analog Filter Design*. CBS College, 1982.

[64] R. Teodorescu, F. Blaabjerg, M. Liserre, and P.C. Loh. Proportional-resonant controllers and filters for grid-connected voltage-source converters. *Proc. IEE Electric Power Applications*, 153(5):750–762, September 2006.

[65] K. De Brabandere et al. A voltage and frequency droop control method for parallel inverters. *IEEE Trans. Power Electron.*, 22(4):1107–1115, July 2007.

[66] R.A. Mastromauro et al. Droop control of a multifunctional PV inverter. In *Proc. IEEE Int. Symp. Industrial Electronics*, July 2008.

[67] P. Kundur. *Power System Stability and Control*. McGraw-Hill, New York, 1994.

[68] F. Jenni and D. Wüest. *Steuerverfahren für selbstgeführte Stromrichter*. ETH University Zurich, 1995.

[69] D.G. Holmes and T. Lipo. *Pulse Width Modulation for Power Converters: Principles and Practice*. IEEE, 2003.

[70] T. Kerekes, R. Teodorescu, P. Rodriguez, G. Vazquez, and E. Aldabas. A new high-efficiency single-phase transformerless PV inverter topology. *IEEE Trans. Ind. Electron.*, 58(1):184–191, January 2011.

Appendix A

LCL Filter

A.1 Basic Equations of the LCL filter

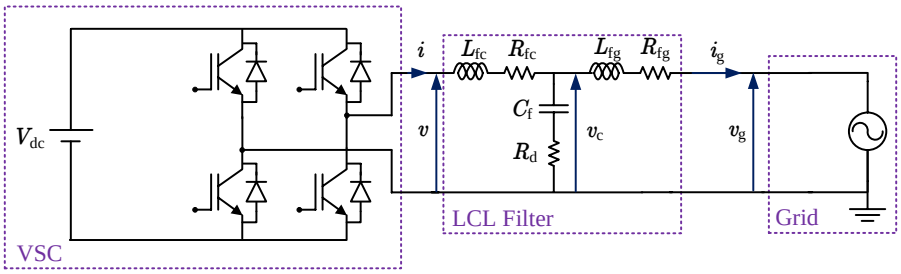

Figure A.1: A single-phase grid-connected VSC with an LCL filter

A single-phase grid-connected VSC that is interfaced to the grid via an LCL filter is shown in Fig. A.1. The VSC consists of a full-bridge inverter and a unipolar PWM technique is used for switching the VSC. Further, the DC-link of the VSC is connected to a constant DC voltage source, V_{dc}. The grid impedance is assumed to be zero. In the figure, L_{fc} and L_{fg} represent the inductances of the converter side and the grid side inductors respectively. R_{fc} and R_{fg} represent the resistance of each inductor. The damping resistor, R_d, is connected in series with the capacitor C_f. Voltages v, v_c and v_g are the voltage at the output of the VSC, the voltage across C_f and R_d and the grid voltage respectively. Currents i and i_g are the output current of the VSC and the current injected to the grid by the VSC respectively.

The harmonic model of the LCL filter shown in Fig. A.1 is given in Fig. A.2. In the figure, "nh" indicates a harmonic number. If the grid voltage is assumed as a pure sinusoid at fundamental frequency, f, the grid voltage appears as a short circuit for all the harmonic voltages created by the VSC. Under such conditions, (A.1) can be derived from Fig. A.2.

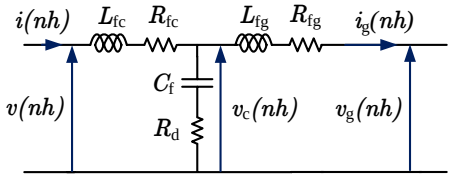

Figure A.2: Harmonic model of the LCL filter

$$G_{\mathrm{LCL}}(s) = \frac{i_{\mathrm{g}}(s)}{v(s)} = \frac{R_{\mathrm{d}}C_{\mathrm{f}}s + 1}{As^3 + Bs^2 + Cs + D} \tag{A.1}$$

where,

$$A = L_{\mathrm{fc}}L_{\mathrm{fg}}C_{\mathrm{f}}$$

$$B = (L_{\mathrm{fc}}R_{\mathrm{fg}} + L_{\mathrm{fg}}R_{\mathrm{fc}} + (L_{\mathrm{fc}} + L_{\mathrm{fg}})R_{\mathrm{d}})C_{\mathrm{f}}$$

$$C = (R_{\mathrm{fg}}R_{\mathrm{fc}} + R_{\mathrm{fc}}R_{\mathrm{d}} + R_{\mathrm{fg}}R_{\mathrm{d}})C_{\mathrm{f}} + L_{\mathrm{fc}} + L_{\mathrm{fg}}$$

$$D = R_{\mathrm{fc}} + R_{\mathrm{fg}}$$

If the resistance of each inductor is neglected;

$$G_{\mathrm{LCL}}(s) = \frac{i_{\mathrm{g}}(s)}{v(s)} = \frac{1 + R_{\mathrm{d}}C_{\mathrm{f}}s}{s[L_{\mathrm{fc}}L_{\mathrm{fg}}C_{\mathrm{f}}s^2 + R_{\mathrm{d}}C_{\mathrm{f}}(L_{\mathrm{fc}} + L_{\mathrm{fg}})s + L_{\mathrm{fc}} + L_{\mathrm{fg}}]} \tag{A.2}$$

Further, if the damping resistor is neglected;

$$G_{\mathrm{LCL}}(s) = \frac{i_{\mathrm{g}}(s)}{v(s)} = \frac{1}{s(L_{\mathrm{fc}}L_{\mathrm{fg}}C_{\mathrm{f}}s^2 + L_{\mathrm{fc}} + L_{\mathrm{fg}})} \tag{A.3}$$

Equation (A.3) can be presented as follows,

$$\frac{i_{\mathrm{g}}(s)}{v(s)} = \frac{Z_{\mathrm{LC}}^2}{sL_{\mathrm{fc}}(s^2 + \omega_{\mathrm{res}}^2)} \tag{A.4}$$

where $Z_{\mathrm{LC}}^2 = 1/L_{\mathrm{fg}}C_{\mathrm{f}}$ and $\omega_{\mathrm{res}}^2 = (L_{\mathrm{fc}} + L_{\mathrm{fg}})/L_{\mathrm{fc}}L_{\mathrm{fg}}C_{\mathrm{f}}$.

Switching frequency (f_{sw}) current harmonics are dominant in the output current of the VSC. Therefore, the LCL filter design procedure will follow to reduce the switching ripple current that flows to the grid. The switching ripple current attenuation by the LCL filter at any frequency can be derived in two ways. First, it is derived assuming that the filter capacitance has very small impedance at high frequencies. Therefore the capacitor branch can be considered as short circuited. Hence, with that assumption, the following relationship between the converter side current and voltage can be derived.

$$\frac{i(s)}{v(s)} \approx \frac{1}{sL_{\mathrm{fc}}} \tag{A.5}$$

From (A.4) and (A.5);

$$\frac{i_{\mathrm{g}}(s)}{i(s)} \approx \frac{Z_{\mathrm{LC}}^2}{(s^2 + \omega_{\mathrm{res}}^2)} \tag{A.6}$$

As the second method, the transfer function for the switching ripple current attenuation can be derived as given in (A.7) without the assumption used to derive (A.6) and considering that the grid voltage appears as short circuited for harmonics.

$$\frac{i_{\mathrm{g}}(s)}{i(s)} = \frac{Z_{\mathrm{LC}}^2}{(s^2 + Z_{\mathrm{LC}}^2)} \tag{A.7}$$

The assumption made to derive (A.6) is for the purpose of developing a relationship between $L_{\mathrm{fc}}, L_{\mathrm{fg}}$ and C_{f} for frequencies higher than the switching frequency of the VSC, f_{sw}. The assumption will be justified while analysing the performance of a designed LCL filter.

Defining base quantities for the VSC system;

$$Z_{\mathrm{b}} = \frac{V_{\mathrm{r}}^2}{P_{\mathrm{r}}} \tag{A.8}$$

$$C_{\mathrm{b}} = \frac{1}{\omega Z_{\mathrm{b}}} \tag{A.9}$$

A.2 Design constraints of LCL filter component sizes

1. The capacitance of C_{f} is limited by the amount of reactive power absorbed by the capacitor (generally less than $0.05P_{\mathrm{r}}$).

2. To limit the AC voltage drop during operation, the total value of inductive reactance, (ωL_{fc}+ωL_{fg}) should be less than 0.1 pu at fundamental frequency.

3. The resonant frequency should be in the range $10f < f_{\mathrm{res}} < \frac{1}{2}f_{\mathrm{sw}}$ to avoid resonance problems. f_{res} is the resonant frequency of the LCL filter.

4. The damping resistor, R_{d} should be large enough to provide sufficient damping at the resonant frequency of the LCL filter but losses cannot be very high.

A.3 Design procedure of an LCL filter

1. Determine the switching current ripple through the converter side inductor and establish the inductance of L_{fc}. Then the grid side inductor of the LCL filter, L_{fg} can be expressed as a function of L_{fc}, using an index, r.

$$L_{\mathrm{fg}} = rL_{\mathrm{fc}} \tag{A.10}$$

2. If x is the percentage of reactive power absorbed under rated condition as mentioned in Constraint 1, the maximum capacitance of C_{f} can be calculated as follows.

$$C_{\mathrm{f}} = xC_{\mathrm{b}} \tag{A.11}$$

3. Equation (A.6) can be rearranged as (A.12) where $a = LC_{\mathrm{b}}\omega_{\mathrm{sw}}^2$. A value for r can be calculated using (A.12) for a given switching ripple current

attenuation. Before using (A.12) to calculate r, the desired switching ripple current attenuation should be multiplied by a factor to account for losses and damping.

$$\left|\frac{i_{\mathrm{g}}}{i}\right| = \frac{1}{|1 + r(1 - ax)|} \tag{A.12}$$

After obtaining a value for r, L_{fg} can be determined from (A.10). If the total inductance of the LCL filter does not respect Constraint 2, a different level of switching ripple current attenuation or a different value for x should be selected.

4. Verify the resonant frequency of the LCL filter using (A.13) where ω_{res} is the resonant frequency of the LCL filter and $\omega_{\mathrm{res}} = 2\pi f_{\mathrm{res}}$.

$$\omega_{\mathrm{res}} = \sqrt{\frac{L_{\mathrm{fc}} + L_{\mathrm{fg}}}{L_{\mathrm{fc}} L_{\mathrm{fg}} C_{\mathrm{f}}}} \tag{A.13}$$

If the calculated ω_{res} is not within the range as per Constraint 3, either x or the attenuation level of the switching ripple current should be changed.

5. The resistance of R_{d} should be chosen to be a similar order of magnitude as the impedance of C_{f} at f_{res}. Then verify the switching current ripple attenuation by the LCL filter. If the attenuation is not adequate, the design should return to step 2 or to step 3.

A.4 LCL filter designing for a 5.4 kVA single-phase VSC

The necessary details of the 5.4 kVA single-phase VSC system that are required to design the LCL filter are given in Table A.1. In Table A.1, P_{r} and V_{r} are the rated active power capacity and the rated voltage of the VSC respectively. As per the specification given in Table A.1, base values can be calculated as $Z_{\mathrm{b}} = 9.8\ \Omega$ and $C_{\mathrm{b}} = 325\ \mu F$ by using (A.8) and (A.9) respectively.

The inductance of L_{fc} to limit the peak switching ripple current, Δi_{p} through L_{fc} to a given value can be obtained from (A.14) [68], [69]. Equation (A.14) is valid only if the VSC is modulated with sinusoidal unipolar PWM and the modulation index, m is $0.5 < m < 1$.

Table A.1: Specifications of the VSC

Parameter	**Value**
P_{r}	5.4 kW
V_{r}	230 V
V_{dc}	400 V
f	50 Hz
f_{sw}	25 kHz

$$L_{\mathrm{fc}} = \frac{V_{\mathrm{dc}}}{16\Delta i_{\mathrm{p}} f_{\mathrm{sw}}} \tag{A.14}$$

In order to attenuate the switching ripple current of the output current of the VSC to 10% of the rated peak current of the VSC, L_{fc} can be calculated as 300 μH using (A.14).

According to Constraint 1 given in Section A.2, $C_{\mathrm{f}} < 16.25\mu$F. Fig. A.3 is a plot of (A.12) when switching current ripple attenuation is 20%. The plot shows variation of r which is the ratio between L_{fg} and L_{fc}, against C_{f}. From the graph, the rate of change of r is not significant when $C_{\mathrm{f}} > 2$ μF. This means that although the capacitance of C_{f} can be increased beyond 2 μF, there will not be much reduction in the size of L_{fg} that can be achieved. Therefore, the value of r when $C_{\mathrm{f}} = 2$ μF is selected for designing the filter. Therefore, from (A.10), $L_{\mathrm{fg}} = 150$ μH.

The resonant frequency of the LCL filter, f_{ref} is 10.7 kHz and the total inductance of the LCL filter is 0.015 pu if $L_{\mathrm{fc}} = 300$ μH, $L_{\mathrm{fg}} = 150$ μH and $C_{\mathrm{f}} = 2$ μF. Hence constraints 2 and 3 are satisfied. The damping resistor, R_{d} is chosen as one third of the impedance of the filter capacitor at 25 kHz.

The designed LCL filter parameters are given in Table A.2.

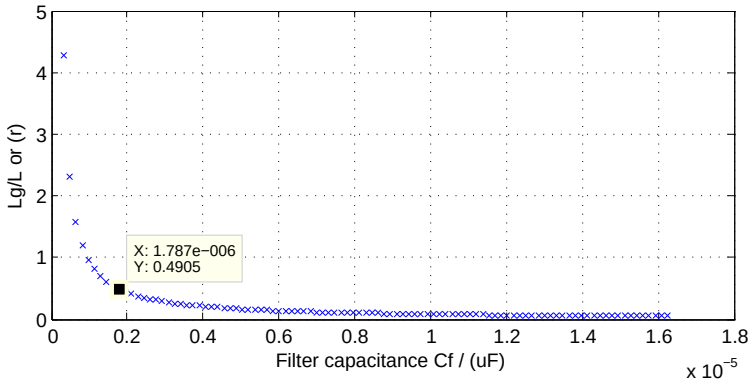

Figure A.3: Variation of r with C_{f} for switching ripple attenuation of 20%

Table A.2: Design parameters of the LCL filter

Parameter	**Value**
L_{fc}	300 μH
L_{fg}	150 μH
C_{f}	2.2 μF
f_{res}	10.7 kHz
$L_{\mathrm{fc}} + L_{\mathrm{fg}}$	0.015 pu

A.5 Analysis of the designed LCL filter

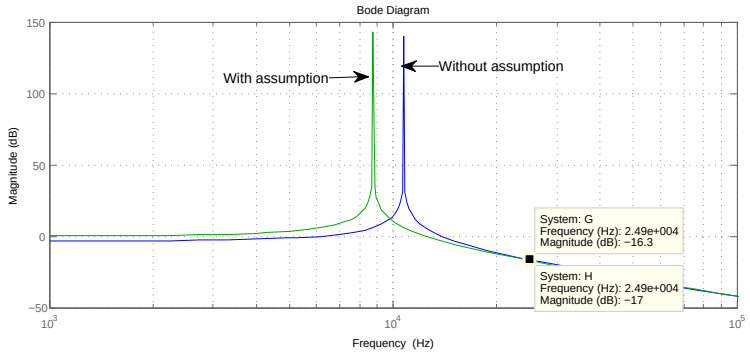

Figure A.4: Switching ripple current attenuation of the LCL filter

The amount of grid side ripple current attenuation with respect to converter side ripple current can be determined by the frequency response of both (A.6) and (A.7). The frequency response of (A.6) and (A.7) are shown in Fig. A.4. The switching ripple current attenuation after f_{res} which is 10.7 kHz is almost the same for both transfer functions. Therefore the assumption made to derive (A.6) can be justified for frequencies above f_{sw}. The switching ripple current

attenuation at f_{sw}, which is determined from two plots in Fig. A.4, is less than 20%. Hence the designed LCL filter parameters given in Table A.2 satisfy the design requirements.

Appendix B

Analysis of the closed-loop current controller of a VSC with an LCL filter

B.1 Simplification of the LCL to an L filter at low frequencies

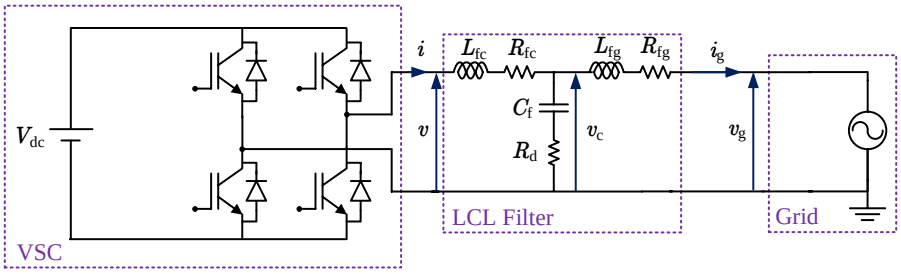

Figure B.1: LCL filter of a single-phase grid-connected VSC

An LCL filter of a single-phase grid-connected VSC is shown in Fig B.1. Equation (A.1) that is derived in Appendix A and that is restated as (B.1) becomes the transfer function of the LCL filter when the closed-loop current controller of a single-phase grid-connected VSC that is interfaced to the grid via an LCL filter is considered. In (B.1), L_{fc} and L_{fg} are the inductances of the converter side and the grid side inductors of the LCL filter respectively. R_{fc} and R_{fg} are the

resistances of inductors of the LCL filter. The damping resistor is R_{d} and that is connected in series with the filter capacitor, C_{f}. v is the voltage at the output of the VSC and i_{g} is the current injected to the grid by the VSC.

$$G_{\mathrm{LCL}}(s) = \frac{i_{\mathrm{g}}(s)}{v(s)} = \frac{R_{\mathrm{d}}C_{\mathrm{f}}s + 1}{As^3 + Bs^2 + Cs + D} \tag{B.1}$$

where,

$$A = L_{\mathrm{fc}}L_{\mathrm{fg}}C_{\mathrm{f}}$$

$$B = (L_{\mathrm{fc}}R_{\mathrm{fg}} + L_{\mathrm{fg}}R_{\mathrm{fc}} + (L_{\mathrm{fc}} + L_{\mathrm{fg}})R_{\mathrm{d}})C_{\mathrm{f}}$$

$$C = (R_{\mathrm{fc}}R_{\mathrm{fg}} + R_{\mathrm{fc}}R_{\mathrm{d}} + R_{\mathrm{fg}}R_{\mathrm{d}})C_{\mathrm{f}} + L_{\mathrm{fc}} + L_{\mathrm{fg}}$$

$$D = R_{\mathrm{fc}} + R_{\mathrm{fg}}.$$

The transfer function an L only filter can be obtained from (B.1) if $C_{\mathrm{f}} = 0$ and that is given in (B.2).

$$G_{\mathrm{L}}(s) = \frac{i_{\mathrm{g}}(s)}{v(s)} = \frac{1}{(L_{\mathrm{fc}} + L_{\mathrm{fg}})s + R_{\mathrm{fc}} + R_{\mathrm{fg}}} \tag{B.2}$$

The frequency responses of (B.1) and (B.2) are shown in Fig. B.2 when R_{fc}, R_{fg}, and R_{d} are assumed to have negligible resistances. The frequency responses of both the LCL filter and the L filter below the resonant frequency of the LCL filter is almost similar as that can be seen in the Fig B.2. Both types of filters attenuate signals of frequencies less than the resonant frequency by -20 dB/decade. If the desired bandwidth of the closed-loop current controller of the VSC is 500 Hz that is far less than the resonant frequency of the LCL filter. Hence, the LCL filter can be simplified to an L filter while designing the closed-loop current controller.

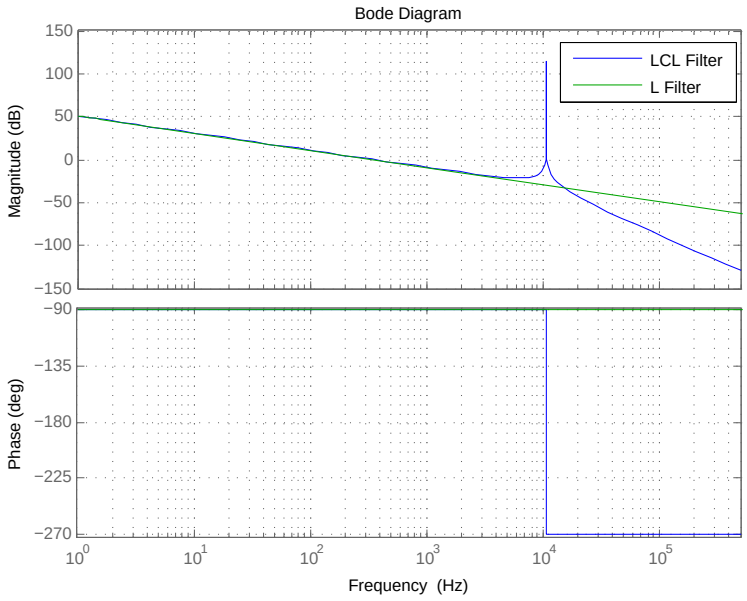

Figure B.2: Frequency responses of an LCL and an L filter

B.2 Effect of the damping resistor in the LCL filter on the dynamic stability of the closed-loop current controller of the VSC

A simplified block diagram of the closed-loop current controller of the VSC is shown in Fig. B.3. In Fig. B.3, $G_{\mathrm{LCL}}(s)$ is the transfer function of the LCL filter that is given in (B.1) and $C(s)$ is a proportional resonant (PR) regulator. The transfer function of the PR regulator that includes both fundamental frequency compensator and low-order odd harmonic compensators (HC), is given in (B.3) where k_{pc} is the proportional gain, k_{ich} is the integral gain and ω_c is the 3 dB cut-off frequency and $\omega_0 = 100\pi$ rad/s.

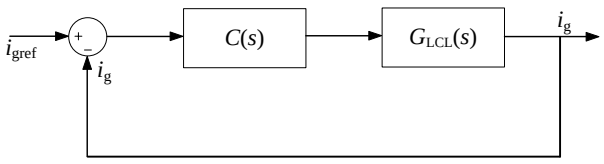

Figure B.3: Simplified block diagram of the closed-loop current controller

$$C(s) = k_{\mathrm{pc}} + \sum_{h=1,3,5,7} \frac{2k_{\mathrm{ich}}\omega_c s}{s^2 + 2\omega_c s + (h\omega_0)^2} \tag{B.3}$$

The open-loop and closed-loop transfer functions of the current controller shown in Fig B.3 are given in (B.4) and (B.5) respectively.

$$G_{\mathrm{ol}}(s) = C(s)G_{\mathrm{LCL}}(s) \tag{B.4}$$

$$G_{\mathrm{cl}}(s) = \frac{C(s)G_{\mathrm{LCL}}(s)}{1 + C(s)G_{\mathrm{LCL}}(s)} \tag{B.5}$$

In the LCL filter shown in Fig B.1, $L_{\mathrm{fc}} = 300\ \mu\mathrm{H}$, $L_{\mathrm{fg}} = 150\ \mu\mathrm{H}$, $C_{\mathrm{f}} = 2.2\ \mu\mathrm{F}$ and $R_{\mathrm{fc}}, R_{\mathrm{fg}} = 0.001\ \Omega$. In the PR regulator that is given in (B.3), $k_{\mathrm{pc}} = 4$, $k_{\mathrm{ic1}} = 100$, $k_{\mathrm{ich}} = 80$ $(h = 3, 5, 7)$ and the 3 dB cut-off frequency, ω_c, is 5 rad/s.

The pole and zero plot of (B.4) is shown in Fig. B.4 when $R_{\mathrm{d}} = 0$. R_{fc} and R_{fc}, which are the resistances of inductors in the LCL filter, are assumed to have negligible values when plotting Fig. B.4.

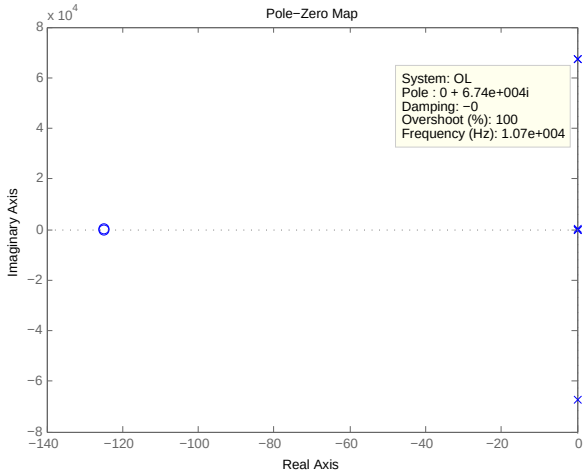

Figure B.4: Pole and zero plot of open-loop system without damping

In Fig. B.4, there are two poles on the imaginary axis that are further away from the origin. Hence the closed-loop current controller is unstable when $R_{\mathrm{d}} = 0\ \Omega$. These unstable poles are the resonant poles of the LCL filter.

The stability of the closed-loop current controller can be improved by adding a damping resistor, R_{d} in series with the LCL filter capacitor C_{f} [60]. The addition of the damping resistor, R_{d} creates an additional zero while attracting unstable poles towards negative side of the imaginary axis in the complex plane and hence

improve the stability of the closed-loop current controller.

The positions of poles and zeros of the open-loop system after adding the damping resistor, R_{d}, in series with the filter capacitor, C_{f}, is shown in Fig. B.5 for a range of values of R_{d}. As shown in Fig. B.5, the unstable poles of the open-loop system have moved to the left hand side of the imaginary axis in the complex plan. Hence the stability of the closed-loop current controller is improved with addition of R_{d}.

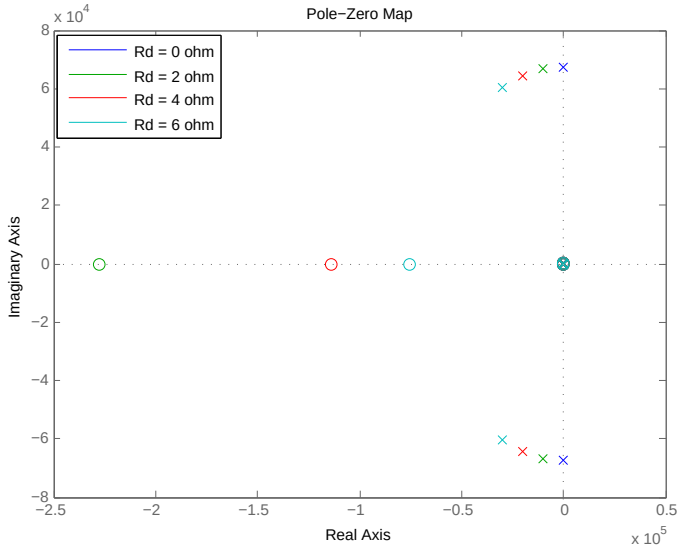

Figure B.5: Pole and zero plot of open-loop system with damping

The Bode plots of (B.4) with and without R_{d} are shown in Fig. B.6 in which resonant peaks at low frequencies are due to the PR regulator and the resonant peak at around 10.7 kHz is because of the LCL filter. The resonant peak caused by the LCL filter has been reduced once R_{d} is added. The stability of the closed-loop current controller improves with increasing damping resistor values, while the attenuation provided the LCL filter for high frequency signals has reduced. Since a higher damping resistor increases resistive losses in the system, a small resistor should be selected which can improve system stability while minimising the losses. In this work, the damping resistor, R_{d} is chosen as one third of the impedance of the filter capacitor at the resonant frequency frequency of the LCL filter, f_{res} [60]. The impedance of filter capacitor at f_{res} is 7 Ω. Hence R_{d} is chosen as 2 Ω.

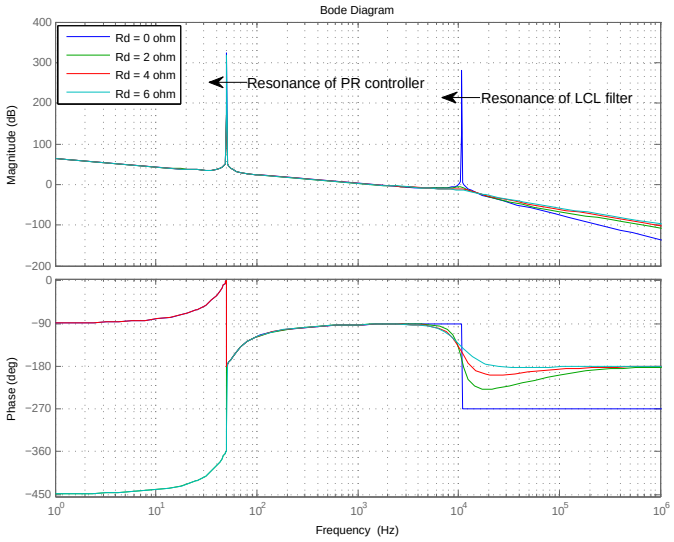

Figure B.6: Frequency response of the open-loop system

B.3 Effect of the grid impedance on the performance of the LCL filter and the closed-loop current controller of the VSC

The LCL filter was designed using the procedure stated in Appendix A considering that the grid impedance is zero. In a real world application, the LCL filter is the front end of a VSC that is connected to the grid. Hence studying the effects of the grid impedance on the performance of the LCL filter is important. Further, the performance of the closed-loop current controller should be evaluated in the presence of the grid impedance as well.

In the following analysis, the grid impedance $(0.4 + j0.25\ \Omega)$ is lumped with the grid side inductance, L_{fg} and the resistance, R_{fg} of the LCL filter. Further, resistances of filter components are neglected.

The Bode plot of the open-loop current controller is shown in Fig. B.7 for two different cases. As shown in Fig. B.7 the resonant frequency of the LCL filter without the grid impedance is 10.7 kHz. Once the grid impedance is added to the system, the resonant frequency of the LCL filter has dropped to 7.1 kHz which is about a 33% reduction from the previous value. The performance of the LCL filter with respect to attenuating high frequency harmonics has improved with addition

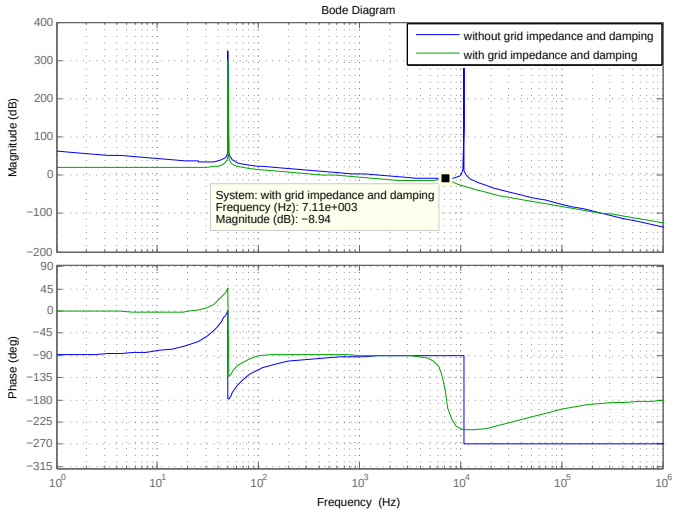

Figure B.7: Frequency response of the LCL filter with grid impedance

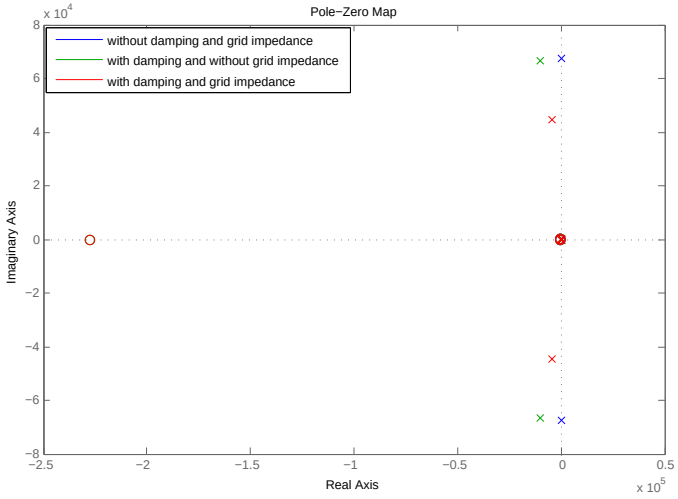

Figure B.8: Poles and zeros plot of open-loop current controller with grid impedance

of grid impedance. However, the decrease in the resonant frequency of the LCL filter with the addition of the grid impedance may cause passive damping that was designed for an ideal grid situation ineffective. Further, with the addition of the grid impedance, the bandwidth of the closed-loop current controller has reduced and that can be observed from Fig B.7. Since the current controller has harmonic compensators, there is a possibility that the current controller could become unstable with the reduction in the bandwidth of that controller. Hence, the effects of the grid impedance on the performance of the LCL filter and the closed-loop current controller should be considered when designing the LCL filter

and tuning the closed-loop current controller.

The pole and zero plot of the open-loop current controller is shown in Fig. B.8 for three different cases; (i) when $R_{\mathrm{d}} = 0$ and without grid impedance, (ii) when $R_{\mathrm{d}} = 2\ \Omega$ and without grid impedance, and (iii) when $R_{\mathrm{d}} = 2\ \Omega$ and with grid impedance. According to Fig. B.8, two complex conjugate poles, which are the resonant poles of the LCL filter, have moved towards imaginary axis with the addition of grid impedance. This confirms the reduction of the effectiveness of designed passive damping when grid impedance is added to the system.

Appendix C

DC-link capacitor of a single-phase VSC

C.1 100 Hz voltage ripple in the DC-link voltage of a single-phase VSC

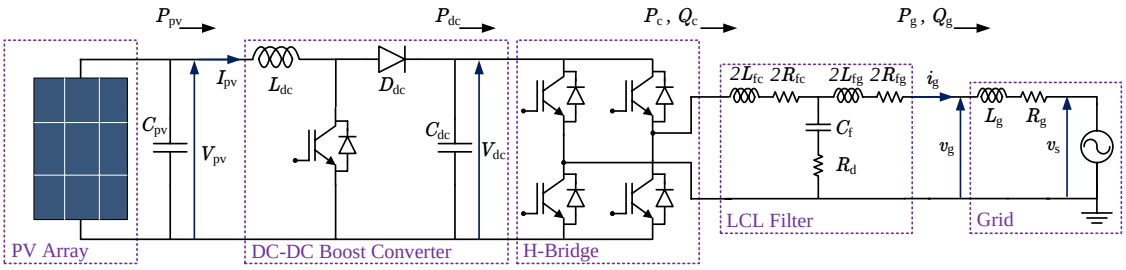

Figure C.1: A grid connected PV system with a VSC

A grid-connected single-phase PV system is shown in Fig. C.1. In the figure v_g and i_g are the instantaneous voltage and the current at the PCC of the PV system where $v_g = V_{gm}\sin(\omega t)$ and $i_g = I_{gm}\sin(\omega t - \phi)$. V_{gm} and I_{gm} are the peak values of v_g and i_g respectively, ϕ is a phase angle and ω is the fundamental frequency.

The instantaneous power, $p(t)$ at the PCC is,

$$p(t) = v_g i_g \tag{C.1}$$

$$p(t) = V_{\rm gm} I_{\rm gm} \sin(\omega t) \sin(\omega t - \phi). \tag{C.2}$$

Equation (C.2) can be simplified given in (C.3).

$$p(t) = \frac{1}{2} V_{\rm gm} I_{\rm gm} \cos\phi [1 - \cos(2\omega t)] - \frac{1}{2} V_{\rm gm} I_{\rm gm} \sin\phi \sin(2\omega t) \tag{C.3}$$

If $P = \frac{1}{2} V_{\rm gm} I_{\rm gm} \cos\phi$ and $Q = \frac{1}{2} V_{\rm gm} I_{\rm gm} \sin\phi$ where P is the average active power and Q is the average reactive power, assigning these values in (C.3), (C.4) can be derived.

$$p(t) = P[1 - \cos(2\omega t)] - Q \sin(2\omega t) \tag{C.4}$$

The instantaneous power variation on the AC side of the VSC that is given in (C.4) is plotted in Fig. C.2 when $P = 1$ and $Q = 1$. According to (C.4) and Fig. C.2, in a single-phase system, the active power delivered to the grid has an average value of P (which is 1 in this particular case) and an oscillating component that is $-P\cos(2\omega t)$. The active power flow is unidirectional since the active power component in (C.4) never becomes negative when power is injecting to the grid. Unlike the active power component, the reactive power component only has an oscillating component, that oscillates at twice the fundamental frequency. Therefore the average value of the reactive power delivered to the grid over half a cycle is zero.

The PV array generates only DC power. Hence, $P_{\rm pv}$ in Fig. C.1 is DC power which is equal to the average power P if the losses in the converter system are disregarded. However, the grid side of the single-phase VSC demands not only the constant active power that can be supplied by the PV but also an oscillating component of active power. The oscillating active power component cannot be supplied by the PV array. Therefore, there is a mismatch in the instantaneous power demand from the AC side and the available power from the PV array. In single-phase VSCs, the DC-link capacitor, ($C_{\rm dc}$) is used to balance the power mis-

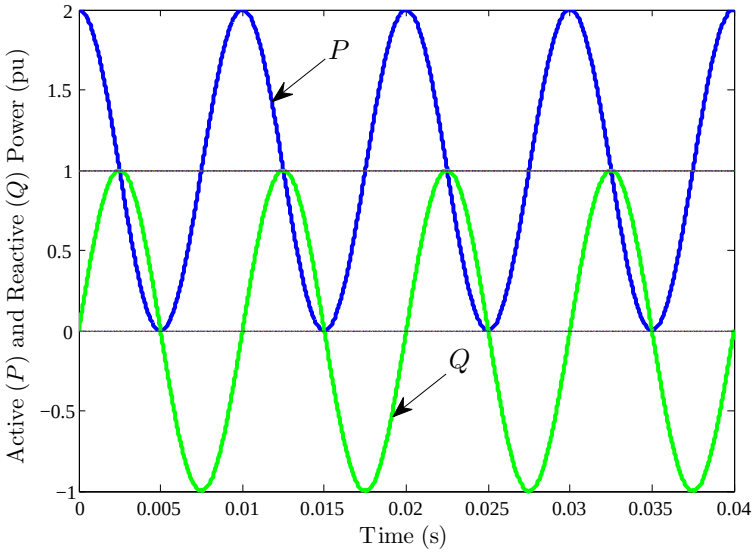

Figure C.2: Variation of the active and the reactive power delivered to the grid in a single-phase VSC

match. When the AC side power demand is less than that is generated by the PV array, the DC-link capacitor, C_{dc}, charges by storing excess energy, whereas when the demand is higher than generated power from the PV array, C_{pv} discharges by releasing stored energy. The charging and discharging of C_{dc} causes a voltage ripple at the DC-link. The frequency of the ripple is equal to the frequency of active power oscillation that is twice the fundamental frequency.

In half a cycle that is 10 ms, the energy transfered to the grid as reactive power is zero. Therefore the amount of energy drawn from the PV array to generate reactive power is zero. Within a quarter cycle, for example, from $t = 0.005$ ms to $t = 0.010$ ms in Fig. C.2, capacitor C_{dc} releases a certain amount of energy as the reactive power to the grid and within the next quarter cycle the capacitor stores the same amount of energy. The energy transfer as the reactive power also causes voltage oscillations at the DC-link at a similar frequency as the active power transfer does.

C.2 Selection of the DC-link capacitor value

An expression for the energy oscillation at the AC side of the VSC can be obtained by considering only the oscillating power components of (C.4) and integrating

that oscillating power components. An expression for the energy oscillation at the DC-link capacitor can be obtained by multiplying the energy oscillation at the AC side by -1. The derived expression for the energy oscillation at the DC-link capacitor, $\Delta e(t)$ is given in (C.5).

$$\Delta e(t) = \frac{P}{2\omega}\sin(2\omega t) - \frac{Q}{2\omega}\cos(2\omega t) \tag{C.5}$$

The oscillating energy at the DC-link that is given in (C.5) is plotted in Fig. C.3 for three different cases; (i) only one unit of active power ($P = 1$, $Q = 0$), (ii) only one unit of reactive power ($Q = 1$, $P = 0$), and (iii) one unit of both P and Q ($Q = 1$, $P = 1$).

In Fig. C.1, the VSC is designed to inject 5 kW of active power and to inject/absorb 2 kVAr of reactive power. Therefore, P to Q ratio is 1:0.4. The oscillating energy at $C_{\rm dc}$ for this particular P to Q ratio is shown in Fig. C.4. The energy variation at the DC-link when the converter is injecting both active and reactive powe and injecting only active power are approximately similar if the P to Q ratio is 1:0.4 as per Fig. C.4. Hence the effect of reactive power on the 100 Hz ripple in the DC-link voltage can be neglected. Equation (C.5) can be simplified to (C.6) if the effect of reactive power is disregarded. Equation (C.6) is plotted in Fig. C.5 for $P = 1$.

$$\Delta e(t) = \frac{P}{2\omega}\sin(2\omega t) \tag{C.6}$$

The difference in the maximum and the minimum energy stored in $C_{\rm dc}$, $\Delta e_{\rm max}$ that is the energy difference when $2\omega t = -\pi/2$ and $2\omega t = \pi/2$ in (C.6) is given in (C.7).

$$\Delta e_{\rm max} = \frac{P}{\omega} \tag{C.7}$$

The maximum and the minimum energy stored in $C_{\rm dc}$ causes the maximum and the minimum voltages at $C_{\rm dc}$ since the voltage across a capacitor is propor-

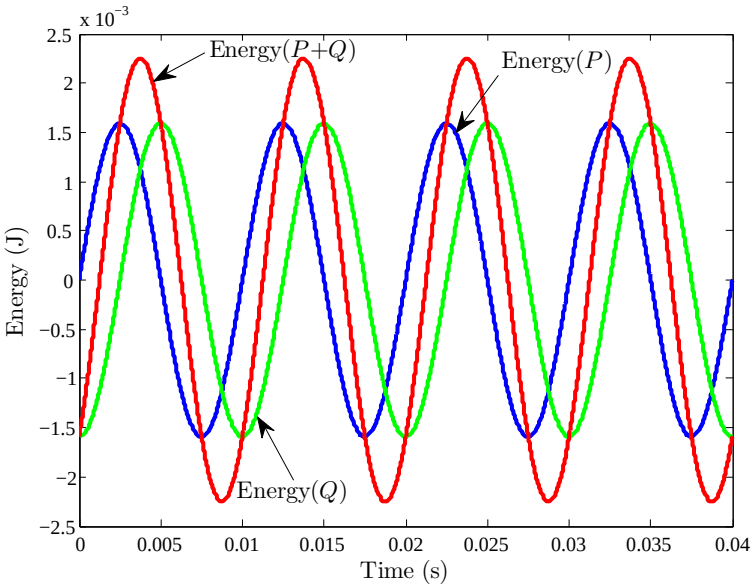

Figure C.3: Energy oscillation at the DC-link capacitor for 1:1 of P to Q ratio

tional to the stored energy in the capacitor. Therefore $\Delta e_{\max}$ can be written in terms of the maximum and the minimum DC-link voltages that are V_{dcmin} and V_{dcmax} respectively as given in (C.8).

$$\Delta e_{max} = \frac{1}{2} C_{\text{dc}} V_{\text{dcmax}}^2 - \frac{1}{2} C_{\text{dc}} V_{\text{dcmin}}^2 \tag{C.8}$$

An expression for the peak-peak 100 Hz DC-link voltage ripple, ΔV_{dc}, can be derived as given in (C.9) from (C.7) and (C.8). In (C.9), $\Delta V_{\text{dc}} = V_{\text{dcmax}} - V_{\text{dcmin}}$ and $V_{\text{dcavg}} = (V_{\text{dcmax}} + V_{\text{dcmin}})/2$ that is the average DC-link voltage of the VSC.

$$\Delta V_{\text{dc}} = \frac{P}{C_{\text{dc}} V_{\text{dc}} \omega} \tag{C.9}$$

An excessively large capacitor at the DC-link can reduce the DC-link voltage ripple almost to zero as per (C.9). But that is practically impossible and there is a limitation to the size of C_{dc}. Hence there is a voltage ripple in the DC-link voltage of a single-phase VSC. The capacitance of the DC-link capacitor of a single-phase VSC is determined to limit the peak-peak ripple of the DC-link voltage.

If $V_{\text{dcavg}} = 400$ V and 5% of V_{dcavg} is desired as ΔV_{dc} in the VSC in Fig. C.1,

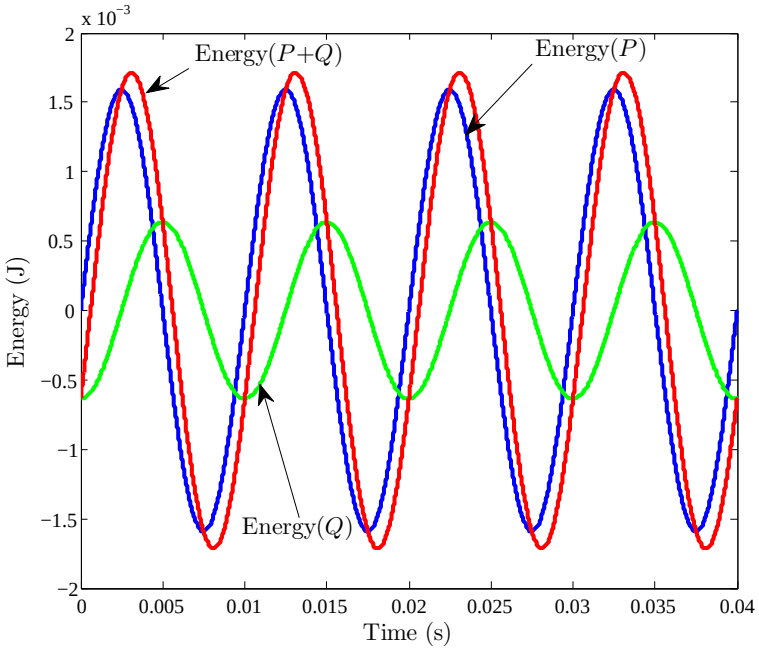

Figure C.4: Energy oscillation at the DC-link capacitor for 1:0.4 of P to Q ratio

C_{dc} should be equal to 2000 μF as per (C.9).

C.3 Control plant model of the DC-link voltage

A power balance equation can be written as in (C.10) for the AC side and the DC side of the VSC in Fig. C.1, neglecting the losses in the VSC and the energy stored in LCL filter components.

$$P_{\text{dc}} - \frac{d}{dt}(\frac{1}{2}C_{\text{dc}}V_{\text{dc}}^2) = P_{\text{g}} \tag{C.10}$$

In (C.10), P_{dc} is the power available at the DC-link from the PV system assuming lossless conversion at the DC-DC converter. The derivative term in (C.10) is the rate of change of energy at C_{dc}. Equation (C.10) can be rearranged as (C.11) that describes a linear model with V_{dc}^2 as the control output, P_{g} as the control input and P_{dc} as the disturbance. According to (C.11), V_{dc} can be controlled by controlling the amount of active power injected to the grid.

$$-\frac{C_{\text{dc}}}{2}\frac{d}{dt}V_{\text{dc}}^2 = P_{\text{g}} - P_{\text{dc}} \tag{C.11}$$

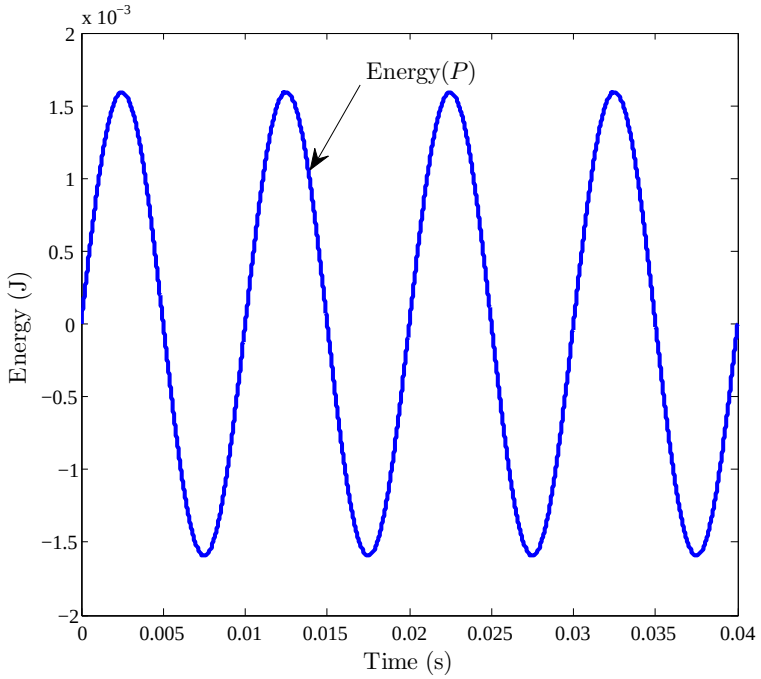

Figure C.5: Energy oscillation at the DC-link capacitor for one unit of active power

The transfer function of the control plant model for the DC-link voltage is given in (C.12).

$$G_{V_{\mathrm{dc}}}(s) = \frac{V_{\mathrm{dc}}^2(s)}{P_{\mathrm{g}}(s)} = -\frac{2}{C_{\mathrm{dc}}s} \tag{C.12}$$

Appendix D

Experimental Setup

D.1 Introduction

In order to validate the simulation model of a grid-connected single-phase, two-stage photovoltaic system that was developed in PSCAD/EMTDC simulation program, an experimental setup was needed. Therefore a laboratory scale experimental setup of two, 5 kW grid-connected single-phase, two-stage PV systems was implemented after acquiring necessary hardware and using the control algorithms developed in the simulation model. The implemented experimental setup is used for validating the simulation model and also for identifying operational and control interactions between multiple PV systems when PV systems are operated electrically very close to each other.

D.2 System description of the experimental setup

A schematic diagram of the implemented experimental setup of the grid connected PV system is shown in Fig. D.1. A picture of the complete experimental setup implemented is shown in Fig. D.1

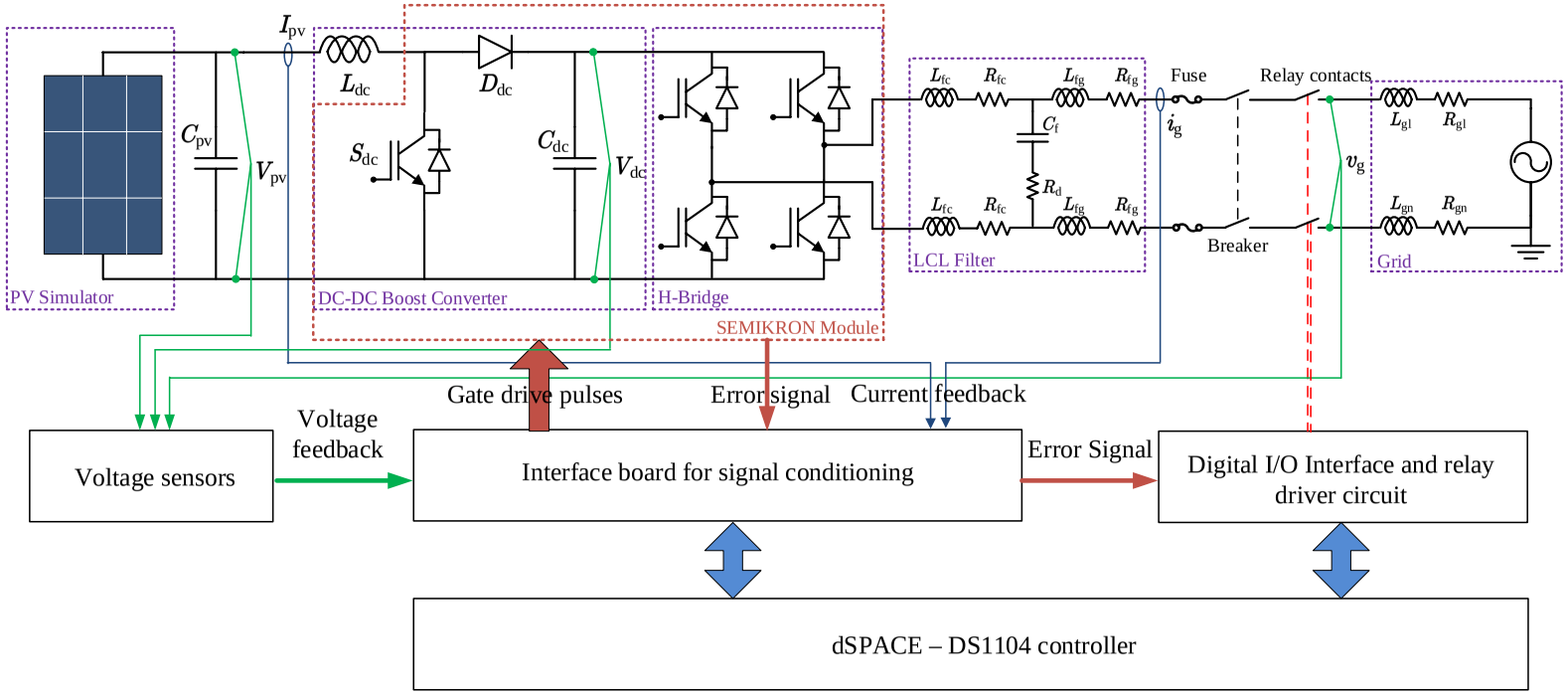

Figure D.1: Schematic diagram of the experimental setup

Figure D.2: Picture of the complete experimental setup

The implemented PV system consists of a two-stage converter that was formed by a combination of a DC-DC boost converter and a VSC. The PV system is interfaced to the grid via an LCL filter. A brief description of various modules and some of the important components shown in Fig. D.1 are given in following subsections.

D.2.1 SEMITEACH-IGBT stack

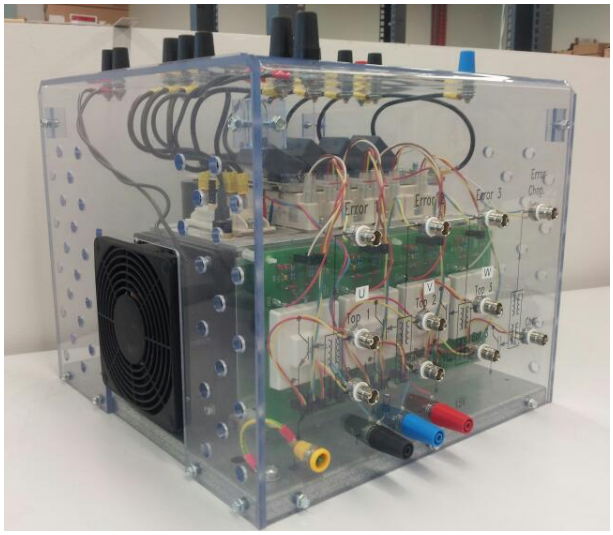

Figure D.3: The Semikron SEMITEACH-IGBT stack

The Semikron SEMITEACH-IGBT stack that was used in the experimental setup is shown in Fig. D.3. This module was used to form most of the power electronic circuitry of the two-stage converter. In the experimental setup, two legs of the 3-phase inverter built into the Semikron SEMITEACH-IGBT stack was used to form the full-bridge. Further, the diode (D_{dc}) and the power electronic switch, S_{dc} that are parts of the DC-DC boost converter and the DC-link capacitor, C_{dc} are integrated components of the Semikron SEMITEACH-IGBT stack. The full-bridge in combination with C_{dc} forms the VSC that is the DC-AC power converter of the PV system. All power electronic switches in the module are IGBTs.

The Semikron SEMITEACH-IGBT stack has built-in IGBT drivers for each leg of the 3-phase inverter built into the stack. The driver imposes roughly a 4 μs

dead-time on top and bottom switches of a leg in order to avoid a short-circuit condition in the power circuit. The IGBT drivers should be supplied with an external 15 V DC power supply. The IGBT driver generates an error in cases where the driver detects a power supply undervoltage condition or an over current condition through an IGBT of the stack. If the driver detects an error, the IGBT is turned off. The error signal that is generated by the driver of each leg is accessible from outside of the stack. Hence in the experimental setup these error signals are integrated to the control circuit to develop protective measures.

D.2.2 LCL filter

The LCL filter minimises the amount of switching frequency harmonic current injected to the grid by the PV system. There were two types of LCL filter configurations considered while implementing the experimental setup and those two configurations are shown in Fig. D.4 where L_{fc} is the converter side inductance and L_{fg} is the grid side inductance. R_{fc} and R_{fg} are resistances of converter side and grid side inductors respectively. C_{f} is the filter capacitor and R_{d} is the damping resistor.

In the experimental setup, the switching frequency of both the DC-DC boost converter and the VSC are 10 kHz and bipolar sinusoidal pulse width modulation (bipolar-SPWM) was used to switch the IGBTs in the VSC due to limitations in the dSPACE-DS1104 controller. Since the LCL filter configuration shown in Fig. D.4(b) leads to less ground leakage current when the VSC is switched with bipolar-SPWM technique, that particular LCL filter configuration is used in the implemented experimental setup of the PV system.

The LCL filter was initially designed by following the procedures described in Appendix A. However, when purchasing inductors for the LCL filter rather than adopting component values that are optimally designed (in terms of inductances and capacitance) a conservative design approach was followed. A considerable margin was allowed for design errors when deciding the component values to pur-

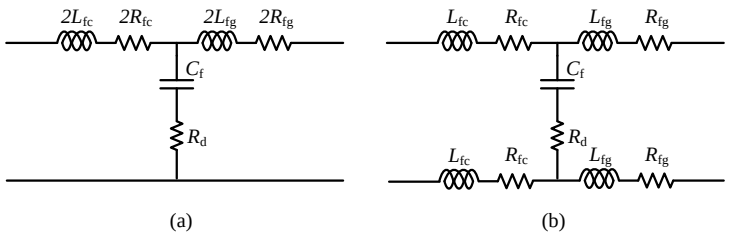

Figure D.4: LCL filter configurations

chase but the design rules depicted in Appendix A were not violated. The values of the components of the LCL filter as used in the implemented experimental setup of the PV system are $L_{\mathrm{fc}} = 900\ \mu\mathrm{H}$, $L_{\mathrm{fg}} = 450\ \mu\mathrm{H}$, $C_{\mathrm{f}} = 4.7\ \mu\mathrm{F}$ and $R_{\mathrm{d}} = 2\ \Omega$.

D.2.3 PV emulator

The PV emulator simulates the electrical characteristics (I-V curve) of a defined PV array. An ELGAR TerraSAS ETS1000X PV emulator is used in the experimental setup. The front view of the ELGAR TerraSAS ETS1000X PV emulator is shown in Fig D.5.

Figure D.5: The front view of a ELGAR TerraSAS ETS1000X PV emulator

The maximum output power, output current and output voltage of the ELGAR TerraSAS ETS1000X PV emulator are 8.5 kW (at 0.85 fill factor), 10 A DC and 1000 V DC respectively. In the design of the DC-DC boost converter of the PV system, the nominal input voltage of the DC-DC boost converter (V_{pv}) was considered as less than 300 V DC. Hence, with the limited current rating of the PV emulator and also with the input voltage limitation of the DC-DC boost converter, the designed PV system cannot be operated at the rated power, 5 kW with one PV emulator. The maximum power rating that the PV system can be

operated with one PV emulator is roughly 3 kW. In order to operate the PV system at the rated power of the converter system, two PV emulators that are connected in parallel can be used.

At the initial stage of the implementation of the experimental setup of the PV system, the LCL filter configuration that is shown in Fig D.4(a) was used and unipolar-SPWM technique was used to switch the VSC. When the PV system was tested with the LCL filter configuration that is shown in Fig. D.4(a) and unipolar-SPWM the ELGAR TerraSAS ETS1000X PV emulator was tripping at the time of grid connection. Since detailed information on the internal circuitry of the PV emulator was not readily available, a proper technical analysis could not be performed to identify the root cause for tripping. Therefore a trial and error method was followed to find a solution.

An analysis performed in [70] has illustrated that in single-phase transformerless PV systems that are designed with the LCL filter configuration shown in Fig. D.4(a) and unipolar-SPWM switching of VSC, the ground leakage current is quite significant. Further, single phase transformerless PV systems that are designed with the LCL filter configuration shown in Fig. D.4(b) and bipolar-SPWM switching of VSC has been identified as a design leading to less ground leakage current. Accordingly, in the implemented experimental setup of the PV system, the LCL filter configuration was changed to the configuration shown in Fig. D.4(b) and bipolar-SPWM switching technique was used to switch the VSC. With these modifications in the PV system, the ELGAR TerraSAS ETS1000X PV emulator functioned as required, without tripping at the time of grid connection. Though the PV emulator stayed connected after the grid connection the output of the PV emulator was not stable. Upon the recommendations received from the supplier of the PV emulator with regard to stabilising the output of the PV emulator, an EMI filter was included at the output of the PV emulator (the EMI filter is not shown in Fig. D.1). A Shaffner FN 2200-25-33 EMI filter is used in the implemented PV system. After the changes such as including a EMI

filter at the output of the PV emulator, changing the LCL filter configuration to that is shown in Fig. D.4(b) and utilising bipolar-SPWM switching technique to switch the VSC, the PV emulator continued to operate satisfactorily.

D.2.4 Power grid

In the experimental setup of the PV system, the power distribution grid was emulated with an electronic power source that is connected in series with an impedance for initial testing purposes. The California Instruments MX30 AC and DC power source in combination with OMNI $3-75$ impedance bank was used to simulate the power distribution grid. The impedance of the simulated grid was $(0.25 + j0.25)\ \Omega$. At the latter stages, the implemented PV system was connected to the actual power distribution grid.

D.2.5 Inductor of the DC-DC boost converter (L_{dc})

The inductance of L_{dc} was calculated using (D.1) to limit the current ripple, ΔI, of the current that is flowing through the inductor [58]. In (D.1), V_{pv} is the voltage across the PV array, V_{dcavg} is the average DC-link voltage and f_{dc} is the switching frequency of the DC-DC boost converter.

$$L_{\mathrm{dc}} = \frac{V_{\mathrm{pv}}(V_{\mathrm{dc\_avg}} - V_{\mathrm{pv}})}{\Delta I f_{\mathrm{dc}} V_{\mathrm{dcavg}}} \tag{D.1}$$

When the PV system is operated at the rated capacity, the input voltage of the DC-DC boost converter, V_{pv} is 300 V. Further, the rated capacity of the DC-DC boost converter is 5 kW, V_{dcavg} is 420 V and f_{dc} is 10 kHz. Hence the inductor, $L_{\mathrm{dc}} = 9$ mH, calculated to limit ΔI to 5% of the rated input current of the DC-DC boost converter. In the implemented PV system two, 6 mH iron core inductors (connected in series) were used instead of a 9 mH inductor.

D.2.6 Input capacitor of the DC-DC boost converter (C_{pv})

The input capacitor of the DC-DC boost converter, C_{pv}, minimises the switching frequency ripple current that is drawn from the PV array and thereby the switching frequency ripple voltage. Also, if a large capacitor is used as C_{pv}, the PV array can be decoupled from AC side dynamics. In the implemented PV system, decoupling of the PV array from AC side dynamics was achieved by means of implemented control techniques. The capacitor C_{pv} was mainly utilised to minimise the switching frequency ripple current that is drawn from the PV array. Hence, a smaller capacitor could be used at the input of the DC-DC boost converter.

$$C_{\text{pv}} = \frac{DV_{\text{pv}}}{4\Delta V_{\text{pv}} L_{\text{dc}} f_{\text{dc}}^2} \tag{D.2}$$

The capacitor, C_{pv}, was calculated based on the equation given in (D.2) [58]. In (D.2), D is the duty cycle of the DC-DC boost converter, V_{pv} is the average voltage across the PV array, ΔV_{pv} is the switching ripple voltage of the PV array, L_{dc} is 12 mH and f_{dc} is 10 kHz. The capacitor, C_{pv}, was selected as 40 μF in the implemented PV system in order to limit ΔV_{pv} to less than 0.5 V.

D.2.7 DC-link capacitor (C_{dc})

The DC-link capacitor, C_{dc}, is an integrated part of the SEMITEACH-IGBT stack. The value of C_{dc} is 1100 μF. The DC-link voltage consists of an average DC component, V_{dcavg}, as well as a 100 Hz voltage ripple. An expression for the peak-to-peak 100 Hz voltage ripple of the DC-link voltage, ΔV_{dc}, is derived in Appendix C and is given in (D.3) where P_{g} is the active power injected to the grid and ω is the fundamental angular frequency of the grid voltage. Since V_{dcavg} is 420 V in the implemented PV system with the given capacitance for C_{dc}, $\Delta V_{\text{dc}} =$ 34 V if the PV system is operated at the rated power that is 5 kW. Hence in the implemented PV system the peak-to-peak 100 Hz voltage ripple of the DC-link voltage is less than 10% of the average DC-link voltage.

$$\Delta V_{\mathrm{dc}} = \frac{P_{\mathrm{g}}}{C_{\mathrm{dc}} V_{\mathrm{dcavg}} \omega} \tag{D.3}$$

Appendix E

Dynamic performance of STARSINE 5 kVA DSTATCOM

The STARSINE 5 kVA DSTATCOM that was initially manufactured by Surtek Pty Ltd in Queensland, Australia is a commercially available small scale DSTATCOM. This converter can be configured to operate in all four quadrants meaning that injection or absorption of any combination of active and reactive power is possible, limiting to the kVA rating of the converter. The Industry Partner of this research project, Essential Energy had utilised these DSTATCOMS to regulate voltage in long distribution feeders in their network and was interested in utilising these converters to regulate network voltage in LV grids to which multiple small scale PV systems are integrated. However, the dynamic performances of STARSINE 5 kVA converters when used in LV grids to which multiple PV systems are integrated were not known. Therefore experimental investigations were carried out in this research project to validate the dynamic performance of STARSINE 5 kVA converters in such an applications.

In the first part of this appendix, terminal characteristics of a STARSINE 5 kVA DSTATCOM and the dynamic behaviour of two of STARSINE 5 kVA DSTATCOMs when operated electrically close to each other are illustrated. In the final part of this appendix, experimental results obtained by integrating two

STARSINE 5 kVA DSTATCOMs and two experimental PV systems developed in this research project to an experimental network are presented.

E.1 STARSINE 5 kVA DSTATCOM

Figure E.1: Front view of a Surtek STARSINE 5 kVA DSTATCOM

The front view of a STARSINE 5 kVA DSTATCOM is shown in Fig. E.1. These DSTATCOMs can be configured to control reactive power output at a reference reactive power level or to regulate the PCC voltage within a voltage bandwidth. The latter configuration a DSTATCOM was used in all the experimental tests of which results are presented in this appendix.

E.1.1 Terminal characteristics

The terminal characteristics of a STARSINE 5 kVA DSTATCOM was investigated by utilising an experimental setup of which the schematic diagram is shown in Fig. E.2. The impedance seen at the PCC of the DSTATCOM was

$(R_g + jX_g) = (0.25 + j0.25)\ \Omega$. The voltage bandwidth of the DSTATCOM was set to 240 ± 3 V. The terminal voltage of the waveform generator, V_s, was set to 240 V and that was stepped up and down to investigate the terminal characteristics of the DSTATCOM. The sequence of voltage steps were, 240 V–247 V–240 V–233 V–240 V. The experimental results obtained by varying V_s as described are shown in Fig. E.3.

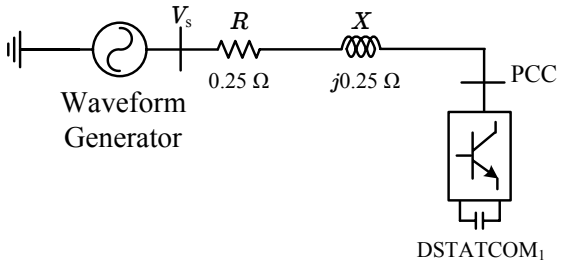

Figure E.2: Schematic diagram of the experimental setup used to investigate the terminal characteristics of a STARSINE 5 kVA DSTATCOM

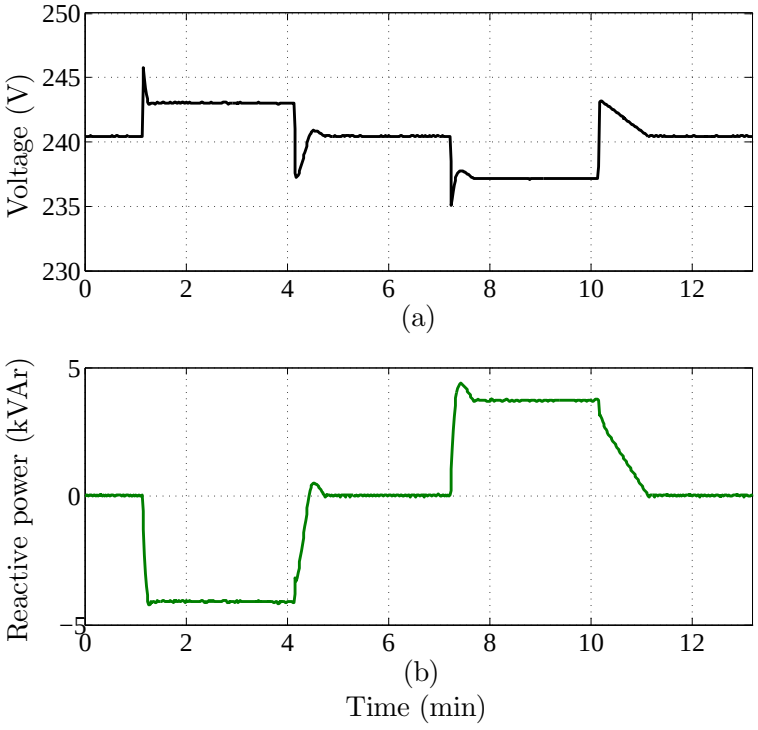

Figure E.3: Terminal characteristics of a STARSINE 5 kVA DSTATCOM

Fig. E.3(a) illustrates that the terminal voltage of the DSTATCOM has been regulated within 240 ± 3 V. According Fig. E.3, the response time of the DSTATCOM is sensitive to the type of voltage step applied since the response times that

can be observed in the figure at each step change in V_s are different to each other. According to the Fig. E.3, the response time of a STARSINE 5 kVA DSTATCOM varies between 10–60 s.

E.1.2 Operation of two STARSINE 5 kVA DSTATCOMs

An experimental setup was developed to investigate the dynamic behaviour of a STARSINE 5 kVA DSTATCOM when another similar unit is operated close to each other. The schematic diagram of the experimental setup is shown in Fig. E.4. The aim was to use this experimental setup to identify any control or operational interactions between the two DSTATCOMS. Therefore, experimental results were obtained by varying the impedance, $(R + jX)$ between two DSTATCOMs and setting different combinations of voltage bandwidths in DSTATCOMs.

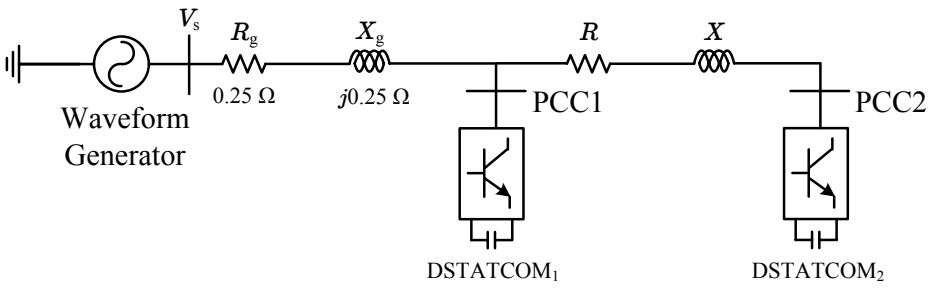

Figure E.4: Schematic diagram of the experimental setup used to test the operation of two STARSINE 5 kVA DSTATCOMs

Impedance between two DSTATCOMs and the set voltage bandwidth of each DSTATCOM in all the experimental cases that were completed utilising two STARSINE 5 kVA DSTATCOMs are listed in Table E.1. The dynamic responses of each DSTATCOM were obtained by applying step voltage changes of V_s in each experimental case. The sequence of voltage steps applied to V_s in each experimental case were, 240 V–247 V–240 V–233 V–240 V. The terminal voltage and reactive power variation of DSTATCOMs in each experimental case are are shown in Fig. E.5–Fig. E.15.

Table E.1: Description of experimental cases completed utilising two STARSINE 5 kVA DSTATCOMs

Experimental case no	**Voltage bandwidth of** DSTATCOM$_1$ **(V)**	**Voltage bandwidth of** DSTATCOM$_2$ **(V)**	$(R + jX)$ (Ω)
Case 1	240 ± 3	240 ± 3	nearly zero
Case 2	240 ± 3	240 ± 2	nearly zero
Case 3	240 ± 3	240 ± 4	nearly zero
Case 4	240 ± 2	240 ± 3	nearly zero
Case 5	240 ± 4	240 ± 3	nearly zero
Case 6	240 ± 3	240 ± 3	$0.04 + j0.03$
Case 7	240 ± 3	240 ± 2	$0.04 + j0.03$
Case 8	240 ± 3	240 ± 4	$0.04 + j0.03$
Case 9	240 ± 2	240 ± 3	$0.04 + j0.03$
Case 10	240 ± 4	240 ± 3	$0.04 + j0.03$
Case 11	240 ± 3	240 ± 3	$0.12 + j0.09$

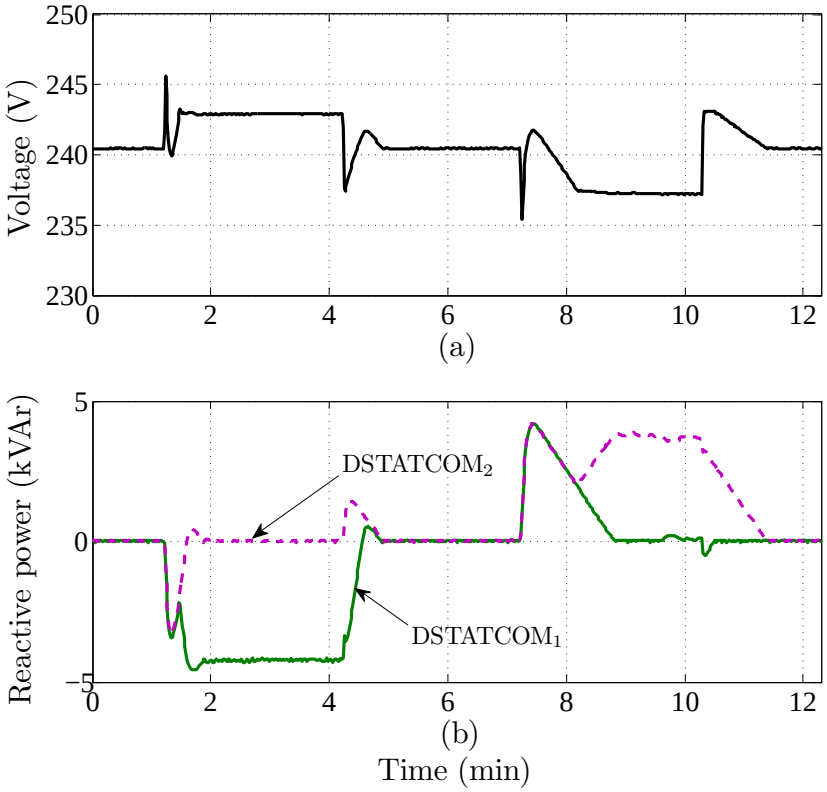

Figure E.5: Experimental results – Case 1

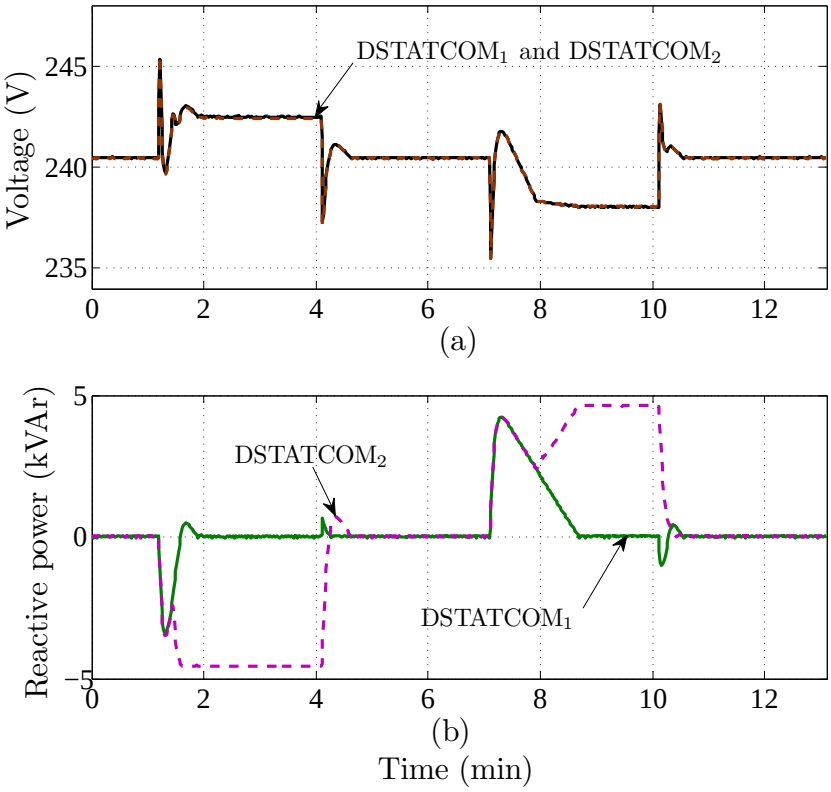

Figure E.6: Experimental results – Case 2

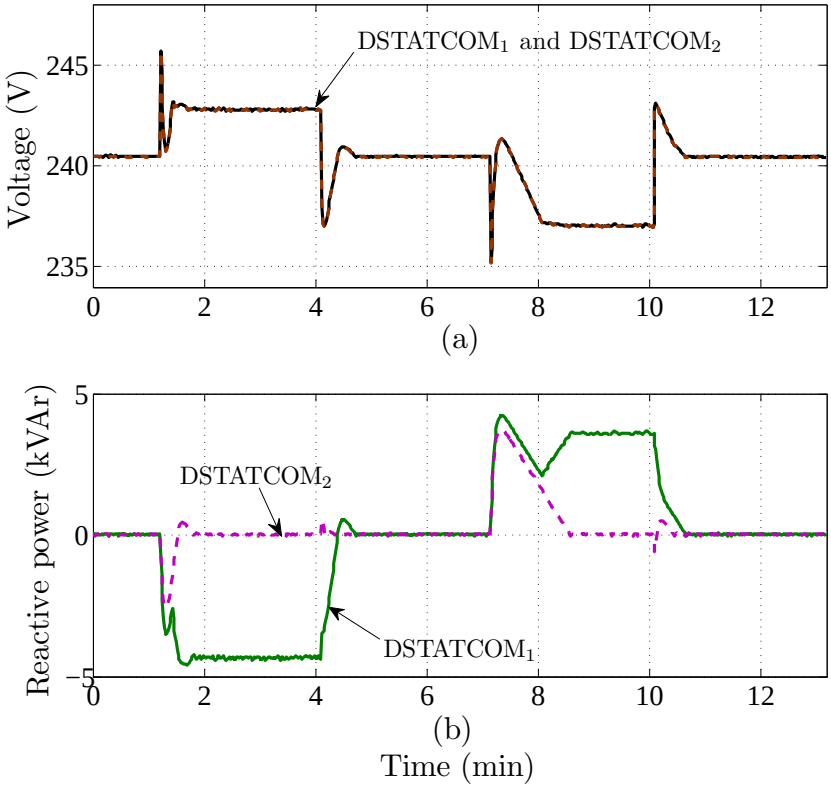

Figure E.7: Experimental results – Case 3

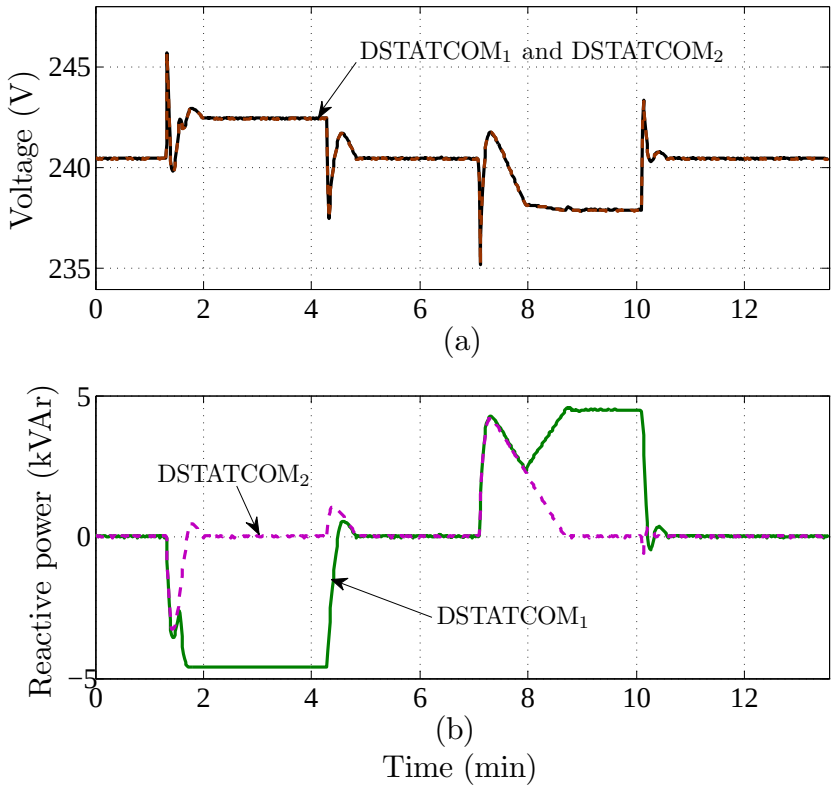

Figure E.8: Experimental results – Case 4

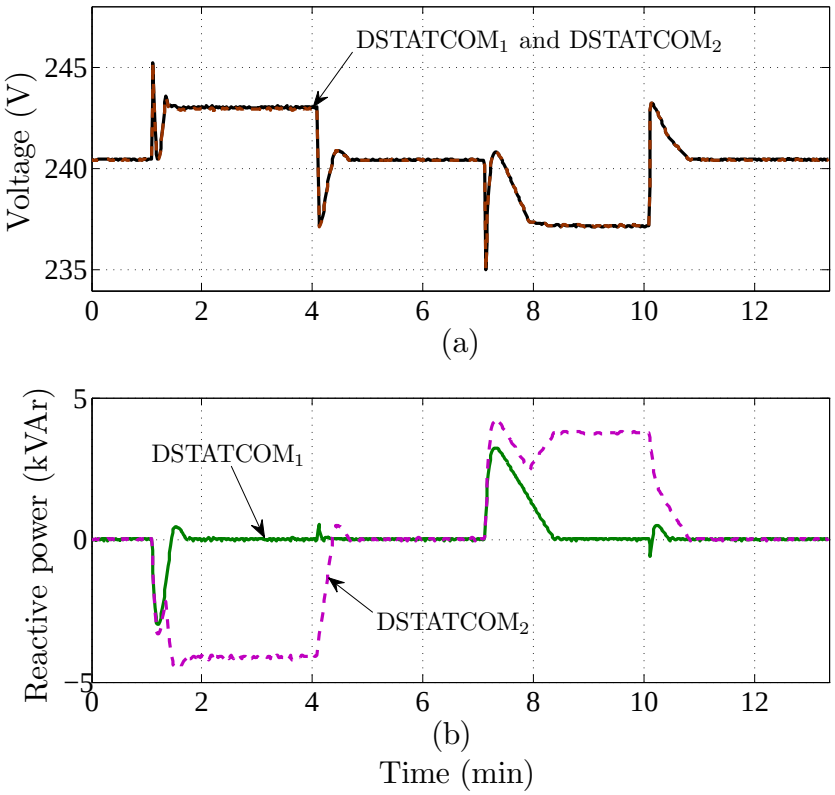

Figure E.9: Experimental results – Case 5

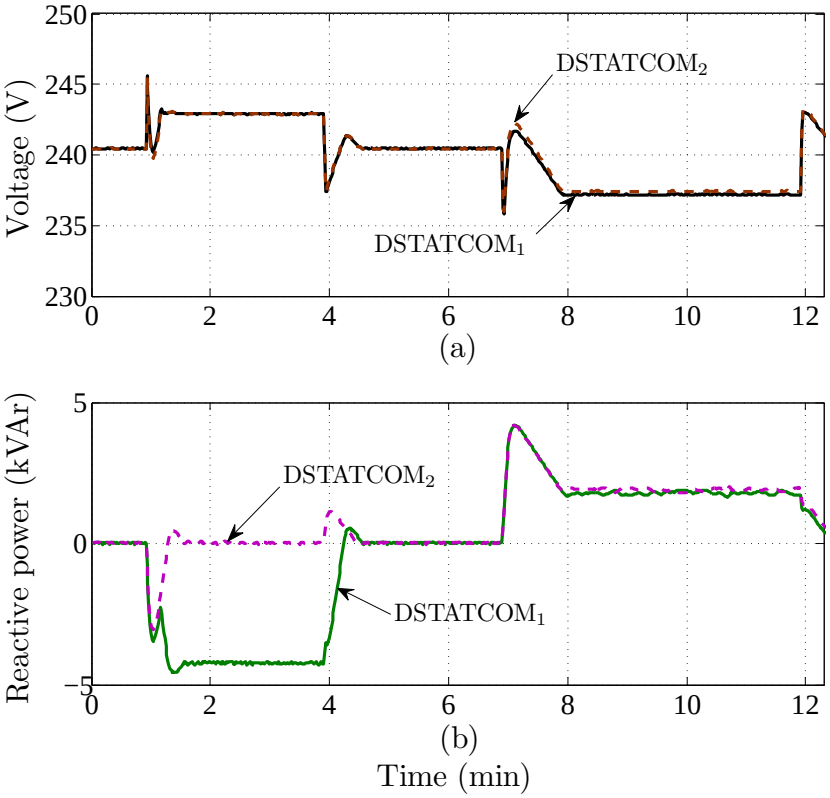

Figure E.10: Experimental results – Case 6

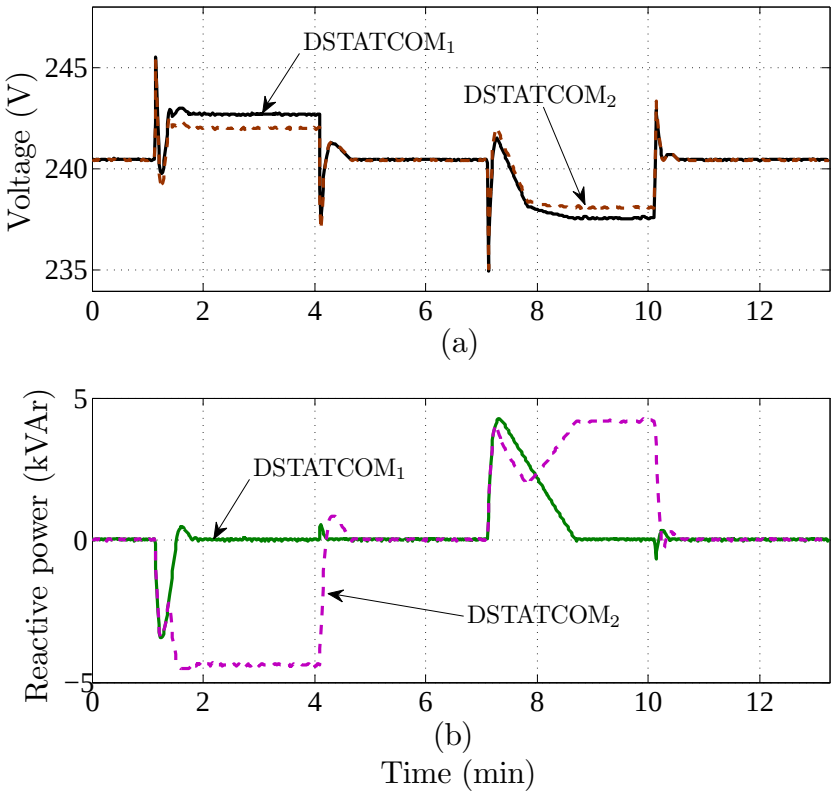

Figure E.11: Experimental results – Case 7

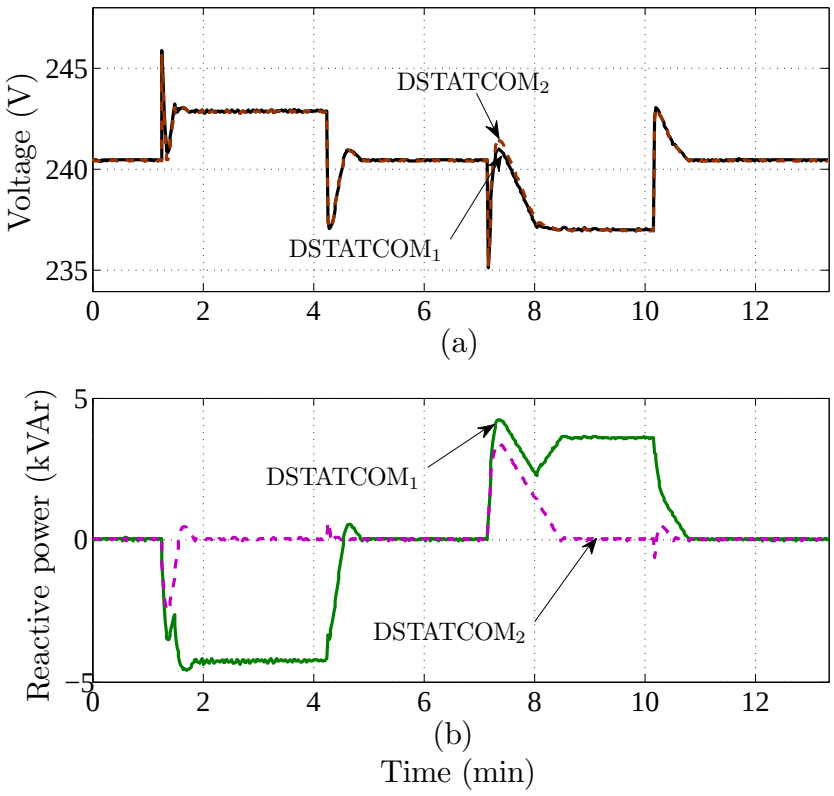

Figure E.12: Experimental results – Case 8

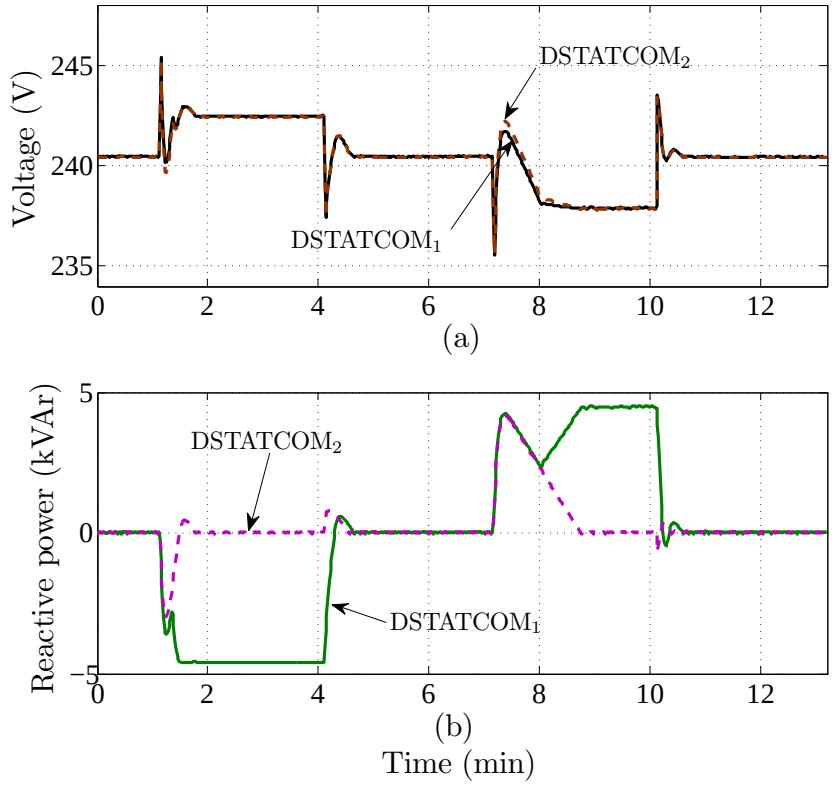

Figure E.13: Experimental results – Case 9

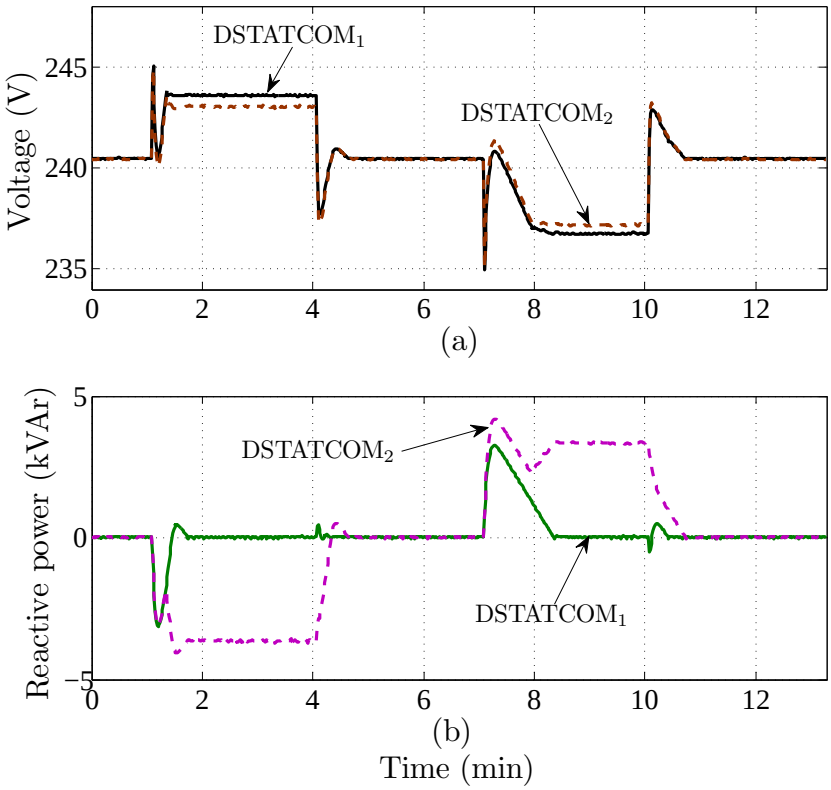

Figure E.14: Experimental results – Case 10

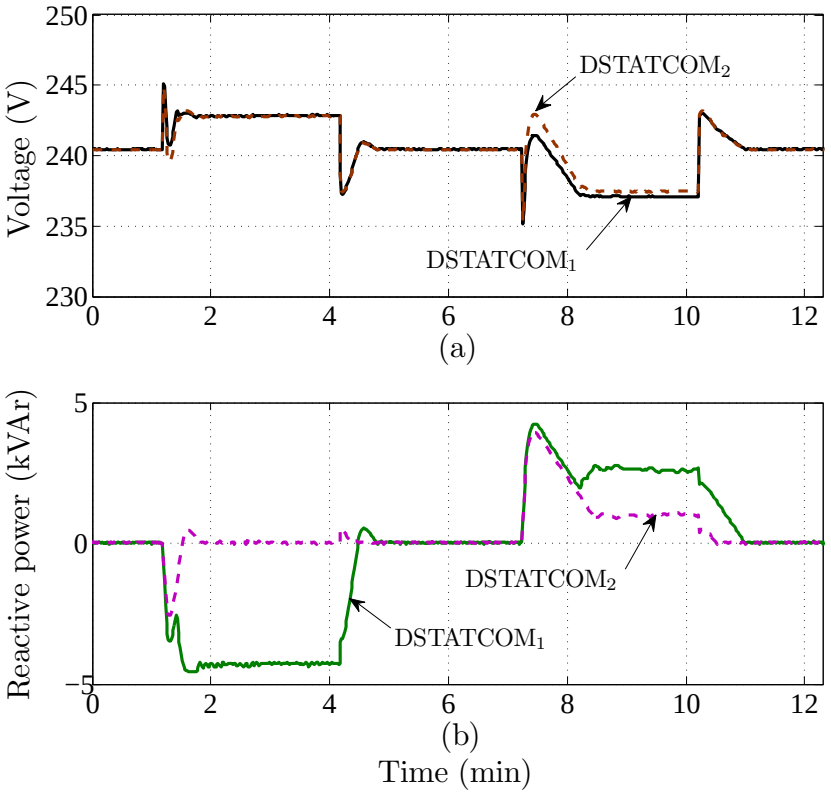

Figure E.15: Experimental results – Case 11

E.1.3 Operation of STARSINE 5 kVA DSTATCOMs and PV systems

The operation of DSTATCOMs were tested in the presence of PV systems. The PV systems developed in this research[1] were integrated with DSTATCOMs and tested to identify dynamic interactions when these systems were operated simultaneously. The schematic diagram of the experimental setup used is shown in Fig. E.16. PV systems were connected at the terminals of DSTATCOMs and $(R + jX) = (0.03 + j0.02)\ \Omega$. In each test performed, each PV systems was injecting about 2.4 kW to the grid. The sequence of voltage steps applied to V_s in all the experiments were, 245 V-251 V–245 V.

The set voltage bandwidth of DSTATCOMs and reference voltages of PCC V_Q controllers[2] of PV systems of experiments carried out utilising two STARSINE 5 kVA DSTATCOMs and two PV systems are listed in Table E.2. In the table NIU (not in use) indicates that the voltage control function of the PV system was not used or the DSTATCOM was not connected in that particular experiment. The terminal voltage and reactive power variation of DSTATCOMs in each experimental case are shown in Fig. E.17–Fig. E.20.

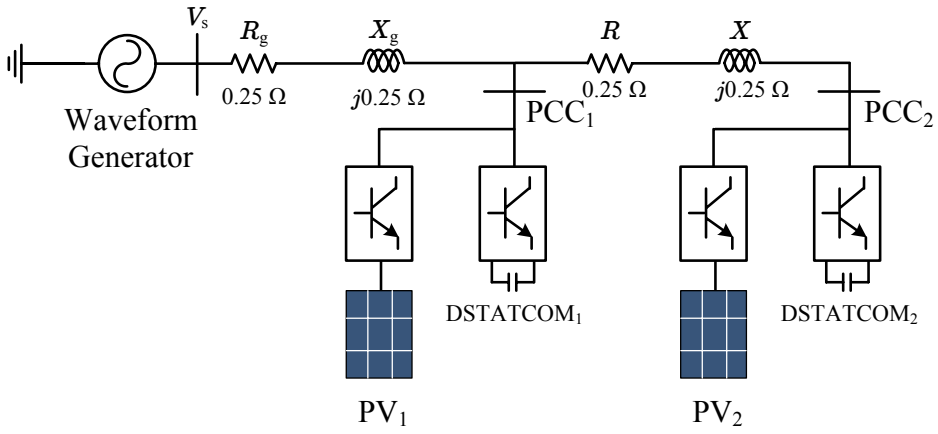

Figure E.16: Schematic diagram of the experimental setup used to test the operation of two STARSINE 5 kVA DSTATCOMs and two PV systems

[1]Refer to Appendix D for more information.
[2]Refer to Chapter 4 for more information.

Table E.2: Description of experimental cases completed utilising STARSINE 5 kVA DSTATCOMs and PV systems

Experiment case no	**Voltage BW of DSTATCOM$_1$ (V)**	**Voltage BW of DSTATCOM$_2$ (V)**	**Voltage ref. of PV$_1$ (V)**	**Voltage ref. of PV$_2$ (V)**
Case 12	NIU	NIU	252.3	253
Case 13	$250 + 2.3$	$250 + 3$	NIU	NIU
Case 14	$250 + 2.3$	NIU	NIU	253
Case 15	NIU	$250 + 3$	252.3	NIU

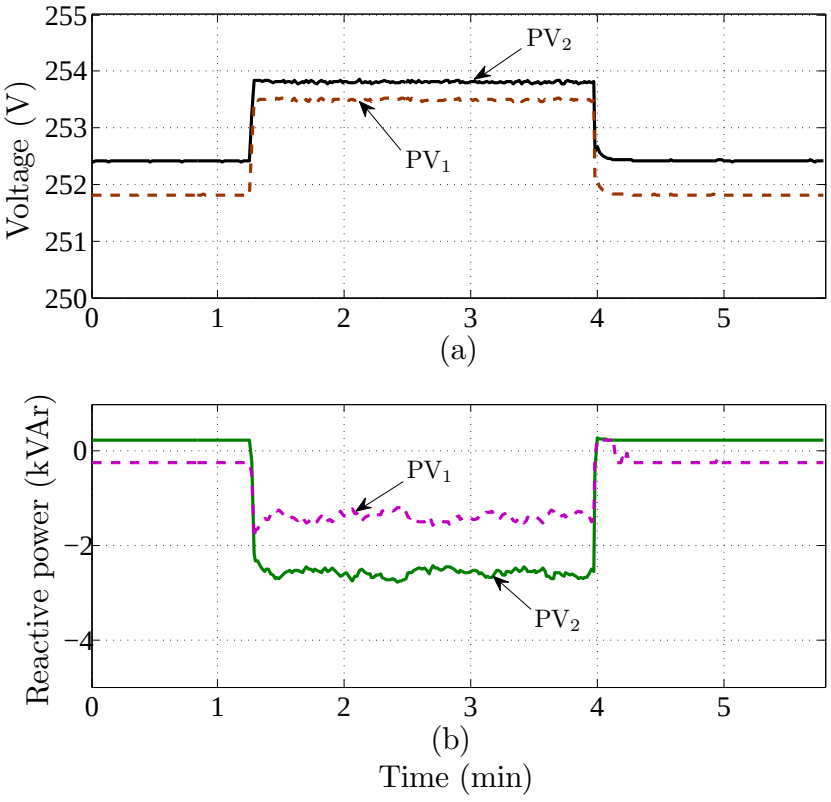

Figure E.17: Experimental results – Case 12

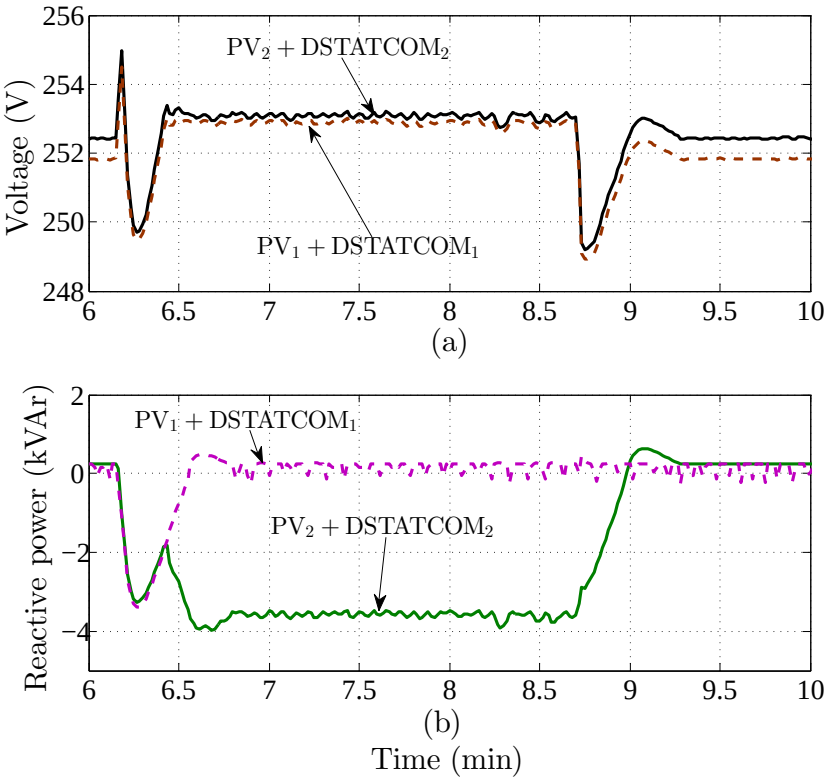

Figure E.18: Experimental results – Case 13

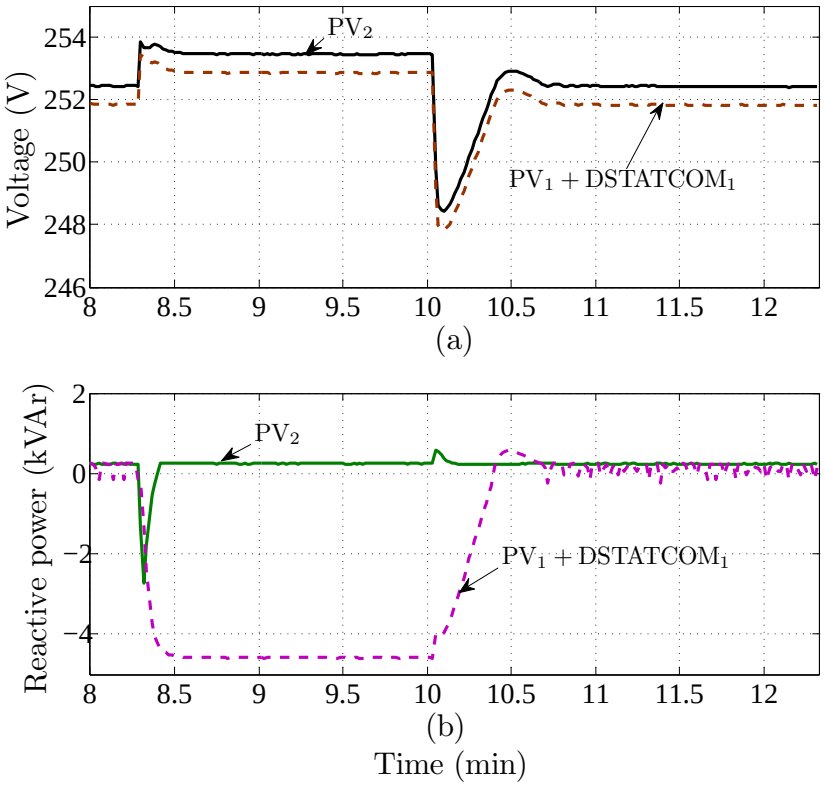

Figure E.19: Experimental results – Case 14

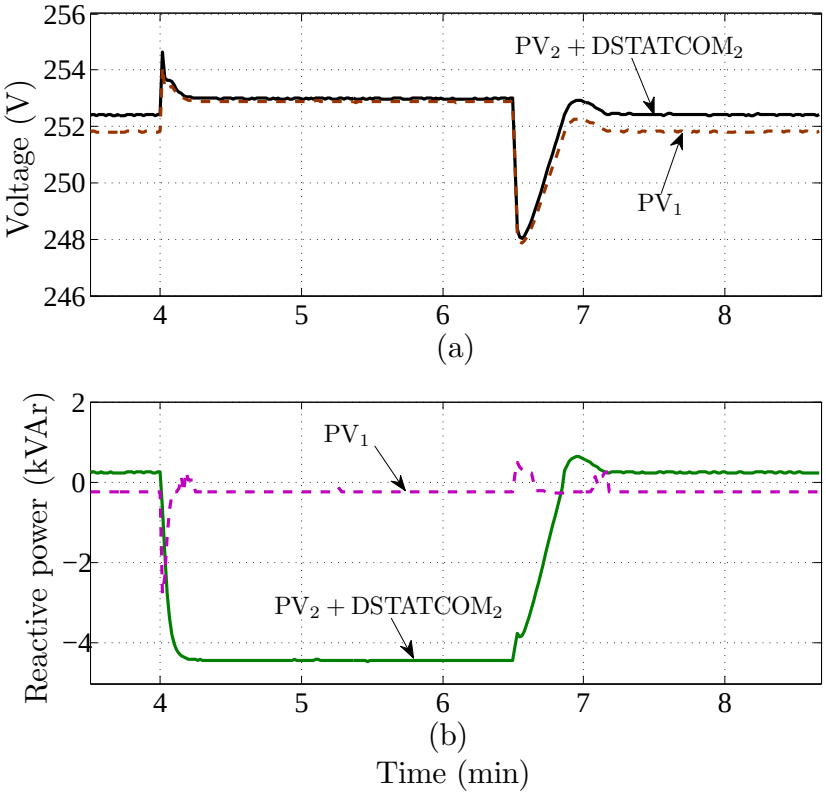

Figure E.20: Experimental results – Case 15

E.1.4 Analysis of experimental results

In experiment, Case 1, it was expected that DSTATCOM_1 and DSTATCOM_2 would share reactive power equally when controlling terminal voltages since these systems were connected at the same node and had the same voltage bandwidth. However, according to experimental results shown in Fig. E.5 such reactive power sharing did not happen. This was primarily due to measurement errors of voltage sensors used in DSTATCOMs to measure the terminal voltage and added impedances of connection wires in the experimental setup.

In experiments, Case 6 and Case 11 of which voltage bandwidth of DSTATCOMs were set to 240 ± 3 V and there was impedance in between DSTATCOMs, reactive power have been shared between DSTATCOMs only when the voltage was regulated at the upper limit. In these experimental cases, only one unit has contributed to regulate voltage at the lower limit. In experiments listed in Table E.1 excluding, Cases 1, 6 and 11, the DSTATCOM that was configured with

the smaller voltage bandwidth has regulated the voltage at steady-state.

Experimental results obtained by operating two PV systems, that is Case 12 are shown in Fig. E.17. In this experiment, PV systems have failed to regulate PCC voltages at the reference voltage levels. This was due to a measurement error of voltage transducers used in PV systems to measure PCC voltage. The measurement error of transducers was found as a negative error meaning that the measured voltage was less than the actual voltage. This voltage measurement error of voltage transducers of PV systems have an impact on results obtained from Case 14 and 15.

The experimental results presented in Fig.E.18, Fig.E.19 and Fig.E.20 indicate that either DSTATCOM_1 or DSTATCOM_2 has contributed to regulate the voltage when the system has reached steady-state. In these experiments, the PV system of which the voltage control function was enabled has only contributed during the transient phase. This was because a DSTATCOM was used to regulate the voltage of the high sensitive node, PCC_2 in Case 13 and 15. In Case 14 only DSTATCOM_1 has contributed to regulate PCC_1 voltage because of voltage measurement errors of voltage transducers of PV systems. PCC_1 and PCC_2 are as marked in Fig. E.16.

In all the experiments of which results are presented in Fig. E.5–Fig. E.15 and Fig. E.17–Fig. E.20, dynamic interactions between DSTATCOMs and between DSTATCOMs and PV systems that may impact the stable operation of theses systems are not present. However, reactive power sharing between utilised converter systems has not been effective in most of the experiments.